Ion Transfer Dynamics of Polyaniline and Its Derivatives in Energy Storage and Water Purification

Thesis submitted for the degree of

Doctor of Philosophy

at the University of Leicester

by

Abdulcabbar Yavuz, BSc (Ankara)

Department of Chemistry

University of Leicester

2015

UNIVERSITY *of* Leicester

Abstract

Ion Transfer Dynamics of Polyaniline and Its Derivatives in Energy Storage and Water Purification

Abdulcabbar Yavuz

This thesis concerns the electrochemistry of electroactive conducting polymer films in novel ionic liquid media of relevance to energy storage devices and in aqueous media for water purification. The processes taking place at the interfaces of the electrolytes and modified electrodes are important for improving the performance of electrochemical devices. Understanding physical and chemical behaviours of both components and their interfacial dynamic are the aims of this thesis. Polyaniline (PANI), its derivatives and copolymer modified electrodes were deposited with a combination of electrochemical (cyclic voltammetry) and acoustic wave (EQCM) measurement. The optical, electrochemical and morphological behaviours of the resulting films were characterised. Quartz crystal impedance analysis was for the first time used to identify deviations in liquid behaviour from Newtonian, depending on temperature. Ion exchange dynamics of PANI modified electrode in deep eutectic solvents (DES) was used to shed light on supercapacitor applications. Various aspects of the behaviour of PANI films exposed to DES media in the potential range corresponding to p-doping were identified. The rate limiting process, different switching processes and performance of resulting films depend not only on the film coverage but also on the growth conditions. PANI films cycled in non-aqueous media for supercapacitor applications were also used in non-acidic medium for the Electrically Switched Ion Exchange (ESIX) process. The concept is that PANI oxidation is accompanied by fluoride uptake in neutral solution and then eliminates fluoride into a different aqueous acidic waste stream. The mechanism and fundamentals of this concept were monitored by using the EQCM.

Acknowledgements

I dedicate this thesis to my parents (Sarya-Osman) and my sister (Gurbet).

It teaches us first by tutors and books, to learn that which is already known to others, and then by the light and methods which belong to science to learn for ourselves and for others; so making a fruitful return to man in the future for that which we have obtained from the men of the past.

Michael Faraday (Lecture notes of 1858, quoted in *The Life and Letters of Faraday*(1870) by Bence Jones, Vol. 2, p. 403)

Life should not be estimated exclusively by the standard of dollars and cents. I am not disposed to complain that I have planted and others have gathered the fruits. A man has cause for regret only when he sows and no one reaps.

Charles Goodyear (a self-taught chemist who developed a process of vulcanisation in 1839, turning rubber into a material with limitless possible uses)

Contents

Chapter 4: Synthesis of Polyaniline and Aniline-based Copolymers from Aqueous Media 78

Chapter 5: Temperature Effects on the Viscosity of DES Electrolytes...133

Chapter 6: Optimization of Polyaniline Ion Exchange Dynamics in Deep Eutectic Solvents for Supercapacitor Applications 179

Chapter 7: Application of Aniline-based (Co)polymers for Extraction of Fluoride Ion from Water

Chapter 8: General Conclusions and Future Work

Abbreviations

A	electrode area (cm^2)
B	bandwith (Hz)
C_{OX}	concentration of oxidised species (mol dm^{-3})
C_{RED}	concentration of reduced species (mol dm^{-3})
C_s	specific capacitance (F g^{-1})
C_∞	concentration in bulk of solution (mol dm^{-3})
Γ	surface coverage of the polymer (mol cm^{-2})
ρ_q	density of quartz (2.65 g cm^{-3})
ρ	density of the liquid (g cm^{-3})
D	diffusion coefficient (cm^2 s^{-1})
δ	decay length (m)
E	electrode potential (V)
E_a	activation energy for viscous flow (J)
E^0	standard electrode potential (V)
E_{pa}	anodic peak potential (V)
E_{pc}	cathodic peak potential (V)
f	frequency (Hz)
f_s	resonant frequency (Hz)
f_0	fundamental frequency of a QCM (Hz)
F	Faraday constant (96 485 C mol^{-1})
γ	shear rate(s^{-1})
h_q	quartz thickness (m)
i	current (A)
i_p	peak current

i_{pa}	anodic peak current (A)
i_{pc}	cathodic peak current (A)
λ	wavelength (m)
λ_q	acoustic wavelength (m)
M_m	slope of the mass change *vs.* charge
m	mass of the film (g)
m_q	mass of the quartz crystal (g cm^{-3})
n	number of electrons
N	harmonic number
η	viscosity of the liquid (Pa)
OX	oxidised redox sites
R	gas constant (J mol^{-1} K^{-1})
RED	reduced redox sites
Q	charge (C)
σ	shear stress (Pa)
t	time (s)
T	temperature
v	scan rate
v_q	wave velocity (3.34x10^5 cm s^{-1})
x	distance (m)
Z_q	acoustic impedance of the quartz (8.84x10^6 kg m^{-2} s^{-1})
ANI	aniline
CE	counter electrode
ChCl	choline chloride
DES	Deep Eutectic Solvent
EQCM	Electrochemical Quartz Crystal Microbalance

FTIR	Fourier Transform Infrared Spectroscopy
G	Glycerol
HBD	Hydrogen Bond Donor
IL	ionic liquid
OAP	*o*-aminophenol
OT	*o*-toluidine
PANI	polyaniline
P(ANI-OAP)	poly(aniline-*co-o-* aminophenol)
P(ANI-OT)	poly(aniline-*co-o*-toluidine)
PG	propylene glycol
POAP	poly(*o*-aminophenol)
POT	poly(*o*-toluidine)
QCM	Quartz Crystal Microbalance
RE	reference electrode
RV	rotational viscometer
SEM	Scanning Electron Microscope
TSM	Thickness Shear Mode
U	urea
W	wateline
WE	working electrode

Chapter 1: Introduction

1.1. Overview

The modification of electrode surfaces with electroactive polymer films has attracted considerable attention due to a variety of possible applications (see section 1.5.). A modified electrode is an electrode having a thin film of material attached onto its surface to change the properties of the electrode depending on its targeted function. The electrode surface, coated with a chemical species, does not have direct contact with the bathing solution. Therefore, the charge transfer reactions must take place through the modifying layer. In doing so, the chemical, electrochemical and optical properties of the surface species dictate the properties of the resultant electrode.[1] Hence, the choice of the modifier could tune the reactivity, selectivity and specificity of the electrode.[2] Therefore, electrochemists have used this novel approach with a variety of materials to design new types of electrodes having the desired properties and characteristics (since the first generation of chemically modified electrodes,[3-10] in which tin oxide was modified with ligands such as amine and pyridyl,[11] as reported by Murray *et al.* in 1975).

The attachment of the modifier onto the electrode substrate can be managed through chemisorption,[12-14] physisorption[15-17] and covalent attachment.[18-20] A variety of materials could be deposited onto the electrode in order to yield unique and specific chemical effects, which lead to various applications in which the modified electrodes are used. Generally, the type of the modifying layers can be subdivided into three main categories based upon the adlayer composition. These include *inorganic thin films* such as metal oxides[21] and zeolites,[22] *self-assembled monolayers* such as thiols[23] and N-heterocyclic carbenes,[24] and various types of *polymer films* such as polyaniline (PANI),[25] polypyrrole,[26] poly(vinylferrocene).[27] Deposition, characterisation and application of polymer modified electrodes are investigated in the research carried out in this thesis.

1.2. Polymer Modified Electrodes

The first modified electrodes in which polymeric materials were used, were reported by van de Mark and Miller[28, 29] using poly(4-nitrostyrene), and Merz and Bard[30, 31]

working on poly(vinylferrocene). Since then, polymer modified electrodes prepared from diverse materials have been studied by other research groups.

Polymer modified electrodes are porous in nature and offer a larger reactive surface area than monolayer modified or bare electrodes. While the reaction occurs in a 2D zone in the interface of a monolayer modified electrode, a 3D reaction zone is created in polymer modified electrodes.[32] Therefore, a far greater species flux can enter into the bulk of the polymer modified films[33] (see Figure 1.1).
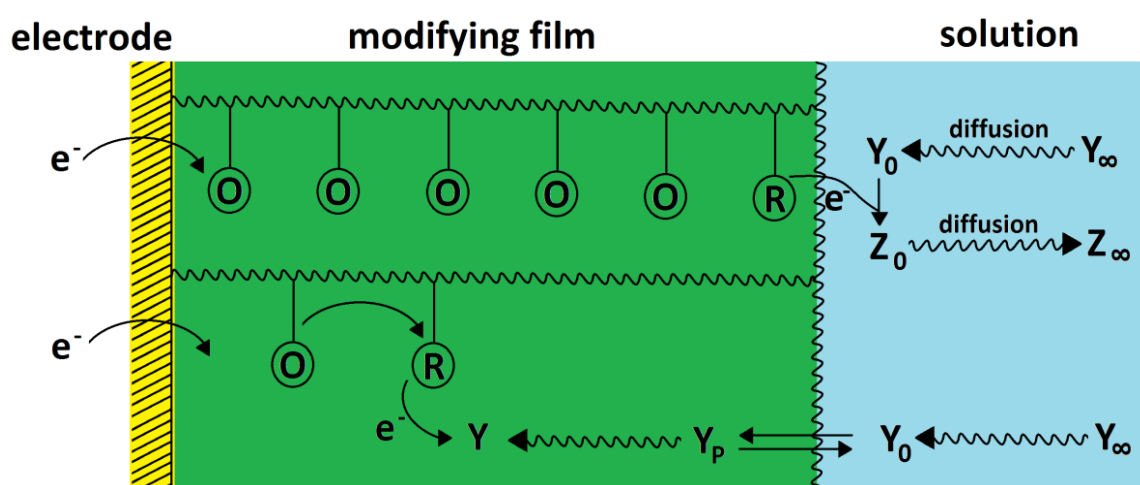
Figure 1.1: Schematic representation of polymer modified electrode. At the polymer/electrode interface, there is an electron exchange due to potential perturbation and at film/solution interface, ion and solvent transfers occur due to electroneutrality and activity constraints. Y and Z represent electroactive species getting reduced/oxidised and the subscript "p" denotes species diffusing in the bulk of the polymer.[34]
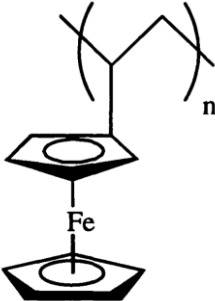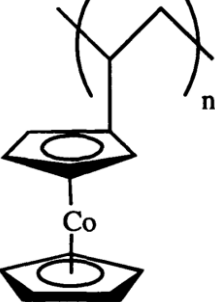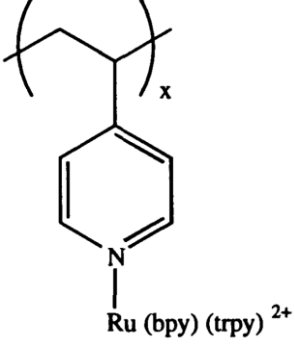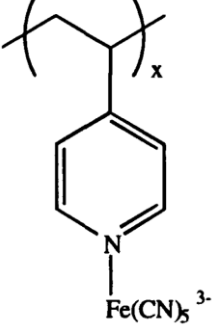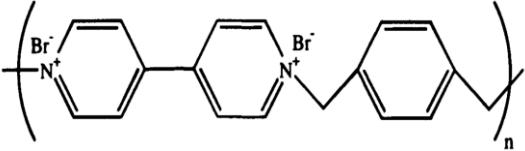
Electron transfer occurs at the electrode/film interface and oxidation (or reduction) of the modified film species involves the incorporation/expulsion of counter ion species in order to maintain electroneutrality within the polymer matrix. Counter ion movement could also accompanied by the ingress/egress of neutral species (solvent or/and salt).

Electroactive polymer films are classified into two main groups based on the backbone of the polymer structure: redox polymers and conducting polymers.

1.2.1. Redox Polymers

Redox polymers containing discrete redox sites can either occupy sites on the polymer branches or be incorporated directly into the polymer backbone.[35] It is proposed that the redox conversion take place through a *hopping-type mechanism*[36-38] between neighbouring redox sites within the film as depicted in Figure 1.1. Counter ions are transfered into/from the film to maintain electroneutrality of redox polymers. Some examples of redox polymers are shown in Table 1.1.

Table 1.1: Examples of redox polymer structures.

Name	Structure
Poly(vinylferrocene)[39-42]	
Poly(vinylcobaltocene)[43]	
Poly(pyridyl) ruthenium(II) complex[44-46]	
Poly(pyridyl) iron(II) complex[47-49]	
Poly(viologen)[50, 51]	

1.2.2. Conducting Polymers

In contrast to redox polymers, conducting polymers have a conjugated backbone and thus they are also referred to as *conjugated polymers*. There is a large degree of delocalisation of π-electrons in the backbone of a conducting polymer. The motion of delocalized electrons takes place via this conjugated system.[52, 53] Oxidation (reduction) of conducting polymers necessitates the introduction of positive (negative) charges into the polymer. The process of oxidation or reduction of the polymer is termed *doping*. Incorporation of anion (cation) occurs simultaneously with p-doping (n-doping) in order to maintain electroneutrality of the oxidised (reduced) film. On doping, the counter-ions do not react chemically with the polymer but associate with simply redox sites along the polymer chain. Conjugated polymers are conducting in the doped state and insulating in the undoped state. Therefore, doping (undoping) of polymers with counter ions associating with the redox site can easily change the conducting (non-conducting) state of polymer.[52]

The first conducting polymer (polyacetylene in the form of a thin film) was discovered by accident in 1974 by Shirakawa,[54] upon doping polyacetylene with halogen, the conductivity of the polymer increased over eleven orders of magnitude.[55, 56] Since then, a vast amount of research related to conducting polymers has been conducted. Five parent systems providing most conducting polymers are shown in Table 1.2.

Conducting polymers, as the main topic of this thesis, are of a great interest in polymer science due to their interesting structure and chemical nature. They have high conductivity,[57] from few S cm^{-1} to 500 S cm^{-1} and which can be increased up to 3065 S cm^{-1} with copolymerisation or pre-treatment processes.[58] The energy gap between the conduction and valence bands for conducting polymers is low, typically 1-3 eV compared with conventional polymers (ca. 10 eV).[59] Conducting polymers have various mechanical properties such as mechanical flexibility, which is a key advantage for technological devices[60] which could be tailored by different processing techniques. Conducting polymers are prepared from inexpensive materials such as aniline, pyrrole, thiophene, and their derivatives, by simple chemical or electrochemical polymerisation

processes. The investigation of aniline polymerisation and the resulting polymer (polyaniline) are studied in the research presented in this thesis.

Table 1.2: Examples of conducting polymer structures.

Name	Structure
Polythiophene[61-65]	
Polyaniline[66-70]	
Polypyrrole[71-74]	
Polyacetylene[75-77]	
Polyparaphenylene[78-80]	

1.3. Polyaniline

PANI was selected for the research presented in this thesis due to a variety of advantages over other conducting polymers. These are high environmental and chemical stability, low cost, high level of electrical conductivity and a wide range of possible applications,[81] given in section 1.5.

1.3.1.   Structure and Synthesis of Polyaniline

The oxidation states of PANI consist of benzoid and quinoid (oxidation of benzoid structure) units,[82] shown in Figure 1.2. PANI is different to most other conducting polymers, such as polythiophene and polypyrrole, as it exists in three different forms depending on the degree of oxidation[83] which include a fully reduced state (leucoemeraldine), a half oxidized state (emeraldine) and a fully oxidised state (pernigraniline), where x is 1, 0.5 and 0 respectively, presented in Figure 1.2.
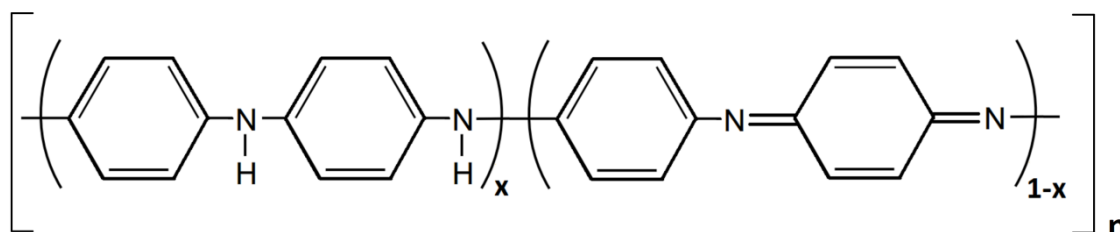
Figure 1.2: Oxidation states of PANI (x = 1, leucoemeraldine), (x = 0.5, emeraldine), (x = 0, pernigraniline)

PANI is different to other conducting polymers as its base and salt forms can be switched rapidly by treatment with acid or base.[84] Another difference of PANI from polythiophene and polypyrrole is the polymerisation process, in which the N heteroatom of PANI participates in the polymerisation process with head to tail configuration.[85] Additionally, the participation of the N heteroatom in the conjugation of the conducting form of PANI is greater extent than the S and N heteroatoms in polythiophene and polypyrrole.[52, 81]

There are several polymerisation techniques used to synthesise PANI from aniline monomers. These include chemical polymerisation,[86] electrochemical polymerisation,[87] vapour-phase deposition,[88] photochemically initiated polymerisation,[89] enzyme-catalysed polymerisation[90] and polymerisation using an electron acceptor.[91] However, among them, electrochemical deposition is the most attractive technique to produce PANI because of its ability to control the desirable properties of PANI film (*e.g.* morphology, thickness and electrical properties) by varying the conditions of electrolyte bath and applied voltage.[92]

1.3.2.   Polymerisation of Aniline

Although reductive polymerisation of aniline has been reported,[77, 93] generally aniline is polymerised with electrochemical (or chemical) oxidation in acidic electrolyte. Higher pH (pH > 4) leads to the formation of short conjugation oligomeric material (undesired branched product).[94, 95] Acidic medium helps aniline to be soluble in water and to generate the doped emeraldine salt form.[96] Electrochemical polymerisation is achieved by employing potentiostatic, potentiodynamic or galvanostatic techniques.[97]

The generally accepted electrochemical mechanism of aniline polymerisation is an $E(CE)_n$ process (see Figure 1.3).[52] Electrochemical polymerisation mainly consists of four different steps. The first step is the formation of aniline cation radicals by the oxidation of aniline on the electrode surface (considered as the rate-determining step).[96, 98] The next step is the coupling of the radicals, mainly via the N- heteroatoms with the para- position of quinoid structure yielding a dicationic dimer species, followed by elimination of two protons.[52, 99] In third step, the oxidation of the dimeric radical cation occurs on the surface of the electrode and the reaction of the radical cation of the dimer with an aniline cation leads to the formation of aniline oligomers. The schematic representation of these steps is shown in Figure 1.3. The fourth step, not shown here as it is the same as third step, is chain propagation by solid state polymerisation.[53]

1st step: Oxidation of aniline monomer
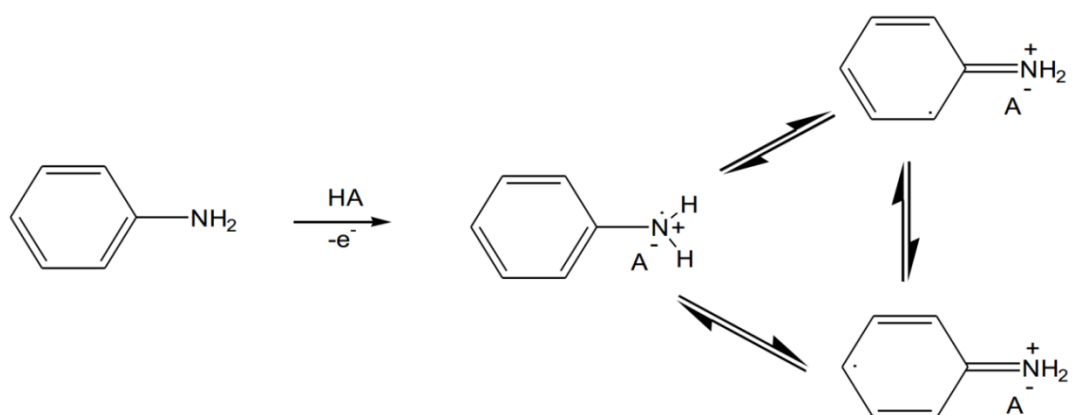
2nd step: Radical coupling and re-aromatisation
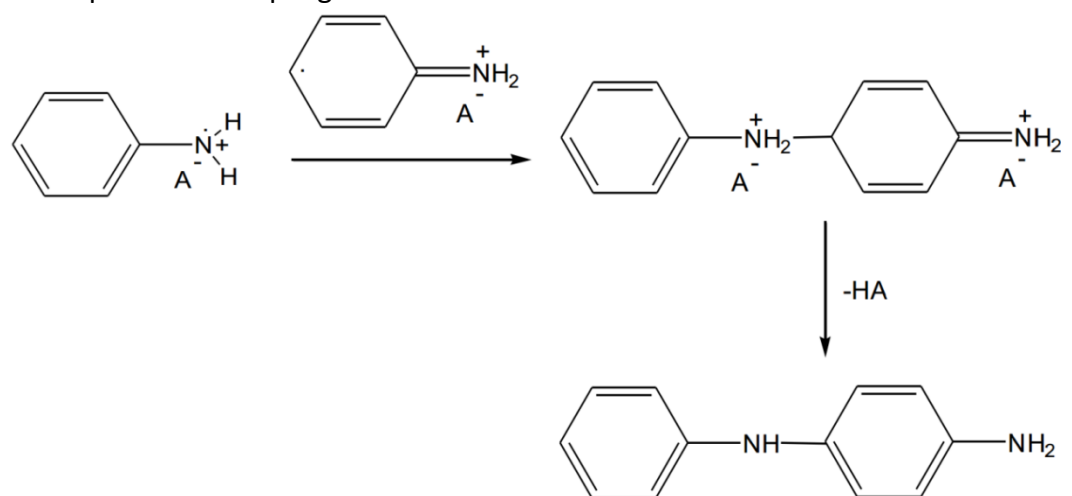
3rd step: Oligomerisation of aniline
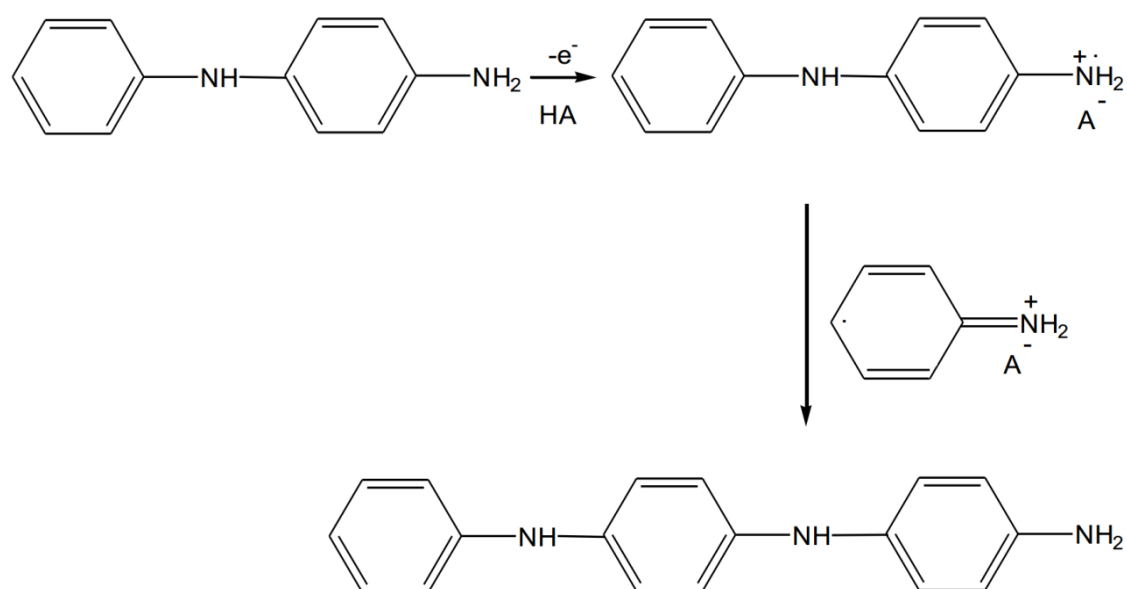
Figure 1.3: Schematic representation of the electropolymerisation of aniline.[52]

1.3.3.　　Properties of Polyaniline

The counter anions present in the deposition electrolyte dope the PANI during film formation to maintain electroneutrality. The doping mechanism shown in Figure 1.4 is between leucoemeraldine base and emeraldine salt.[53, 83, 100] As indicated previously, the partly oxidised form of PANI (emeraldine salt) is conducting and all other forms of PANI are non-conducting.

The switching between oxidation states of PANI influences not only conductivity changes of the film but also the optical changes. When the emeraldine salt of PANI is formed, the addition of acid (or a base) for protonation (deprotonation) changes the PANI oxidation states, leading to the optical change of PANI shown in Figure 1.4.
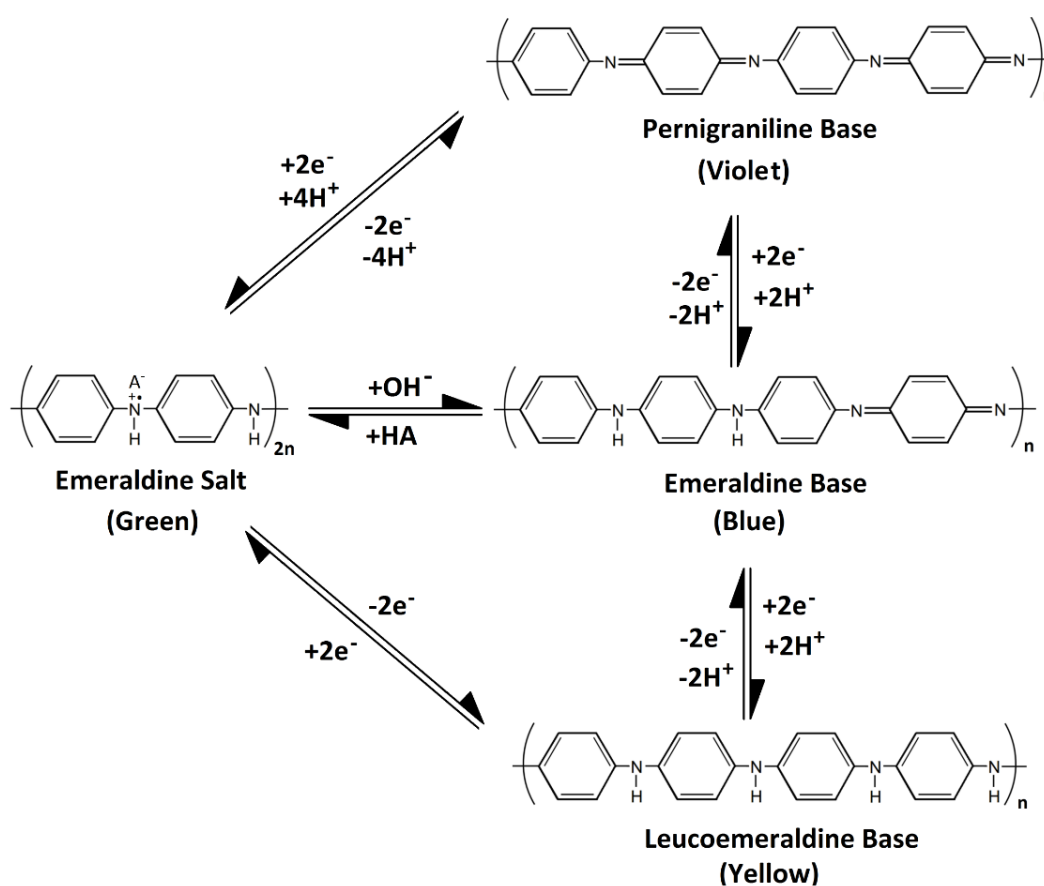
Figure 1.4: The redox reactions between the forms of PANI.

When the pH of the aqueous electrolyte used for PANI switching is greater than 4, the formation of the emeraldine salt does not occur and PANI becomes non-electroactive.[101]

The conducting emeraldine salt (green) can be converted to fully oxidised dark blue pernigraniline salt (not shown here) and the treatment of pernigraniline salt with alkali forms violet pernigraniline base. The emeraldine salt is turned to blue non-conducting emeraldine by alkali solution and also the emeraldine salt is reduced to yellow leucoemeraldine form of PANI.[102] Cyclic voltammetry can readily monitor the electrochemical switching amongst the oxidation states of PANI.

PANI has a unique electronic conduction mechanism due to the involvement of the nitrogen atom in the formation of radical cation in PANI. The radical cation of the most other conducting polymers is formed over carbon atoms.[52] Additionally, the nitrogen atom in PANI is involved in the conjugated double bond system of the PANI structure for doping during the oxidation reaction.

The complexity of chemical and physical behaviour of PANI has been studied by different research groups to understand the composition, structural and dynamic properties of PANI film by using different techniques.

1.4. Characterisation Techniques of Polymer Modified Electrodes

Over the last three decades, a vast amount of research related to modified electrodes and their potential applications has been conducted.[103-110] The physical and chemical characterisation of modified electrodes is a necessity to improve the design and performance of the resulting film. The electrochemical, morphological and optical properties of electroactive polymer films require to be explored in depth. Great interest was given in this thesis to the mechanism of the charge transfer, mass transport, redox composition and extent of solvation (salt) across the interfaces of films and electrolyte (both aqueous and ionic liquid electrolyte). Additionally, the

kinetics and mechanism of the polymerisation of the monomers and the correlation of the structures and compositions of resulting films were studied.

A number of different techniques provide complementary information on different features of modified electrodes.[111-114] Among them, electrochemical methods are powerful methods to study the redox transformation of electroactive films and they can provide useful information on thermodynamic and kinetic parameters of the system.[53, 115-121] However, as expected, electrochemical techniques alone cannot be sufficient to obtain all information related to characterisation of polymer modified electrodes. Non-electrochemical methods (described below) are also introduced to provide compositional and structural information of conducting polymer electrodes.[122-127] Therefore, the selection of characterisation techniques reviewed briefly below splits into two different categories: electrochemical techniques and non-electrochemical techniques.

1.4.1. Electrochemical Techniques

Electrochemical techniques are used so widely for characterisation of polymer modified electrodes that conducting polymers can be categorised as a sub-discipline of electrochemistry. Electrochemical techniques are used to monitor not only the film response to their electrolyte but also the deposition mechanism of films. Among these techniques, cyclic voltammetry is the most popular one.

1.4.1.1. Cyclic Voltammetry

Cyclic voltammetry is an easy and popular technique to use and provides a wealth of information related to the electrochemical production of modified electrodes and the surface species of the resulting modified film.[68, 128-131]

A standard electrochemical cell requires a three-electrode system consisting of the working electrode (WE), counter electrode (CE) and reference electrode (RE) in an electrolyte solution. This technique involves sweeping the potential of the WE back and forth two or more times between pre-set points (E_1 and E_2) at a steady scan rate (v

/ Vs^{-1}); more experimental details are presented in chapter three. A potentiostat controls the applied potential between the WE and RE and the current is measured between the WE and CE. The current is presented as a function of the potential, which provides information about the characteristics and properties of the electrochemical processes in solution or at the electrode surface.[132, 133] The charge, which is a quantity directly related to the amount of the electroactive species, can be calculated from the integration of current with respect to time. Kinetic data from electrochemical processes can be extracted by using cyclic voltammetry with variation of the scan rate (experimental timescale). Cyclic voltammetry can detect less than a monolayer of species adsorbed onto the electrode. More theoretical aspects will be discussed later in chapter two.

1.4.1.2. Potential Step

While the potential is scanned between two points at a constant scan rate in cyclic voltammetry, in this technique the potential of the WE is instantaneously changed from an initial value in which there is no chemical reaction at the electrode surface to a final value where the electrochemical reaction of interest occurs. A current – time (chronoamperometry) or charge – time (chronocoulometry) response is recorded for potential step experiments. While chronoamperometry measures the rate of reaction, chronocoulometry monitors the extent of reactions.[132, 133] Depends on the potential applied the diffusion coefficient of the system is determined by potential step experiments.

1.4.2. Non-Electrochemical Techniques

1.4.2.1. Electrochemical Quartz Crystal Microbalance

The electrochemical quartz crystal microbalance (EQCM) is based upon the converse piezoelectric effect experienced when an alternating voltage is applied to two electrodes, situated on the opposite faces of the quartz crystal shown in chapter two. Mechanical oscillation then takes place within the crystal lattice but at the resonant frequency of the crystal. The crystal loaded with mass causes a decrease in the

resonant frequency. The frequency decrease can be determined accurately and is proportional to the mass change.[134] In the EQCM technique, one side of the quartz is in direct contact with the electrolyte solution and is used as the WE, the another side is exposed to the air.[135] This *in-situ* technique monitors changes in the mass of the WE during electrochemical experiments. Electropolymerisation of material onto the metal electrode surface of quartz crystal leads to a mass change detectable by EQCM.[66, 136-142] The mass change occurring during redox switching of a electroactive modified electrode can also be measured by using EQCM.[66, 141-146] The EQCM response is used to monitor the electrochemically driven changes of the populations of ion, salt and solvent species in polymer films through the associated mass changes. When the mass changes are measured with the voltammetric response, a quantitative correlation between the mass changes and the electron flux can be measured. As the EQCM allows the measurement of very small mass changes (10^{-9} g cm^{-2}) and the charge of exchange is identified by potentiostatic measurement, the insertion (expulsion) of counter ion, salt and/or solvent ingress (egress) can be identified through the combination of the QCM and electrochemistry techniques.[51, 66, 127, 146]

The EQCM is used as a complementary and routine technique for the investigation of modified electrode processes by providing invaluable *in-situ* information. As EQCM is used for the mass change of rigidly compact material onto the surface, it can also be used for non-rigid deposited film to provide information about the viscoelastic properties[126, 147-154] of the modified films.

1.4.2.2. Spectroscopic Techniques

Information of structural changes of modified electrodes at the atomic and molecular level in response to electrochemical stimuli can be extracted by conventional spectroscopic techniques. The most common spectroscopic techniques are Ultraviolet-visible (UV-vis) absorbance and IR spectroscopies. The nature of the redox entities introduced onto the electrode surface is examined by means of these techniques. In this section, the significance of these techniques used for the characterisation of polymer modified electrodes[33, 155-160] is reviewed.

1.4.2.2.1. Ultraviolet- Visible Spectroscopy

UV-vis spectroscopy is used to investigate the amount of transmitted – absorbed light near ultraviolet and visible range by the materials. Requirement of a tiny amount of sample to detect the monolayers at the electrode surface suggests the technique has high sensitivity. The polaron and bipolaron forming during the oxidation of conducting polymers can be identified and band gap energies of the conducting polymers can be calculated.[161, 162] As an optically transparent substrate electrode is required to collect transmission spectra of polymers,[163-166] the commercially available tin oxide or indium doped tin oxide electrodes are employed as substrate electrode on glass. An electrochemical cell is constructed to obtain the UV-vis spectra *in-situ* in which a metal wire as CE and a small RE can be used without blocking the optical beam. The limitation of non-transparent electrodes is overcome by using reflectance mode UV-vis spectroscopy.[167] Monitoring of the absence (or appearance) of additional absorption bands, which were not present before the potential perturbation, can be used as fingerprints for the electrogenerated species.[168, 169]

1.4.2.2.2. Infrared Spectroscopy

Infrared spectroscopy is used to investigate the vibrational motions of the molecules.[170] Infrared radiation is absorbed at the frequencies that correspond to different energy level for molecular bond vibrations. Infrared spectroscopy provides invaluable information on chain branching and chemical functionality of the polymer modified electrodes. A variation of the infrared technique is Fourier transform infrared spectroscopy (FTIR) which allows the acquisition of complete spectra in less than one second.

FTIR, providing specific information on molecular orientation and identity at electrode surfaces, probes vibrational motions based on conducting polymer films. Characteristic vibrations, due to the nature of molecules in the polymer and structure of the polymer, are excited by the application of infrared radiation to the system.[172-176]

1.4.2.3. Surface Imaging Techniques

The study of topographic and morphological properties of polymers on electrode surfaces can be used to understand the growth mechanism and local structural changes of electroactive polymers with preparation conditions.[177-181] The most two common imaging techniques are given in this section for the characterisation of polymer modified electrodes: scanning electron microscopy (SEM) and atomic force microscopy (AFM).

1.4.2.3.1. Scanning Electron Microscopy

SEM, using electrons rather than light to form an image, has some advantages while used for surface imaging of modified electrodes.[156, 163, 182-188] These are that a large amount sample could be studied at one time, producing high magnification images and even obtaining images at high resolution.

A SEM is a microscope that produces an image of the sample of interest by scanning a beam of electrons across the surface. When the electrons interact with the atoms, secondary electrons (producing SEM images), backscattered electrons and photons (characteristic X-rays which are utilized for elemental analysis and continuum X-rays) are produced and information about the sample (morphology, chemical composition, crystalline structure) is revealed. Secondary and backscattered electrons are the most commonly used electrons to image samples.

The electron gun generates a beam of electrons and these electrons are accelerated to an energy of between 1 and 30 keV by the anode. A series of condenser lenses focusses the electron beam to a spot about 0.4 nm to 100 nm in diameter. Two electromagnetic coils beneath of magnetic lens accomplish scanning in the raster pattern. One coil deflects the beam in the x direction and another deflects the beam in the y direction. After the electron beam hits each spot on the sample, secondary electrons are removed from the surface. The secondary electron current which reaches the detector is recorded to obtain an image. A plot of the secondary electron current and the probe position on the surface gives the microscope image. A schematic representation of scanning electron microscope is given in Figure 1.5.

Normally in SEM, the sample has to be conductive and the instrument must be capable of operation in a low vacuum mode in order to enable the electron beam to travel in straight lines.
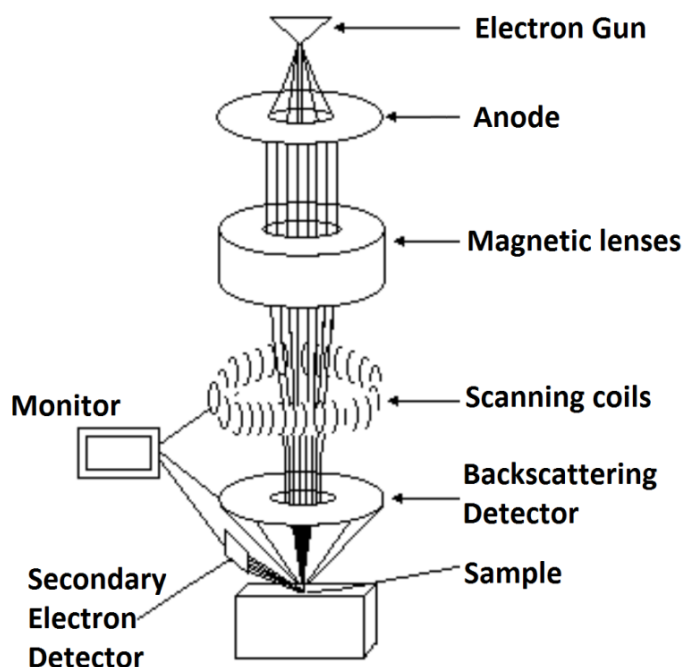
Figure 1.5: Schematic representation of SEM

1.4.2.3.2. *Atomic Force Microscopy*

AFM is a technique used to obtain an image of the sample surface, interpreted as a topographical image commonly used for morphological characterisation of electroactive polymer electrodes.[176, 179-181, 189-191] A probe single atom tip attached to a cantilever mounted on a scan head is scanned horizontally along the x-axis recording each point as a height. The probe is returned to the start of the line. After the probe is moved down the sample (y direction), the next line is scanned. This process is repeated for the whole surface area of interest. The movement of the cantilever is monitored by the movement of a laser beam reflected from an attached mirror. An AFM image is a plot of tip deflection *vs.* lateral position. A repulsive interaction between two surfaces is considered as contact. This occurs just when the distance is very small. When the repulsive interactions are not dominant, the force between the

two surfaces is attractive because of van der Waals interactions. Figure 1.6 demonstrates a schematic representation of atomic force microscope.
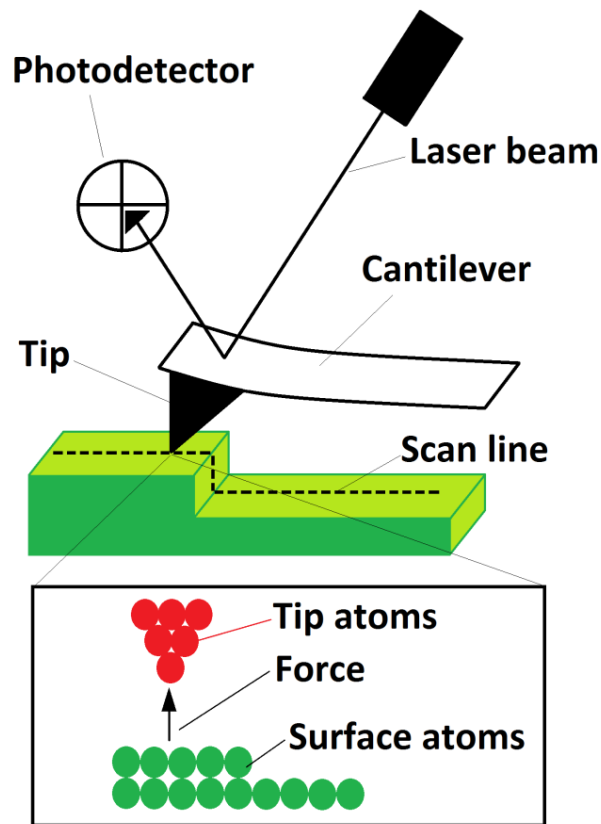
Figure 1.6: Schematic representation of AFM.

The AFM can be implemented in three different modes: tapping mode, contact mode or non-contact mode. In contact mode, which is destructive, the tip is dragged across the surface of the sample. Non-contact mode has a small distance (500 – 1500 nm) between probe and the sample. Attractive and repulsive interatomic forces occur between the sample and the tip. In tapping mode, interatomic forces between the sample surface and the probe tip lead to the cantilever to be deflected as the samples's surface topography changes. The cantilever is oscillated intermittently - generally at a frequency of 50 kHz to 500 kHz- by an external drive signal. A laser light reflected from the back of the cantilever measures the deflection of the cantilever. Tapping mode is not as destructive as contact mode and is used to image soft materials. The advantage of this technique is that sample does not need to be conducting.

1.5. Application of Polymer Modified Electrodes

The properties of conducting (π-conjugated) polymers have been studied for numerous novel technological devices such as organic light-emitting diodes,[192, 193] organic photodetectors,[194-196] organic solar cells,[197-200] organic thin film transistors,[201-203] sensor devices,[204-207] electrochromic devices,[208-210] corrosion inhibitors,[211-213] actuators,[214-216] energy storage devices,[128, 217, 218] electromagnetic interference shielding,[219-221] electrocatalysis[120, 222, 223] and water purification.[224] Most of these applications depend on the redox reaction of the conducting polymer accompanied by the compositional and structural changes of polymer materials.

The concept of electrochromism used in display devices is based upon the change of the polymer with the change of the redox states of conducting polymers. Swelling/shrinking of materials are the key factors in artificial muscles and conducting polymers used in these applications as they are doped. In electrocatalysis and sensors, the conducting polymer films act as a host mediating electron exchange between the electroactive species in the solution and the underlying electrode. Since conducting polymer electrodes are promising materials in technological and commercial markets, there are some practical challenges requiring further investigation. Their composition and structure are widely studied by using different techniques. However, their dynamics for practical application have not been studied widely. The dynamics and mechanism of PANI for energy storage and water purification applications are studied in depth in chapter six and chapter seven of this thesis, respectively.

1.6. Deep Eutectic Solvents

Classical solutions are formed from solvent molecules and solvated ions. The salts can also be melted thermally. These liquids are called molten salts or ionic liquids (IL) and consist of only ions without any molecular solvents. Addition of other salts into the ILs can lower the high melting points of ILs forming a eutectic.[225] The salts, having a low melting point and maintaining liquid phase at room temperature, are called room temperature ionic liquids (RTIL).[226] The physical and chemical properties of RTILs are similar to ILs but RTILs have superior practical applications [225] as they can be handled

easier. RTILs are mainly used in the industry as synthesis media[227-229] and as metal processing electrolytes.[230-232]

RTILs have high ionic conductivity, wide electrochemical windows, wide thermal stability and non-flammability.[233] DESs share similar physical properties when compared to ILs[234] but DESs have their own advantages as they are made of cheap raw materials, are simple to prepare[235] and have good biocompatibility.[236] For example Ethaline, used mainly in this research, consists of choline chloride (an additive in chicken feed) and ethylene glycol.

DESs contain large, non-symmetric ions having low lattice energy and thus low melting points. They are formed from a eutectic mixture of Lowry (Brønsted) acids and bases containing a variety of ionic species. The charge delocalisation takes place via hydrogen bonding between an anion and hydrogen bond donor. This charge delocalisation makes the melting point of the mixture smaller than melting points of the individual components.[237]

Negligible volatility and non-flammability of DESs eliminates the problem of solvent evaporation and makes them desired solvents over more toxic molecular solvents. Additionally inexpensive components of DESs and large scale availability and consideration as "green solution" makes them a good candidate in the field of electrochemistry.[234] Therefore, DESs are under investigation as solvents for electrochemical applications such as batteries, fuel cells, metal surface finishing, and nuclear waste treatment. In this project, the using of DESs as electrolyte in supercapacitor application was studied.

1.7. Aims and Scope

The general objective of the research carried out in this thesis is to enhance the understanding of electroactive conducting polymer films with regard to their application in energy storage and water purification devices.

The first set of objectives involves the characterisation of polymer modified electrodes and the novel electrolytes to which they are exposed. As the processes which take place at the interfaces of the modified electrodes and electrolytes are important for improving the performance of electrochemical devices, both components (electrode and electrolyte) are required to be well understood. The first objective was to characterise the electrochemical, optical and spectroscopic behaviour of aniline-based conducting (co)polymers. The second objective was to determine the temperature effect on ionic liquid electrolyte viscosity. In both instances the goal is to rationalise diffusion phenomena. The method chosen to accomplish this is detailed analysis of the frequency response of high frequency quartz crystal resonators.

The second set of objectives is to determine and parameterize the ion transfer dynamics of PANI films under conditions (of film thickness and ambient medium) relevant to supercapacitor and water purification devices. The goal in the case of supercapacitor application is to determine the variation of ion exchange dynamics during charging/discharging of PANI films in DESs media as a function of film surface coverage and growth conditions, the composition of the DES and experimental variables (timescale, number of scans, temperature, waiting time). The objective for the application of water purification is to elucidate the dynamics, mechanism, performance and regeneration ability of the (co)polymer films for defluoridation of water.

More specific and detailed objectives for each area are presented at the beginning of each chapter. The interconnection of different facets of the research presented in this thesis is summarised in Figure 1.7.
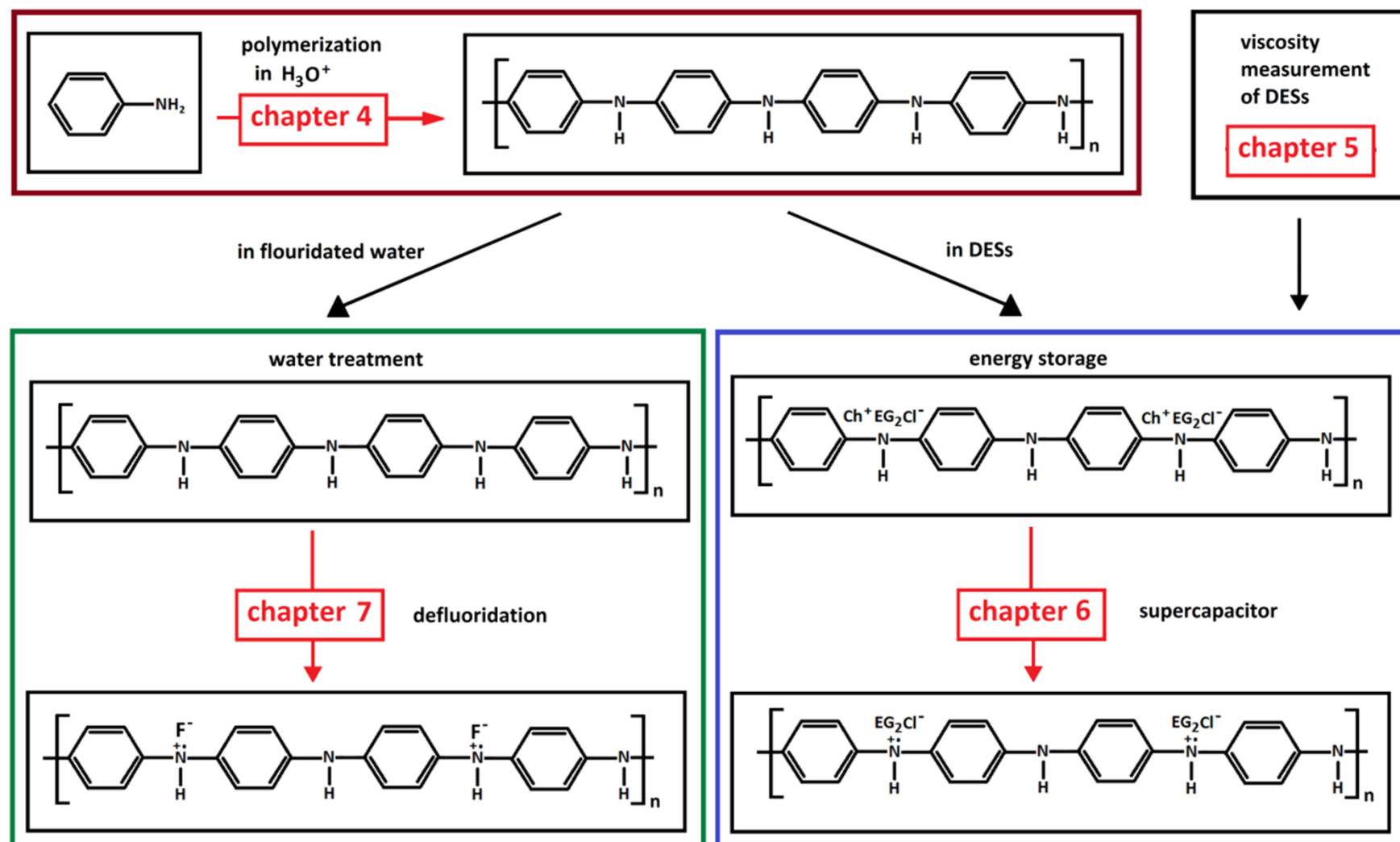
Figure 1.7: Schematic summary of research presented in this thesis.

1.8.   References

1 W. J. Albery and A. R. Hillman, *J. Electroanal. Chem.,* 1984, **170**, 27-49.

2 C. Andrieux, J. Saveant and R. Murray, Molecular Design of Electrode Surfaces, *Wiley & Sons: New York,* 1992, **25**, 10-17.

3 J. R. Lenhard and R. W. Murray, *J. Electroanal. Chem.,* 1977, **78**, 195-201.

4 C. M. Elliott and R. W. Murray, *Anal. Chem.,* 1976, **48**, 1247-1254.

5 P. Moses, L. M. Wier, J. C. Lennox, H. Finklea, J. Lenhard and R. W. Murray, *Anal. Chem.,* 1978, **50**, 576-585.

6 J. Lenhard, R. Rocklin, H. Abruna, K. Willman, K. Kuo, R. Nowak and R. W. Murray, *J. Am. Chem. Soc.,* 1978, **100**, 5213-5215.

7 R. W. Murray, *Acc. Chem. Res.,* 1980, **13**, 135-141.

8 P. K. Ghosh and A. J. Bard, *J. Am. Chem. Soc.,* 1983, **105**, 5691-5693.

9 R. W. Murray, *Annual Review of Materials Science,* 1984, **14**, 145-169.

10 W. Albery and A. Hillman, *Annu.Rep.Prog.Chem., Sect.C: Phys.Chem.,* 1981, **78**, 377-437.

11 P. Moses, L. Wier and R. Murray, *Anal. Chem.,* 1975, **47**, 1882-1886.

12 M. Venanzi, E. Gatto, M. Caruso, A. Porchetta, F. Formaggio and C. Toniolo, *J. Phys. Chem. A,* 2014, **17**, 6674-6684.

13 T. Zaba, A. Noworolska, C. M. Bowers, B. Breiten, G. M. Whitesides and P. Cyganik, *J. Am. Chem. Soc.,* 2014, **136**, 11918-11921.

14 G. Zheng, M. Chen, X. Liu, J. Zhou, J. Xie and G. Diao, *Electrochim. Acta,* 2014, **136**, 301-309.

15 L. Rassaei, M. Sillanpää and F. Marken, *Electrochim. Acta,* 2008, **53**, 5732-5738.

16 Y. Zhou, C. Fuentes-Hernandez, J. Shim, J. Meyer, A. J. Giordano, H. Li, P. Winget, T. Papadopoulos, H. Cheun, J. Kim, M. Fenoll, A. Dindar, W. Haske, E. Najafabadi, T. M. Khan, H. Sojoudi, S. Barlow, S. Graham, J. L. Bredas, S. R. Marder, A. Kahn and B. Kippelen, *Science,* 2012, **336**, 327-332.

17 V. M. García-Suárez, R. Ferradás, D. Carrascal and J. Ferrer, *Physical Review B,* 2013, **87**, 235425.

18 S. Khezrian, A. Salimi, H. Teymourian and R. Hallaj, *Biosensors and Bioelectronics,* 2013, **43**, 218-225.

19 A. Azadbakht and M. B. Gholivand, *Electrochim. Acta,* 2014, **125**, 9-21.

20 S. Zhang, N. Wang, H. Yu, Y. Niu and C. Sun, *Bioelectrochemistry,* 2005, **67**, 15-22.

21 B. Tian, J. Światowska, V. Maurice, S. Zanna, A. Seyeux, L. H. Klein and P. Marcus, *Langmuir,* 2014, **30**, 3538-3547.

22 L. Bonaccorsi, L. Calabrese, A. Freni, E. Proverbio and G. Restuccia, *Appl. Therm. Eng.,* 2013, **50**, 1590-1595.

23 E. H. Wong, G. L. May and C. P. Wilde, *Electrochim. Acta,* 2013, **109**, 67-74.

24 C. M. Crudden, J. H. Horton, I. I. Ebralidze, O. V. Zenkina, A. B. McLean, B. Drevniok, Z. She, H. Kraatz, N. J. Mosey and T. Seki, *Nature Chemistry,* 2014, **6**, 409-414.

25 M. A. Mohamoud, *Electrochim. Acta,* 2014, **139**, 201-208.

26 T. Raudsepp, M. Marandi, T. Tamm, V. Sammelselg and J. Tamm, *Electrochim. Acta,* 2014, **122**, 79-86.

27 P. E. Erden, C. Kaçar, F. Öztürk and E. Kılıç, *Talanta, 134,* 2014, 488-495.

28 Van de Mark, Michael R and L. L. Miller, *J. Am. Chem. Soc.,* 1978, **100**, 3223-3225.

29 L. L. Miller and Van de Mark, Michael R, *J. Am. Chem. Soc.,* 1978, **100**, 639-640.

30 A. Merz and A. J. Bard, *J. Am. Chem. Soc.,* 1978, **100**, 3222-3223.

31 P. J. Peerce and A. J. Bard, *J. Electroanal. Chem.,* 1980, **114**, 89-115.

32 A. Hillman and R. Linford, *Chapters,* **5**, 103-291.

33 R. W. Murray, *Techniques of Chemistry: Molecular Design of Electrode Surfaces*, Wiley-Interscience, New York 1992.

34 M. A. Mohamoud, Ph.D. Thesis, University of Leicester, 2007.

35 G. Inzelt, *Conducting Polymers,* Berlin, Springer, 2012, pp.7-82.

36 F. C. Anson, D. N. Blauch, J. M. Saveant and C. F. Shu, *J. Am. Chem. Soc.,* 1991, **113**, 1922-1932.

37 K. Habermüller, M. Mosbach and W. Schuhmann, *Fresenius J. Anal. Chem.,* 2000, **366**, 560-568.

38 A. Akhoury, L. Bromberg and T. A. Hatton, *J. Phys. Chem. B,* 2012, **117**, 333-342.

39 J. B. Flanagan, S. Margel, A. J. Bard and F. C. Anson, *J. Am. Chem. Soc.,* 1978, **100**, 4248-4253.

40 I. Jureviciute, S. Bruckenstein and A. R. Hillman, *J Electroanal Chem,* 2000, **488**, 73-81.

41 A. R. Hillman, D. C. Loveday and S. Bruckenstein, *Langmuir,* 1991, **7**, 191-194.

42 W. J. Albery and A. R. Mount, *J. Chem. Soc., Faraday Transactions,* 1993, **89**, 327-331.

43 M. Chu, J. K. Takemoto and S. J. Visco, *Secondary cell using organosulfur/metal charge transfer materials as positive electrode,* 1996, US5516598 A.

44 A. Lever, *Inorg. Chem.,* 1990, **29**, 1271-1285.

45 S. Lu, J. Luo, S. Ji, N. Li, H. Li and W. Li, *Electrochim. Acta,* 2014, **136**, 130-137.

46 A. M. Lapides, D. L. Ashford, K. Hanson, D. A. Torelli, J. L. Templeton and T. J. Meyer, *J. Am. Chem. Soc.,* 2013, **135**, 15450-15458.

47 J. E. Monat and J. K. McCusker, *J. Am. Chem. Soc.,* 2000, **122**, 4092-4097.

48 J. B. Asbury, E. Hao, Y. Wang and T. Lian, *J. Phys. Chem.,* 2000, **104**, 11957-11964.

49 G. J. Britovsek, M. Bruce, V. C. Gibson, B. S. Kimberley, P. J. Maddox, S. Mastroianni, S. J. McTavish, C. Redshaw, G. A. Solan and S. Strömberg, *J. Am. Chem. Soc.,* 1999, **121**, 8728-8740.

50 R. Sydam, M. Deepa, S. Shivaprasad and A. Srivastava, *Solar Energy Mater. Solar Cells,* 2015, **132**, 148-161.

51 A. R. Hillman and E. F. Mallen, *J. Electroanal. Chem.,* 1991, **309**, 159-171.

52 G. G. Wallace, P. R. Teasdale, G. M. Spinks and L. A. Kane-Maguire, *Conductive electroactive polymers: intelligent polymer systems*, CRC press, Florida, 2008.

53 J. Heinze, B. A. Frontana-Uribe and S. Ludwigs, *Chem. Rev.,* 2010, **110**, 4724-4771.

54 T. Ito, H. Shirakawa and S. Ikeda, *Journal of polymer science: polymer chemistry edition,* 1974, **12**, 11-20.

55 H. Shirakawa, E. J. Louis, A. G. MacDiarmid, C. K. Chiang and A. J. Heeger, *J.Chem.Soc., Chem.Commun.,* 1977, **16**, 578-580.

56 C. K. Chiang, C. Fincher Jr, Y. Park, A. Heeger, H. Shirakawa, E. Louis, S. Gau and A. G. MacDiarmid, *Phys. Rev. Lett.,* 1977, **39**, 1098.

57 O. Bubnova, Z. U. Khan, H. Wang, S. Braun, D. R. Evans, M. Fabretto, P. Hojati-Talemi, D. Dagnelund, J. Arlin and Y. H. Geerts, *Nature Materials,* 2014, **13**, 190-194.

58 Y. Xia, K. Sun and J. Ouyang, *Adv Mater,* 2012, **24**, 2436-2440.

59 K. Gurunathan, A. V. Murugan, R. Marimuthu, U. Mulik and D. Amalnerkar, *Mater. Chem. Phys.,* 1999, **61**, 173-191.

60 T. Park, C. Park, B. Kim, H. Shin and E. Kim, *Energy & Environmental Science,* 2013, **6**, 788-792.

61 A. R. Hillman and E. F. Mallen, *J. Electroanal. Chem.,* 1987, **220**, 351-367.

62 Y. Kim, S. Cook, S. M. Tuladhar, S. A. Choulis, J. Nelson, J. R. Durrant, D. D. Bradley, M. Giles, I. McCulloch and C. Ha, *Nature Materials,* 2006, **5**, 197-203.

63 P. Piotrowski, K. Zarębska, M. Skompska and A. Kaim, *Electrochim. Acta,* 2014, **148**, 145-152.

64 J. Li, X. Li, Y. Zhang, R. Li, D. Wu, B. Du, Y. Zhang, H. Ma and Q. Wei, *RSC Advances,* 2015, **5**, 5432-5437.

65 J. Bredas, R. Silbey, D. Boudreaux and R. Chance, *J. Am. Chem. Soc.,* 1983, **105**, 6555-6559.

66 A. R. Hillman and M. A. Mohamoud, *Electrochim. Acta,* 2006, **51**, 6018-6024.

67 A. MacDiarmid, J. Chiang, A. Richter and A. Epstein, *Synth. Met.,* 1987, **18**, 285-290.

68 W. Wu, D. Pan, Y. Li, G. Zhao, L. Jing and S. Chen, *Electrochim. Acta,* 2015, **152**, 126-134.

69 W. Huang, B. D. Humphrey and A. G. MacDiarmid, *Journal of the Chemical Society, Faraday Transactions 1: Physical Chemistry in Condensed Phases,* 1986, **82**, 2385-2400.

70 A. Heller, B. J. Feldman, N. Mano and Y. Loo, *Method comprising co-crosslinking polyaniline, polymer acid and redox enzyme to produce polymeric matrix,* 2014, US8703458 B2.

71 A. Hamnett, S. J. Higgins, P. R. Fisk and W. J. Albery, *J. Electroanal. Chem.,* 1989, **270**, 479-488.

72 A. F. Diaz, J. I. Castillo, J. Logan and W. Lee, *J. Electroanal. Chem.,* 1981, **129**, 115-132.

73 S. Bruckenstein, K. Brzezinska and A. R. Hillman, *Electrochim. Acta,* 2000, **45**, 3801-3811.

74 E. Karaca, N. Ö Pekmez and K. Pekmez, *Electrochim. Acta,* 2014, **147**, 545-556.

75 A. C. Pauly, C. D. Varnado, C. W. Bielawski and P. Theato, *Macromolecular rapid communications,* 2014, **35**, 210-213.

76 W. Su, J. Schrieffer and A. J. Heeger, *Phys. Rev. Lett.,* 1979, **42**, 1698.

77 G. Inzelt, M. Pineri, J. Schultze and M. Vorotyntsev, *Electrochim. Acta,* 2000, **45**, 2403-2421.

78 J. Brédas, B. Thémans, J. Fripiat, J. André and R. Chance, *Physical Review B,* 1984, **29**, 6761.

79 M. Bajpai, R. Srivastava, R. Dhar, R. Tiwari and S. Chand, *RSC Advances,* 2014, **4**, 47899-47905.

80 F. Schlütter, T. Nishiuchi, V. Enkelmann and K. Müllen, *Polymer Chemistry,* 2013, **4**, 2963-2967.

81 G. Ćirić-Marjanović, *Synth. Met.,* 2013, **170**, 31-56.

82 N. Sariciftci and H. Kuzmany, *Synth. Met.,* 1987, **21**, 157-162.

83 A. G. MacDiarmid and A. J. Epstein, *Synth. Met.,* 1995, **69**, 85-92.

84 W. W. Focke, G. E. Wnek and Y. Wei, *J. Phys. Chem.,* 1987, **91**, 5813-5818.

85 A. G. MacDiarmid and A. J. Epstein, *Faraday Discuss. Chem. Soc.,* 1989, **88**, 317-332.

86 K. Lee, S. Cho, S. H. Park, A. Heeger, C. Lee and S. Lee, *Nature,* 2006, **441**, 65-68.

87 J. Li, L. Liu, P. Wang and J. Zheng, *Electrochim. Acta,* 2014, **121**, 369-375.

88 J. Kim, J. Lee and S. Kwon, *Synth. Met.,* 2007, **157**, 336-342.

89 Y. Kim, S. Fukai and N. Kobayashi, *Synth. Met.,* 2001, **119**, 337-338.

90 Z. Gao, S. Rafea and L. H. Lim, *Adv Mater,* 2007, **19**, 602-606.

91 S. Su and N. Kuramoto, *Macromolecules,* 2001, **34**, 7249-7256.

92 A. Baba, M. Park, R. C. Advincula and W. Knoll, *Langmuir,* 2002, **18**, 4648-4652.

93 M. M. Gvozdenović, B. Z. Jugović, J. S. Stevanović, T. L. Trišović and B. N. Grgur, *Electropolzmeriyation, E.Schab-Balcerzak (Ed.), InTech, Rijeka,* 2011.

94 N. Gospodinova, P. Mokreva and L. Terlemezyan, *Polymer,* 1993, **34**, 2438-2439.

95 K. M. Molapo, P. M. Ndangili, R. F. Ajayi, G. Mbambisa, S. M. Mailu, N. Njomo, M. Masikini, P. Baker and E. I. Iwuoha, *Int.J Electrochem.Sci,* 2012, **7**, 11859-11875.

96 G. Zotti, S. Cattarin and N. Comisso, *J. Electroanal. Chem.,* 1988, **239**, 387-396.

97 B. Dong, B. He, C. Xu and H. Li, *Materials Science and Engineering: B,* 2007, **143**, 7-13.

98 G. Zotti, S. Cattarin and N. Comisso, *J. Electroanal. Chem.,* 1987, **235**, 259-273.

99 N. Gospodinova and L. Terlemezyan, *Progress in Polymer Science,* 1998, **23**, 1443-1484.

100 J. Chiang and A. G. MacDiarmid, *Synth. Met.,* 1986, **13**, 193-205.

101 J. De Albuquerque, L. Mattoso, R. Faria, J. Masters and A. MacDiarmid, *Synth. Met.,* 2004, **146**, 1-10.

102 T. Kobayashi, H. Yoneyama and H. Tamura, *J. Electroanal. Chem.,* 1984, **161**, 419-423.

103 T. K. Das and S. Prusty, *Polym. Plast. Technol. Eng.,* 2012, **51**, 1487-1500.

104 M. Gerard, A. Chaubey and B. Malhotra, *Biosensors and Bioelectronics,* 2002, **17**, 345-359.

105 B. Guo, L. Glavas and A. Albertsson, *Progress in polymer science,* 2013, **38**, 1263-1286.

106 J. W. Gardner and P. N. Bartlett, *Sensors and Actuators A: Physical,* 1995, **51**, 57-66.

107 M. Ates, *Materials Science and Engineering: C,* 2013, **33**, 1853-1859.

108 M. Trojanowicz, *Microchimica Acta,* 2003, **143**, 75-91.

109 P. Wang, L. Liu, D. Alemu Mengistie, K. Li, B. Wen, T. Liu and C. Chu, *Displays,* 2013, **34**, 301-314.

110 N. Kumar, S. Vadera, J. Singh, G. Das, S. Negi, P. Aparna and A. Tuli, *Def. Sci. J.,* 2013, **46**, 91-104.

111 J. D. Stenger-Smith, *Progress in Polymer Science,* 1998, **23**, 57-79.

112 P. Chandrasekhar, *Conducting polymers, fundamentals and applications: a practical approach*, Springer, New York, 1999.

113 S. Cosnier and A. Karyakin, *Electropolymerization: concepts, materials and applications*, John Wiley & Sons, Weinheim, 2010.

114 M. Ates, *Progress in Organic Coatings,* 2011, **71**, 1-10.

115 A. Fedorczyk, J. Ratajczak, A. Czerwiński and M. Skompska, *Electrochim. Acta,* 2014, **122**, 267-274.

116 A. J. Magenau, N. Bortolamei, E. Frick, S. Park, A. Gennaro and K. Matyjaszewski, *Macromolecules,* 2013, **46**, 4346-4353.

117 M. Babaei and N. Alizadeh, *Sensors Actuators B: Chem.,* 2013, **183**, 617-626.

118 P. N. Bartlett, P. Archer and S. K. Ling-Chung, *Sensors and Actuators,* 1989, **19**, 125-140.

119 P. Data, P. Zassowski, M. Lapkowski, W. Domagala, S. Krompiec, T. Flak, M. Penkala, A. Swist, J. Soloducho and W. Danikiewicz, *Electrochim. Acta,* 2014, **122**, 118-129.

120 A. Malinauskas, J. Malinauskiene and A. Ramanavičius, *Nanotechnology,* 2005, **16**, R51.

121 A. Ramanavicius, A. Finkelsteinas, H. Cesiulis and A. Ramanaviciene, *Bioelectrochemistry,* 2010, **79**, 11-16.

122 R. M. Sapstead, N. Corden and A. R. Hillman, *Electrochim. Acta,* 2014, **162**, 119-128.

123 C. Laslau, D. E. Williams, B. Kannan and J. Travas-Sejdic, *Advanced Functional Materials,* 2011, **21**, 4607-4616.

124 R. Kiefer, N. Aydemir, J. Torop, P. A. Kilmartin, T. Tamm, F. Kaasik, A. Keskula, J. Travas-Sejdic and A. Aabloo, 2014, 90561V-90561V-7.

125 H. C. Söyleyici, M. Ak, Y. Şahin, D. O. Demikol and S. Timur, *Mater. Chem. Phys.,* 2013, **142**, 303-310.

126 I. Efimov, A. Ispas and A. Bund, *Electrochim. Acta,* 2014, **122**, 16-20.

127 A. R. Hillman, K. S. Ryder, C. J. Zaleski, V. Ferreira, C. A. Beasley and E. Vieil, *Electrochim. Acta,* 2014, **135**, 42-51.

128 E. Mitchell, J. Candler, F. De Souza, R. Gupta, B. K. Gupta and L. Dong, *Synth. Met.,* 2015, **199**, 214-218.

129 T. Zhou, Y. Qin, J. Xu, Y. Tao, M. Lu and Y. Kong, *Synth. Met.,* 2015, **199**, 169-173.

130 D. Mo, W. Zhou, X. Ma and J. Xu, *Electrochim. Acta,* 2014, **132**, 67-74.

131 S. Soylemez, S. O. Hacioglu, M. Kesik, H. Unay, A. Cirpan and L. Toppare, *ACS applied materials & interfaces,* 2014, **6**, 18290-18300.

132 D. Pletcher, *A first course in electrode processes*, RSC Publishing, Cambridge, 2009.

133 A. J. Bard and L. R. Faulkner, *Electrochemical methods: fundamentals and applications*, Wiley New York, 1980.

134 G. Sauerbrey, *J. Physik*, 1959, **155**, 206-212.

135 S. Bruckenstein and M. Shay, *Electrochim. Acta,* 1985, **30**, 1295-1300.

136 O. Schneider, A. Bund, A. Ispas, N. Borissenko, S. Zein El Abedin and F. Endres, *J. Phys. Chem. B,* 2005, **109**, 7159-7168.

137 G. Zotti, S. Zecchin, G. Schiavon and A. Berlin, *Chemistry of materials,* 2002, **14**, 3607-3614.

138 I. Efimov, S. Winkels and J. Schultze, *J Electroanal Chem,* 2001, **499**, 169-175.

139 R. Kiefer, D. G. Weis, A. Aabloo, G. Urban and J. Heinze, *Synth. Met.,* 2013, **172**, 37-43.

140 V. Syritski, R. Gyurcsanyi, A. Öpik and K. Toth, *Synth. Met.,* 2005, **152**, 133-136.

141 J. A. Irvin and J. R. Carberry, *Journal of Polymer Science Part B: Polymer Physics,* 2013, **51**, 337-342.

142 M. M. Salamone, M. Sassi, L. Beverina, C. M. Mari and R. Ruffo, *Electrochim. Acta,* 2014, **140**, 152-159.

143 M. Grzeszczuk and M. Chmielewski, *J Electroanal Chem,* 2012, **681**, 24-35.

144 Y. Kong, X. Li, J. Ni, C. Yao and Z. Chen, *Electrochemistry Communications,* 2012, **14**, 17-20.

145 J. Agrisuelas, C. Gabrielli, J. García-Jareño, H. Perrot and F. Vicente, *Electrochim. Acta,* 2014, **125**, 83-93.

146 A. R. Hillman, K. S. Ryder, C. J. Zaleski, C. Fullarton and E. M. Smith, *Z. Phys. Chem*,. 2012, **226**, 1049-1068.

147 V. Lyutov, I. Efimov, A. Bund and V. Tsakova, *Electrochim. Acta,* 2014, **122**, 21-27.

148 H. Bandey, A. Robert Hillman, M. Brown and S. Martin, *Faraday Discuss.,* 1997, **107**, 105-121.

149 P. A. Topart and M. A. Noel, *Anal. Chem.,* 1994, **66**, 2926-2934.

150 A. Bund and M. Schneider, *J. Electrochem. Soc.,* 2002, **149**, E331-E339.

151 A. R. Hillman, M. A. Mohamoud and I. Efimov, *Anal. Chem.,* 2011, **83**, 5696-5707.

152 M. A. Mohamoud and A. R. Hillman, *Electrochim. Acta,* 2007, **53**, 1206-1216.

153 S. Koehler, M. Ueda, I. Efimov and A. Bund, *Electrochim. Acta,* 2007, **52**, 3040-3046.

154 J. Tedim, C. Freire and A. R. Hillman, *Physical Chemistry Chemical Physics,* 2009, **11**, 268-277.

155 W. J. Albery, Z. Chen, B. R. Horrocks, A. R. Mount, P. J. Wilson, D. Bloor, A. T. Monkman and C. M. Elliott, *Faraday Discuss. Chem. Soc.,* 1989, **88**, 247-259.

156 M. Guascito, P. Boffi, C. Malitesta, L. Sabbatini and P. Zambonin, *Mater. Chem. Phys.,* 1996, **44**, 17-24.

157 M. Trchová and J. Stejskal, *Pure and Applied Chemistry,* 2011, **83**, 1803-1817.

158 X. Feng, C. Mao, G. Yang, W. Hou and J. Zhu, *Langmuir,* 2006, **22**, 4384-4389.

159 O. Bubnova, Z. U. Khan, A. Malti, S. Braun, M. Fahlman, M. Berggren and X. Crispin, *Nature materials,* 2011, **10**, 429-433.

160 R. Kerr, C. Pozo-Gonzalo, M. Forsyth and B. Winther-Jensen, *Electrochim. Acta,* 2015, **154**, 142-148.

161 A. Patil, A. Heeger and F. Wudl, *Chem. Rev.,* 1988, **88**, 183-200.

162 T. F. Otero and M. Bengoechea, *Langmuir,* 1999, **15**, 1323-1327.

163 B. Haspulat, A. Gülce and H. Gülce, *J. Hazard. Mater.,* 2013, **260**, 518-526.

164 M. Dietrich, J. Heinze, G. Heywang and F. Jonas, *J Electroanal Chem,* 1994, **369**, 87-92.

165 W. Baek, M. Choi, T. Yoon, H. H. Lee and Y. Kim, *Appl. Phys. Lett.,* 2010, **96**, 133506.

166 K. Sheng, H. Bai, Y. Sun, C. Li and G. Shi, *Polymer,* 2011, **52**, 5567-5572.

167 C. Martin, C. Foss, P. Kissinger and W. Heineman, *Laboratory Techniques in Electroanalytical Chemistry*, Marcel Dekker, New York, 1996.

168 X. Feng, R. Li, Y. Ma, R. Chen, N. Shi, Q. Fan and W. Huang, *Advanced Functional Materials,* 2011, **21**, 2989-2996.

169 R. B. Kaner, D. Li and J. Huang, *Fabrication of polyaniline nanofiber dispersions and films,* 2013, US8470503 B2.

170 P. A. Christensen and A. Hamnett, Techniques and Mechanisms in Electrochemistry, Chapman and Hall, Oxford, 1994.

171 A. Bewick, K. Kunimatsu, B. S. Pons and J. W. Russell, *J. Electroanal. Chem.,* 1984, **160**, 47-61.

172 R. Deka, M. M. Bora, M. Upadhyaya and D. K. Kakati, *J Appl Polym Sci,* 2015, **132**.

173 O. Inganäs, B. Liedberg, W. Chang-Ru and H. Wynberg, *Synth. Met.,* 1985, **11**, 239-249.

174 S. S. Patil, K. V. Harpale, S. P. Koiry, K. R. Patil, D. K. Aswal and M. A. More, *J Appl Polym Sci,* 2015, **132**.

175 P. Christensen, A. Hamnett, A. Hillman, M. Swann and S. Higgins, *J.Chem.Soc., Faraday Trans.,* 1992, **88**, 595-604.

176 S. Cetiner, F. Kalaoglu, H. Karakas and A. S. Sarac, *Polymer Composites,* 2011, **32**, 546-557.

177 E. Detsri and S. T. Dubas, *J Appl Polym Sci,* 2013, **128**, 558-565.

178 M. F. Suárez and R. G. Compton, *J Electroanal Chem,* 1999, **462**, 211-221.

179 J. S. Mondschein, A. Kowalski, J. D. Kehlbeck, M. E. Hagerman and R. Cortez, *Mater Lett,* 2014, **131**, 262-265.

180 S. R. Dupont, F. Novoa, E. Voroshazi and R. H. Dauskardt, *Advanced Functional Materials,* 2014, **24**, 1325-1332.

181 C. Musumeci, J. A. Hutchison and P. Samorì, *Nanoscale,* 2013, **5**, 7756-7761.

182 H. Lin, L. Li, J. Ren, Z. Cai, L. Qiu, Z. Yang and H. Peng, *Scientific reports,* 2013, **3**.

183 Q. Zhang, Y. Li, Y. Feng and W. Feng, *Electrochim. Acta,* 2013, **90**, 95-100.

184 S. Koussi-Daoud, D. Schaming, P. Martin and J. Lacroix, *Electrochim. Acta,* 2014, **125**, 601-605.

185 Y. Han, M. Chang, H. Li, K. Ho, T. Hsieh and P. Huang, *Mater Lett,* 2014, **117**, 146-149.

186 S. Radhakrishnan, C. Sumathi, A. Umar, S. Jae Kim, J. Wilson and V. Dharuman, *Biosensors and Bioelectronics,* 2013, **47**, 133-140.

187 G. Yue, X. Ma, Q. Jiang, F. Tan, J. Wu, C. Chen, F. Li and Q. Li, *Electrochim. Acta,* 2014, **142**, 68-75.

188 S. Chebil, M. Monod and P. Fisicaro, *Electrochim. Acta,* 2014, **123**, 527-534.

189 A. Gelmi, M. J. Higgins and G. G. Wallace, *Biochimica et Biophysica Acta (BBA)-General Subjects,* 2013, **1830**, 4305-4313.

190 J. M. Pelto, S. P. Haimi, A. S. Siljander, S. S. Miettinen, K. M. Tappura, M. J. Higgins and G. G. Wallace, *Langmuir,* 2013, **29**, 6099-6108.

191 M. A. Vorotyntsev, D. V. Konev, U. Lange, Y. V. Tolmachev and M. Skompska, *Electrochim. Acta,* 2013, **110**, 452-458.

192 Y. Li, X. Hu, S. Zhou, L. Yang, J. Yan, C. Sun and P. Chen, *Journal of Materials Chemistry C,* 2014, **2**, 916-924.

193 W. Kim, A. Mäkinen, N. Nikolov, R. Shashidhar, H. Kim and Z. Kafafi, *Appl. Phys. Lett.,* 2002, **80**, 3844-3846.

194 B. Friedel, P. E. Keivanidis, T. J. Brenner, A. Abrusci, C. R. McNeill, R. H. Friend and N. C. Greenham, *Macromolecules,* 2009, **42**, 6741-6747.

195 G. Yu, J. Gao, J. Hummelen, F. Wudl and A. Heeger, *Science-AAAS-Weekly Paper Edition,* 1995, **270**, 1789-1790.

196 H. S. Nalwa, *Handbook of advanced electronic and photonic materials and devices*, Academic Press, London, 2000.

197 S. Günes, H. Neugebauer and N. S. Sariciftci, *Chem. Rev.,* 2007, **107**, 1324-1338.

198 F. Livi, J. E. Carlé and E. Bundgaard, Top. Heterocycle. Chem. 2015, **39**, 203-226.

199 H. Ellis, N. Vlachopoulos, L. Häggman, C. Perruchot, M. Jouini, G. Boschloo and A. Hagfeldt, *Electrochim. Acta,* 2013, **107**, 45-51.

200 H. Kim, G. Veerappan and J. H. Park, *Electrochim. Acta,* 2014, **137**, 164-168.

201 P. Sonar, T. R. B. Foong, S. P. Singh, Y. Li and A. Dodabalapur, *Chemical Communications,* 2012, **48**, 8383-8385.

202 H. Klauk, *Chem. Soc. Rev.,* 2010, **39**, 2643-2666.

203 Y. Li, Y. Lin, C. Wei and Y. Wang, *Solid-State Electronics,* 2013, **79**, 56-59.

204 C. C. Buron, M. Quinart, T. Vrlinic, S. Yunus, K. Glinel, A. M. Jonas and B. Lakard, *Electrochim. Acta,* 2014, **148**, 53-61.

205 V. Ratautaite, S. D. Janssens, K. Haenen, M. Nesládek, A. Ramanaviciene, I. Baleviciute and A. Ramanavicius, *Electrochim. Acta,* 2014, **130**, 361-367.

206 A. Aydogan, A. Koca, M. K. Şener and J. L. Sessler, *Org. Lett.,* 2014, **16**, 3764-3767.

207 C. Bianchini, A. Curulli, M. Pasquali and D. Zane, *Food Chem.,* 2014, **156**, 81-86.

208 A. S. Shaplov, D. O. Ponkratov, P. Aubert, E. I. Lozinskaya, C. Plesse, F. Vidal and Y. S. Vygodskii, *Chemical Communications,* 2014, **50**, 3191-3193.

209 S. Xiong, Z. Li, M. Gong, X. Wang, J. Fu, Y. Shi, B. Wu and J. Chu, *Electrochim. Acta,* 2014, **138**, 101-108.

210 P. R. Somani, *Optical Properties of Functional Polymers and Nano Engineering Applications,* CRC Press, Florida, 2014, 187-204.

211 D. Flamini, M. Saugo and S. Saidman, *Corros. Sci.,* 2014, **81**, 36-44.

212 J. Hou, G. Zhu, J. Xu and H. Liu, *Journal of Materials Science & Technology,* 2013, **29**, 678-684.

213 P. P. Deshpande, N. G. Jadhav, V. J. Gelling and D. Sazou, *Journal of Coatings Technology and Research,* 2014, **11**, 473-494.

214 E. W. Jager, E. Smela and O. Inganas, *Science,* 2000, **290**, 1540-1545.

215 W. Lu, A. G. Fadeev, B. Qi, E. Smela, B. R. Mattes, J. Ding, G. M. Spinks, J. Mazurkiewicz, D. Zhou, G. G. Wallace, D. R. MacFarlane, S. A. Forsyth and M. Forsyth, *Science,* 2002, **297**, 983-987.

216 B. Gaihre, S. Ashraf, G. M. Spinks, P. C. Innis and G. G. Wallace, *Sensors and Actuators A: Physical,* 2013, **193**, 48-53.

217 D. Vonlanthen, P. Lazarev, K. A. See, F. Wudl and A. J. Heeger, *Adv Mater,* 2014, **26**, 5095-5100.

218 R. Holze and Y. Wu, *Electrochim. Acta,* 2014, **122**, 93-107.

219 F. Wu, Z. Xu, Y. Wang and M. Wang, *RSC Advances,* 2014, **4**, 38797-38803.

220 P. Liu, Y. Huang and X. Sun, *ACS Applied Materials & Interfaces,* 2013, **5**, 12355-12360.

221 P. Liu, Y. Huang and X. Zhang, *J. Alloys Compounds,* 2014, **617**, 511-517.

222 M. P. Gustafson, K. Matsumoto, D. R. MacFarlane and B. Winther-Jensen, *Electrochim. Acta,* 2014, **122**, 166-172.

223 Y. Yang, M. Diao, M. Gao, X. Sun, X. Liu, G. Zhang, Z. Qi and S. Wang, *Electrochim. Acta,* 2014, **132**, 496-503.

224 C. Weidlich, K. Mangold and K. Jüttner, *Electrochim. Acta,* 2001, **47**, 741-745.

225 M. Galiński, A. Lewandowski and I. Stępniak, *Electrochim. Acta,* 2006, **51**, 5567-5580.

226 T. Welton, *Chem. Rev.,* 1999, **99**, 2071-2084.

227 N. E. Leadbeater, *Chemical Communications,* 2014, **50**, 1515-1518.

228 J. P. Hallett and T. Welton, *Chem. Rev.,* 2011, **111**, 3508-3576.

229 S. B. Phadtare and G. S. Shankarling, *Green Chem.,* 2010, **12**, 458-462.

230 B. Kuzmanovic, Van Strien, Cornelis Johannes Govardus, C. E. Bartel, M. Zeitler and J. C. Speelman, *Method to electrodeposit metals using ionic liquids,* 2013, US8361300 B2.

231 H. H. Elsentriecy, H. Luo, H. M. Meyer, L. L. Grado and J. Qu, *Electrochim. Acta,* 2014, **123**, 58-65.

232 A. Abbott, G. Frisch, S. Gurman, A. Hillman, J. Hartley, F. Holyoak and K. Ryder, *Chemical Communications,* 2011, **47**, 10031-10033.

233 H. Ohno, *Electrochemical aspects of ionic liquids*, John Wiley & Sons, New Jersey, 2011.

234 E. L. Smith, A. P. Abbott and K. S. Ryder, *Chem. Rev.,* 2014, **114**, 11060-11082.

235 M. Francisco, A. van den Bruinhorst and M. C. Kroon, *Angewandte Chemie International Edition,* 2013, **52**, 3074-3085.

236 K. Radošević, M. C. Bubalo, V. G. Srček, D. Grgas, T. L. Dragičević and I. R. Redovniković, *Ecotoxicol. Environ. Saf.,* 2015, **112**, 46-53.

237 A. P. Abbott, D. Boothby, G. Capper, D. L. Davies and R. K. Rasheed, *J. Am. Chem. Soc.,* 2004, **126**, 9142-9147.

Chapter 2: Theory

2.1.   Introduction

This chapter provides the fundamental electrochemical concepts and theory of the quartz crystal microbalance (QCM). The combination of electrochemical and the QCM techniques, called electrochemical quartz crystal microbalance (EQCM) was used for the deposition of polymer films and the characterization of the resulting modified electrodes, is given in this chapter as well.

2.2.   Electrochemistry Concepts

2.2.1.   Fundamentals

The work presented in chapters four, six and seven used the EQCM to investigate the growth and redox switching processes of an electroactive polymer. The foundation of this work is based on the fundamental principles of cyclic voltammetry. The required information about the electrochemical reaction is studied. The electrochemical reaction of a conducting polymer modified electrode can be expressed as[1]:

$$RED \rightleftharpoons OX + e^- \qquad (2.1)$$

where RED and OX represent the oxidised and reduced redox sites in the film, respectively. When a potential is applied to a conducting polymer modified electrode, the kinetics of reaction (2.1) determine the current response. The research field related to the modification of electrodes with conjugated (conducting) polymers within electrochemistry has been studied widely over the last few decades. The most commonly used electrochemical techniques for the analysis of conducting polymer films are cyclic voltammetry[2-4] and chronoamperometry.[5-7]

2.2.2.   Mass Transport

The mechanism of mobile species exchange takes place in the three steps: the first step is the transport of the reactant molecules from the bulk solution to the electrode surface, the second step is the electron exchange occurring at the electrode surface and the forming of the reaction products, the third step is the removal of reaction

products from the electrode surface (reaction site). The type of movement of ion is known as "mass transport" and necessary for the electrochemical reaction to proceed. The slowest process of mass transport (the first and the third steps) or the kinetics of electron exchange (the second step) controls the overall rate of the electrochemical reaction. While mass transport is rate limiting for rapid electrochemical reactions, the study of the electron transfer kinetics becomes more important than the observation of mass transport for very slow electrochemical reactions.

Transport of species (ions or solvent) to the electrode surface can proceed by three different processes: diffusion, convection and migration.[1, 8-10]

2.2.2.1. Diffusion

Diffusion is the spontaneous movement of chemical species (ions or molecules) due to a concentration gradient. The species moves from a region with a high concentration to a low concentration region until the system reaches a uniform distribution of the chemical species. Diffusion occurs inevitably in all electrode reactions as the reactant concentration is lowered and product concentration is increased, compared to the bulk solution, by the electron transfer at the surface.

The rate of transport by diffusion is quantified by using the Cottrell equation (2.5) and Fick's laws of diffusion depending on a specific electrochemical technique.

2.2.2.2. Migration

Migration is the movement of ions due to the influence of a potential gradient. Migration occurs in the vicinity of the electrode/electrolyte interface. Migration is an electrostatic phenomenon and is not an important mode of mass transport for the reactant and product of the electrode reactions, as in most electrochemical systems, the effect of migration is minimized by using a large excess of an inert electrolyte.

The excess of supporting electrolyte reduces the field strength on the target species to only very near the electrode surface (< 10 nm). The presence of a supporting electrolyte suppressing potential gradients limits the mass transport to the diffusion

rate. As DESs consist of only ions, they do not need supporting electrolyte to eliminate migration.

2.2.2.3. Convection

Convection is the movement of chemical species due to mechanical forces. Convection, also called *hydrodynamic mass transport*, is a process taking place deliberately by stirring the solution, shaking the cell or moving the electrode, which is a *forced convection*. There could be *natural convection* in unstirred solution due to small density gradients from both concentration and/or temperature changes within the vicinity of the electrode arising from the electron transfer reaction at the electrode surface. Random vibrations in the laboratory may also lead to *natural convection*. When the electrochemical experiment is introduced by forced convection, diffusion dominates the rate of mass transport species by convection. However, the effect of convection is negligible at short experimental timescale in an unstirred cell.

2.2.3. Electrochemical Techniques

There are numerous techniques available to study modified electrode processes. Among them cyclic voltammetry is the most important and most commonly used technique. In this section, the electrochemical techniques used for polymer deposition and characterisation are described briefly.

2.2.3.1. Cyclic Voltammetry

The information related to the mechanism of reaction, the rate of reaction and the processes of adsorption can be gained by data obtained from cyclic voltammetry.[11] Cyclic voltammetry (with a three electrode cell) is conducted in a solution having supporting electrolyte to suppress the migration of the ions. Cyclic voltammetry involves repeatedly sweeping the potential linearly between two potential points at a selected scan rate, *v*, and recording the corresponding current as a function of the potential at the working electrode. The potential of the electrode is swept between two values (switching potentials). Panel a of Figure 2.1 shows the potential swept in

the forward direction until it reaches a pre-programmed potential at switching potential the sweep is reversed. A partial cycle, full cycle or repetitive cycles can be used to obtain required results depending on the nature of the experiment.[12-15]

Panel b of Figure 2.1 illustrates a cyclic voltammogram for a reversible process. Initially value of the potential cycle (E_i) is lower than E^0 where only non-faradaic currents flow. When the potential approaches to E^0, oxidation of the reaction begins at the electrode (faradaic current). The current increases exponentially until a potential value in which the concentration of RED approaches zero. Following that, the electrochemical consumption rate constant of the RED species become faster than the mass transfer of RED from bulk electrolyte to the electrode surface and diffusion governs the voltammetric response. Similar behaviour is observed with OX species at the electrode surface during the reversing the potential. Apart from this basic description, there are several factors affecting the electrode reaction rate and current. These include 1) rate of electron transfer at the surface of the electrode, 2) mass transfer of species between the electrode surface and the bulk solution, 3) homogenous/heterogeneous chemical reactions following or preceding the electron transfer and 4) additional surface processes such as electrodeposition and adsorption/desorption.
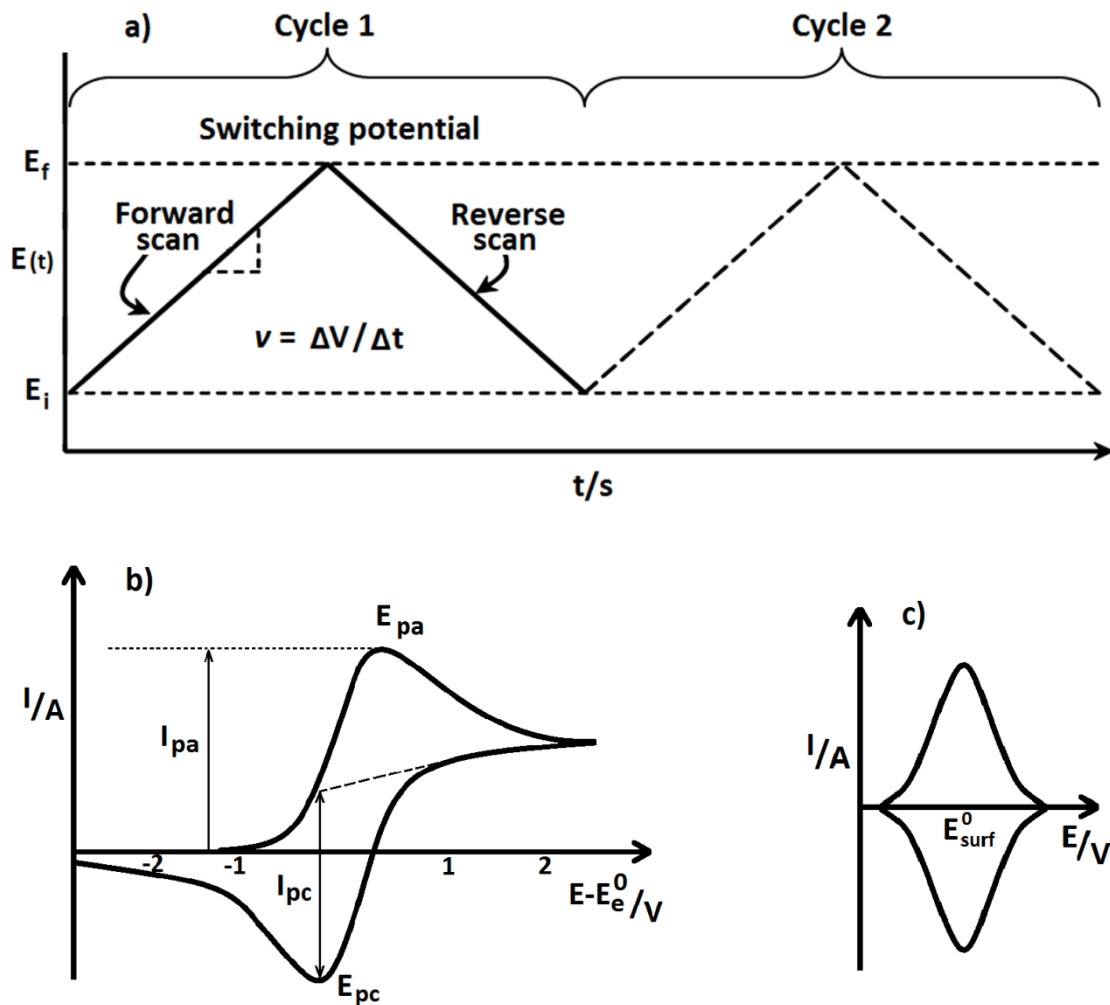
Figure 2.1. Schematic representation of cyclic voltammetry experiments. a) cyclic voltammetry waveform with respect to time; b) cyclic voltammogram for a reversible process (under diffusion control); c)cyclic voltammogram of an immobilised redox species (diffusionless system).

The shape of the cyclic voltammogram depends on the electrochemical reversibility of the redox couple. The characteristics of reversible systems are:

1) the potential voltage separation between the current peak is

$$\Delta E = E_{pa} - E_{pc} = \frac{59}{n} \ (mV)$$

2) the peak potential is independent of scan rate.

3) the ratio of peak currents is equal to one

$$\left(\frac{i_{pa}}{i_{pc}} = 1\right)$$

4) Peak currents (i_p) are proportional to the square root of scan rate ($v^{1/2}$).

In a fully electrochemical reversible system, mass transport rates constant at all potentials are slower than the electron transfer rates constant. Therefore, it has diffusional control mechanism. The concentration of the oxidised and reduced species at the electrode surface is described by the Nernst equation (2.2):

$$\Delta E = E^0 + \frac{RT}{nF} ln \frac{C_{OX}}{C_{RED}} \qquad (2.2)$$

in which E^0 is the formal reduction potential, C_{OX} and C_{RED} are the surface concentrations of oxidised and reduced species, n is the number of electrons transferred for each electroactive redox site, F is the Faraday constant. When the electron transfer reaction is slower than the mass transport reaction, the shape of the cyclic voltammogram changes to an electrochemically irreversible system. In this system, a given current requires a greater driving force and the increasing separate of peaks, *hysteresis*, is observed with increasing scan rate.

The total charge passed, required for surface film analysis, is calculated from the integration of the area under the cyclic voltammogram. If the dopant level of conducting polymers is known, the surface coverage of the polymer (Γ) can be calculated by the application of Faraday's law, equation (2.3):

$$\Gamma = \frac{Q}{nFA} \qquad (2.3)$$

where Q is the amount of charge to perform the electrochemical reaction and A is the electrode area.

The species which are uniformly adsorbed on an electrode surface and able to undergo an electrochemically reversible one-electron transfer, give sharp and symmetrical voltammetric peaks as shown in panel c of Figure 2.1. The difference of

potential between anodic and cathodic peaks is zero ($E_{pa} = E_{pc}$). The peak current is described by:

$$i_p = \frac{n^2 F^2 A \Gamma_{OX}}{4RT} v \qquad (2.4)$$

The linear dependence of the peak current on scan rate ($i_p \propto v$) indicates that diffusion of species within the film (or electrode) is not a limiting factor. The symmetrical shape of the cyclic voltammogram illustrated in panel c of Figure 2.1 is rarely seen even with the application of the slowest scan rate, which suggests redox cycling has some alternative mechanisms. The reason of the simple model of the equation (2.4) and panel c of Figure 2.1 is Langmuir isotherm assuming there are no interactions between the sites.

2.2.3.2. Chronoamperometry

Chronoamperometry was used as one of the techniques to characterise the electroactive films for water purification in this thesis. As explained in section 1.4.1.2, during chronoamperometric experiments, the applied potential of the WE is changed instantaneously from an initial value of E_i, where no electrochemical reaction takes place at the electrode surface (*i.e.* no current is flowing), to a final value, E_f, where the reaction of interest occurs (*i.e.* current flows). Figure 2.2 illustrates the potential control function, current response and charge response during a typical chronoamperometric experiment. The current and charge responses plotted as a function of time are named chronoamperometry and chronocoulometry, respectively. Chronocoulometry is the integration of the current-time curve to obtain the quantity of charge.
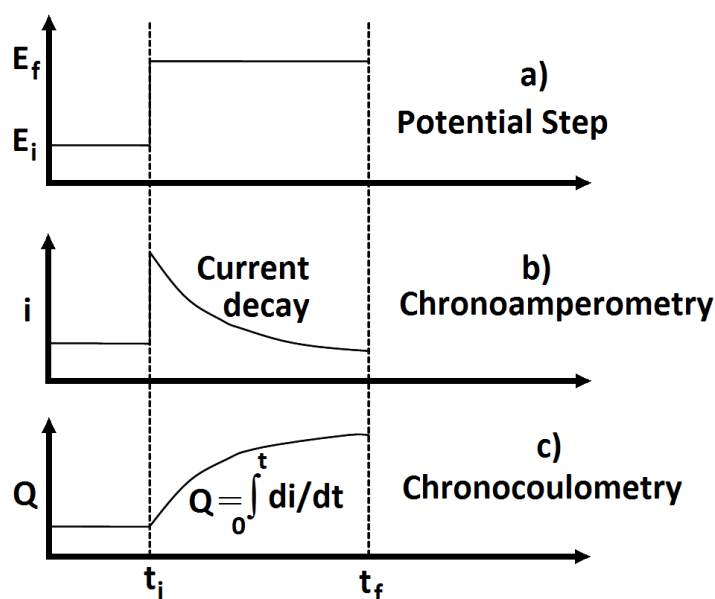
Figure 2.2: Responses of chronoamperometric experiments. Schematic of a) the potential profile; b) the current response (chronoamperometry); c) the charge response (chronocoulometry).

An application of a large overpotential leads to the consumption of all reactant at the film/metal interface. The current is initially very high but decreases speedily and become zero where the electroactive surface of the electrode is ended. The current response of chronoamperometry decays with $t^{-1/2}$, described by Cottrell equation (2.5):

$$i = nFAC_\infty \left(\frac{D}{\pi t}\right)^{1/2}$$

(2.5)

where D is the diffusion coefficient of the reactant, C_∞ is the bulk concentration. The rate limiting process is the diffusion of species into/out of film. A plot of i *vs.* $t^{-1/2}$ yields the diffusion coefficient, D, via the slope.

2.3.   Quartz Crystal Microbalance

The quartz crystal microbalance (QCM) is a powerful technique used as a gravimetric sensor and a probe for the measurement of physical properties of the materials.[16-24]

Understanding the basic principles of the QCM technique is important for the research presented in this thesis.

2.3.1. Fundamentals

2.3.1.1. The Piezoelectric Effect

In 1880, Jacques and Pierre Curie discovered the connection between the crystal structure and the piezoelectric effect. They demonstrated that a mechanical stress applied to the surface of a certain crystal produces an electrical potential across the crystal, which is proportional to the applied stress. This is known as the *direct piezoelectric effect.*[25]

The application of stress generates the charge in a crystal as displacement of atoms produces a shift of the dipoles. Conversely, the application of sufficient electrical potential across a small piece of crystal creates a corresponding physical displacement (*converse piezoelectric effect*)[26] given in Figure 2.3. The piezoelectric effect is only seen in materials that crystallise in non-centrosymmetric space groups. Generally solids are electrically neutral but some of them consist of electrically charged particles and the polar bond atoms having different electronegativities lead to the formation of dipole moments. The rearrangements of the ions cancel the individual dipole moments in the majority of materials. Quartz produces the net dipole moments when it is deformed potentially/mechanically and hence it is piezoelectric.
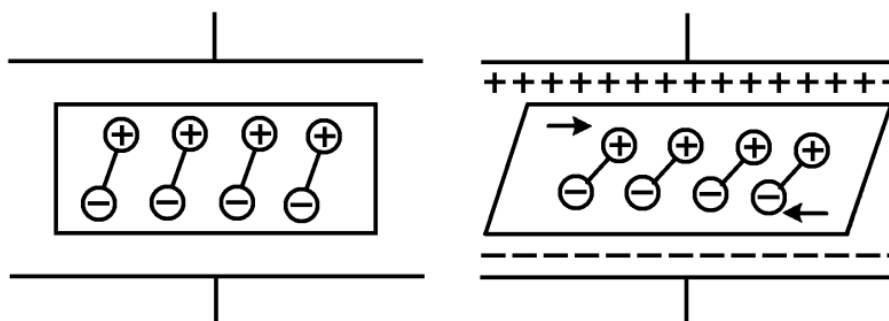
Figure 2.3: Schematic representation of the converse piezoelectric effect.

There are several types of crystal showing piezoelectric behaviour including quartz, tourmaline, Rochelle salts, barium/lead titanate, and lead zirconate. Among these, quartz is the most popular and important material used to date due to its high sensitivity, high frequency stability, low price, chemical inertness and elastic deformation.

2.3.1.2. Modes of Vibration and Crystallographic Orientation

Quartz, which is an ideal candidate to be used in frequency control devices and highly stable oscillators, exhibits piezoelectric vibrations in different directions in its perfect natural form shown in Figure 2.4.
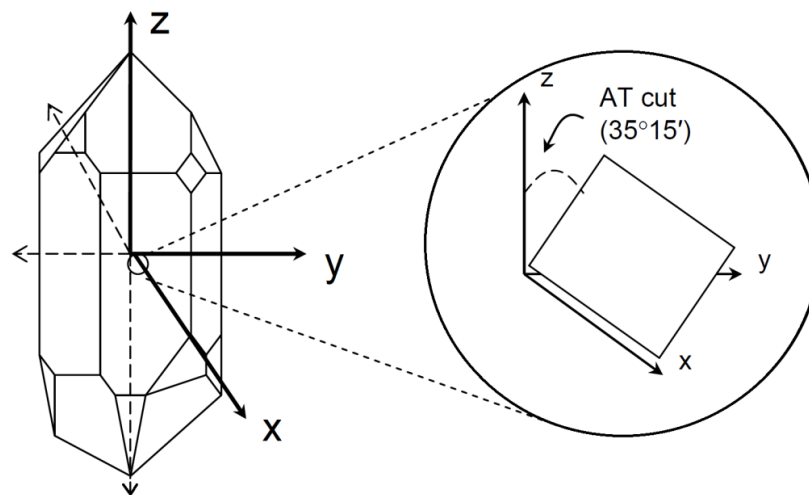
Figure 2.4: Schematic diagram showing the assignment of the axes to a quartz block (left) and cutting angle of AT-cut quartz crystal plate.[27]

There are many different types of vibrations such as lateral (thickness – shear and flexural), longitudinal (extensional) and torsional (twist) depending on the orientation of the quartz crystal lattice in the electric field. Ideally for the quartz crystal resonator, oscillation in only one mode is required. The quartz crystal is cut at a specific shape and orientation in order to suppress other vibration modes than the required one. If a quartz crystal is cut at a specific orientation with the AT-cut angle of 35°15' with respect to the crystallographic axis, vibrations in the thickness – shear mode, shown in Figure 2.5, are obtained.
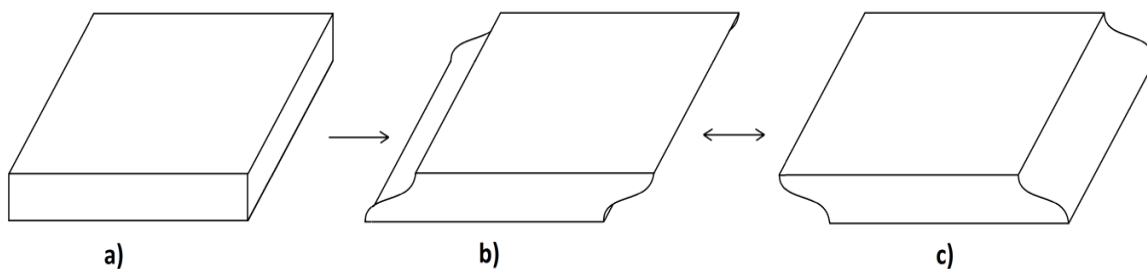
Figure 2.5: Schematic representation of AT-cut quartz crystal oscillating in the fundamental thickness – shear mode.

The resonant frequency of AT-cut quartz is more commonly used than other cuts due to the lack of attached mass sensitivity and over temperature sensitivity around room temperature. The measurements of DESs viscosity and some redox study of polymer modified electrodes films in DESs were carried out at high temperatures (50 °C), therefore the quartz crystal with least temperature sensitive was required in the works presented in this thesis.

2.3.2. The Mass – Frequency Relationship

The natural vibrating frequency of thickness – shear mode oscillator is known as the fundamental frequency or resonant frequency, analogous to a vibrating string or the resonant frequency of a mass on a spring. In 1945, Lord Rayleigh studied the relationship between the mass and frequency and found that the mass of a vibrating body is inversely proportional to its resonant frequency.[28] However, the link between the added mass and frequency shift of the quartz crystal was clarified by Sauerbrey in 1959.[29]

2.3.2.1. Sauerbrey Equation

Sauerbrey demonstrated that rigidly attached extra mass onto the AT-cut quartz crystal surface, (ΔMq), can be calculated from measuring the change in the resonant frequency of an oscillating quartz crystal (Δf). The resonant frequency of a crystal is a standing wave which is set up within the crystal.
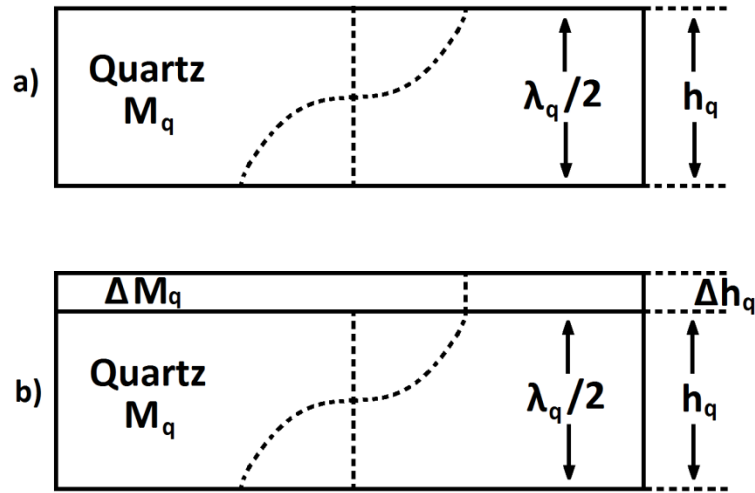
Figure 2.6: Schematic representation of a thickness – shear mode resonator. a) the thickness of quartz plate, $\boldsymbol{h_q}$, is related to acoustic wavelength, $\boldsymbol{\lambda_q}$; b) an increase quartz thickness, $\boldsymbol{h_q}$, results in an increase in the wavelength, $\boldsymbol{\lambda_q}$.

The equation (2.6) where the wavelength, λ, is related to the velocity of the wave, v, via the frequency can describe any wave,

$$v = f\lambda \tag{2.6}$$

and the thickness of the quartz crystal is related to acoustic wavelength, λ_q, (see Figure 2.6) by equation (2.7),

$$h_q = \frac{\lambda_q}{2} \tag{2.7}$$

Equation (2.6) is combined with equation (2.7) specifically for a QCM to give equation (2.8), in which v_q is wave velocity.

$$f_q = \frac{v_q}{2h_q} \tag{2.8}$$

The increase of thickness of the quartz crystal, *i. e.* the addition of a mass, leads to an increase in wavelength and therefore a decrease in resonant frequency shown in Figure 2.6. This relationship can be expressed mathematically as:

49

$$\frac{\Delta f}{f_q} = -\frac{\Delta M_q}{M_q} \qquad (2.9)$$

Assumption of mass added uniformly across the quartz crystal allows the equation (2.9) to be written in the approximate form using areal mass density which is mass per unit area:

$$\frac{\Delta f}{f_q} = -\frac{m_f}{m_q} \qquad (2.10)$$

in which m_f and m_q are areal mass density of the uniformly distributed mass added on to the crystal and mass of the quartz crystal, respectively. The areal mass density is equal to the density (ρ_q) and thickness (h_q) of the added mass/quartz crystal.

$$m_q = h_q \rho_q \qquad (2.11)$$

Substituting equation (2.8) into equation (2.11) leads to equation (2.12):

$$m_q = \frac{v_q \rho_q}{2 f_q} \qquad (2.12)$$

Equation (2.12) can be combined with (2.10) as:

$$m_f = -\Delta f_q \frac{v_q \rho_q}{2 f_q^2} \qquad (2.13)$$

Equation (2.13) is known as the Sauerbrey equation. Sauerbrey assumed that small, uniformly distributed mass added rigidly to the top of quartz crystal could be treated as an extension the mass of the crystal itself. This is a valid approximation when the thickness of the film is much less than that of the crystal.[30] The negative sign on the equation (2.13) indicates that a decrease in frequency results from an increase in mass. This can be simplified for a specified material by replacing constants. For quartz,

ρ_q and v_q are 2.65 g cm^{-3} and 3.34x10^5 cm s^{-1}, respectively. A 10 MHz AT-cut crystal shows high sensitivity as a 1 Hz frequency change is caused by the addition of 1.08 ng of material to the surface for the crystal used in the work presented in this thesis (piezoelectric area of crystal = 0.21 cm^2).

2.3.2.2. Harmonics

The quartz crystal resonators can be oscillated at a higher harmonic frequency to increase the sensitivity (see equation (2.8). Therefore, thickness of the crystal must be decreased to obtain this higher resonant frequency of a crystal (see Figure 2.6). However, the decreasing of thickness makes the crystal more fragile.

One solution is to apply a higher frequency to the crystal is to excite with frequency values in which there are higher harmonics of the crystal.

$$f_N = \frac{N v_q}{2 h_q}$$

(2.14)

Here f_N indicates the resonant frequency, N is the harmonic number (an integer number). Only odd harmonics are excited by the electrodes on the surface due to the appearance of anti-nodes at surface of the crystal presented in Figure 2.7.
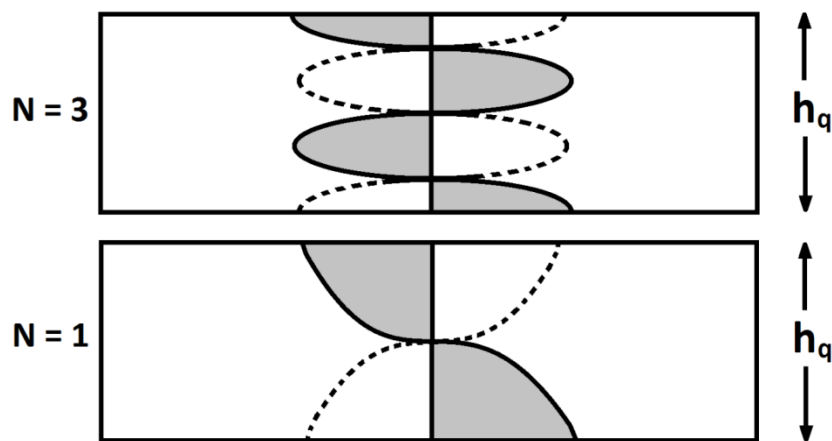
Figure 2.7: Displacement profiles across quartz thickness for the first and the third harmonics.

2.3.3.   The Viscosity – Frequency Relationship

The QCM was initially used as a quantitative tool to measure film masses in vacuum or gaseous environments. In the early 1980's a few studies demonstrated that the QCM could be used as a possible tool for liquid samples used in liquid chromatography[31] and analysis of organic liquids.[32, 33] Figure 2.8 displays one surface of AT-cut quartz crystal contacting with liquid.
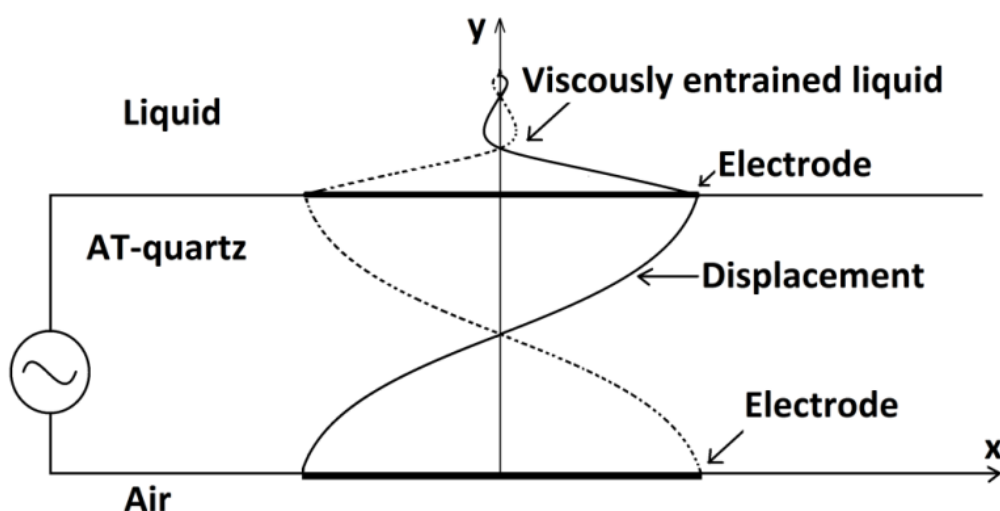
Figure 2.8: A quartz crystal oscillating in an alternating electric field.

When the QCM is operated at frequency in a liquid environment, its surface oscillation entrains liquid and the resonance is damped. Hence, the frequency of the crystal decreases (shown in Figure 2.8). Frequency data depending on resonant frequency of the crystal can be used to characterize some of the physical properties of the liquid (such as density,[23] viscosity[16, 17, 34]) contacting to the crystal.

A transverse acoustic wave propagating into a contacting medium has a distance known as the decay length. The traverse wave decay length in a Newtonian liquid is:

$$\delta = \left(\frac{2\eta_l}{\omega\rho_l}\right)^{1/2} \tag{2.15}$$

in which ω is $2\pi f_s$ (f_s is the resonant frequency). The decay length of a traverse acoustic wave for a 10 MHz TSM resonator immersed in water is 0.18 μm calculated

from equation (2.15). As DESs are more viscous than classical electrolyte, the decay length is higher.

2.3.3.1. Kanazawa – Gordon Equation

Equation (2.16) is the modified Sauerbrey equation where the factors of liquid properties are included. The decrease in square of the frequency is proportional to the viscosity-density of the liquids measured with QCM for Newtonian liquids described by Kanazawa and Gordon[24, 35] equation (2.16):

$$\frac{\Delta f}{f_0} = -\frac{1}{Z_q} \left(\frac{f_s \eta \rho}{\pi}\right)^{\frac{1}{2}} \tag{2.16}$$

where, Z_q is the specific acoustic impedance of the quartz $\left[Z_q = \left(\mu_q \rho_q\right)^{\frac{1}{2}} = 8.84 \; x \; 10^6 \; kg \; m^{-2} \; s^{-1}\right]$, ρ is density of liquid and η is the viscosity of liquid contacted to the quartz crystal resonator. The viscosity measurement by means of QCM is presented in chapter five with technical and experimental details.

2.4.   Electrochemical Quartz Crystal Microbalance

The EQCM is a sensitive technique for monitoring mass changes of surface films (section 2.3) during electrochemical measurements (section 2.2) *i.e.* the combination of the electrochemistry techniques with the quartz crystal resonator. The first work of this combination was the detection of Ag deposition by means of QCM published in 1981.[36] The first description of practical experiment used QCM with an electrochemical control function was published by Bruckenstein and Shay[37] in 1985. Since then, the quartz crystal resonator has been an invaluable tool for electrochemists to study solid/liquid interface due to its short data acquisition time (typically < 0.1 s) and high sensitivity which allows measurement at the nanogram level.

The QCM consist of a thin quartz crystal sandwiched between two vacuum deposited electrodes one of which is used as the WE (see Figure 2.9).
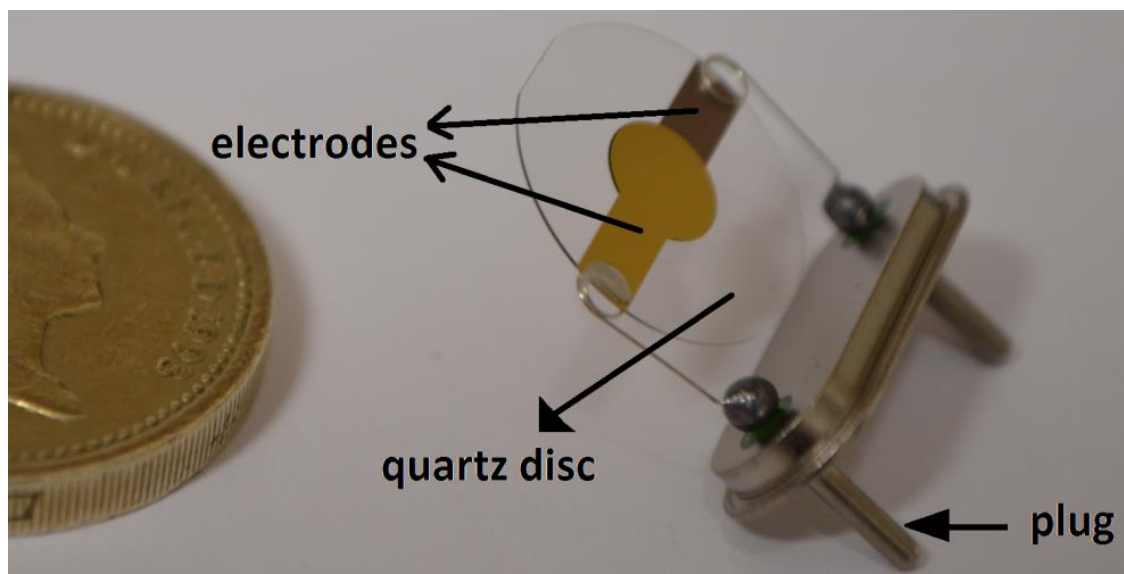
Figure 2.9: A quartz thickness – shear mode resonator. Both sides of the quartz have gold electrodes.

With EQCM, the mass changes caused by electrochemical reaction can be monitored via the associated mass (frequency) changes for sufficiently thin and rigid electroactive films. The deposition of conducting polymer films and ion – solvent transfer during redox switching of the resulting films have been measured directly in plenty of studies.[38-42]

Several different electrode materials including gold, platinum, copper and nickel may be used on top of the quartz disc. The most popular one is gold due to its ease of preparation and electroinactivity in relatively wide potential windows. The connection of quartz crystal to the experimental set-up is shown in the following chapter.

2.4.1.   Crystal Impedance Analysis

Gravimetric analysis of a modified electrode by using EQCM is conducted up to a limiting point. When polymer is non-rigid (acoustically thick), the crystal response is not directly related to the mass on the quartz crystal electrode but it is a function of the viscoelastic characteristic of the films.[43, 44] Therefore, the recognition of rigidity

level is important for gravimetric measurements. Crystal impedance analysis is a useful technique used to identify the extent of viscoelastic behaviour of the films[45] for film deposition and/or redox cycling.[46] The complete impedance responses as a function of frequency acquired by a network analyser are required for crystal impedance analysis. More commonly, admittance, which is the reciprocal of impedance, is obtained as a function of frequency near the crystal resonance. The rigidity or viscoelasticity of a coupled film is indicated by the change of the shape of the admittance – frequency (Y –f) spectra given in Figure 2.10.
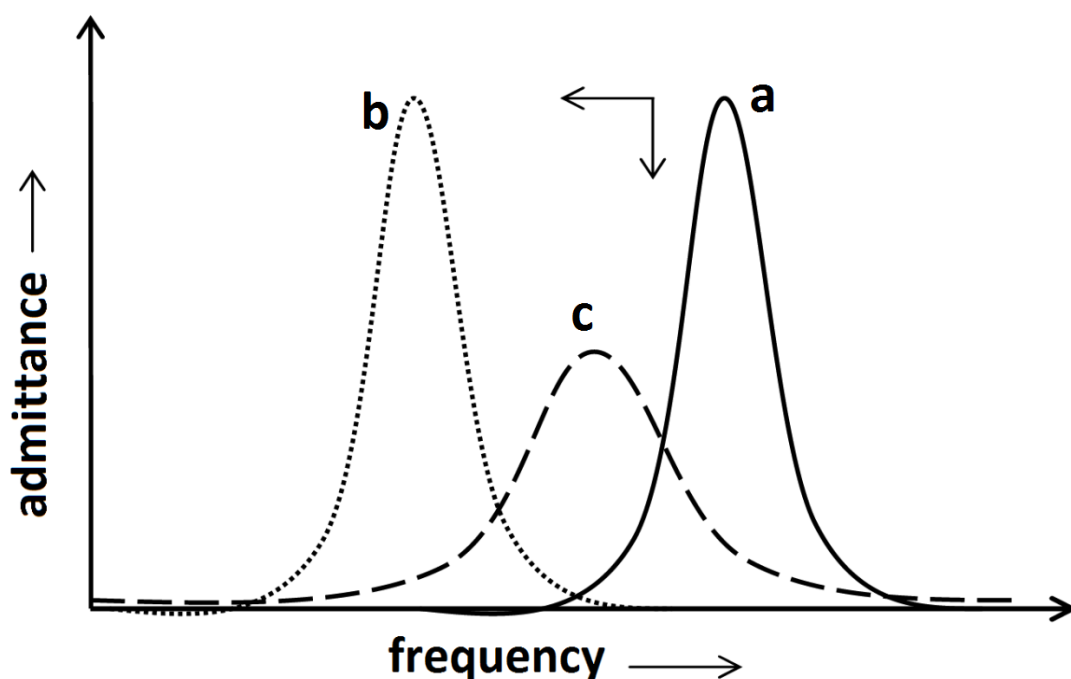
Figure 2.10: Typical schematic representation of Admittance – frequency spectra. a) unloaded crystal called bare crystal; b) thin –rigid mass layer; c) viscoelastic layer.

Qualitative information related to the viscoelastic properties of the modified films can be extracted from $Y - f$ spectra. For example, a large admittance and small full width at half maximum (FWHM) is the characteristic shape of the rigid film whereas a lower admittance and broader bandwidth shows the response of a non-rigid film. More specifically, when the crystal impedance of unperturbed responses is compared with bare crystal response, it can be deduced whether the modified electrode on the crystal is rigid or non-rigid. As Figure 2.10 (b) shows the shape of spectra for rigidly added

masses is constant with (a) but the frequency axis is merely shifted and this frequency difference can be used to calculate the mass of the film (by the Sauerbrey equation given in section 2.3.2.1). However the response of a viscoelastic film is very different as the shapes of spectra are changed to a more damped response. The FWHM of non-rigid film increases significantly and in this case the Sauerbrey equation could not be valid. Crystal impedance technique has been used for many systems including for film coating crystals in air, solution analysis (viscosity, density and dielectric constant). More detailed information about crystal admittance analysis could be found in the literature.[47-53] In this thesis films were chosen to be sufficiently thin that viscoelastic effects were minimal. To do this, we tolerated admittance decrease until 20% as the spectra and q factor were not changed significantly at this range. This was verified using admittance spectra as shown in Figure 2.10.

2.5.   References

1 D. Pletcher, *A first course in electrode processes*, RSC Publishing, Cambridge, 2009.

2 L. Gao, X. Mao, W. Xiao, F. Gan and D. Wang, *Electrochim. Acta,* 2014, **136**, 97-104.

3 Y. Fan, J. Liu, C. Yang, M. Yu and P. Liu, *Sensors Actuators B: Chem.,* 2011, **157**, 669-674.

4 W. Huang, B. D. Humphrey and A. G. MacDiarmid, *Journal of the Chemical Society, Faraday Transactions 1: Physical Chemistry in Condensed Phases,* 1986, **82**, 2385-2400.

5 U. Vanamo and J. Bobacka, *Electrochim. Acta,* 2014, **122**, 316-321.

6 T. Qiu, B. Luo, M. Liang, J. Ning, B. Wang, X. Li and L. Zhi, *Carbon,* 2015, **81**, 232-238.

7 M. R. Nateghi and B. Savabieh, *Electrochim. Acta,* 2014, **121**, 128-135.

8 A. Fischer, *Electrode dynamics*, Oxford Univ. Press, Oxford, 1996.

9 C. M. Brett and A. M. O. Brett, *Electrochemistry: principles, methods, and applications*, Oxford university press, Oxford, 1993.

10 A. J. Bard and L. R. Faulkner, *Electrochemical Methods: Fundamentals and Applicationss*, *Wiley and Sons,* New Jersey, 2001.

11 Nicholson, R. S., *Anal. Chem*, 2010, **37**, 1351-1355.

12 M. Ertas, R. M. Walczak, R. K. Das, A. G. Rinzler and J. R. Reynolds, *Chemistry of Materials,* 2012, **24**, 433-443.

13 J. Agrisuelas, C. Gabrielli, J. García-Jareño, H. Perrot and F. Vicente, *Electrochim. Acta,* 2014, **125**, 83-93.

14 W. Wu, D. Pan, Y. Li, G. Zhao, L. Jing and S. Chen, *Electrochim. Acta,* 2015, **152**, 126-134.

15 E. Sefer, H. Bilgili, B. Gultekin, M. Tonga and S. Koyuncu, *Dyes and Pigments,* 2015, **113**, 121-128.

16 G. McHale, C. Hardacre, R. Ge, N. Doy, R. W. Allen, J. M. MacInnes, M. R. Bown and M. I. Newton, *Anal. Chem.,* 2008, **80**, 5806-5811.

17 N. Doy, G. McHale, M. I. Newton, C. Hardacre, R. Ge, R. Allen and J. MacInnes, *Biomicrofluidics*, 2009, **4**, 1043-1045.

18 S. J. Martin, G. C. Frye and K. O. Wessendorf, *Sensors and Actuators A: Physical,* 1994, **44**, 209-218.

19 J. Auge, P. Hauptmann, J. Hartmann, S. Rösler and R. Lucklum, *Sensors Actuators B: Chem.,* 1995, **24**, 43-48.

20 R. Thalhammer, S. Braun, B. Devcic-Kuhar, M. Groschl, F. Trampler, E. Benes, H. Nowotny and P. Kostal, *Ultrasonics, Ferroelectrics and Frequency Control, IEEE Transactions on,* 1998, **45**, 1331-1340.

21 H. Nowotny and E. Benes, *J. Acoust. Soc. Am.,* 1987, **82**, 513-521.

22 M. Rodahl, F. Höök and B. Kasemo, *Anal. Chem.,* 1996, **68**, 2219-2227.

23 F. Herrmann, D. Hahn and S. Büttgenbach, *Sensors and Actuators A: Physical,* 1999, **78**, 99-107.

24 K. K. Kanazawa and J. G. Gordon, *Anal. Chem.,* 1985, **57**, 1770-1771.

25 J. Curie and P. Curie, *Comptes Rendus,* 1880, **91**, 294-295.

26 J. Curie and P. Curie, *Comptes-rendus de l'Académie des Sciences,* 1881, **93**, 1137-1140.

27 M. A. Mohamoud, Ph.D. Thesis, University of Leicester, 2007.

28 L. Rayleigh, *Doverpress,* New York, 1945.

29 G. Sauerbrey, *J.Physik,* 1959, **155**, 206-212.

30 A. R. Hillman, *Journal of Solid State Electrochemistry,* 2011, **15**, 1647-1660.

31 P. L. Konash and G. J. Bastiaans, *Anal. Chem.,* 1980, **52**, 1929-1931.

32 T. Nomura and A. Minemura, *Nippon Kagaku Kaishi,* 1980, **10**, 1621-1625.

33 T. Nomura and M. Okuhara, *Anal. Chim. Acta,* 1982, **142**, 281-284.

34 N. Doy, G. McHale, M. I. Newton, C. Hardacre, R. Ge, J. MacInnes, D. Kuvshinov and R. Allen, *Biomicrofluidics,* 2010, **4**, 014107.

35 K. Keiji Kanazawa and J. G. Gordon II, *Anal. Chim. Acta,* 1985, **175**, 99-105.

36 T. Nomura and M. Iijima, *Anal. Chim. Acta,* 1981, **131**, 97-102.

37 S. Bruckenstein and M. Shay, *Electrochim. Acta,* 1985, **30**, 1295-1300.

38 M. Erginer, E. Sezer, B. Ustamehmetoğlu and J. Heinze, *Electrochim. Acta,* 2012, **67**, 181-186.

39 G. Inzelt, M. Pineri, J. Schultze and M. Vorotyntsev, *Electrochim. Acta,* 2000, **45**, 2403-2421.

40 M. A. Mohamoud, *Electrochim. Acta,* 2014, **139**, 201-208.

41 M. Jafeen, M. Careem and S. Skaarup, *Ionics,* 2014, **20**, 535-544.

42 T. Chiang, M. Huang and C. Tsai, *Appl. Surf. Sci.,* 2014, **308**, 293-300.

43 V. Gruia, A. Ispas, M. Wilke, I. Efimov and A. Bund, *Electrochim. Acta,* 2014, **118**, 88-91.

44 Q. Xie, Y. Zhang, C. Xiang, J. TANG, Y. LI, Q. ZHAO and S. YAO, *Analytical sciences,* 2001, **17**, 613-620.

45 H. L. Bandey, S. J. Martin, R. W. Cernosek and A. R. Hillman, *Anal. Chem.,* 1999, **71**, 2205-2214.

46 M. J. Brown, A. R. Hillman, S. J. Martin, R. W. Cernosek and H. L. Bandey, *Journal of Materials Chemistry,* 2000, **10**, 115-126.

47 M. D. Levi, S. Sigalov, G. Salitra, R. Elazari, D. Aurbach, L. Daikhin and V. Presser, *The Journal of Physical Chemistry C,* 2013, **117**, 1247-1256.

48 B. Gollas, J. M. Elliott and P. N. Bartlett, *Electrochim. Acta,* 2000, **45**, 3711-3724.

49 A. R. Hillman, *Solid State Ionics,* 1997, **94**, 151-160.

50 L. Daikhin, S. Sigalov, M. D. Levi, G. Salitra and D. Aurbach, *Anal. Chem.,* 2011, **83**, 9614-9621.

51 Q. Xie, J. Wang, A. Zhou, Y. Zhang, H. Liu, Z. Xu, Y. Yuan, M. Deng and S. Yao, *Anal. Chem.,* 1999, **71**, 4649-4656.

52 A. R. Hillman, A. Jackson and S. J. Martin, *Anal. Chem.,* 2001, **73**, 540-549.

53 A. Bund and G. Schwitzgebel, *Electrochim. Acta,* 2000, **45**, 3703-3710.

Chapter 3: Experimental

3.1. Introduction

This chapter contains the description of the experimental work in terms of the instrumentation, materials and procedures for the results presented in chapters four to seven.

3.2. Materials

3.2.1. Chemicals

Table 3.1 displays the list of chemicals used to obtain the results presented in this thesis. Their sources and purities are also shown in the table. All chemicals presented in Table 3.1 were used as received, without any further purification. When monomers were not used, they were kept in cold room (4 °C). The aqueous solutions were prepared by using deionised water.

Table 3.1: List of chemicals used during the research presented in this thesis.

Compound	Application	Source	Purity
Choline chloride	Quaternary ammonium salt	Sigma Aldrich	98%
Ethylene glycol	Hydrogen bond donor (HBD)	Sigma Aldrich	99.8%
Propylene glycol	HBD	ReAgent	99%
Glycerol	HBD	Fisons	99%
Urea	HBD	Fisher Chemical	99.8%
Aniline	Monomer of the conducting polymer	Sigma Aldrich	99%

o-toluidine	Monomer of the conducting polymer	Sigma Aldrich	99%
o-aminophenol	Monomer of the conducting polymer	Sigma Aldrich	99%
Sulphuric acid	Supporting electrolyte and film characterisation	Fisher Chemical	98%
Sodium fluoride	Electrolyte for fluoride extraction	Analar	99%
Nitric acid	Cleaning electrodes	Fisher Scientific	70%
Potassium ferricyanide	Reference electrode calibrant	Acros Organics	98%
Potassium chloride	Electrolyte of the reference electrode	Fisher Scientific	99%

3.2.2.   Preparation of DESs

Choline chloride (ChCl) shown in panel a of Figure 3.1 was added to ethylene glycol ($C_2H_6O_2$) in a 1:2 molar ratio to form Ethaline. The resulting mixture was continually stirred in a beaker on a hotplate at 50°C (panel b of Figure 3.1) until a homogeneous and colourless liquid phase (*ca.* 30 minutes), as shown in panel c of Figure 3.1, was formed.
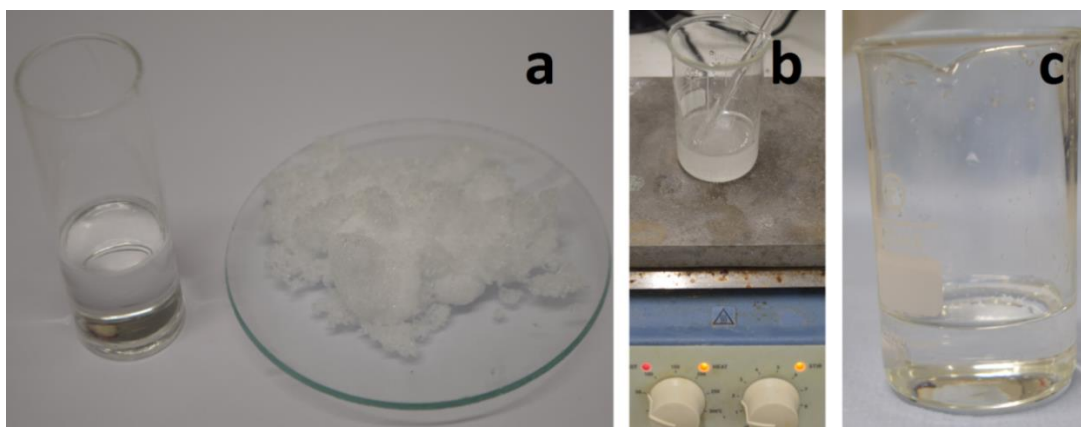
Figure 3.1: The process of the preparation of Ethaline. a) Choline Chloride (white solid) and ethylene glycol; b) heating and stirring of the mixture on a hotplate (50°C); c)the formation of homogeneous and colourless Ethaline.
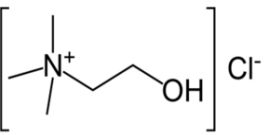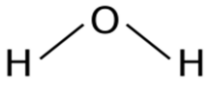
All other DESs were produced using a 1:2 molar ratio of ChCl:HBD given in Table 3.2. The process of mixing and moderate heating of the other DESs is similar to the preparation process of Ethaline until a homogenous, colourless liquid was formed. However, they differ in terms of heating time depending on the type of DES. The type, abbreviated names of DESs and the ions forming each DESs are given in Table 3.2.
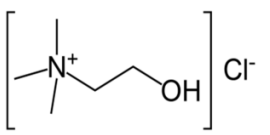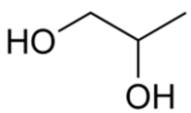
Table 3.2: The names and structures of ions formed DESs and the nomenclatures.
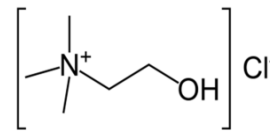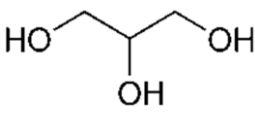
Ethaline	Structure		
	Name	Choline chloride	Ethylene glycol
	Shown in this thesis	Ch⁺Cl⁻	EG

Reline	Structure		
	Name	Choline Chloride	Urea

	Shown in this thesis	Ch$^+$Cl$^-$	U

	Structure		
Wateline	Name	Choline Chloride	Water
	Shown in this thesis	Ch$^+$Cl$^-$	W

	Structure		
Propaline	Name	Choline Chloride	Propylene Glycol
	Shown in this thesis	Ch$^+$Cl$^-$	PG

	Structure		
Glyceline	Name	Choline Chloride	Glycerol
	Shown in This Thesis	Ch$^+$Cl$^-$	G

Once Ethaline is formed, it is liquid, homogenous and colourless at room temperature. However, Propaline and Wateline are crystalline at room temperature. The crystallisation of Propaline is shown in Figure 3.2.

Once DESs were prepared, they were stored in the sealed containers in an oven at *ca.* 50°C until further use in order to minimise water content. These DESs were used as

electrolyte in the PANI films given in chapter six and their viscosity were measured by means of the QCM and RV presented in chapter five.
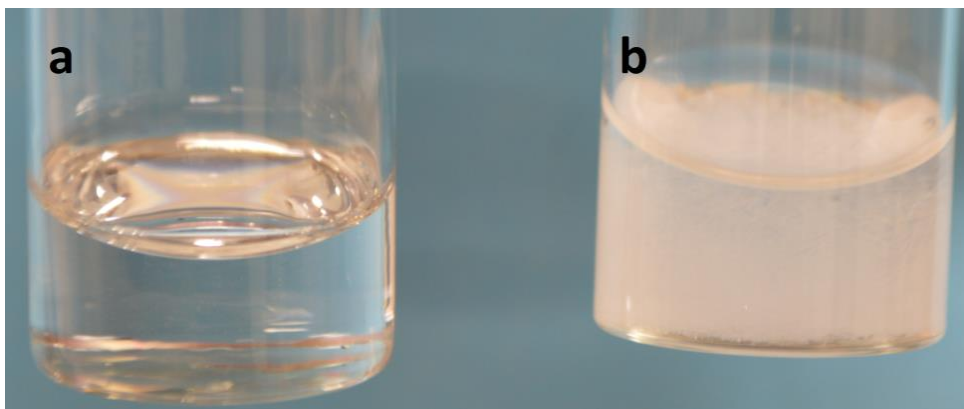
Figure 3.2: Crystallisation of Propaline a) homogeneous liquid phase of propaline; b) heterogeneous crystallisation of propaline, after few hours.

3.3. Instrumentation

The main experimental technique was the EQCM which was used to study the electropolymerisation of conducting (co)polymers and ion exchange dynamics of polymers in aqueous and DESs media. SEM and FTIR were used for the characterisation of the films. Rotational viscometer and the QCM were used to obtain the viscosities of the electrolytes.

3.3.1. Electrochemical Measurements

All electrochemical experiments were conducted in a standard three-electrode cell described in chapter two. The working electrode (WE) was gold, the counter electrode (CE) was a platinum flag and the reference electrode (RE) was Ag/AgCl (or Ag wire for DESs experiments). Prior to explaining procedure of the electrochemical experiments; the information about the electrodes is presented below.

3.3.1.1. Working Electrodes

Two types of Au WEs were used in all electrochemical experiments in this thesis. One of the WEs was one of the Au electrodes on the surface of the AT-cut quartz crystals,

displayed in chapter two, used for the EQCM measurements. The other electrode was a home-made WE, having 0.44 mm^2 surface area whose around was covered by glue and glass, which was used for obtaining SEM images.

The AT-cut quartz crystals used in the work presented in this thesis were described, in chapter two. There are two types of the 10 MHz AT-cut quartz crystals in terms of surface finish: polished and unpolished crystals. Both types were supplied by the International Crystal Manufacturing (ICM) Co. Ltd. (Oklahoma City, USA) and consist of a thin slice of AT-cut quartz (*ca.* 0.18 mm) between vacuum deposited gold electrodes on either side. The electrochemical and piezoelectric active area of the quartz crystals are 0.23 cm^2 and 0.21 cm^2, respectively. The area difference (0.02 cm^2) between electroactive and piezoelectric active area is due to the connecting tab of the electrode. While unpolished (etched) crystals have a surface finish of about 0.3 μm, polished crystals have surface finish of less than 0.1 μm. Whereas there is a chromium under layer of gold in the polished crystal, the gold is directly deposited onto the surface for the unpolished crystal. As PANI and its derivatives (also copolymers of PANI with its derivatives) deposited well onto the both type of the quartz crystals, it was decided later to use only polished quartz crystals. All the EQCM experimental results, presented in this thesis were obtained using polished quartz crystals to decrease mass trapping effect in the surface of the quartz crystals.[1]

3.3.1.2. Reference Electrodes

The RE in aqueous solution is well-studied and mainly secondary reference electrodes are used in electrochemical experiments.[2] Saturated calomel electrode (SCE) (E = +0.241 V *vs.* standard hydrogen electrode –SHE-) and silver chloride electrode (Ag/AgCl RE) (E = +0.197 V, saturated, *vs.* SHE) were mostly used in the literature for aqueous solution due to the ease of preparation,[3] being inexpensive, reproducible, stable and usable under a variety of aqueous conditions. The RE used in aqueous experiments given in this thesis, was a home-made Ag/AgCl RE comprising of a Ag wire (1 mm diameter, 99%), coated with AgCl layer, and saturated potassium chloride (~3.5 M) electrolyte in a glass body having a porous Vycor glass frit on the bottom of the body. It is known that the reaction of Ag/AgCl RE occurs between the Ag(s) and AgCl salt.[4]

Ag/AgCl RE is not suitable for use in DESs as there is a liquid junction potential due to the difference between the viscosity of the aqueous and DESs solutions changing ion mobility. In DESs, a silver wire was used as a pseudo-reference electrode directly immersed into the solution of DESs. Quasi REs or pseudo REs (Ag or Pt wires)[5, 6] are immersed into the RTIL solutions as REs in most of the studies carried out with RTIL.[7] It is assumed that the potential is not likely to change significantly throughout the measurements when pseudo RE is used in RTILs.[8]

There is a high concentration of Cl^- ions in DESs (4.2 M Cl^- ion in Ethaline). Cl^- ions surround the Ag wire which is immersed into the DESs. Therefore, the probable reaction of Ag wire pseudo RE is between Ag and AgCl the same as Ag/AgCl RE in aqueous solution. As the RE potential is a major issue in non-aqueous solution experiments[9] due to their unknown standard potentials, the standardisation of REs is required to compare the standard potential of REs with other studies. Therefore, the ferricyanide/ferrocyanide ($Fe(CN)_6^{3-}/Fe(CN)_6^{4-}$) couple was used for the standardisation of the REs. The E_0 of $Fe(CN)_6^{3-}/Fe(CN)_6^{4-}$ couple was 0.256 V in an aqueous solution using Ag/AgCl RE while The E_0 of $Fe(CN)_6^{3-}/Fe(CN)_6^{4-}$ couple was 0.213 V in Ethaline using Ag wire, 0.252 V in Reline, 0.231 V in Glyceline, 0.233 V in Wateline, which were measured from the potential differences of oxidation and reduction peaks. Ag wire pseudo RE, before using in a solution, was polished with fine sandpaper and cleaned with deionised water, acetone and the solution into which it would be immersed.

3.3.1.3. Counter Electrode

A Pt flag CE was used in all electrochemical experiments. Its surface area was 2 cm^2 which was larger than all WE used to avoid the current being limited by reaction on the CE electrode. The CE was immersed into concentrated HNO_3 for 2 minutes at 20 ± 2 °C to clean the electrode and then washed with deionised water, acetone and the electrolyte in which it would be immersed. The CE was positioned parallel with the WE during the electrochemical experiments to ensure a uniform electric field in order to obtain a uniform film onto the surface of WE (and uniform redox exchange during film oxidation/reduction). Uniform film across the surface of the QCM is essential for the validation of the Sauerbrey equation[10] for detecting mass changes of the films.[11]

3.3.1.4.   Electrochemical cell

The electrochemical and gravimetric data were recorded simultaneously by using two different network analysers. One of them was a Hewlett Packard 8751A 5 Hz – 500 MHz network analyser connected through a 50 Ω coaxial cable and an HP87512A transmission/reflection unit to make the crystal impedance measurements[12, 13] for the electrochemical deposition of films (homopolymers or copolymers). Another equipment for the EQCM measurement was Gamry Instruments eQCM 10M connected with Gamry Instruments Reference 600 potentiostat used for in-situ electrochemical and gravimetric measurements. The advantage of using Gamry equipment is its feature producing the electrochemical and gravimetric output automatically which does not require a separate fitting program. The two instruments operate differently and give data of different types, each of which is optimal for a particular purpose. Specifically, the Gamry instrument has a faster response, but achieves this by sacrificing the acquisition of the full admittance spectrum. This is ideal for short timescale experiments. In a complementary manner, the HP instrument provides the full admittance spectrum, but this more detailed analysis necessarily results in a slower acquisition rate. This is ideal for situations in which one must diagnose whether the film response is gravimetrically or viscoelastically controlled.[14-16] If it is gravimetrically controlled, then the Gamry instrument can be used and the data interpreted using the Sauerbrey equation. In this thesis, the validity of the Sauerbrey equation was determined with admittance-frequency spectra[15] using Hewlett Packard network analysis. After the films were obtained by monitoring with Hewlett Packard network analysis, electrochemical redox reactions of the films were conducted with Gamry eQCM.

The cells used in the EQCM experiments were home-made and one of them is shown in Figure 3.3.
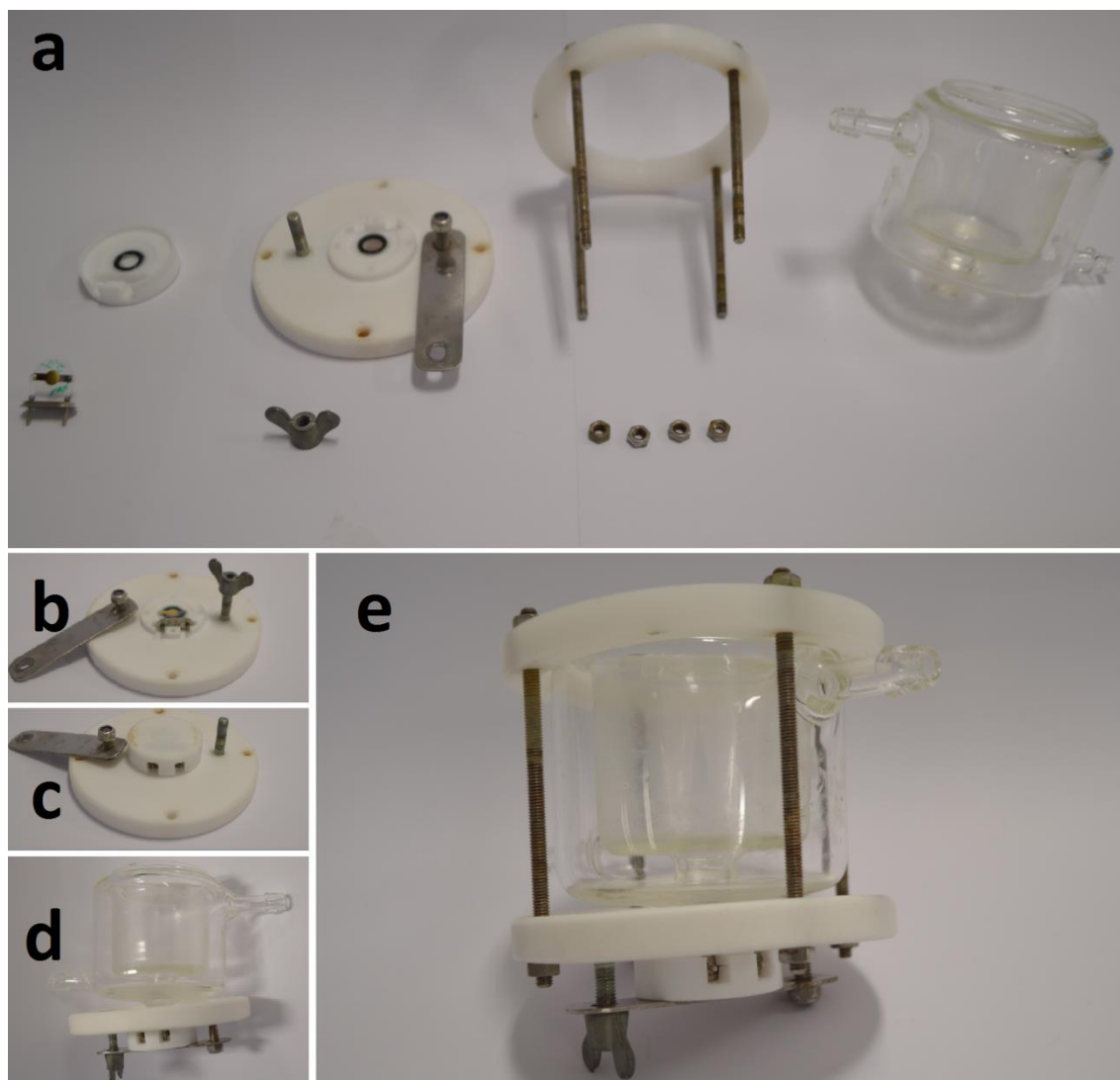
Figure 3.3: The process of the insertion of the WE into the cell, home-made designed, used for electrochemical experiments. a) glass, iron and Teflon elements of the cell; b) insertion of AT-cut quartz crystal into Teflon parts; c) tightening the quartz crystal; d) connection of the glass cell to Teflon bottom; e) whole cell.

AT-cut quartz crystal, whose one surface was used as WE exposed to the electrochemical solution, was mounted into the Teflon parts in the base of the glass cell, photographed in panel b Figure 3.3. It was then tightened with screws in the Teflon parts of the cell not to allow the electrochemical solution leak into the other side of crystal to prevent the loss of oscillation.[17] Three electrodes (RE, CE and WE) were kept to close to each other during electrochemical experiments and their set-up is shown in Figure 3.4 which is the combination of an network analyser with the potentiostat.[18, 19]
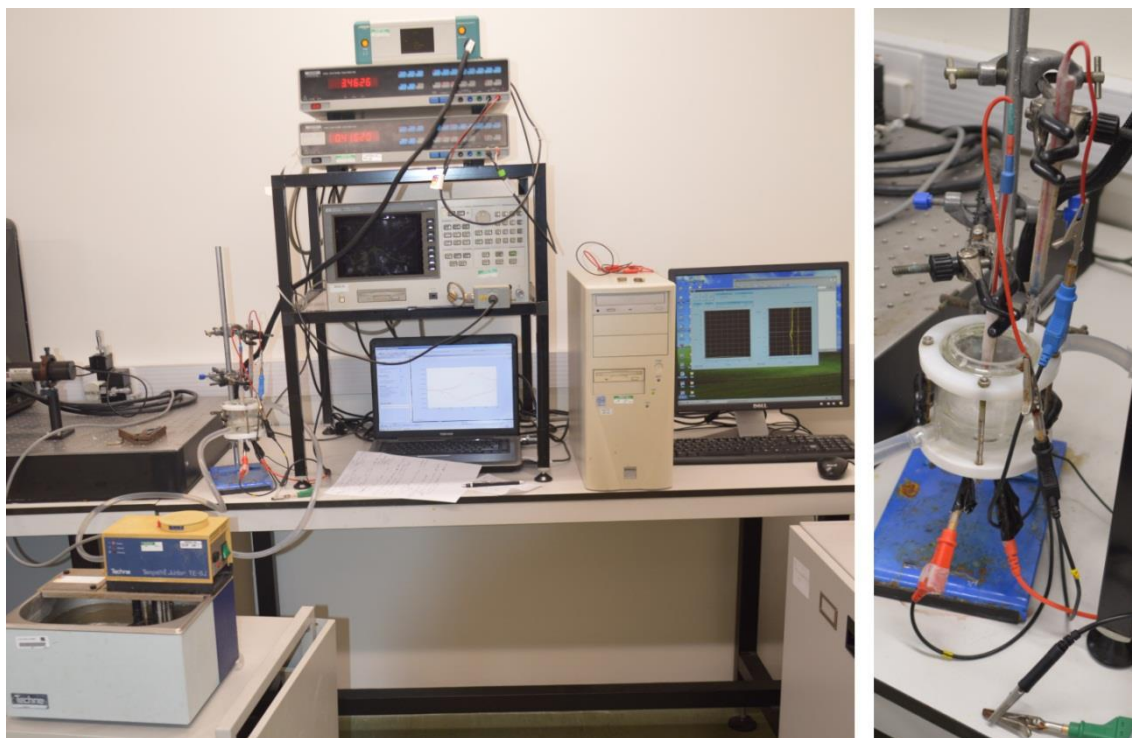
Figure 3.4: The cell connected to electrochemical system and a network analyser, given in the text, for the EQCM experiments in working arrangement with water bath.

A new AT-cut quartz crystal (Au WE) was used for each film to obtain a fresh film to avoid the possible effect of previous film used. However, the WEs covered by glass (0.44 mm^2) were cleaned for each SEM measurements or for pre-QCM experiments. The cleaning process is conducted as explained here: WEs were mechanically polished to a mirror finish with 0.3 μm alumina (Beuhler) on a cloth and were washed with deionised water, acetone and the solution in which the WE would be immersed. RE was washed with deionised water and the electrolyte. Electrochemical studies were conducted by using a μAUTOLAB Type III potentiostat controlled by GPES software.

3.3.2.   Non-Electrochemical Measurements

3.3.2.1.   Scanning Electron Microscopy

The SEM instrument for surface analysis of the work presented in this thesis was a FEI SIRION SEM. SEM analyses were carried out under vacuum (10^{-5} Pa) with an accelerator voltage of between 5 keV and 8 keV due to the use of soft materials

(conducting polymers) which did not require gold sputtered coating. A typical distance used for the measurement in FEGSEM was 7 mm to 15 mm depending on the resolution of the images.

3.3.2.2. Fourier Transform Infrared Spectroscopy

The spectra were recorded on the Perkin Elmer Spotlight 400 FTIR imaging system in the region of 650 cm^{-1} – 4000 cm^{-1}. Reflectance mode with a resolution of 8 cm^{-1} (at 20 ±2 °C) was performed to take the images and representative points from the images were selected in order to compare the films with each other.

3.3.2.3. Quartz Crystal Microbalance

Viscosity was measured by frequency data obtained from the QCM[20] explained in chapter two. The viscosity results obtained from the QCM data were compared with the viscosity measured by Rotational Viscometer (RV). Therefore, The QCM data for the calculation of viscosity was obtained in tandem with the RV measurement of viscosity. An Agilent technologies E5061A 300 kHz – 1.5 GHz ENA Series Network Analyser was used to acquire all the QCM readings for the viscosity calculations from the data of admittance against frequency of a polished crystal. The delay time to obtain a spectrum of the QCM data was 10 s. One multimeter (TTi 1705 True RMS Programmable Multimeter) was attached to the network analyser to record the output of the attached thermocouple (J type Omega thermocouple) used to accurately measure the temperature *in-situ* during the collection of the QCM data for viscosity of the fluids.

3.3.2.4. Rotational Viscometer

The DV-II+ Pro Brookfield's Rotational Viscometer was used for the collection of the viscosity data. The sample volume, required for optimum results, should be at least 600 mL in order to leave sufficient space between the vessel walls and the guardleg attaching to the RV. All measurements were conducted using the Teflon cylindrical spindle (shown in chapter 5).

In this study, viscosity measurements, calculated from the QCM, are compared to viscosity measured with the DV-II+ Pro Brookfield's Digital RV. The motor in the device drives a spindle and changes in torque, which required rotating an immersed spindle in a liquid, are detected by a coiled spring wrapped around the drive shaft. The torque can be used to calculate the viscosity of the liquid by RV. Higher viscosity of the sample creates greater drag requiring that the motors work harder to maintain the rotation speed. Resistance to flow is related to the size and the shape of the spindles and proportional to the speed of the spindle rotations. During the measurement of viscosity by RV, the %torque of the RV must be between 10% and 100% in order to obtain reliable viscosity data. The most accurate viscosity readings could be obtained when the %torque is close to 100%. As %torque depends on the type of the spindle, the speed of spindle rotation and viscosity of the liquid, optimum conditions of the viscosity measurement requires pre-measurement. When the value of %torque is greater than 100%, a small value of the speed of spindle rotation was selected in order to decrease %torque. The value of the relative error of the viscosity, which is dependent upon the %torque reading, decreases as the reading of the %torque approaches 100%. RV was controlled via a software program named Rheocalc controlled by a PC during all measurements allowing viscosity data collection every second.

3.4. Procedures

3.4.1. Film Deposition

Firstly, polyaniline (PANI) films were deposited potentiodynamically with a potential range of -0.2 V to 0.95 V (*vs.* Ag/AgCl RE) from 0.1 M aniline in 1 M H_2SO_4 solution at different potential scan rates to calculate the water content as a function of the number of deposition cycles.

Secondly, poly(*o*-toluidine) (POT) films, were obtained by potentiodynamic electrodeposition (see Figure 3.5) from 0.1 M *o*-toluidine in 1 M H_2SO_4. The conditions of electrodeposition of POT are the same as aniline polymerisation (same potential window and scan rate) except for the number of deposition cycles.
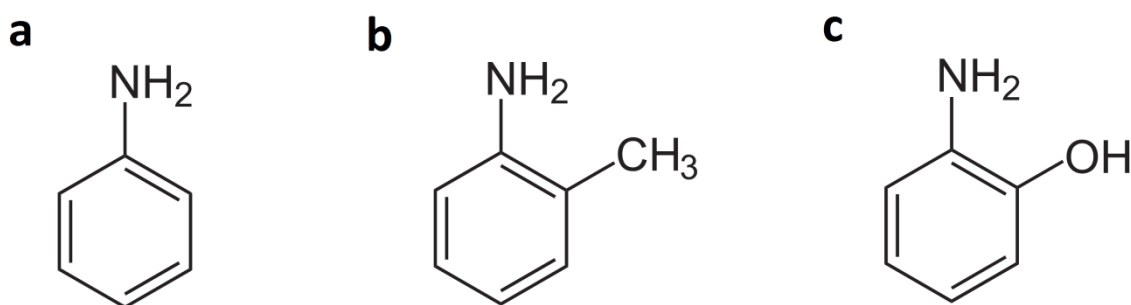
Figure 3.5: Structures of a) aniline; b) o-toluidine and; c) o-aminophenol.

Thirdly; *o*-aminophenol (Figure 3.5) was polymerized from 0.1 M *o*-aminophenol in 1 M H_2SO_4 by cycling from -0.2 V to 0.95 V at a scan rate of 50 mV s^{-1} as for aniline and *o*-toluidine polymerisation (POT). All homopolymers (PANI, POT and POAP) were deposited potentiodynamically with the same potential range by means of the EQCM to compare the kinetics of growth of the homopolymers.

After obtaining homopolymers, poly(aniline-*co*-*o*-toluidine) P(ANI-OT) and poly(aniline-*co*-*o*-aminophenol) P(ANI-OAP) copolymer films were deposited potentiodynamically onto gold WE. Different concentration of aniline and/or *o*-toluidine, with a total monomer concentration 100 mM in 1 M H_2SO_4 were used for deposition (-0.2 ≤ E/V ≤ 0.95, *v* = 50 mV s^{-1}) in order to analyse the effect of monomer ratio for 10 deposition scans. P(ANI-OAP) films were grown with the same way as P(ANI-OT).

Prior to the measuring mass changing during electrochemical experiments in DESs or aqueous solution, admittance spectra were used to establish whether the films were acoustically thin (rigid) to use the Sauerbrey equation for gravimetric analysis and free from any viscoelastic effects.[21]

The growth of all homo and copolymers were stopped with the applied potential held at -0.2 V. After withdrawal from solution, the film was rinsed with deionised water for voltammetric characterisation and using in NaF solution to test fluoride extraction.

The polymerisation was driven by applying a voltage from -0.2 V to 0.9 (or 0.95 V) *vs.* Ag/AgCl (sat. KCl), for various numbers of deposition cycles (2 - 15) at various scan rates (5 mV s^{-1} - 100 mV s^{-1}) to analyse the effect of thickness and the growth

conditions in DESs. After the films were deposited onto 10 MHz AT-cut Au polished quartz crystal, the growth of the films were stopped at the reduced end of the potential cycle (E = -0.2 V) as applied for the film prepared for the characterisation. Prior to transferring the PANI films from the acidic aqueous (deposition) solution to DESs, the films were washed with deionised water and rinsed several times (typically six-seven) with hot (50 °C) DESs to remove aqueous solution from the voids in the PANI films.

3.4.2. Film Characterisation

The freshly prepared films were tested in monomer-free (1 M H_2SO_4) electrolyte. A potential range of -0.2 ≤ E/V ≤ 0.6 *vs.* Ag/AgCl was applied to observe p-doping of the films (v = 50 mV s^{-1}). All experiments based on growth of homo and copolymers and their characterisation were conducted at room temperature (20 ± 2 ^{o}C).

Films grown on quartz crystal were left at room conditions for two days to dry in order to characterize their optical behaviour by means of FTIR. SEM images were obtained about the same amount of PANI films, which were grown with different numbers of cycles and scan rates and left for two days on the top of glass WE, in order to observe their morphologic properties and see porosity differences of the films.

3.4.3. Electrolyte Characterisation

The work in chapter five aims to measure the viscosity of DESs over a wide range of temperatures ranging from 25 to 80 °C. Initially, viscosities of Ethaline as a function of temperature, obtained from the QCM data, were collected in a small jacketed cell which is connected with a water pump having a thermostatic heating element to control the temperature of the fluid. The initial results of viscosity measured from RV were rather different to those obtained from the QCM data. Therefore, a new cell was designed and the procedure was changed. The details of the cell and experimental development are given in chapter five.

3.4.4.   Ion Transfer Measurement

3.4.4.1.   Films in Deep Eutectic Solvents

The PANI films were transferred into DESs electrolyte, to observe the ion-exchange dynamics during redox switching by means of the EQCM at various scan numbers, scan rates, potential windows and temperatures. Multiple scans (more than 30 000 cycles) were applied to PANI film exposed to Ethaline from 0 V to 0.6 V at a scan rate of 100 mV s^{-1} for long-term cycling performance.

The cyclic voltammetry responses of PANI film, exposed to Ethaline cycling at various scan rates ranging from 1 mV s^{-1} to 100 mV s^{-1} applying voltage from 0 V(or 0.2 V) to 0.6 V (*vs.* Ag wire), were recorded to observe the effect of scan rate.

Two films, deposited with the same conditions, were prepared and one of them was left for longer duration under open circuit conditions and the other film was immediately was cycled in Ethaline to observe the effect of waiting time.

Ion transfer dynamics were checked at higher temperatures to understand the effect of temperature of the electrolyte. During switching of one of the PANI films, the temperature was increased from room temperature to 50 °C using a home-made cell (see Figure 3.3 and Figure 3.4) to observe the mass change during increase in temperature.

The experiments based on PANI film in monomer-free electrolyte (1 M H_2SO_4), before and after cycling in Ethaline, are conducted to see the differences. Different DESs were used as electrolyte in PANI redox reaction as well to compare the responses of mass and charge of them with Ethaline responses at 50 °C. In addition, PANI film was cycled in crystallised DESs (Propaline and Wateline).

3.4.4.2.   Films in Aqueous Solutions

The electrochemical behaviour of PANI electrode was firstly investigated by the cyclic voltammetric mode of the EQCM in aqueous electrolyte containing 0.1 M NaF.

Chronoamperometric form of the EQCM was used to see F^- molarity range PANI could extract from aqueous solutions. For this, -0.2 V was applied for 10 s and then 0.6 V was applied for 30 s to the PANI film in solutions of different F^- concentration.

POT, POAP and their copolymers with PANI were investigated by the CV mode of the EQCM in 0.1 M fluoride solution. All films, used for fluoride extraction, was transferred to 0.1 M H_2SO_4 cycling from -0.2 V to 0.6 V at a scan rate of 50 mV s^{-1} to compare before cycling in F^- solution in order to explore the reusability of the films. All experiments of fluoride extraction were conducted at room temperature (20 ± 2 ^{o}C).

3.5. References

1 R. Schumacher, G. Borges and K. Kanazawa, *Surface Science Letters,* 1985, **163**, L621-L626.

2 P. Spitzer, S. Wunderli, K. Maksymiuk, A. Michalska, A. Kisiel, Z. Galus and G. Tauber, in *in Handbook of Reference Electrodes,* Springer, 2013, pp.77-143.

3 G. A. East and M. del Valle, *J. Chem. Educ.,* 2000, **77**, 97.

4 R. Bates and J. Macaskill, *Pure Appl. Chem.,* 1978, **50**, 1701-1706.

5 U. Schröder, J. D. Wadhawan, R. G. Compton, F. Marken, P. A. Suarez, C. S. Consorti, R. F. de Souza and J. Dupont, *New Journal of Chemistry,* 2000, **24**, 1009-1015.

6 D. MacFarlane, S. Forsyth, J. Golding and G. Deacon, *Green Chem.,* 2002, **4**, 444-448.

7 B. Huber and B. Roling, *Electrochim. Acta,* 2011, **56**, 6569-6572.

8 L. Barrosse-Antle, A. Bond, R. Compton, A. Mahony, E. Rogers and D. Silvester, *Chem.Asian J,* 2010, **5**, 202-230.

9 K. Izutsu, *Electrochemistry in Nonaqueous Solutions,* John Wiley & Sons, Weinheim, 2009, p167-200.

10 B. A. Martin and H. E. Hager, *J. Appl. Phys.,* 1989, **65**, 2627-2629.

11 G. Sauerbrey, *J.Physik,* 1959, **155**, 206-212.

12 M. A. Mohamoud and A. R. Hillman, *Electrochim. Acta,* 2007, **53**, 1206-1216.

13 S. J. Martin, V. E. Granstaff and G. C. Frye, *Anal. Chem.,* 1991, **63**, 2272-2281.

14 A. R. Hillman, K. S. Ryder, V. C. Ferreira, C. J. Zaleski and E. Vieil, *Electrochim. Acta,* 2013, **110**, 418-427.

15 A. R. Hillman, *Journal of Solid State Electrochemistry,* 2011, **15**, 1647-1660.

16 I. Efimov, A. R. Hillman and J. Walter Schultze, *Electrochim. Acta,* 2006, **51**, 2572-2577.

17 D. A. Buttry and M. D. Ward, *Chem. Rev.,* 1992, **92**, 1355-1379.

18 S. Bruckenstein and M. Shay, *Electrochim. Acta,* 1985, **30**, 1295-1300.

19 A. Glidle and A. R. Hillman, *Journal of electroanalytical chemistry and interfacial electrochemistry,* 1991, **318**, 411-420.

20 K. Keiji Kanazawa and J. G. Gordon II, *Anal. Chim. Acta,* 1985, **175**, 99-105.

21 A. R. Hillman, M. A. Mohamoud and I. Efimov, *Anal. Chem.,* 2011, **83**, 5696-5707.

Chapter 4: Synthesis of Polyaniline and Aniline-based Copolymers from Aqueous Media

4.1. Introduction

4.1.1. Overview

Conducting polymers (CP) have attracted great interest for the last three decades owing to their wide range of potential applications as described in chapter one. Among CP, polyaniline (PANI) is widely used due to its optical properties, high electrical conductivity, low cost, high environmental and chemical stability and its applications in various areas[1, 2] as explained in chapter one. Chemical polymerisation,[3] electrochemical polymerisation,[4] vapour-phase deposition,[5] photochemically initiated polymerisation,[6] enzyme – catalysed polymerisation[7] are used to synthesise PANI. However, among them, electrochemical deposition is the most attractive technique to obtain PANI because of its ability to control desirable properties of PANI (*e.g.* morphology and electrical properties) by varying the conditions of electrolyte bath and applied voltage.[8]

Recently, the fabrication of copolymers and nanocomposite – conducting polymer hybrid materials have been studied widely to design new films. Prior to improvement and using CP, understanding the physical-chemical behaviour of simple polymers and their kinetics should be recognised. The key factor for the use of CPs in real life devices is to improve their performance, through understanding the growth and preparation of the films.

If the growth of CP is well understood; their flexibility, rigidity, stability and processability can be controlled and evaluated for new applications. To enrich literature for helping researchers who will design the application of a CP, detailed attention should be given to the first step of the film design, which is the formation of the polymers. Not only the formation of polymer itself but also composite material and/or copolymer formation is important. Understanding the chemical, electrical and mechanical properties of PANI and its derivatives is complicated. Experiments monitoring growth of the film were conducted to shed some light on deposition of the film. Therefore, this chapter focuses on the formation of PANI, poly(o-toluidine) (POT), poly(o-aminophenol) (POAP) and copolymer of PANI with POT and POAP.

4.1.2. Aims and Objectives

The objectives of the work in this chapter are (i) the identification of the masses calculated from the QCM and cyclic voltammetry for potentiodynamically deposited PANI film growth, then the estimation of mass differences between cyclic voltammetry and the QCM, based on the film efficiency or electrolyte and/or solvent insertion into the film, during each scan and the influences of the number of scans on mass differences for the same amount of the film deposited; (ii) the exploration of the morphology of the film deposited with different number of scans using the same amount of PANI by means of SEM; (iii) the fabrication of PANI copolymers with POT and POAP growth during potentiodynamical polymerisation; (iv) the identification of the effect of the ratio of monomers during electrocopolymerisation using constant number of scans and the effect of number of scans in the copolymerisation, additionally the examination monomer dominations in the electrocopolymerisation; (v) the interpretation of the redox behaviour and ion transfer dynamics for all obtained polymers and copolymers transferred into acidic electrolytes; (vi) the characterisation of all (co)polymers using FTIR and the investigation of (co)polymers in terms of electrochemical and optical behaviour.

4.2. Results

4.2.3. Dynamics of Film Growth

Polymer deposition procedures were explained in detail in chapter three. All films shown in this chapter were deposited potentiodynamically with a potential range of -$0.2 \leq E/V \leq 0.95$ vs. Ag/AgCl (sat.) from 0.1 M total monomer(s) in 1 M H_2SO_4 solution. For P(ANI-OT) and P(ANI-OAP) copolymer films, the total concentration of monomers was 0.1 M. The growth of the film was stopped at the reduced end of potential cycle (E = -0.2 V) and the film was then rinsed with deionised water.

4.2.3.1 Polyaniline

Figure 4.1, Figure 4.2, and Figure 4.3 represent the deposition of PANI film for different scan rates and number of scans (panel a is for the current and panel b is for

mass traces) from the EQCM. The films were obtained from 0.1 M aniline in 1 M H_2SO_4 by cycling the voltage from -0.2 V to 0.95 V. The i *vs.* E graphs are similar to those reported in the literature.[9-12] The anodic peak, seen in Figure 4.2 and Figure 4.3, is the transformation of leucoemeraldine to emeraldine state of PANI observed around 0.22 V and its further oxidation to pernigraniline[13, 14] was observed around 0.6 V as mentioned in chapter one. Panel b of Figure 4.3 shows that the polymerisation rate ($\Delta m/\Delta t$) increase rapidly indicating an autocatalytic reaction as explained in-depth in the literature.[15] When polymerisation starts at the bare electrode, PANI forms and a redox active area of substrate that is enlarged with more film. Electropolymerisation increases significantly with every deposition scan, this process is referred to as an "*autocatalitical reaction*"[16, 17] in this thesis. The rationale behind showing the graph of PANI polymerisation here is to compare the reaction kinetics with POT and POAP in the following section of this chapter. Scan rate was changed for each experiment shown here but potential window was constant between -0.2 V and 0.95 V. Otherwise; for the same scan rate, wider potential window would cause more film to be deposited after the polymerisation point.

Admittance spectra used as a diagnostic to establish whether the film is acoustically thin (rigid) in which case the Sauerbrey equation is valid. PANI film was deposited up to a point that the film was still rigid and the Sauerbrey equation was valid in which admittance decreases 20%. Also, q factor, which was not changed significantly, could be used for the validation of the Sauerbrey equation.[18] In this thesis, admittance-frequency graph has been used to determine whether the Sauerbrey equation is valid.[19] In panel c of Figure 4.1 and panel c of Figure 4.2, it is seen that there was a shift of Y and f to lower values. However, the peak admittance was not changed significantly, which suggests the characteristic of a rigid (acoustically thin) film.
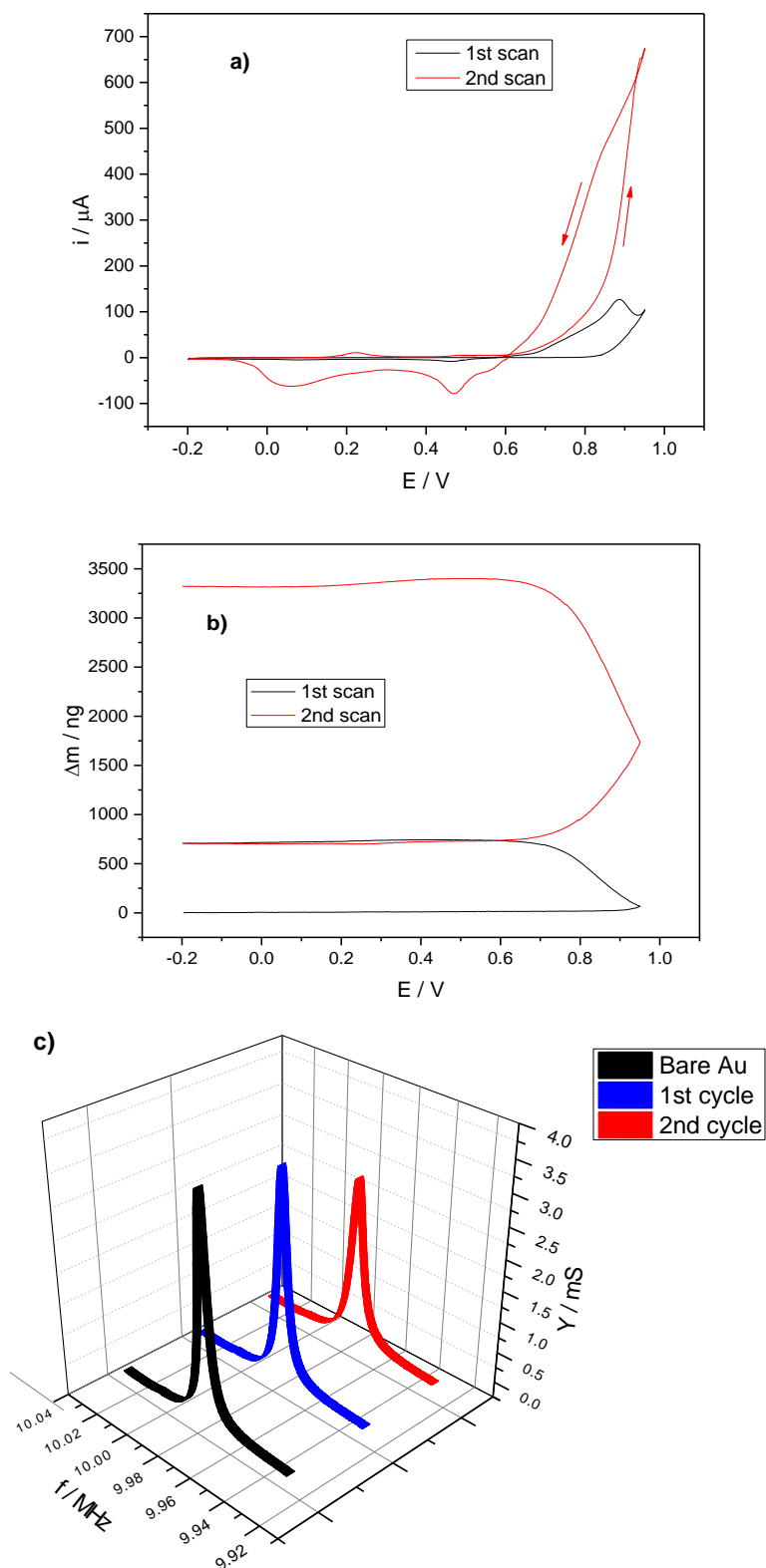
Figure 4.1: EQCM data for the preparation of a PANI film deposited potentiodynamically (-0.2 V to 0.95 V; 10 mV s^{-1}) from 0.1 M monomeric ANI / 1 M H$_2$SO$_4$, 2 scans a)current vs. potential plot; b) mass change vs. voltage plot; c) crystal admittance spectra, Y/mS vs. f/MHz, recorded at the end of each potentiodynamic cycle.
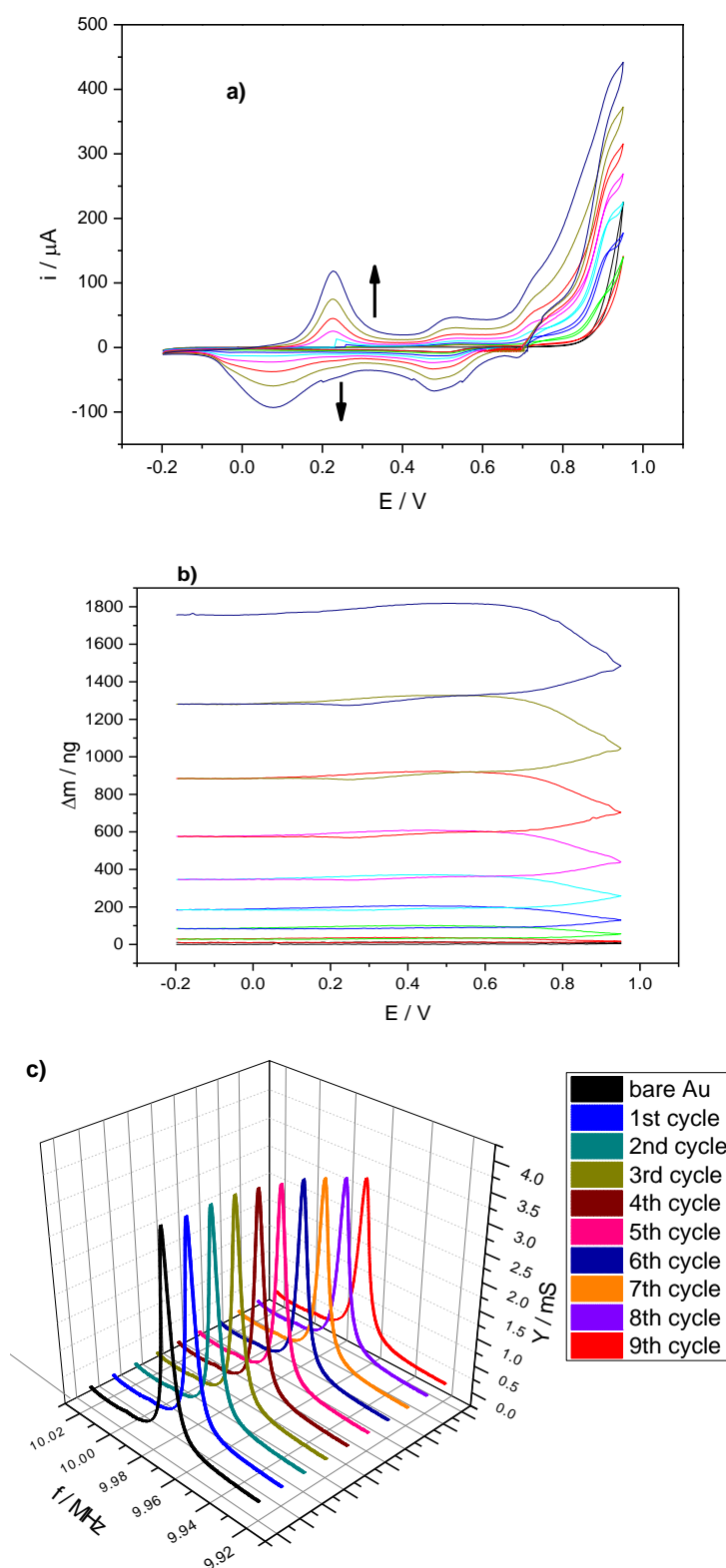
Figure 4.2: EQCM data for the preparation of a PANI film deposited potentiodynamically (-0.2 V to 0.95 V; 100 mV s^{-1}) from 0.1 M monomeric ANI / 1 M H$_2$SO$_4$, 9 scans a) cyclic voltammetry, current vs. potential plot; b) EQCM, mass change vs. voltage plot; c) crystal admittance spectra, Y/mS v.s f/MHz, recorded at the end of each potentiodynamic cycle
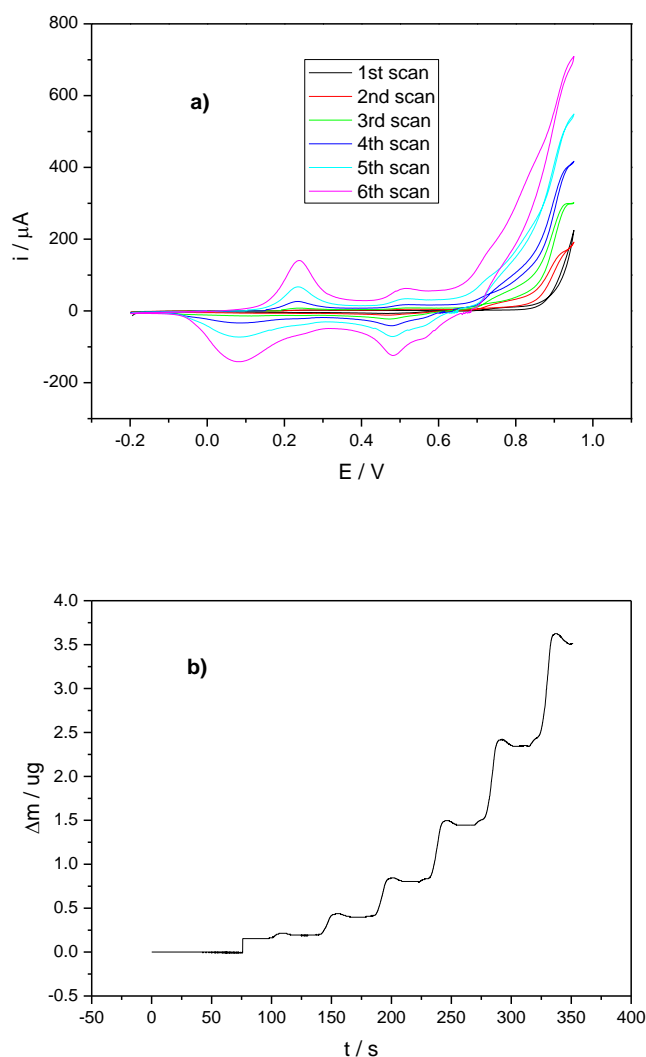
Figure 4.3: EQCM data for the preparation of a PANI film deposited potentiodynamically (-0.2 V to 0.95 V; 50 mV s^{-1}) from 0.1 M monomeric ANI / 1 M H$_2$SO$_4$, 6 scans a) cyclic voltammetry, current vs. potential plot; b) QCM, mass change during growth

Panel b of Figure 4.1 and Figure 4.2 illustrates that the mass of PANI films increased when the voltage reached 0.76 V. Despite having the same polymerisation point, there was a clear difference in terms of time scale, when 10 mV s^{-1} and 100 mV s^{-1} scan rate was applied separately. When the former scan rate was applied, the limit of validity of Sauerbrey equation was reached with less scan numbers compared to when 100 mV s^{-1} scan rate was applied. Therefore, two scans of PANI polymerisation for 10 mV s^{-1} met the Sauerbrey equation limit. However, when the scan rate was 100 mV s^{-1} for the same potential window (from -0.2 V to 0.95 V), PANI deposition took 9 scans to require the Sauerbrey validity. Therefore, scan numbers were controlled depending on

scan rate applied. PANI mass shown in Table 4.1 can easily be measured using the Sauerbrey equation (chapter 2).

Coverage of electroactive PANI film sites (Γ/mol cm^{-2}) were calculated according to equation given in 4.1:

$$\Gamma = \frac{Q_r}{nFA} \qquad\qquad (4.1)$$

In Eq 4.1, Q_r (C) represents all polymer sites for the given scan number and was calculated from the charge under the more cathodic of the reduction peaks; n is the number of electrons in the redox process (n = 1); F is the Faraday constant. For the typical example presented as panel a of Figure 4.1, surface coverage of PANI was 71.7 nmol cm^{-2}. In this case "mol" is used for dimeric aniline redox units, for which the number of electron is one (n = 1). The change in the mass of the film for each scan of deposition of PANI film can be directly calculated from frequency differences by using the Sauerbrey equation. The molar mass was calculated from the correlation of the coverage measured from cyclic voltammetry with mass obtained from the QCM. According to this calculation, it was found the molar mass of PANI deposition was 201 g mol^{-1}. Since dimeric aniline molar mass in PANI was 182 g mol^{-1}, the difference of 19 g mol^{-1} (201 − 182) was considered as the electrolyte incorporated into the film. This equals *ca.* 1.06 water molecules per redox site (per dimeric aniline). This result is in agreement with previous calculations by Hillman *et al.*[20] However, water contents measured in other experiments were different from the result found previous results in which there was 1.06 water molecules per redox site. All water contents during the electropolymerisation of PANI stopped at the reduced end (-0.2 V), are given in Table 4.1.

Table 4.1: Water contents for each cycle during growing PANI film for a) 2; b) 9; and c) 6 scans (10, 100 and 50 mV s⁻¹ respectively), growth from 0.1 M monomeric ANI / 1 M H_2SO_4, between -0.2 V and 0.95 V

a)

(Fig. 4.1) 2 scans 10 mV s⁻¹	Γ (nmol cm⁻²) (from cyclic voltammetry)	m (ng cm⁻²) (from QCM)	Molar Mass (g mol⁻¹)	H_2O/(ANI)$_2$
1st scan	6.43	3070	478	16.4
2nd scan	71.7	14400	201	1.06

b)

(Fig. 4.2) 9 scans 100 mV s⁻¹	Γ (nmol cm⁻²) (from cyclic voltammetry)	m (ng cm⁻²) (from QCM)	Molar Mass (g mol⁻¹)	H_2O/(ANI)$_2$
6th scan	3.26	2500	767	32.5
7th scan	5.09	3840	754	31.8
8th scan	7.57	5570	736	30.8
9th scan	11.2	7640	682	27.8

c)

(Fig. 4.3) 6 scans 50 mV s⁻¹	Γ (nmol cm⁻²) (from cyclic voltammetry)	m (ng cm⁻²) (from QCM)	Molar Mass (g mol⁻¹)	H_2O/(ANI)$_2$
4th scan	10.4	6300	606	23.6
5th scan	17.1	10200	597	23.1
6th scan	30.2	15200	503	17.8

Initial cycles demonstrated in Figure 4.2 and Figure 4.3 are not given in Table 4.1 as charge under the more cathodic of the reduction peaks are not clear to calculate. Generally, the faradaic efficiency of PANI is less than 100%. As the ratio of water content per dimeric aniline was not affected we could assume it to be 100%.

For the 4th scan shown in Figure 4.3, per dimeric PANI redox site included 23.6 water molecules and when scan number increased the content of water molecules decreased through 23.1 to 17.8 respectively for 5th and 6th scans. The same trend is observed for other experiments shown in this chapter: Figure 4.1, Figure 4.2 and also for the other experiments that has not been included in this thesis. The decrease in water content by scan number could be explained through the growth of the polymer whose schematic illustration is presented in Figure 4.4.
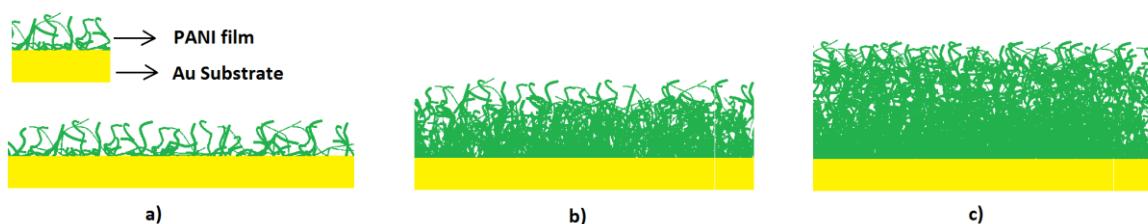
Figure 4.4: Schematic illustration of the deposition of PANI on Au substrate (cross-section) for the same experiment a) early stages of the polymerisation, b) increasing scan numbers, c) later stages of the polymerisation

The higher mass obtained from the QCM could arise from presence of the water molecules between PANI branches. Water molecules moved together with film itself behave like a part of the rigid film. There were more water per PANI in the initial scans of the polymerisation depicted in panel a of Figure 4.4 than in the latter scans of polymerisation presented in panel b and c of Figure 4.4. The ratio of vertical growth to horizontal growth of PANI in early scan numbers was relatively higher than latter stages. Therefore, the water content in PANI decreased with increasing thickness through increasing scan numbers.

When the numbers of scans were compared for the same amount of film (*e.g.* comparing 9th scan in Figure 4.2 having 11.2 nmol cm^{-2} with 4th scan in Figure 4.3

having 10.4 nmol cm^{-2}), it is obviously seen in Table 4.1 that PANI films deposited from more scans had more water as a result of differences in film growth. Film having more water could be more porous than its equivalence amount of film having less water. In order to show film porosity SEM images of film have been taken and a figure is given and discussed in 4.2.4.8 at the end of this chapter.

Calculation of electroactive mass from cyclic voltammetry for 6th scan presented in panel c of Table 4.1 was 5490 ng (6.94*10^{-9} mol x 182 g mol^{-1}/0.23 cm^2) while mass obtained from the QCM was 15200 ng. One could suppose that this difference was observed due to having electro*in*active PANI film. However, in Figure 4.5 PANI films were taken out of the solution, the experiments were stopped at -0.2 V and photographed immediately shown in panel a of Figure 4.5 and two days later, the dry film was photographed (see panel b of Figure 4.5) as well and the colours were compared. Based on the comparison in optical density, it is obvious that the film obtained with 2 scans had more PANI than the one obtained with 6 scans (more PANI is seen greener).
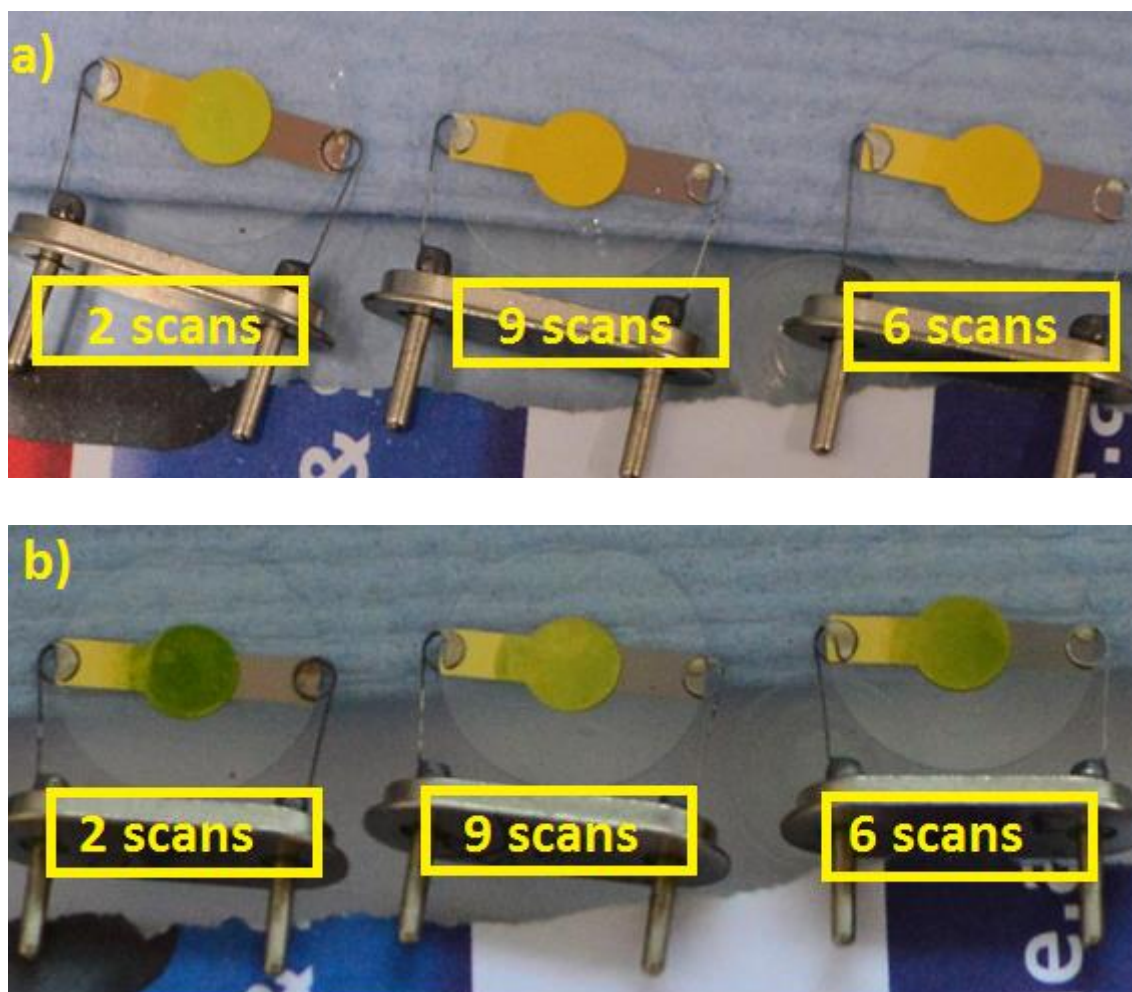
Figure 4.5: Images of PANI films for 2, 9 and 6 scans (10 mV s^{-1}, 100 mV s^{-1} and 50 mV s^{-1} respectively), growth from 0.1 M monomeric ANI / 1 M H$_2$SO$_4$, between -0.2 and 0.95 V, a) immidiately after growth PANI films; b) 2 days after the growth.

The mass of the films grown with 2 and 6 cycles calculated from the QCM were similar to each other (14400 and 15200 ng respectively as shown in Table 4.1). However, the mass of PANI deposited with 2 scans calculated from cyclic voltammetry was 13100 ng (pale green) and 6 scan film, whose mass calculated from cyclic voltammetry was 5490 ng (yellow) in panel a of Figure 4.5. Two days after the growth, the mass differences between the films were observed more clearly by naked eye. Obviously, the film obtained with 2 scans had more PANI than the one obtained with 6 scans. Therefore, the calculated mass differences, cyclic voltammetry *vs.* the QCM, were not arisen from having electro*in*active PANI, actually it was the water molecules PANI films retained.

4.2.3.2 Poly(*o*-toluidine)

POT deposition, which is compared and contrasted with PANI, was investigated before producing copolymer films of (PANI-OT). Figure 4.6 shows the responses obtained during electropolymerisation of OT film from 0.1 M *o*-toluidine in 1 M H_2SO_4 applying the voltage from -0.2 V to 0.95 V at a scan rate of 50 mV s^{-1}. Figure 4.6, similar to polymerisation of ANI, shows an irreversible oxidation peak at 0.87 V, indicating monomer oxidation. Panel a in Figure 4.6 shows for the first 10 scans that there is one oxidation and one reduction peak, around 0.45 V and 0.42 V, respectively, which could be because of the dimer soluble products[21] or quinone/hydroquinone hydrolysis products bound to the surface loosely.[22] Two more oxidation and reduction peaks (indicated by small arrows in panel b and d of Figure 4.6) at *ca.* 0.3 V and 0.7 V are due to the formation of emeraldine salt from leucoemeraldine base and its further oxidation to pernigraniline[13, 14] like PANI.

Figure 4.6: Cyclic voltammetric data for the preparation of a POT film deposited potentiodynamically (-0.2 V to 0.95 V; 50 mV s^{-1}) from 0.1 M monomeric OT / 1 M H$_2$SO$_4$, a) 1-10 scans; b) 1-20 scans; c) 1-30 scans; d) 1-40 scans. Arrows indicate the change of curves with increasing the number of scans.

Figure 4.7 shows the graphs acquired from the EQCM recorded during the electrosynthesis of POT film formed from 0.1 M *o*-toluidine in 1 M H_2SO_4 by applying the voltage from -0.2 V to 0.95 V at the scan rate of 50 mV s^{-1}. Panel a of Figure 4.7 demonstrates that the peak currents increased with increasing the number of scans. Green POT film was deposited until 20% decrease in admittance spectrum was observed and the result is shown in panel b Figure 4.7.

The mass increase between 2nd and 8th cycles of OT polymerisation, as seen in panel c of Figure 4.7, did not indicate an autocatalytic deposition. However, in panel d of Figure 4.7, it is clearly demonstrated that the increase in mass in the latter stage of polymerisation of OT was faster than early stage of polymerisation, indicating that the polymerisation of OT was also an autocatalytic reaction which shows similar polymerisation kinetics to PANI.
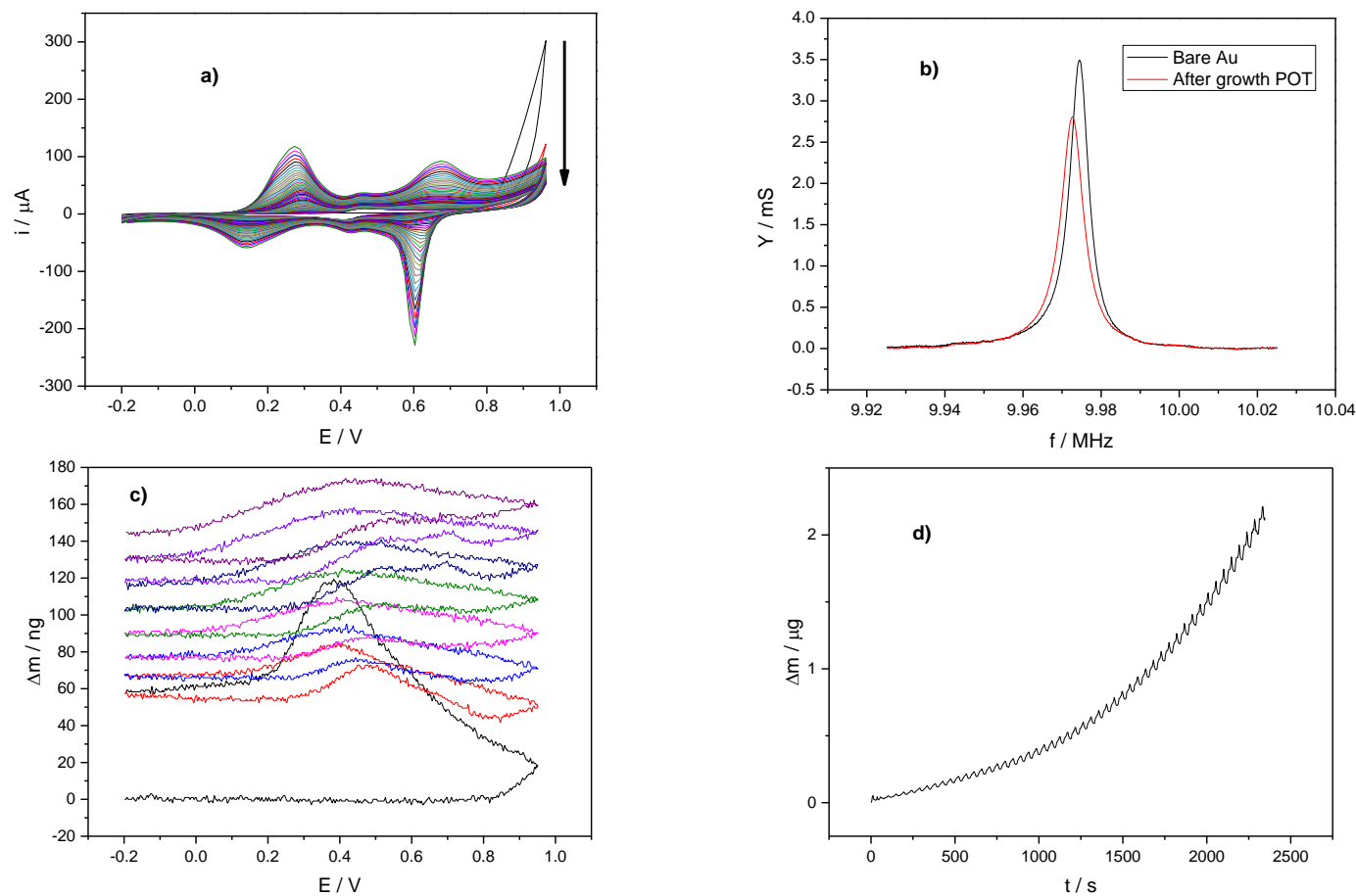
Figure 4.7: EQCM data for the preparation of a POT film deposited potentiodynamically (-0.2 V to 0.95 V; v = 50 mV s^{-1}) from 0.1 M monomeric OT / 1 M H$_2$SO$_4$, 51 scans; a) i-E curves; b) crystal admittance spectra, Y/mS vs. f/MHz, recorded before and after growth POT; c) mass change during growth for first 8 scans; d) mass changing during growth for all scans

4.2.3.3 Poly(*o*-aminophenol)

OAP which has a hydroxyl functional group was polymerised to compare its reaction behaviour with PANI and POT. Its polymerisation is also important to study to compare with P(ANI-OAP) copolymers given in the next section. Figure 4.8 shows the responses obtained during electropolymerisation of an OAP film from 0.1 M *o*-aminophenol in 1 M H_2SO_4 by cycling the voltage from -0.2 V to 0.95 V at a scan rate of 50 mV s^{-1}. The electrochemical oxidation of OAP and its polymerisation mechanism with the redox couple peak attribution were explained elsewhere in-depth[23-26]. What is significant in the graphs shown in Figure 4.8 is that there was a shift in current peaks given in the graphs, indicated with arrows with increasing scan number. The current increased (at the positive direction for the oxidation and negative direction for reduction of the POAP) up to around 150 scans. After that point, the current decreased (as seen between 200 and 300 cycles in Figure 4.8). However, there was no current change between 300 and 400 cycles (as seen in Figure 4.8), indicating electrochemical deposition discontinued. From the 400th to 590th scans, the peak current was constant.

95
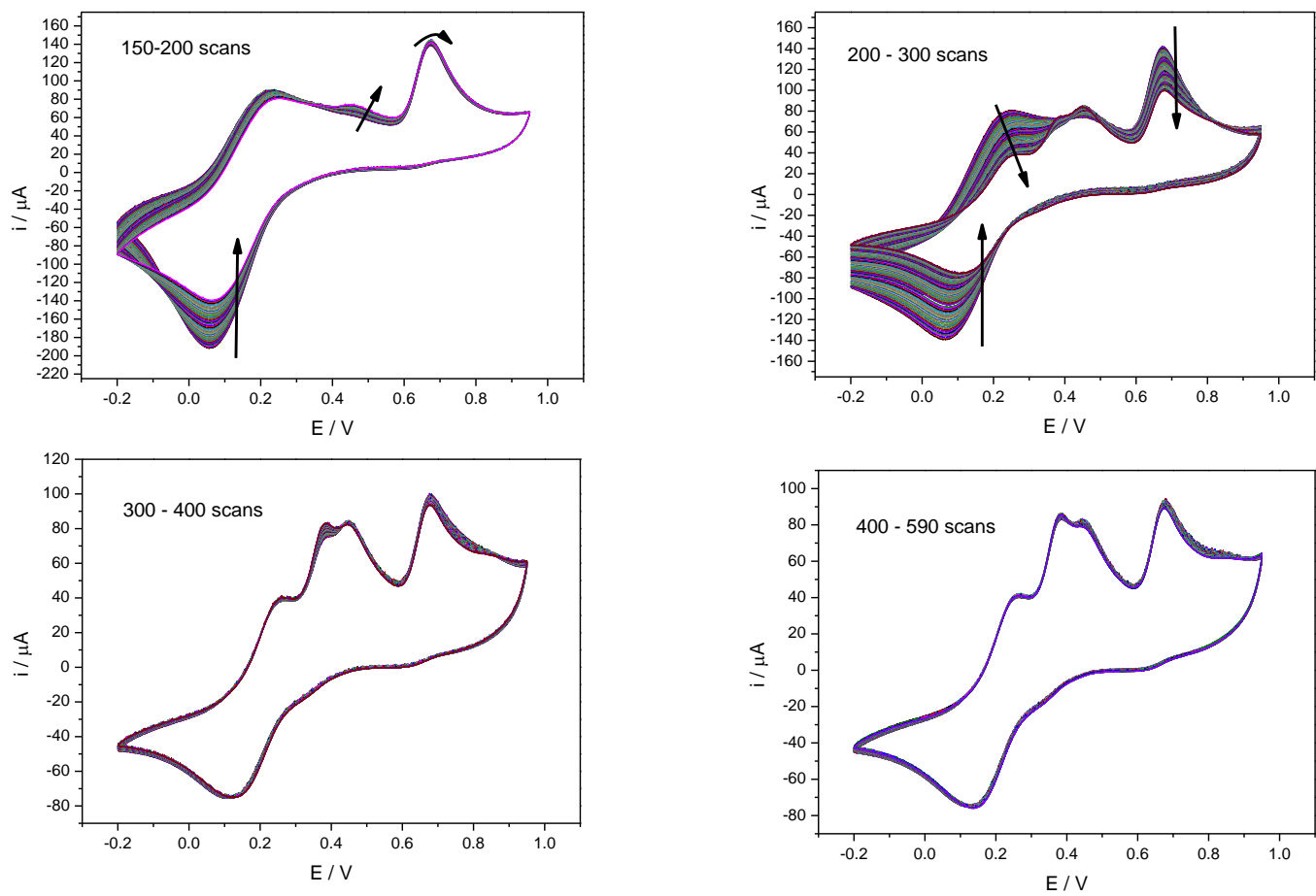
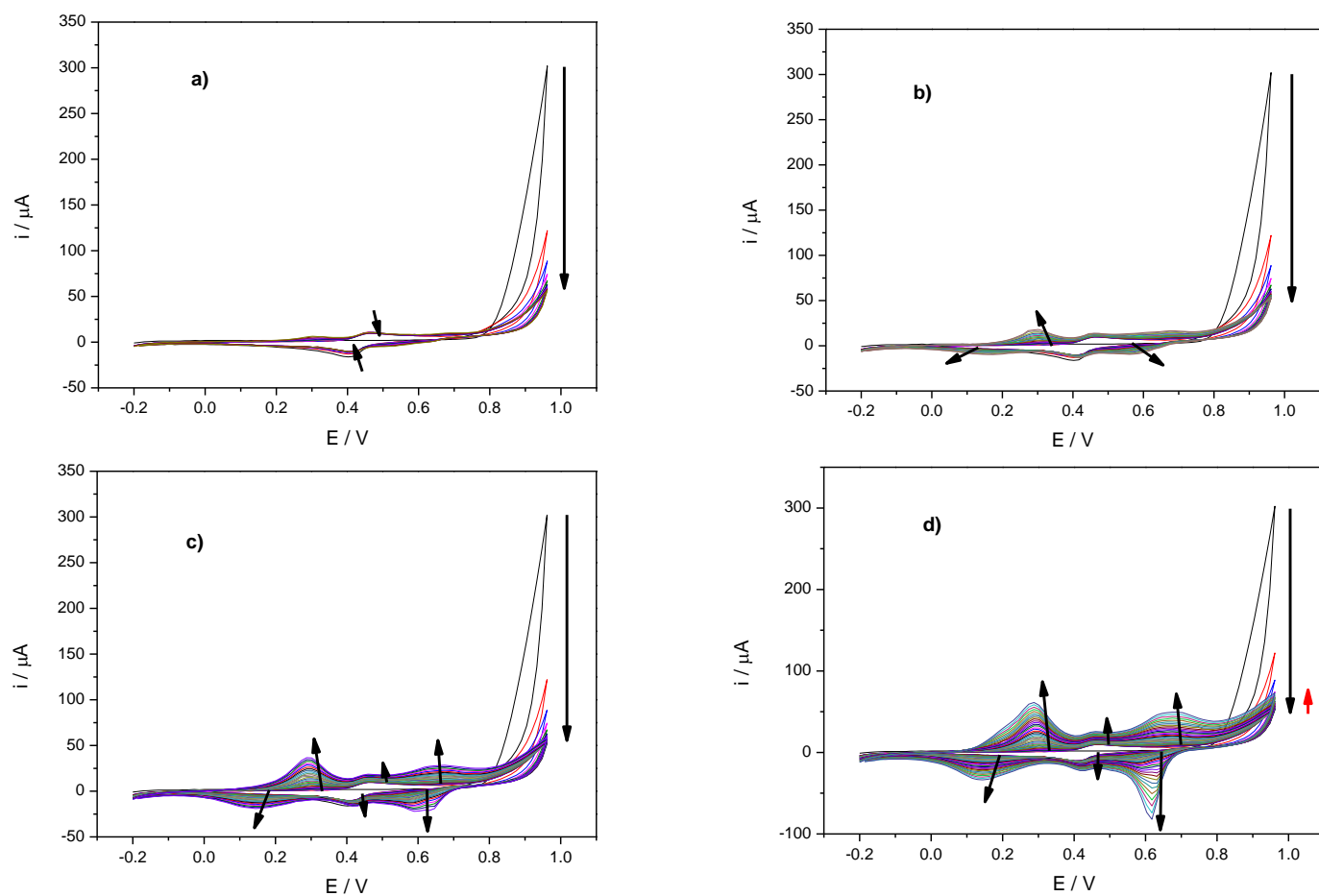*Figure 4.8: Cyclic voltammetric data for the preparation of a POAP film deposited potentiodynamically (-0.2 V to 0.95 V; 50 mV s^{-1}) from 0.1 M monomeric OAP / 1 M H$_2$SO$_4$, 590 scans.*

The EQCM was used to understand whether or not electropolymerisation stopped, after a particular number of scans. Figure 4.9 shows the data for POAP film deposition obtained from 0.1 M OAP/ 1 M H_2SO_4 by cycling the voltage from -0.2 V to 0.95 V at a scan rate of 50 mV s^{-1} by means of EQCM; similar conditions were used for the deposition of PANI (shown in Figure 4.3) and POT (shown in Figure 4.7). The only difference was the number of deposition cycles. Black POAP film was deposited onto Au crystal until admittance decrease was 20% (as done for POT and PANI films) in panel b of Figure 4.9. Panel d in Figure 4.9 shows that the amount of deposited POAP film continued to increase. Oyama et al.[26] explained that charge passed during the electrolysis control POAP film thickness on an ITO electrode whose charge density was larger than 0.5 C cm^{-2} and Zhang et al.[27] found that Δm/Δt for the POAP deposition decreased in parallel with increasing scan number in the experiment carried out for 10 scans. This behaviour was shown for the first 8 scans in panel c of Figure 4.9, Δm/Δt was constant for the later stages of polymerisation indicating POAP growth (in panel d of Figure 4.9) was not an autocatalytic reaction like PANI (panel b of Figure 4.3) or POT (panel d of Figure 4.7). The change in mass (Δm) increased autocatalitically for PANI and POT shown in panel b of Figure 4.3 and panel d of Figure 4.7 respectively but here for POAP, it did not. In brief, after approximately 300 scans, the current was constant but the amount of polymerised film increased linearly for 300 scans (see Figure 4.8) corresponding to 14000 seconds deposition time (see panel d of Figure 4.7). This suggests that forming the amount of POAP film and metamorphosing of electroactive film to electro*in*active POAP film were equal to each other. If this transformation to electroinactive film could happen at the bottom of the film, electron transfer between the conducting substrate and film would stop. Therefore, probably electroinactive POAP was formed in every part of the film to some extent.
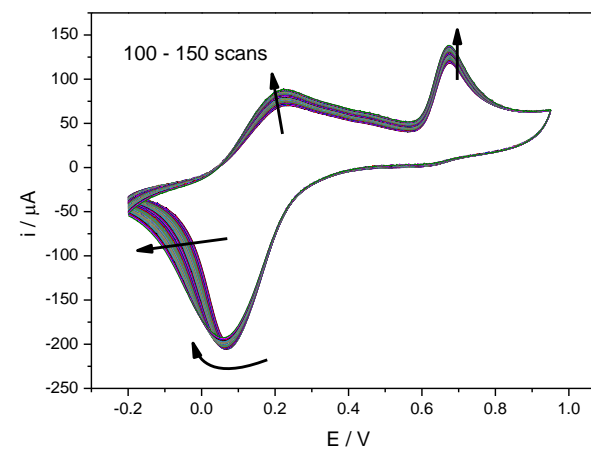
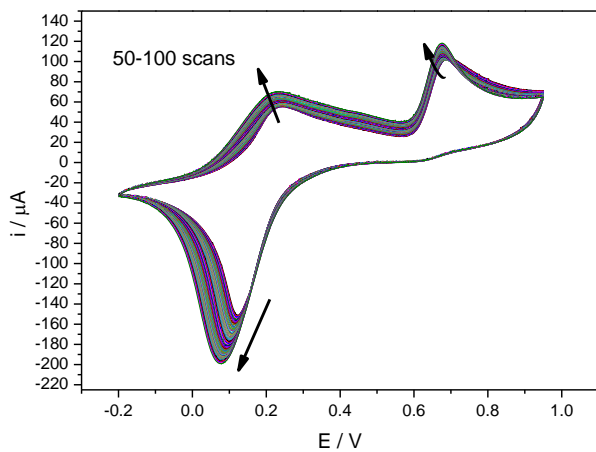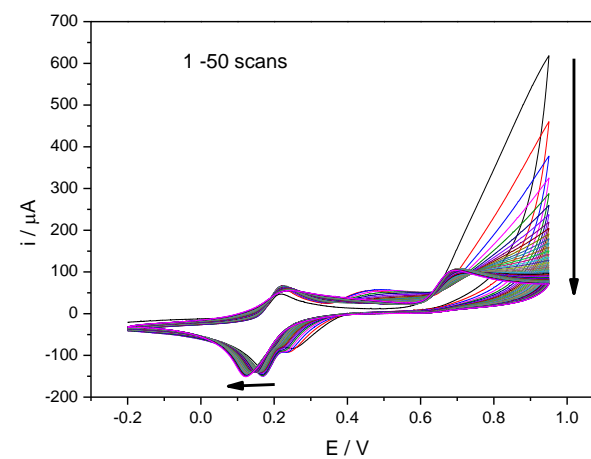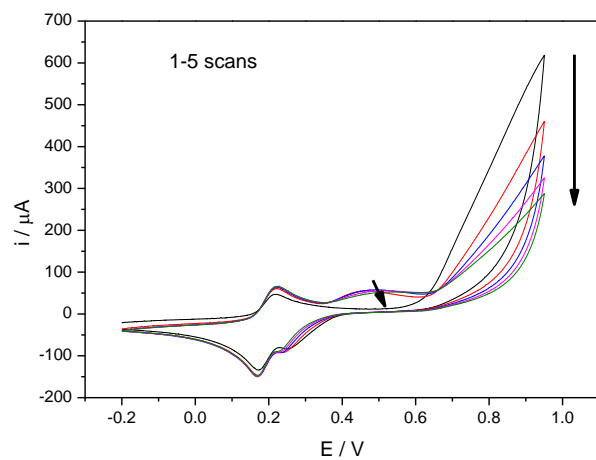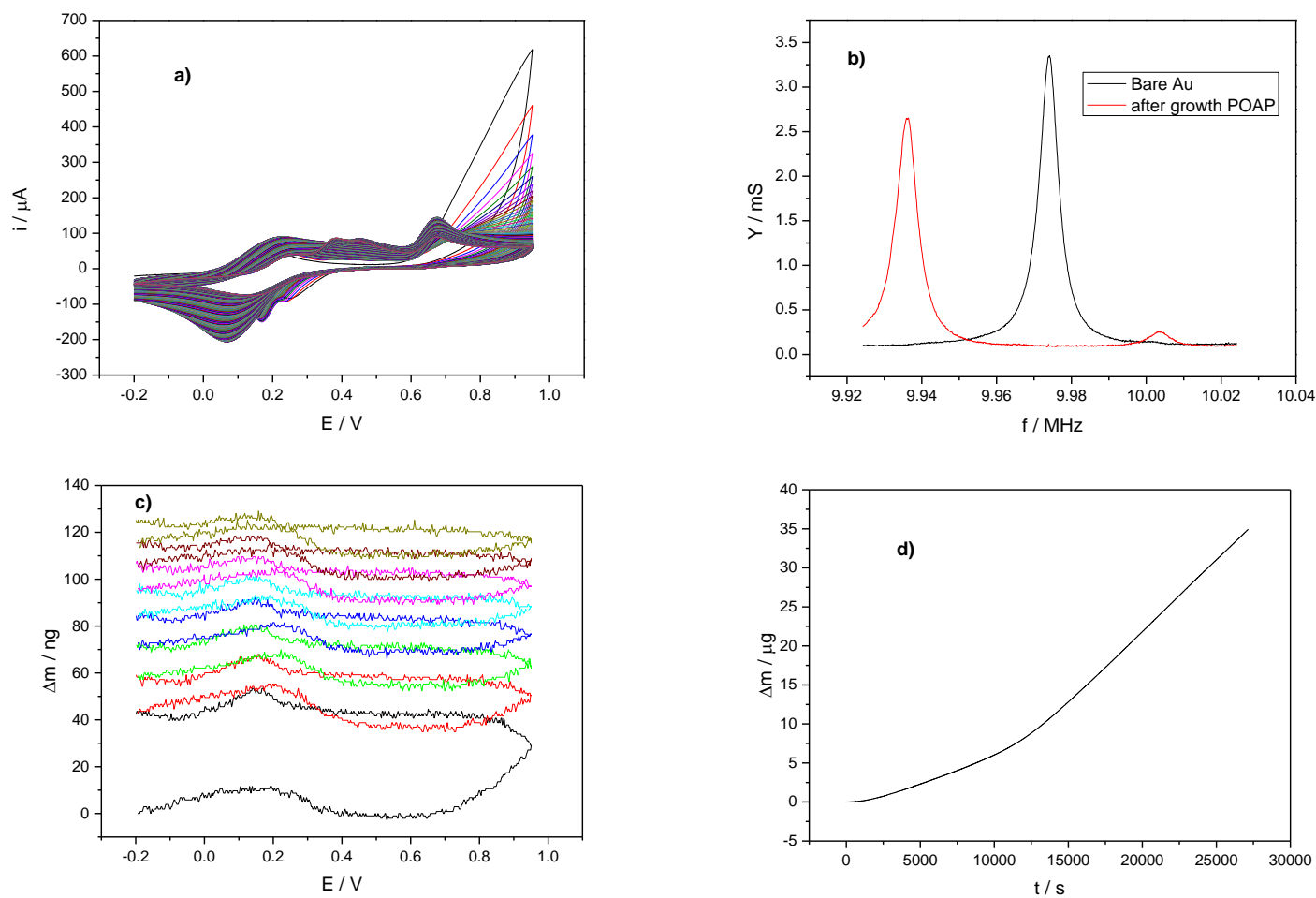*Figure 4.9: EQCM data for the preparation of a POAP film deposited potentiodynamically (-0.2 V to 0.95 V; v = 50 mV s⁻¹) from 0.1 M OAP / 1 M H₂SO₄, 590 scans; a) i-E curves; b) crystal admittance spectra, Y/mS vs. f/MHz, recorded before and after growth POT in the electrolyte; c) mass changes during growth for first 8 scans; d) mass changing during growth for all scans.*

The amount of POAP film formed was obviously much more than overall for a given change of PANI and POT as admittance *vs.* frequency graph shows in panel d of figure 4.9. Table 4.2 shows the mass and charge of the films obtained. The mass of PANI, POT and POAP was calculated from frequency differences between bare Au, before starting growth in the electrolyte, and the resulting film just after the growth in the the same electrolyte (Δf). Charge was calculated from under the more cathodic of the reduction peaks of the films. Although the currents were close to each other, the change in frequency (Δf) of POAP film shown in panel d of Figure 4.9 was significantly larger than Δf of PANI (Figure 4.7) and POT films (panel d of Figure 4.7) and hence it must be more compact than PANI and POT. Thus; when mass-charge ratio, an important parameter for energy storage devices, was calculated for these three films, it could be seen that POAP film is 16 and 21 times heavier than POT and PANI for the same amount of charge applied. Results are tabulated in Table 4.2.

Table 4.2: Mass and charge of the films and mass/charge ratio for PANI, POT and POAP with different numbers of deposition cycles given in Figure 4.3, Figure 4.7 and Figure 4.9.

	PANI (in Figure 4.3)	POT(in Figure 4.4)	POAP (in Figure 4.5)
Δm / µg from QCM	3.52	2.13	34.9
Q / µC from cyclic voltammetry	672	297	310
Δm/Q mg/C	5.24	7.17	112

4.2.3.4 Poly(aniline-*co-o*-toluidine)

Wei *et al.*[28, 29] reported that ANI copolymerisation with OT can control conductivity of copolymer in a broad range. Borole *et al.*[30-32] investigated PANI, POT and poly(ANI-OT) in inorganic and organic supporting electrolytes, which strongly influenced the electrochemical, optical and conducting properties of resulting films. It is known that

copolymer growth is affected by the ratio of monomers. Here, we will show how the ratio of monomer affects copolymerisation and also show the effect of potential cycles during potentiodyamical electropolymerisation.

4.2.3.4.1 The Effect of Monomer Ratio

Figure 4.10 shows the current responses during potentiodynamic deposition of P(ANI-OT) films onto a gold WE (0.03 cm^2) using different concentration of ANI and/or OT with a total monomer concentration of 100 mM in 1 M H$_2$SO$_4$ (-0.2 V to 0.95 V at a scan rate of 50 mV s^{-1}). The peak current decreased with the number of cycles for the polymerisation of OT in panel a of Figure 4.10. If more cycles had been applied, the height of the current peak would have been increased as seen in Figure 4.6, which had three oxidation and three reduction peaks for 40 scans. Just 10 potential cycles were applied for each experiment shown here to keep constant scan numbers. Only the amount of the monomers in the electrolyte was changed to compare polymerisation points and redox peaks of the films grown. The height of current peaks increased with the number of cycles for ANI polymerisation indicated in panel g of Figure 4.10 as illustrated earlier.
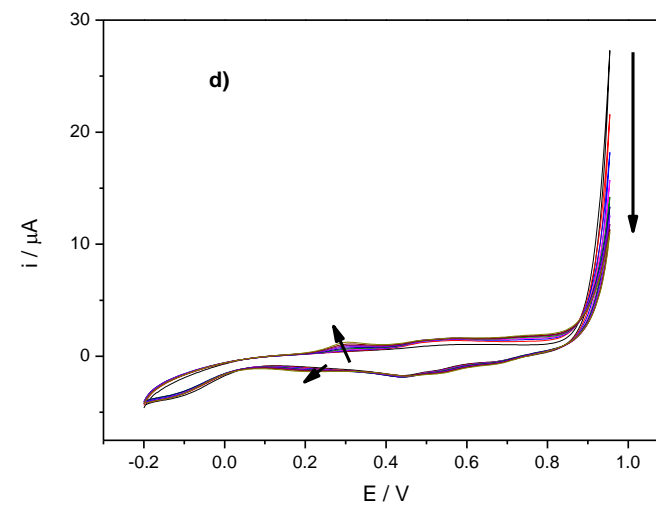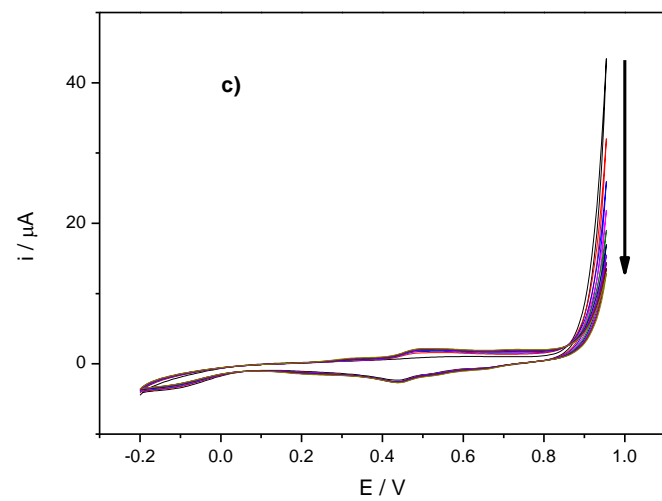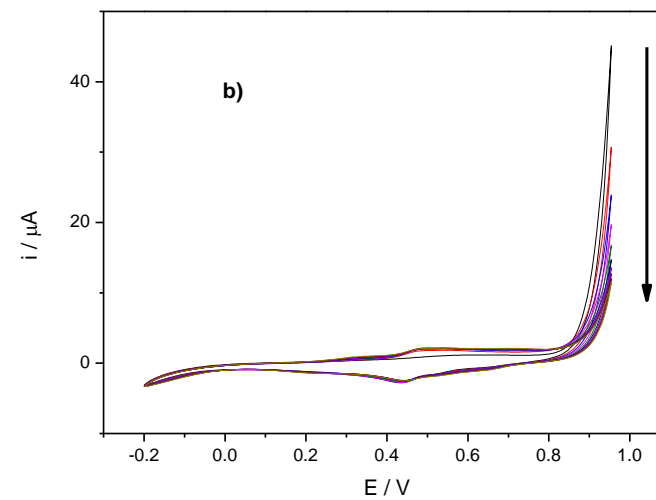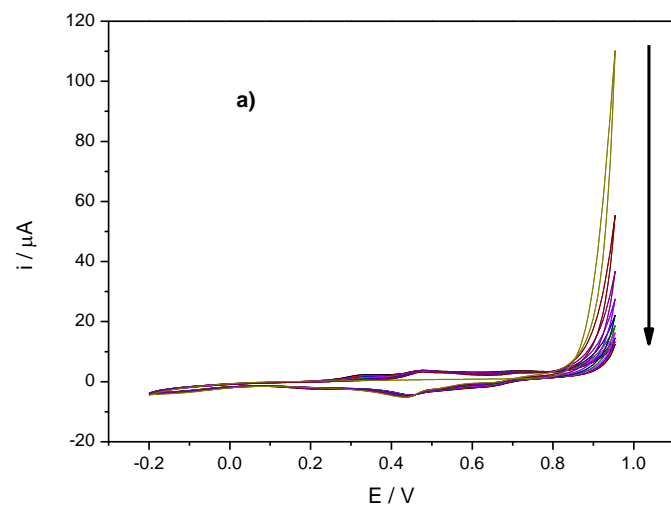
continued overleaf
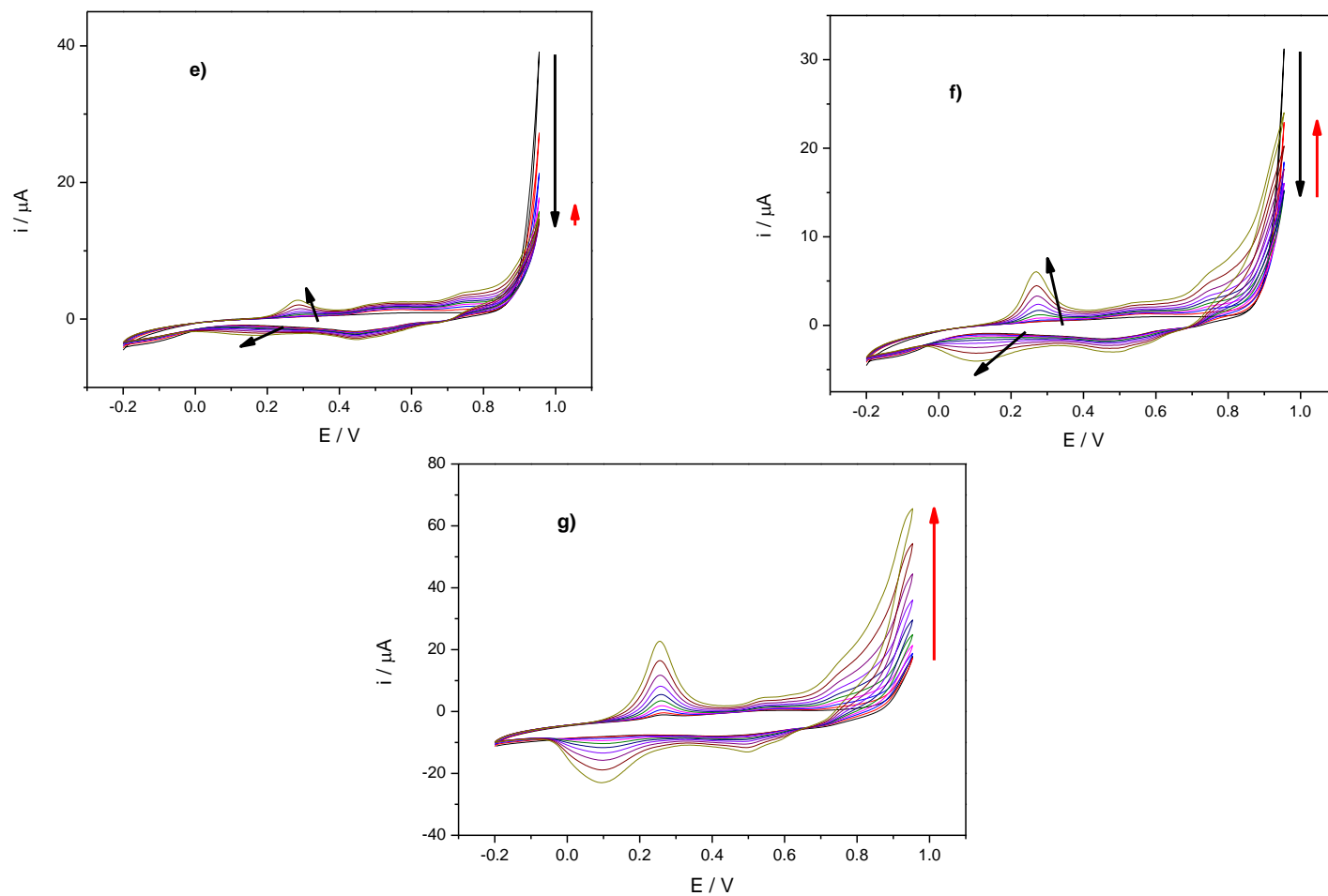
Figure 4.10: Cyclic voltammogram recorded during the synthesis of polymers and copolymers: a) POT, b) P(ANI-OT) (50:50), c) P(ANI-OT) (75:25), d) P(ANI-OT) (90:10), e) P(ANI-OT) (95:5), f) P(ANI-OT) (98:2), g) PANI. In all cases potential windows are between -0.2 V and 0.95 V, 50 mV s^{-1}, 10 scans, in aqueous solution of 1 M H$_2$SO$_4$ as electrolyte.

Panel b in Figure 4.10 shows copolymerisation of 50 mM ANI and 50 mM OT in 1 M H_2SO_4, abbreviated as P(ANI-OT) (50:50), in which the first number indicates the concentration of aniline and second one indicates the concentration of OT in the electrolyte in mM. The cyclic voltammogram curve of P(ANI-OT) (50:50) shown in panel b was similar to POT given in panel a. OT also dominated copolymerisation of P(ANI-OT) (75:25) in panel c of Figure 4.10.

All electrolytes that had more than 25 mM OT in electrolyte would show the same graph as P(ANI-OT) (75:25) which was POT dominated, thereby these experiments were not required to be conducted. Therefore, the ANI ratio in the electrolyte was increased stepwise to see how (co)polymerisation changes the cyclic voltammetric curve. In the 10th cycle the curves of P(ANI-OT) (90:10) and P(ANI-OT) (95:5) film shown in panel d and e of Figure 4.10 were different indicating the monomer ratios in the copolymer is different as they had an oxidation and a reduction peak around 0.29 V and 0.18 V respectively.

Peak potentials having more negative value in 10th scan of polymerisation of PANI, POT and P(ANI-OT) shown in Figure 4.10 are given in Table 4.3.

Table 4.3: Polymer oxidation peak and its corresponding reduction peak for 10th scans of polymerisation of PANI, POT and P(ANI-OT) for the data of Figure 4.10

ANI (mM)	OT (mM)	E_{pa1} (V)	E_{pc1} (V)
0	100	0.465	0.453
50	50	0.543	0.448
75	25	0.484	0.448
90	10	0.299	0.228
95	5	0.276	0.175
98	2	0.264	0.115
100	0	0.253	0.109

Upon increasing the ANI ratio in the electrolyte, redox peaks were shifted to more negative potential, as seen for P(ANI-OT) (98:2) in panel f of Figure 4.10 which was getting closer to PANI given in panel g of Figure 4.10 as shown in Table 4.3. Increasing ANI ratio in the electrolyte made the current density of peaks of P(ANI-OT) to resemble PANI having the highest current density.

Figure 4.11 drawn from data used in Table 4.3 shows the mol fraction of OT in electrolyte *vs.* potential of current peaks to see how one of homopolymers depending on the ratio of monomers could be dominated in electrocopolymerisation for the constant scan numbers.
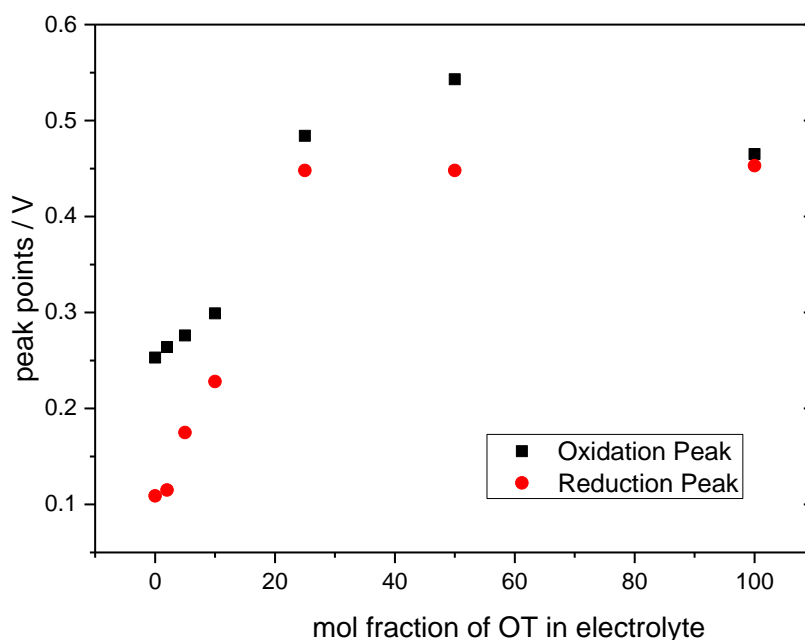
Figure 4.11: Plot of ratio of OT in electrolyte vs. peak points shown in Table 4.3. for the electropolymerisation of PANI, POT and P(ANI-OT).

If the numbers of potential cycles are constant, the ratio of monomer can control the formation of copolymer. While i-E curve of P(ANI-OT) (50:50) was similar to POT, decreasing OT monomer ratio approached the P(ANI-OT) to PANI as shown Figure 4.11. This could be confirmed by the polymerisation point in which a film started to grow. Figure 4.12 shows current response during the first scan of the growth of PANI,

POT and P(ANI-OT) film given in Figure 4.10. OT polymerisation, which had a high current peak, started at the earlier potential than PANI did. Therefore, the ratio of OT should be less than ANI in electrolyte to produce a copolymer. Otherwise, the copolymer was dominated by POT. Table 4.4 quantitatively shows the points of polymerisation starting (polymerisation points) of PANI, POT and P(ANI-OT) for the data obtained from Figure 4.10 to compare films. How these points are obtained is shown in Figure 4.12 for PANI (pink line) and POT (black line).
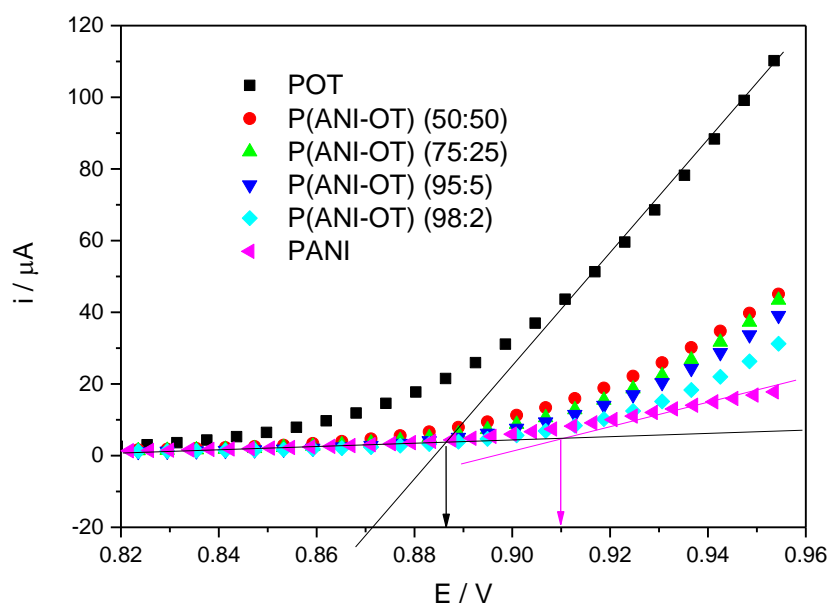
Figure 4.12: Higher magnification of voltammograms showing the first scan of polymerisation point of PANI, POT and P(ANI-OT) for the data of Figure 4.10

When a (co)polymer starts to grow, the potential changes where current raises. Therefore, the voltammogram shape of copolymerisation is also important to be able to distinguish differences between the copolymer and each homopolymer. For example, the polymerisation point of the P(ANI-OT) copolymers was between PANI and POT polymerisation points. Upon increasing ANI ratio, polymerisation point of copolymer increased and approached aniline polymerisation point. Therefore, first cycle (triggering step) was a polymer-determining step.

Table 4.4: Polymerisation points of PANI, POT and P(ANI-OT) for data of first cycle of Figure 4.10 for comparison

ANI (mM)	OT (mM)	Polymerisation point (V)
0	100	0.886
50	50	0.901
75	25	0.903
95	5	0.906
98	2	0.908
100	0	0.910

4.2.3.4.2   The Effect of Number of Cycles

Figure 4.13 shows the peak progression of P(ANI-OT) films deposited onto the gold electrode potentiodynamically in the solution including 75 mM ANI and 25 mM OT in 1 M H_2SO_4 by cycling the voltage from -0.2 V to 0.95 V at a scan rate of 50 mV s^{-1}.
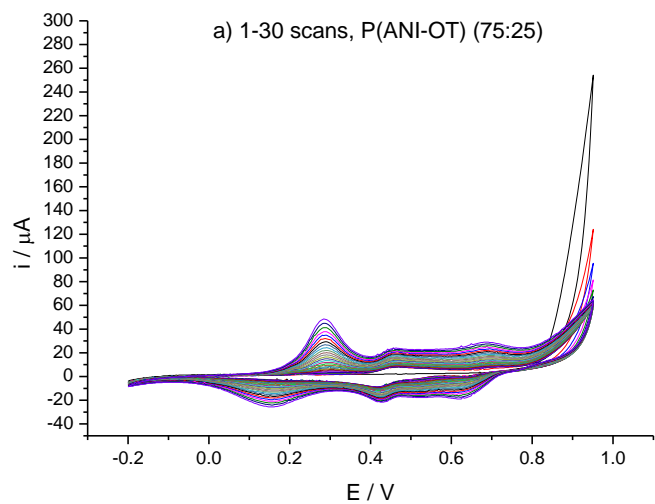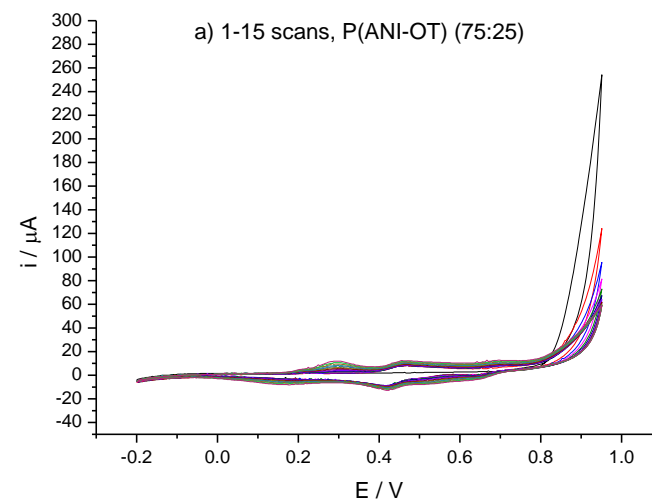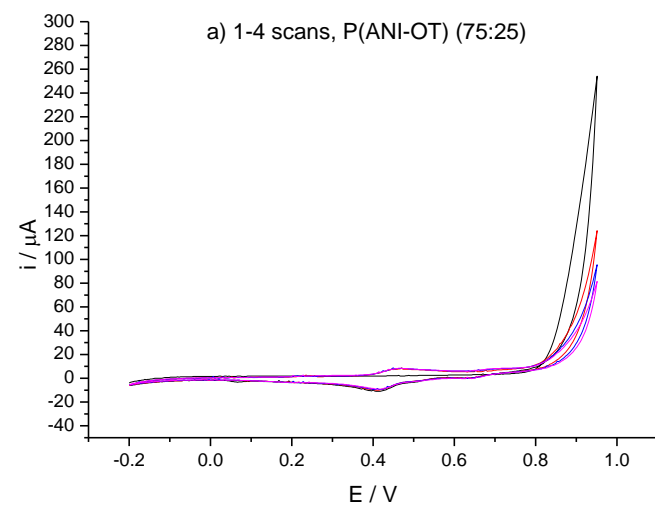
Figure 4.13: Cyclic voltammograms (48 cycles) of the electrocopolymerisation of P(ANI-OT) (75:25) in 1 M H$_2$SO$_4$ on gold, v = 50 mV s^{-1}.

48 cycles were applied to obtain a thick P(ANI-OT) (75:25) film to see the effect of scan numbers in electrocopolymerisation. However, it was still thin enough to apply the Sauerbrey equation (from Y-f spectra) to characterise in an aqueous acidic medium shown in following section.

P(ANI-OT) (75:25) has three redox peaks similar to POT, shown in Figure 4.6, which was deposited with 51 scans. However, altering the components of the electrolyte to P(ANI-OT) (95:5) again in 1 M H_2SO_4 (from -0.2 V to 0.95 V, v = 50 mV s^{-1}) is illustrated in Figure 4.14. The i-E curve of P(ANI-OT) (95:5) was getting similar to PANI shown Figure 4.3, which had 2 redox peaks. As copolymer is getting similar to PANI, we can call this process as "*polyanilinisation*" in this thesis.
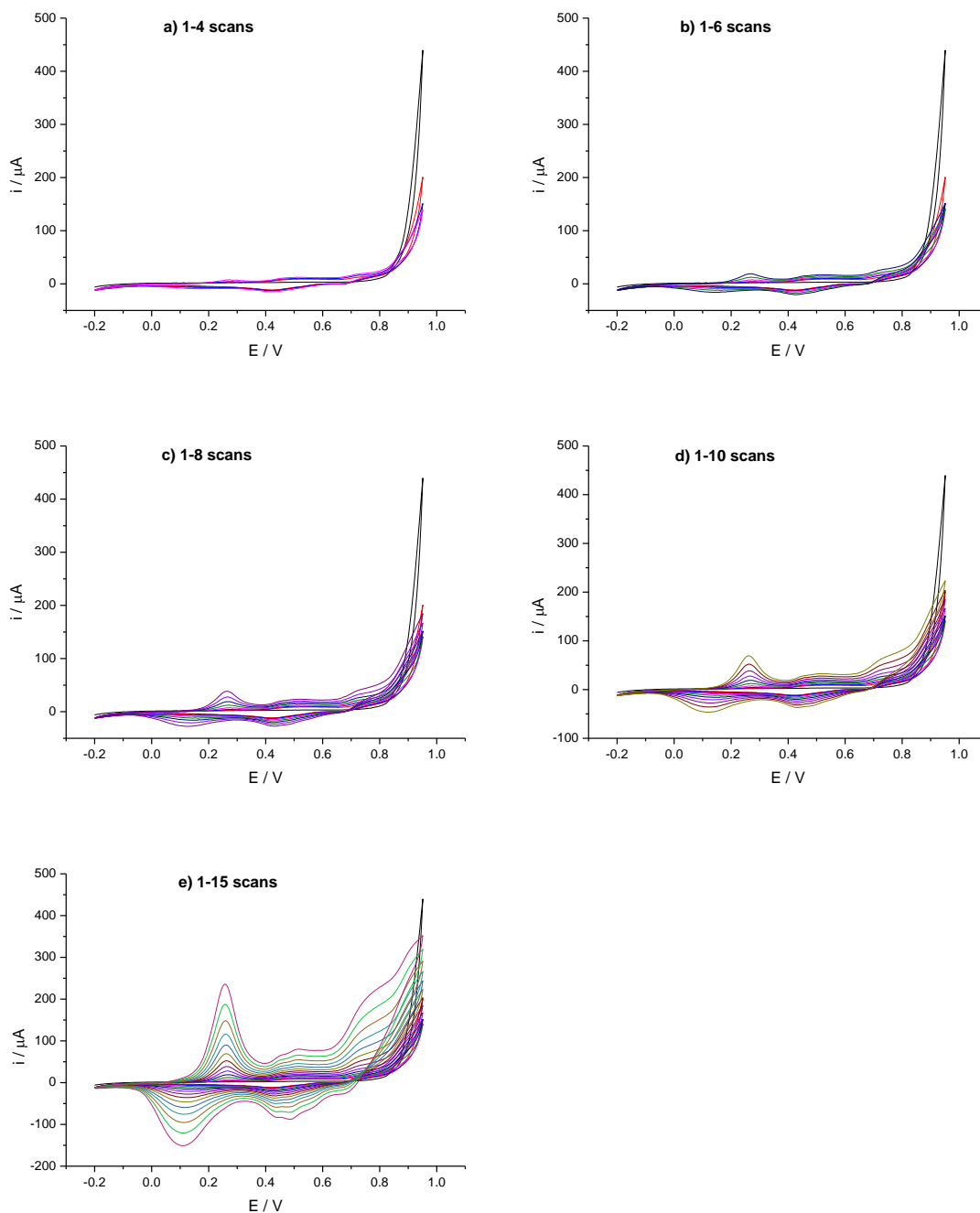
Figure 4.14: Cyclic voltammograms (15 cycles) of the electrocopolymerisation of P(ANI-OT) (95:5) in 1 M H$_2$SO$_4$ on gold WE, v = 50 mV s^{-1}

P(ANI-OT) (95:5) polymerisation (after 0.8 V) increased significantly and had 15 number of scans shown in Figure 4.14. However, P(ANI-OT) (75:25) deposited with 48 scans did not increase as much as P(ANI-OT) (95:5) after 0.8 V. PANI itself had 6 scans (see Figure 4.3) and POT itself had 51 scans (see panel a of Figure 4.7) to be deposited

for approximately the same amount of film. These might suggest that increasing scan numbers can produce copolymer similar to one of monomer components. Film characterisation is needed to see if there is one of monomer domination in electrocopolymerisation which will be given in the end of this chapter.

4.2.3.5 Poly(aniline-*co-o*-aminophenol)

Keeping the numbers of scans constant (for 10 scans), the effect of monomer ratio for P(ANI-OAP) is the same as P(ANI-OT) shown in 4.2.3.4.1 in detail. In this section we will concentrate on the investigation of the effect of cycle numbers on P(ANI-OAP) films. Figure 4.15 represents the growth of P(ANI-OAP) films deposited potentiodynamically from 80 mM ANI and 20 mM OAP in 1 M H_2SO_4 called P(ANI-OAP) (80:20) by applying the voltage from -0.2 V to 0.95 V at a scan rate of 50 mV s^{-1}.
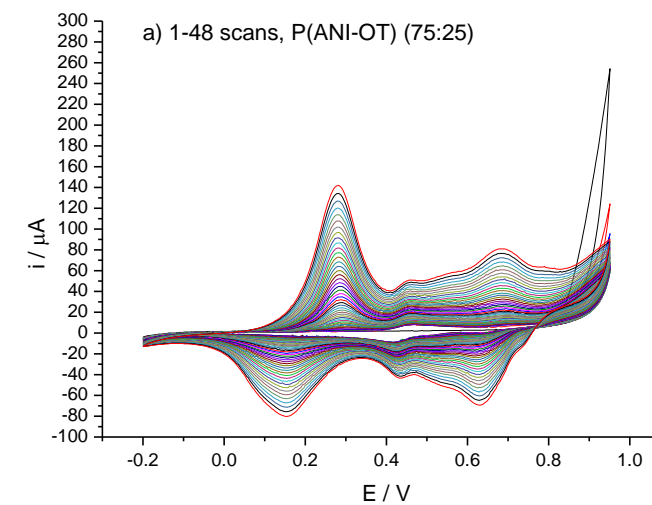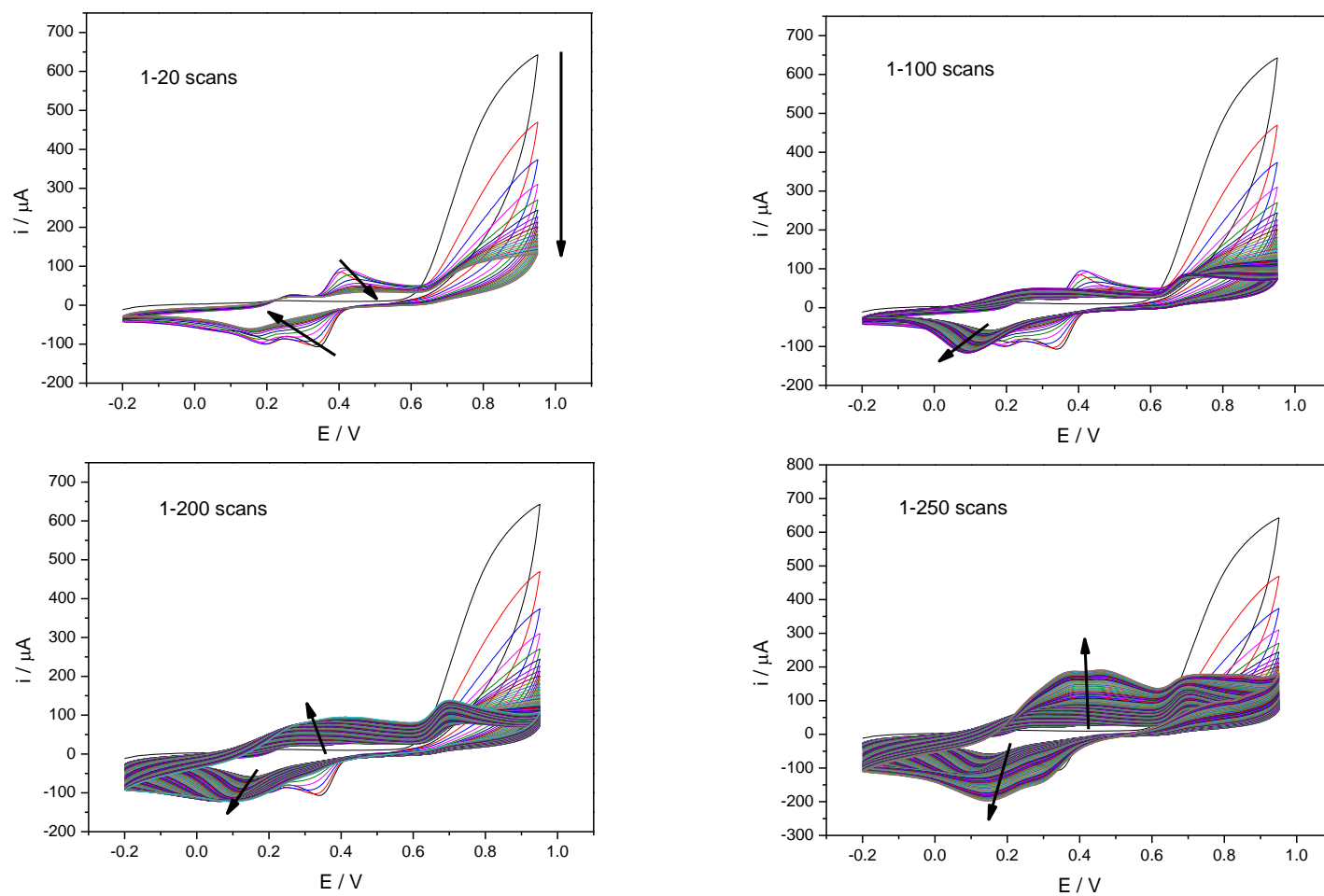
Figure 4.15: Cyclic voltammograms (250 cycles) of the electrocopolymerisation of P(ANI-OAP) (80:20) in 1 M H_2SO_4 on gold WE, v = 50 mV s^{-1}

The growth of P(ANI-OAP) film (80:20), given in 1-20 scans of Figure 4.15, starts similarly with POAP shown previously in Figure 4.8. However, current of redox peaks did not decrease or become constant after a point like POAP in Figure 4.8. Current peaks increased continuously, hence it was a copolymer. The current peaks of 200-250 scans were higher than 1-200 scans and indicated an autocatalytic reaction like PANI but unlike POAP. However, the potential points of the redox peaks P(ANI-OAP) film had, were much different than the PANI given in panel a of Figure 4.3. One can suppose that POAP domination occured as P(ANI-OAP) film was obtained with 250 scans (large scan numbers like POAP) gave an acoustically thin film. In fact it was a copolymer and one of monomer domination was not observed.

Figure 4.16. shows the i – E responses of the film deposited from 98 mM ANI and 2 mM OAP in 1 M H_2SO_4 called P(ANI-OAP) (98:2) grown by cycling between -0.2 V and 0.95 V at a scan rate of 50 mV s^{-1}.
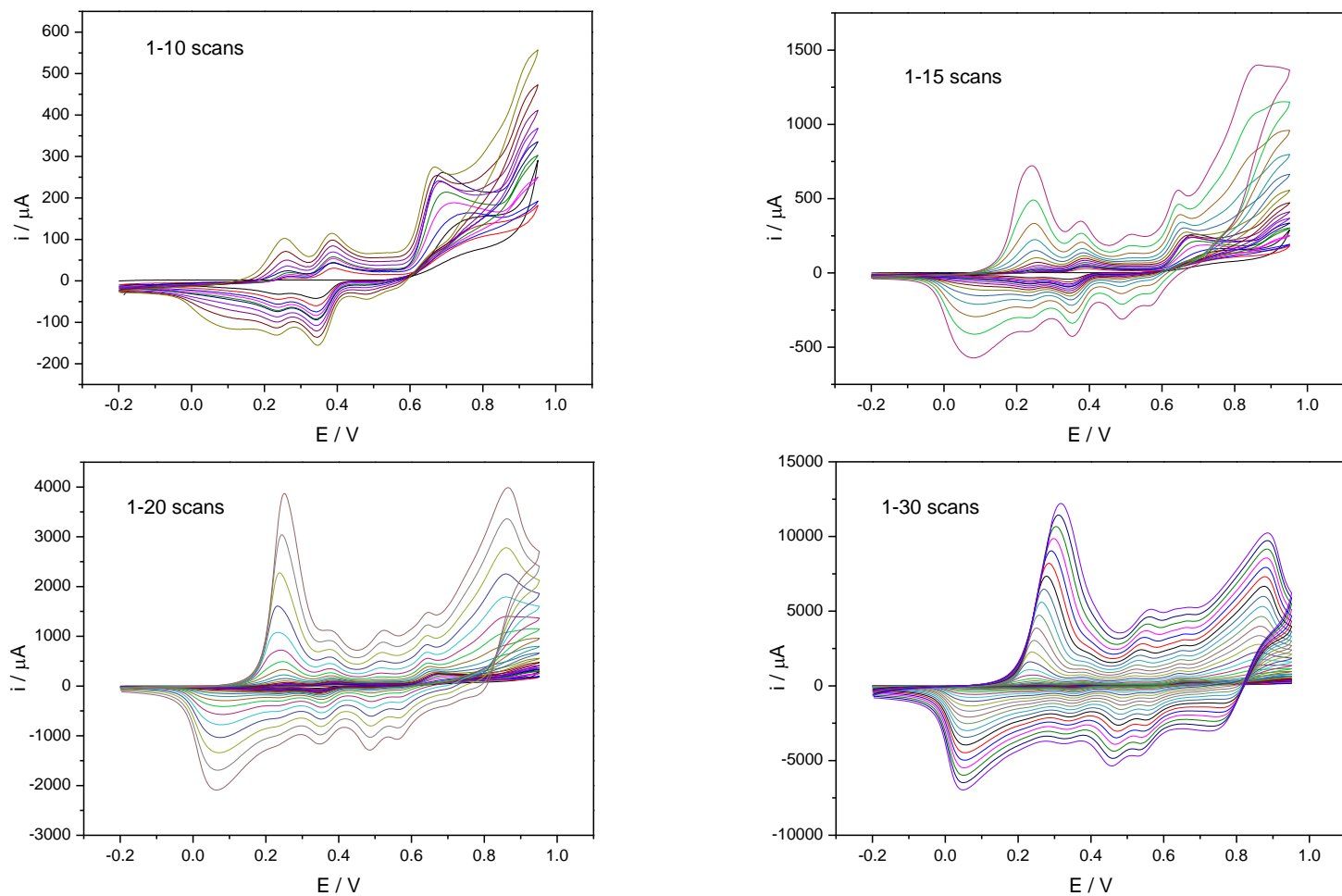
Figure 4.16: i vs. E responses of the electrocopolymerisation of P(ANI-OAP) (98:2) in 1 M H_2SO_4 on gold WE, v = 50 mV s^{-1}. The numbers of cycles are indicated in figure.

The progression of the growth of P(ANI-OAP) (98:2) film shows how "*polyanilinisation*" occurs. 1-10 scans in Figure 4.16 had 3 oxidation and 2 reduction peaks and 1-15 scans in Figure 4.16 had 4 oxidation (apart from 1 oxidation peak for polymerisation after 0.8 V) and 3 reduction peaks. If the growth of the film is stopped at this scans, it has had a copolymer characteristic as i-E responses are different peaks than monomer components. However; when the experiment was continued growing the film by increasing the number of scans (shown in 1-30 scans in Figure 4.16), polyanilinisation was observed. This film was not acoustically thin for redox characterisation (highly decreased admittance spectra), thus a rigid film was acquired with the same conditions that Figure 4.16 had. Only difference for this rigid film from Figure 4.16 was the scan number applied shown in Figure 4.17.
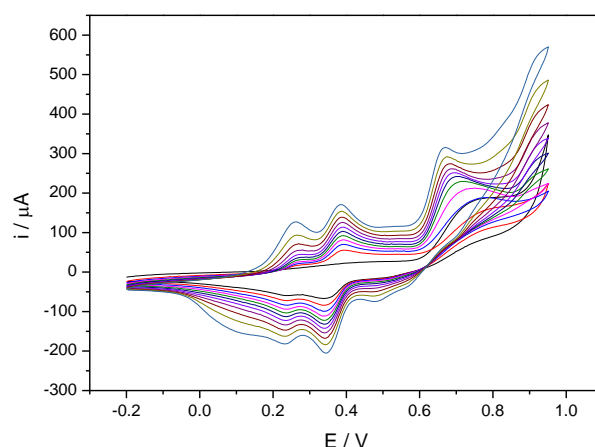
Figure 4.17: Cyclic voltammograms (11 cycles) of the electrocopolymerisation of acoustically thin P(ANI-OAP) (98:2) in 1 M H_2SO_4 on gold WE, v = 50 mV s^{-1}.

This acoustically thin film was grown to characterise the redox behaviour of copolymer in an aqueous acidic electrolyte.

4.2.4.   Film Characterisation

The growth experiment given in detail in section 4.2.3 was stopped at the reduced end (E = -0.2 V) and rinsed with deionised water for voltammetric characterisation. The freshly prepared films were tested in monomer-free 1 M H_2SO_4 electrolyte. A potential

range of -0.2 ≤ E/V ≤ 0.6 was applied to observe p-doping of the films. For SEM and FTIR, films were left at room conditions for two days.

4.2.4.6 Film Redox Behaviour

4.2.4.6.1　Homopolymer Redox Behaviour

EQCM data during polymer redox conversion in 1 M H_2SO_4, (v=50 mV s^{-1}) for PANI, POT and POAP films prepared from 0.1 M monomers are shown in Figure 4.18.

In Figure 4.18

panel a is PANI film whose growth was given in Figure 4.3

panel b is POT film whose growth was given in Figure 4.7

panel c is POAP film whose growth was given in Figure 4.9.

PANI has been oxidised and reduced in aqueous acidic solution using cyclic voltammetry by many researchers.[33-35] The ion exchange of polyaniline was investigated by means of EQCM[36-39] in depth. Panel a of Figure 4.18 shows that the mass was almost linear at the early stage of oxidation and after that mass increased with PANI oxidation, suggesting that proton exit from the early stage and anion entered into the film later stage of oxidation to maintain electroneutrality. It is clearly seen that anion transfer dominates the overall redox switching process as mass of anion is bigger than proton. Panel d of Figure 4.18 shows the charge *vs.* mass graph of this PANI film (black line), with an end-to-end Δm-Q slope of 35.6 g mol^{-1}.

116
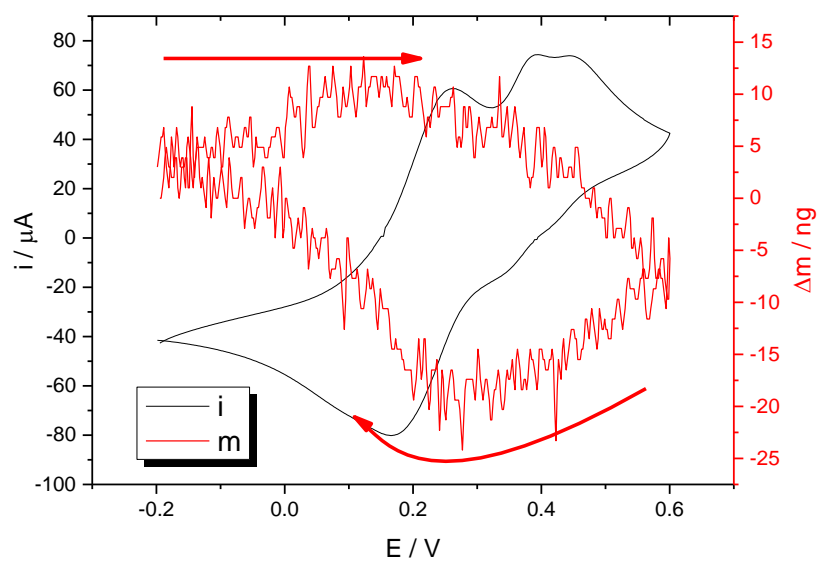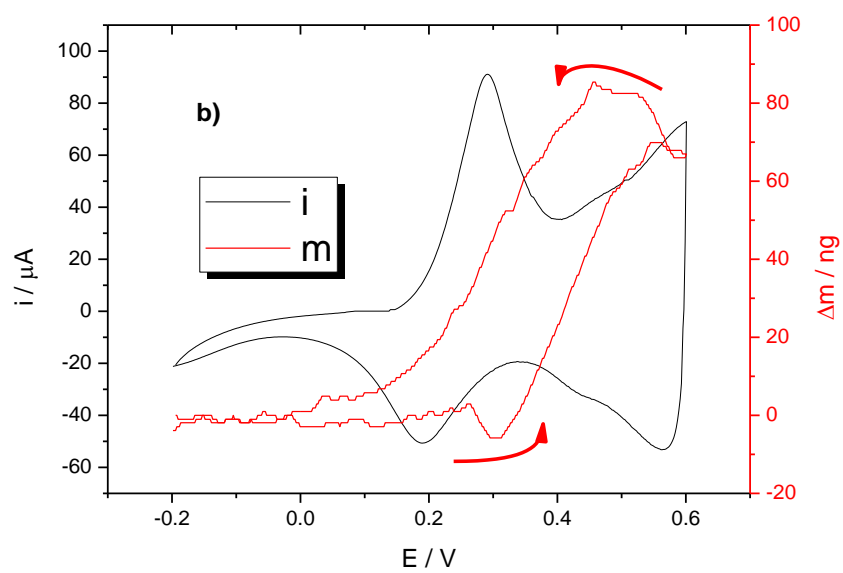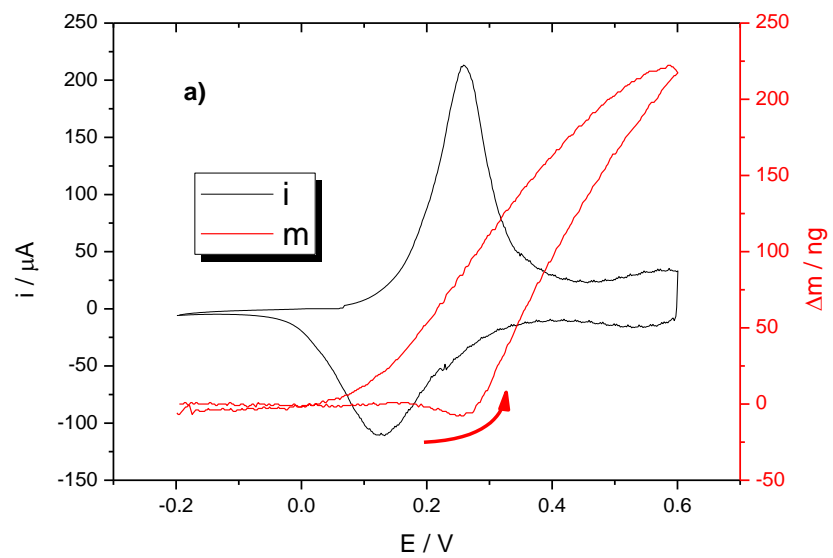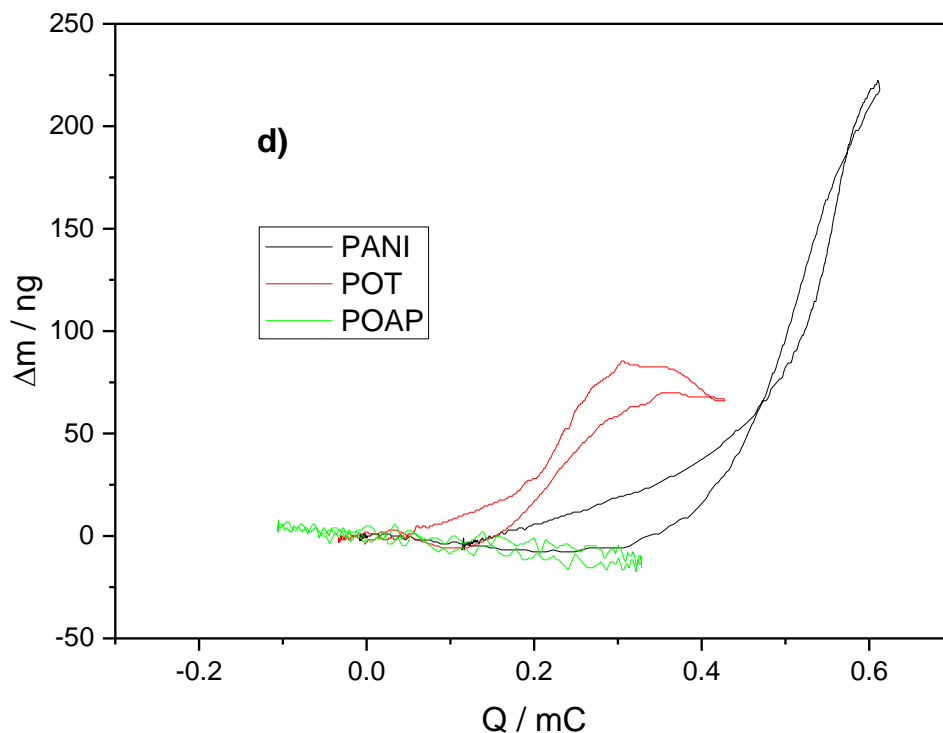
Figure 4.18: EQCM data for redox switching of polymer films in 1 M H_2SO_4, v = 50 mV s^{-1}, films prepared from 0.1 M monomers a) PANI (Γ = 27.5 nmol cm^{-2}) (growth given in Figure 4.3) for comparison with b) POT (Γ = 10.2 nmol cm^{-2}) (growth given in Figure 4.7) and c) POAP (Γ = 15.3 nmol cm^{-2}) (growth given in Figure 4.9); d) Plot of Δm-Q for PANI, POT and POAP, where charge is calculated from the integration of current shown in a, b and c respectively. Film mass changes calculated using Saurbrey equation shown in chapter two.

The focus of this study is not given to this process as there are many papers published on this subject[37, 40, 41] and the main aim of this work is to characterise copolymers films and analyse optical and redox behaviour of PANI. Here, p-doped of PANI with POT and POAP films in aqueous acidic medium at a 50 mV s^{-1} scan rate is going to be compared.

P-doping of a POT film is shown in panel b of Figure 4.18. Detailed cyclic voltammogram responses for POT films can also be found in the literature covering wide potential window and the characteristic of POT curve was the same as those reported previously.[42, 43] Panel a of Figure 4.19 represents POT in the states of leucoemeraldine base and emeraldine salt of POT which is similar to PANI itself.[44]

EQCM analysis with PBD was also used to analyse ion exchange between POT film and aqueous acidic electrolyte.[45, 46]

Redox behaviour of POAP films was investigated by cyclic voltammetry,[47, 48] panel b of Figure 4.19 shows POAP oxidation structure in acid medium during the redox transformation of the film.[49] However, the EQCM of POAP requires some detailed works[50] which will be shown in this thesis. The first cycle effect,[51] not shown here, was also observed for all polymers (PANI, POT, POAP) we used to date.
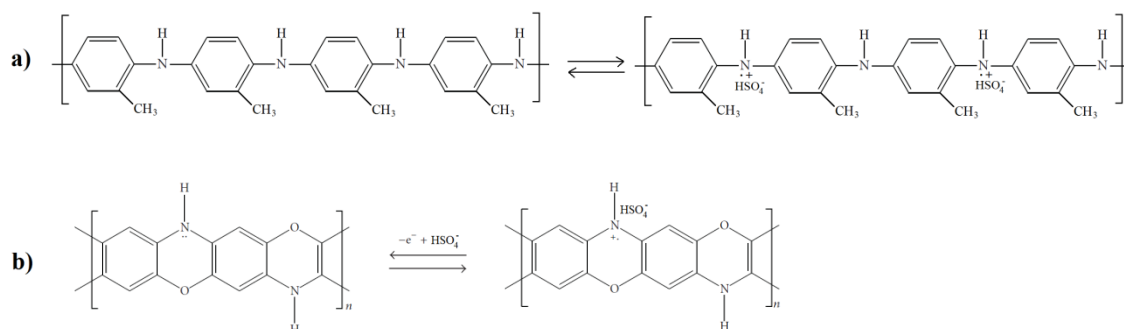
Figure 4.19: Schematic representation of POT in the transformation states of leucoemeraldine base and emeraldine salt b) POAP oxidation in aqueous acid medium.

Figure 4.18 shows that for POT film, electroneutrality was attained mainly by anion insertion similar to PANI. Panel d of Figure 4.18 shows that PANI and POT are anion dominated, and their Δm-Q slopes are 36 g mol^{-1} and 15 g mol^{-1} respectively. However, POAP was cation dominated, and its Δm-Q slope is -2.5 g mol^{-1}. This suggests that anion (HSO$_4^-$) transfer requires water transfer in the opposite direction for the maintenance of electroneutrality. The difference of mass direction of POAP from PANI and POT arises from the presence of the activated groups OT and OAP have and the polymerisation mechanism of them. As shown in Figure 4.9 and Table 4.2, POAP (35 µg) is much heavier than PANI (3.5 µg) and POT (2 µg). Therefore, POAP probably has a less porous structure. Also, the Y-f graph (panel b of Figure 4.9) confirms the rigidity of PAOP (panel b of Figure 4.9) is similar to metal as it is still rigid up to 35 µg.

4.2.4.6.2   Copolymer Redox Behaviour

Redox behaviour of P(ANI-OT)[52] and P(ANI-OAP)[53] was investigated. Here the film will be characterised to see how copolymers act in aqueous acidic solution and if one of the monomers dominates mass change during redox reaction.

The prepared copolymer films were tested in a monomer-free 1 M H_2SO_4 electrolyte. A potential range of -0.2 ≤ E/V ≤ 0.6 was applied to see just p-doping of the films. EQCM data during copolymer film redox conversion were obtained in a monomer-free 1 M H_2SO_4 electrolyte (v = 50 mV s^{-1}) for P(ANI-OT), P(ANI-OAP) films prepared from a total of 0.1 M of the monomers.

EQCM redox characterisation of P(ANI-OT) copolymer films are shown in Figure 4.20:

panel a is P(ANI-OT) (75:25) film whose growth was given in Figure 4.13

panel b is P(ANI-OT) (95:5) film whose growth was given in Figure 4.14.
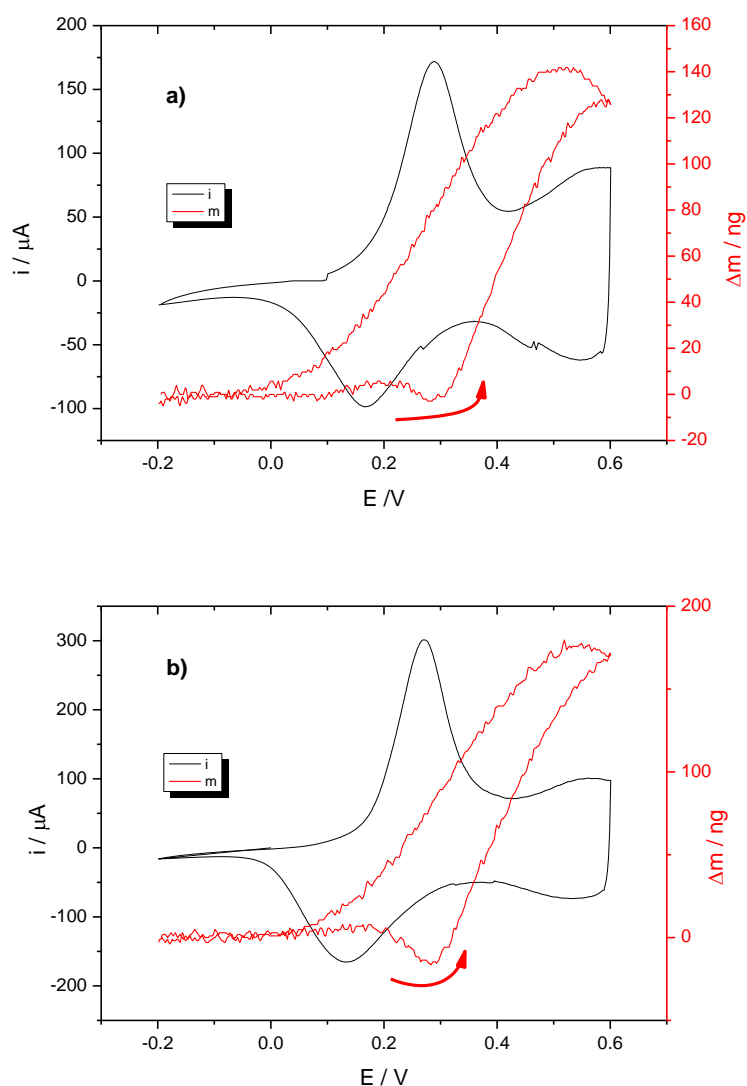
Figure 4.20: Cyclic voltammograms and simultaneously recorded responses of mass change during copolymer redox conversion in 1 M H_2SO_4, v = 50 mV s^{-1}, films shown a) P(ANI-OT) (75:25) (Γ = 21.9 nmol cm^{-2}) (growth given in Figure 4.13) ; b) P(ANI-OT) (95:5) (Γ = 35.8 nmol cm^{-2}) (growth given in Figure 4.14).

Figure 4.20 shows the similar behaviour of mass change for P(ANI-OT) (75:25) and P(ANI-OT) (95:5). As both PANI and POT have similar mass changing behaviour in aqueous acidic medium individually, they do not show electrochemically different behaviour. FTIR measurements, which will be presented in the following section, were conducted to investigate if one of monomer was dominated.

EQCM redox characterisation of P(ANI-OAP) copolymer films are shown in Figure 4.21:

panel a is P(ANI-OAP) (80:20) film whose growth was given in Figure 4.15,

panel b is P(ANI- OAP) (98:2) film whose growth was given in Figure 4.17.
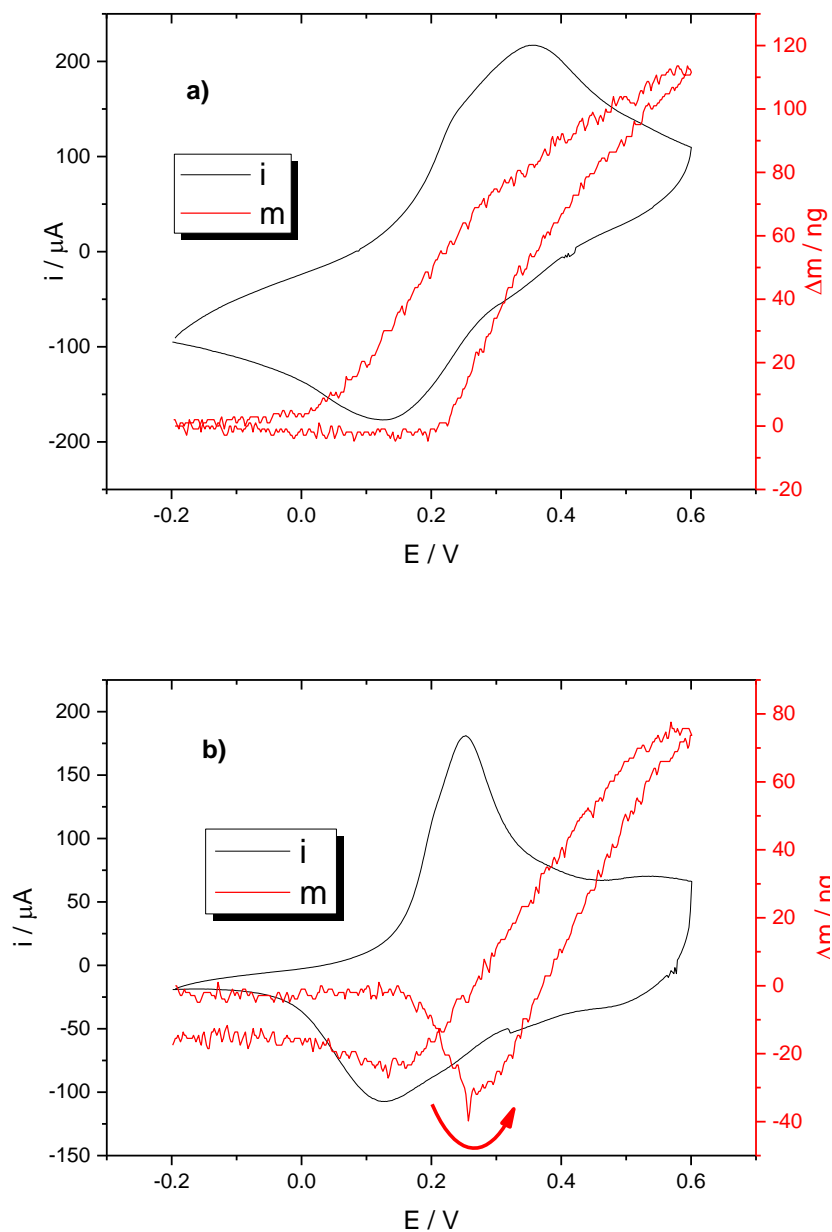
Figure 4.21: Cyclic voltammograms and simultaneously recorded responses of mass change during copolymer redox conversion in 1 M H_2SO_4, v = 50 mV s^{-1}, films shown a) P(ANI-OAP) (80:20) (Γ = 46.6 nmol cm^{-2}) (growth given in Figure 4.15); b) P(ANI-OAP) (98:2) (Γ = 35.5 nmol cm^{-2}) (growth given in Figure 4.17)

Figure 4.21 illustrates that P(ANI-OAP) (80:20) had different mass changing behaviour than P(ANI-OAP) (98:2) in aqueous acidic electrolyte but both of them were anion dominated mechanism. While mass of P(ANI-OAP) (80:20) just increased during oxidation and *vice-versa* during reduction; mass of P(ANI-OAP) (98:2) decreased at the early stage of the oxidation and mass increased more at the latter of the oxidation. This supports what was said for P(ANI-OAP) (98:2), which had polyanilinisation during electropolymerisation and for P(ANI-OAP) (80:20) which had copolymeric behaviour.

4.2.4.7 Film Composition

Figure 4.22 presents the FT-IR spectra of the PANI and POT homopolymers with P(ANI-OT) (95:5) and P(ANI-OT) (75:25). Reflectance mode of FTIR was used for the (e*x-situ*) results presented in this section.
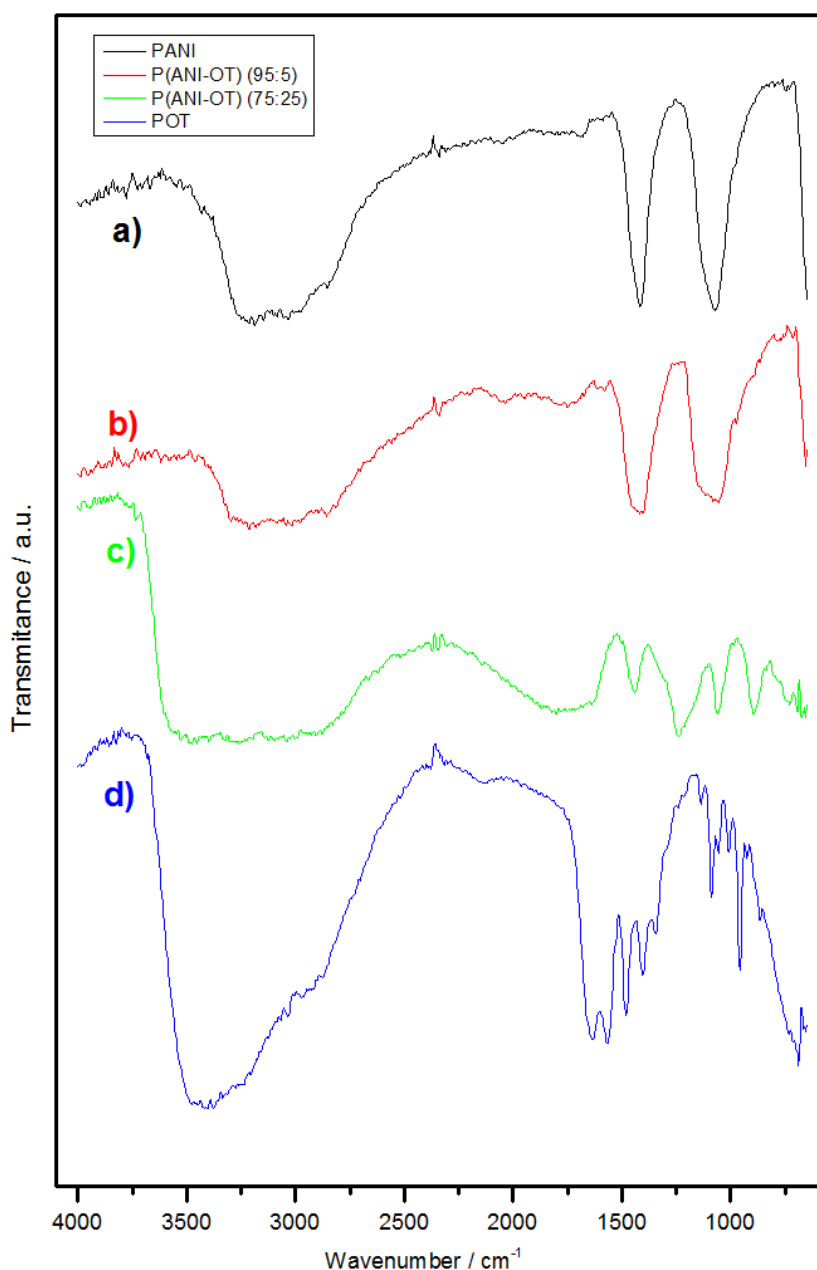
Figure 4.22: FTIR spectra of a) PANI (27.5 nmol cm^{-2}); b)P(ANI-OT) (95:5) (35.8 nmol cm^{-2}); c) P(ANI-OT) (75:25) (21.9 nmol cm^{-2}); d) POT (10.2 nmol cm^{-2}). Growth conditions and redox characterisation of these films shown in previous sections.

Band spectrum of the FTIR for PANI is shown in Figure 4.22.a. The broad band obtained around 3300 cm^{-1} is because of the N-H stretching mode. The peak at 1430 cm^{-1} is attributed to the C=C stretching vibrations. C-N stretching vibration in aromatic amine is 1092 cm^{-1}. The band at 650 cm^{-1} are ascribed to the absorption band for 1-4 substitution on the benzene ring.[54-56]

In the band spectrum for the POT in Figure 4.22.d, stretching vibration of N-H is at the 3492 cm^{-1}. Peaks around the regions of 1400 cm^{-1} and 1600 cm^{-1} are attributed to C-N stretching of benzoid and quinoid rings. The peak of 1092 cm^{-1} was attributed to vibrational band of the dopant structure. Vibration of 1088 cm^{-1} is corresponding in plane bending vibration.[57, 58]

P(ANI-OT) (95:5) shows much higher response for ANI than for OT in the electrocopolymerisation as seen in the similarity between PANI and P(ANI-OT) (95:5) spectra. However, the copolymers of P(ANI-OT) (75:25) give rise to new bands at especially around 840 cm^{-1} and 1480 cm^{-1}, the spectra of which differ from PANI and POT homopolymer (the combination of the peaks). These establish that P(ANI-OT) (75:25) was a copolymer rather than a mixture of homopolymers or just POT domination. Indeed it was expected from cyclic voltammogram of growth that POT was dominant. Mass transfer behaviour in aqueous acidic medium did not affect momomer ratio in electrocopolymerisation (section 4.2.4.6.2.) but here with FTIR we would see the copolymerisation of P(ANI-OT) for a selected ratio. Therefore, defining optimum conditions are necessary for the copolymerisation.

Figure 4.23 represents the FT-IR spectra of the PANI, POAP, P(ANI-OAP) (98:2) and P(ANI-OAP) (80:20). The spectrum of POAP (Figure 4.23.d) demonstrates that the band at 3340 cm^{-1} is assigned to the characteristic bands of N–H stretching-vibration bonds as seen for PANI and POT. The band at 1582 cm^{-1} was attributed the axial stretching of the C=O groups in the POAP structure. The peaks around 1460–1568 cm^{-1} are assigned to the stretching of C-H and C=C groups. The peak at 1296 cm^{-1} is related to C-N stretching-vibration bond and the peak at 1195 cm^{-1} was attributed to the stretching of C-O-C linkages. The peak of 650 cm^{-1} corresponds to the absorption of 1-4 substitution on the benzene ring.[59-61]

The FTIR spectrum of P(ANI-OAP) (98:2) is presented in Figure 4.23.b exhibiting a great similarity to PANI spectrum (Figure 4.23.a) which may support PANI domination. This also confirms the success of polyanilinisation because it was getting similar to PANI. However, the copolymers for P(ANI-OAP) (80:20) shown in Figure 4.23.c cause a new,

different spectra than any of PANI and POAP homopolymers indicating a copolymer which neither of homopolymer is dominant.
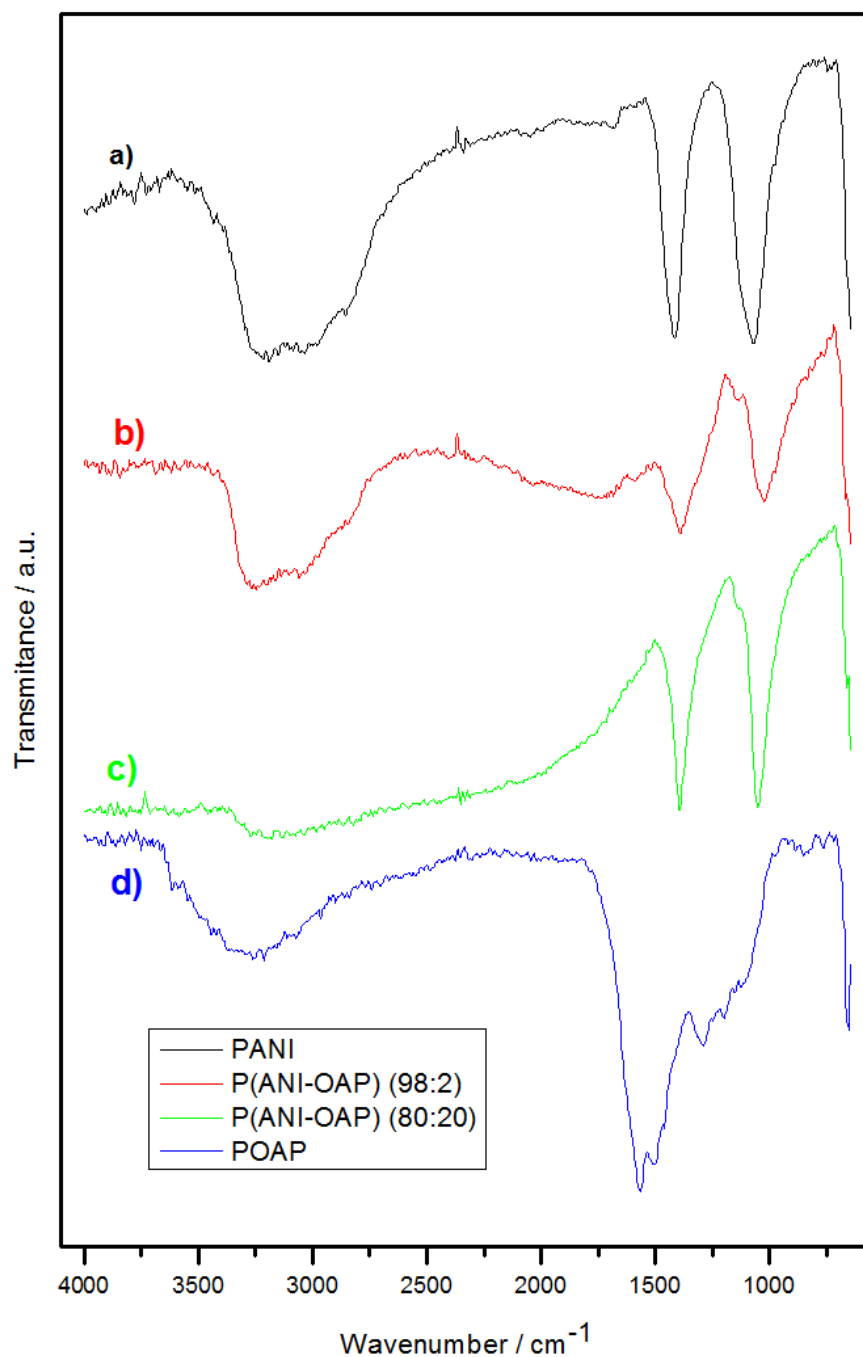
Figure 4.23: FTIR spectra of a) PANI (27.5 nmol cm^{-2}); b)P(ANI-OAP) (98:2) (35.5 nmol cm^{-2}); c) P(ANI-OAP) (80:20) (46.6); d) POAP (15.3 nmol cm^{-2}). Growth conditions and redox characterisation of these films shown in previous sections.

4.2.4.8 Film Morphology

Figure 4.24 shows SEM images for comparable amount of PANI films (80 ± 11 nmol cm^{-2}) which were grown with different scan numbers and scan rates to compare their images.
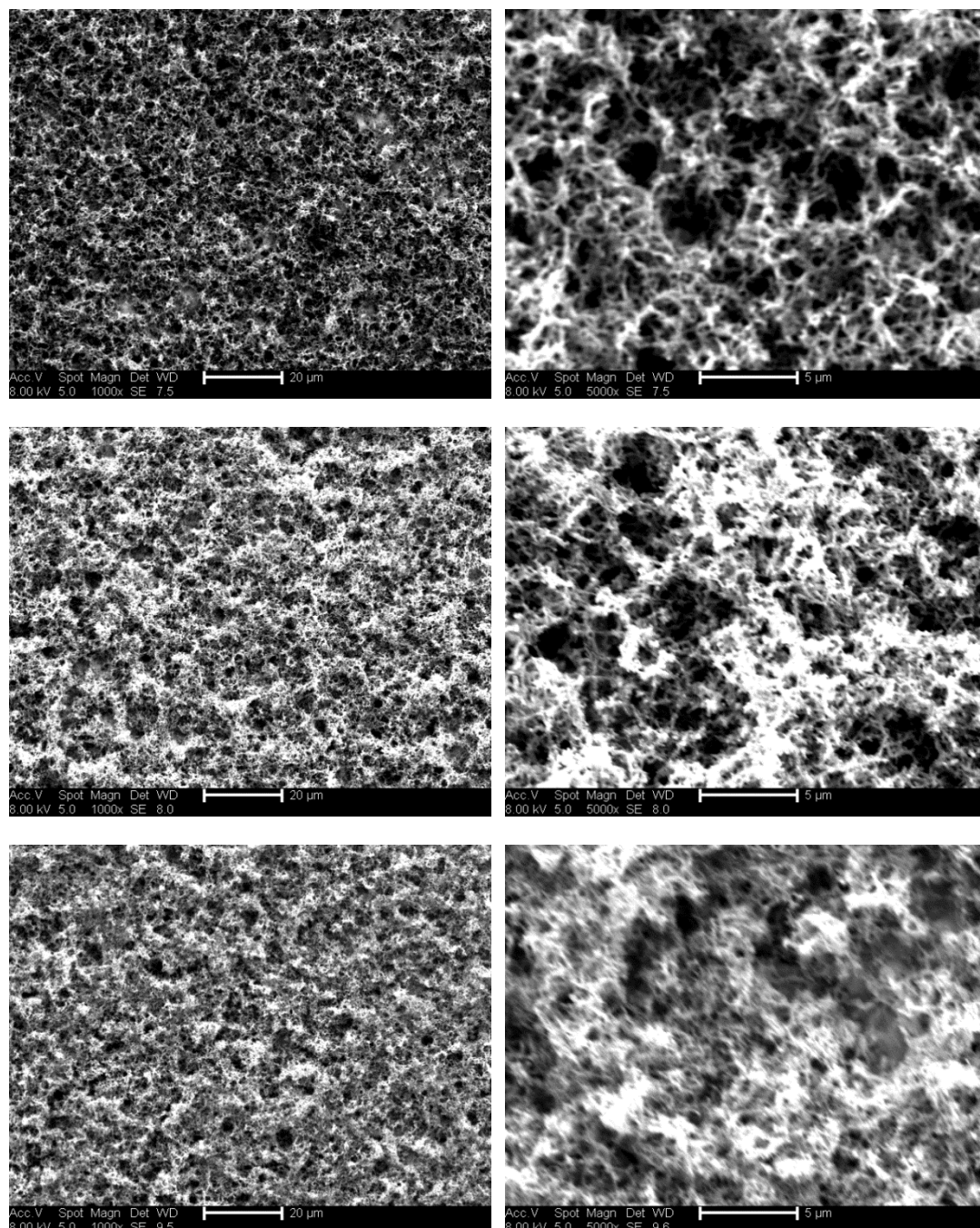
Figure 4.24: SEM images of PANI synthesized with 0.1 M ANI in 1 M H_2SO_4; Top two images (2 scans), 5 mV s^{-1}, 70.5 nmol cm^{-2}; Middle two images (16 scans), 50 mV s^{-1}, 91.1 nmol cm^{-2}; Bottom two images (30 scans), 100 mV s^{-1}, 79.4 nmol cm^{-2}; left images are at low magnification (1000x); right images are at high magnification (5000x)

SEM images demonstrated that there were not any distinguishable differences between the films having the different amount of water. Mu *et al.* showed[62] that the growth and formation of PANI were controlled by the potential scan rate which also can change the morphology of PANI. However, what they did not monitor was to compare the same amount of film. Recently, a detailed study of PANI morphology has been reviewed.[63]

As mentioned earlier in this chapter, the film having more scans (compare with the same amount of film having less scan) had more water. One can expect; the film having less water is more compact because of less water void inside the film structure. However, the morphology of the films was the same for all films deposited equally with different scan numbers shown in Figure 4.24. In this stage two scenarios are possible. First one is that just surfaces of the films were the same but the rigidity of the film could be different beneath the surface (near interface of PANI and Au). In this case, the film having averagely more water could be more porous, shown in Figure 4.25. Therefore, the films deposited with different scan numbers probably had different thickness when they were wet in electrolyte but the films could be shrunk when they became dry. Therefore, the same amount of films *in-situ* deposited with different scan numbers was expected different than each other in terms of porosity because EQCM measurements show that the amount of water they have were different. However, SEM images of dry films showed their morphologies were similar. Second scenario is that all films, grown differently, were collapsed when they became dry (for *ex-situ* imaging) and hence their surfaces appeared the same.

a)   b)
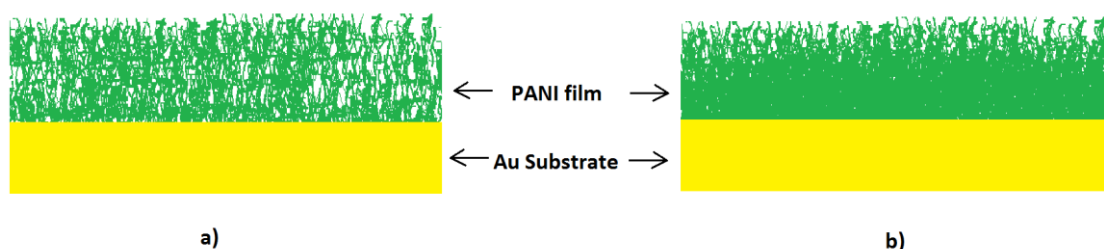
Figure 4.25: Speculative schematic illustration of the electrodeposited PANI on Au substrate (cross-section); PANI film having a) more scan numbers b)less scan numbers for the same amount of film used.

4.3. Conclusions

As it is known that conditions of polymerisation can effect the growth of the films. In this work it has been shown that solvent in electrolyte play a significant role during potentiodynamic growth of PANI. Upon increasing potential scan number in polymerisation of PANI, water content per dimeric aniline site decreases. The effect of scan number provided different amount of water content for the same amount of the films grown. The film produced with less scan numbers, has less water than the film obtained using more scan numbers. However, it does not have significant effect on the morphology of the films.

POT growth is an autocatalytic reaction similar to PANI. However, POAP growth has different growth kinetics. POAP is not autocatalytic reaction and after some cycles, mass of the film increased but the electroactive area of that film was constant. Mass-charge ratio of POAP is therefore significantly higher than POT and PANI. Early stages of PANI and POT oxidation is associated with proton exit and the latter stages were associated with anion entry in an acidic medium, but unlike them, POAP is just cation dominated reaction during redox cycling.

The ratio of the two monomers and scan numbers forming copolymer have a significant influence on the electrocopolymerisation and the electrochemical behaviour of the resulting copolymers. When scan numbers are constant and ratio of monomer is changed in electrocopolymerisation, one of the monomers can dominate copolymerisation reaction proven by cyclic voltammogram curve of the resulting copolymer which could be similar to one of homopolymers. When the ratio of monomers in the electrolyte is constant and potential scan numbers are varied, copolymer could be altered to one of the homopolymers. Before preparing a copolymer film, the growth conditions of the film should be optimized to produce a copolymer that can be used for further applications. Otherwise, copolymer can show the behaviour of one of the monomers.

Cyclic voltammograms of growth copolymer suggested that P(ANI-OT) (75:25) is electrochemically similar to POT and P(ANI-OT) (95:5) is similar to PANI. However, FTIR

spectra distinguish that polyanilinisation is occurred for P(ANI-OT) (95:5) but P(ANI-OT) (75:25) is a copolymer not similar to POT. Mass transfer direction of P(ANI-OT) (75:25) and P(ANI-OT) (95:5) copolymers in aqueous acidic medium during p-doped are identical. The growth cyclic voltammogram of copolymer itself is not enough to guess one of monomer domination. Cyclic voltammogram of P(ANI-OAP) (98:2) growth is similar to PANI curve and cyclic voltammogram of P(ANI-OAP) (80:20) growth is differentiated from any of PANI or POAP homopolymers. FTIR confirms that P(ANI-OAP) (98:2) was polyanilinazed. However, FTIR clearly supports the formation of a copolymer for P(ANI-OAP) (80:20).

The results shown in this chapter can be used to decide whether the ion exchange properties of conducting polymers for water purification could or could not be predicted. Δm-Q slopes can help to identify the performance for ion uptake. Additionally, potential fluoride extraction and the best polymer for fluoride uptake are addressed in chapter seven. Chapter four and seven can identify how ion exchange processes occur depending on copolymerisation.

4.4. References

1 G. G. Wallace, P. R. Teasdale, G. M. Spinks and L. A. Kane-Maguire, *Conductive electroactive polymers: intelligent polymer systems*, CRC press, Raton, 2008.

2 A. Guerfi, J. Trottier, I. Boyano, I. De Meatza, J. Blazquez, S. Brewer, K. Ryder, A. Vijh and K. Zaghib, *J. Power Sources,* 2014, **248**, 1099-1104.

3 K. Lee, S. Cho, S. H. Park, A. Heeger, C. Lee and S. Lee, *Nature,* 2006, **441**, 65-68.

4 Q. Zhang, Y. Li, Y. Feng and W. Feng, *Electrochim. Acta,* 2013, **90**, 95-100.

5 J. Chen, B. Winther-Jensen, Y. Pornputtkul, K. West, L. Kane-Maquire and G. G. Wallace, *Electrochemical and solid-state letters,* 2006, **9**, C9-C11.

6 Y. Kim, S. Fukai and N. Kobayashi, *Synth. Met.,* 2001, **119**, 337-338.

7 Q. Sheng, J. Wang, J. Zheng, Z. Xu and H. Zhang, *Biosensors and Bioelectronics,* 2010, **25**, 2071-2077.

8 A. Baba, M. Park, R. C. Advincula and W. Knoll, *Langmuir,* 2002, **18**, 4648-4652.

9 A. Baba, S. Tian, F. Stefani, C. Xia, Z. Wang, R. C. Advincula, D. Johannsmann and W. Knoll, *J Electroanal Chem,* 2004, **562**, 95-103.

10 A. Baba, R. C. Advincula and W. Knoll, *The Journal of Physical Chemistry B,* 2002, **106**, 1581-1587.

11 L. P. Bauermann and P. N. Bartlett, *Electrochim. Acta,* 2005, **50**, 1537-1546.

12 S. Cui and S. Park, *Synth. Met.,* 1999, **105**, 91-98.

13 A. G. Macdiarmid, J. C. Chiang, A. F. Richter and A. J. Epstein, *Synth. Met.,* 1987, **18**, 285-290.

14 D. E. Stilwell and S. Park, *J. Electrochem. Soc.,* 1989, **136**, 427-433.

15 Y. Shim and S. Park, *Synth. Met.,* 1989, **29**, 169-174.

16 G. Inzelt, *Electroanalysis,* 1995, **7**, 895-903.

17 K. Martinusz, E. Czirok and G. Inzelt, *J Electroanal Chem,* 1994, **379**, 437-444.

18 A. P. Abbott, M. Azam, G. Frisch, J. Hartley, K. S. Ryder and S. Saleem, *Physical Chemistry Chemical Physics,* 2013, **15**, 17314-17323.

19 A. R. Hillman, *Journal of Solid State Electrochemistry,* 2011, **15**, 1647-1660.

20 A. R. Hillman and M. A. Mohamoud, *Electrochim. Acta,* 2006, **51**, 6018-6024.

21 D. E. Stilwell and S. Park, *J. Electrochem. Soc.,* 1989, **136**, 427-433.

22 D. Borole, U. Kapadi, P. Mahulikar and D. Hundiwale, *J Appl Polym Sci,* 2003, **90**, 2634-2642.

23 S. Mu, *Synth. Met.,* 2004, **143**, 259-268.

24 H. J. Salavagione, J. Arias, P. Garcés, E. Morallón, C. Barbero and J. L. Vázquez, *J Electroanal Chem,* 2004, **565**, 375-383.

25 D. Gonçalves, R. C. Faria, M. Yonashiro and L. O. S. Bulhões, *J Electroanal Chem,* 2000, **487**, 90-99.

26 S. Kunimura, T. Ohsaka and N. Oyama, *Macromolecules,* 1988, **21**, 894-900.

27 Q. Yang, Y. Zhang, H. Li, Y. Zhang, M. Liu, J. Luo, L. Tan, H. Tang and S. Yao, *Talanta,* 2010, **81**, 664-672.

28 Y. Wei, W. W. Focke, G. E. Wnek, A. Ray and A. G. MacDiarmid, *J. Phys. Chem.,* 1989, **93**, 495-499.

29 Y. Wei, R. Hariharan and S. A. Patel, *Macromolecules,* 1990, **23**, 758-764.

30 D. Borole, U. Kapadi, P. Mahulikar and D. Hundiwale, *J Appl Polym Sci,* 2003, **90**, 2634-2642.

31 D. D. Borole, U. R. Kapadi, P. P. Kumbhar and D. G. Hundiwale, *Mater Lett,* 2002, **57**, 844-852.

32 D. D. Borole, U. R. Kapadi, P. P. Kumbhar and D. G. Hundiwale, *Mater Lett,* 2002, **56**, 685-691.

33 W. Huang, B. D. Humphrey and A. G. MacDiarmid, *Journal of the Chemical Society, Faraday Transactions 1: Physical Chemistry in Condensed Phases,* 1986, **82**, 2385-2400.

34 G. G. Wallace, P. R. Teasdale, G. M. Spinks and L. A. Kane-Maguire, *Conductive electroactive polymers: intelligent polymer systems*, CRC press, Raton, 2008.

35 P. Nunziante and G. Pistoia, *Electrochim. Acta,* 1989, **34**, 223-228.

36 S. L. de Albuquerque Maranhão and R. M. Torresi, *Electrochim. Acta,* 1999, **44**, 1879-1885.

37 A. R. Hillman and M. A. Mohamoud, *Electrochim. Acta,* 2006, **51**, 6018-6024.

38 M. C. Miras, C. Barbero, R. Kötz and O. Haas, *J Electroanal Chem,* 1994, **369**, 193-197.

39 G. Inzelt and V. Kertész, *Electrochim. Acta,* 1997, **42**, 229-235.

40 J. Desilvestro, W. Scheifele and O. Haas, *J. Electrochem. Soc.,* 1992, **139**, 2727-2736.

41 H. Varela, de Albuquerque Maranhão, Silvanna L, R. M. Mello, E. A. Ticianelli and R. M. Torresi, *Synth. Met.,* 2001, **122**, 321-327.

42 S. Bilal, A. A. Shah and R. Holze, *Electrochim. Acta,* 2009, **54**, 4851-4856.

43 M. Leclerc, J. Guay and L. Dao, *Journal of electroanalytical chemistry and interfacial electrochemistry,* 1988, **251**, 21-29.

44 V. Bavastrello, S. Carrara, M. K. Ram and C. Nicolini, *Langmuir,* 2004, **20**, 969-973.

45 M. J. Henderson, A. R. Hillman and E. Vieil, *Electrochim. Acta,* 2000, **45**, 3885-3894.

46 M. J. Henderson, A. R. Hillman and E. Vieil, *J Electroanal Chem,* 1998, **454**, 1-8.

47 M. G. Mahjani, A. Ehsani and M. Jafarian, *Synth. Met.,* 2010, **160**, 1252-1258.

48 C. Barbero, J. J. Silber and L. Sereno, *Journal of Electroanalytical Chemistry and Interfacial Electrochemistry,* 1990, **291**, 81-101.

49 A. A. Shah and R. Holze, *J Electroanal Chem,* 2006, **597**, 95-102.

50 Q. Yang, Y. Zhang, H. Li, Y. Zhang, M. Liu, J. Luo, L. Tan, H. Tang and S. Yao, *Talanta,* 2010, **81**, 664-672.

51 M. Kalaji, L. Nyholm and L. Peter, *Journal of electroanalytical chemistry and interfacial electrochemistry,* 1991, **313**, 271-289.

52 D. Kumar, *Synth. Met.,* 2000, **114**, 369-372.

53 S. Mu, *Synth. Met.,* 2004, **143**, 259-268.

54 T. Ohsaka, Y. Ohnuki, N. Oyama, G. Katagiri and K. Kamisako, *Journal of Electroanalytical Chemistry and Interfacial Electrochemistry,* 1984, **161**, 399-405.

55 P. Pawar, S. Sainkar and P. Patil, *J Appl Polym Sci,* 2007, **103**, 1868-1878.

56 J. Zhang, D. Shan and S. Mu, *Polymer,* 2007, **48**, 1269-1275.

57 M. V. Kulkarni, A. K. Viswanath and U. Mulik, *Mater. Chem. Phys.,* 2005, **89**, 1-5.

58 R. Li, Z. Chen, J. Li, C. Zhang and Q. Guo, *Synth. Met.,* 2013, **171**, 39-44.

59 A. Ehsani, M. G. Mahjani and M. Jafarian, *Synth. Met.,* 2012, **162**, 199-204.

60 S. Kunimura, T. Ohsaka and N. Oyama, *Macromolecules,* 1988, **21**, 894-900.

61 R. Tucceri, P. M. Arnal and A. N. Scian, *Journal of Spectroscopy,* 2012, **2013**.

62 S. Mu and Y. Yang, *The Journal of Physical Chemistry B,* 2008, **112**, 11558-11563.

63 G. Ćirić-Marjanović, *Synth. Met.,* 2013, **177**, 1-47.

Chapter 5: Temperature Effects on the Viscosity of DES Electrolytes

5.1. Introduction

5.1.1. Overview

Ionic liquids (ILs) have gained interest by industry and academia in the last decade due to their superior properties in comparison to conventional solvents. Numerous reviews have been written about ILs recently[1-6] and more than 500 ionic liquids have been commercially available[7] to date and the interests related to ILs continuously increases.

The ease in changing the ion types and hence having a variety of physical properties make ILs a good candidate to be used in specific applications. Although millions of potential ionic liquids could be tailored, the database of their physical properties is limited. Some of the important physical properties of ILs include freezing point, density, viscosity, ionic conductivity and surface tension. Obtaining data on these physical properties of ionic liquids can be difficult because the production of large volumes of pure ionic liquids could be required and hence the characterisation could be costly. Small scale characterisation processes should be developed to reduce the cost of process and the volume of samples required. One of the techniques developed for this purpose is the QCM, which is used to measure the viscosity-density properties of ILs.[8-10]

ILs are used in separation techniques,[11] organic synthesis,[12] pharmaceutical solvents,[13] catalysis,[14] heat transfer fluids,[15] fuel cells,[16] energy storage devices (see chapter six of this thesis), solar cells[17] and lubricants.[18] Since ILs are proposed as alternative electrolytes in electrochemical devices due to their advantageous properties of high thermal stability, low volatility, high ionic conductivity and wide potential windows, transport properties of ILs are very important as electrolytes in electrochemical devices. Therefore, their transport (diffusion) properties should be characterised for electrochemical application. Some studies focused on the viscosity measurement at room temperature by the QCM and the analysis of Newtonian behaviour of the ILs with added water at room temperature.[8-10]

DESs have been chosen as model electrolytes to measure viscosity in this work to due to their novel solvent properties[19] as they have different chemical properties but similar physical properties when compared to ILs.[20] If the QCM is a valid technique to measure the viscosity of DESs and the activation energy of DES flow over a range of temperature, it could be valid for ILs as well as their physical properties are similar.

Rotational Viscometer (RV)

The viscosity of a fluid is a measurement of the internal friction of the fluid caused by molecular attraction which makes it resist flow. When a layer of fluid moves to pass over another layer while a force is applied, this friction becomes apparent. The force is required to create movement called "shear". The greater the friction, the greater the shear and therefore the more viscous the liquid as explained by Figure 5.1. Additionally less viscous fluids, as expected, require less force to move.
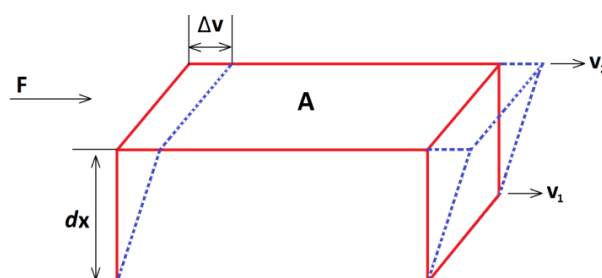
Figure 5.1: Newton's model of viscosity. Explanations of abbreviations are given in the text.

Figure 5.1 explains Newton's Law of viscosity. In this model; **F** (N) is the force applied to the area of the same size of two parallel plates of the fluid **A** (m^2) which are separated by **dx** (m) distance and travelling in the same direction at velocities v_1 (m s^{-1}) and v_2 (m s^{-1}). Shear stress, shear rate and viscosity are defined by Equ 5.1, Equ 5.2 and Equ 5.3 where Δv is the change of velocity (m s^{-1}), σ is shear stress (Pa), γ is shear rate (s^{-1}) and η is viscosity (Pa.s).

$$\sigma = \frac{F}{A}$$

Equ 5.1

$$\gamma = \frac{\Delta v}{dx} \qquad\qquad \text{Equ 5.2}$$

$$\eta = \frac{\sigma}{\gamma} \qquad\qquad \text{Equ 5.3}$$

Newtonian fluids display a linear relationship between shear stress and shear rate. In this case, the viscosity of Newtonian fluids must remain constant independent of shear rate. Water and thin motor oils are assumed to be Newtonian liquids. However, there are no liquids that meet the description of Newtonian behaviour perfectly. Non-Newtonian fluids do not have a constant relationship between shear stress and shear rate. Therefore, the viscosity of non-Newtonian fluids changes with alteration in the shear rate. Examples of the non-Newtonian fluids are salt solutions and molten polymers.

In this study, viscosity measurements, calculated from the QCM, are compared with viscosity measured with the DV-II+ Pro Brookfield's Digital RV. The motor in the device drives a spindle and changes in torque, which required rotating an immersed spindle in a liquid, are detected by a coiled spring wrapped around the drive shaft (see Figure 5.2). The torque can be used to calculate the viscosity of the liquid by RV.
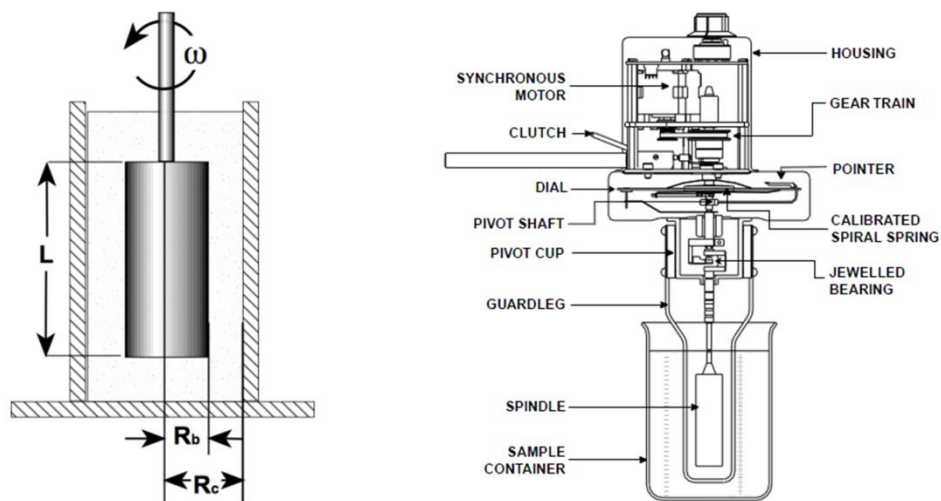
Figure 5.2: Left side) schematic diagram of a basic rotational viscometer in which ω is the angular momentum of the spindle and R_b, R_c, L are the dimensions of the spindle ; right side) a cross-section of the viscometer with the ideal set-up (from Brookfield manual[21]).

Higher viscosity of the sample creates greater drag requiring that the motors work harder to maintain the rotation speed. Resistance to flow is related to the size and the shape of the spindles and proportional to the speed of the spindle rotations.

QCM as a Viscometer

The QCM was initially used in mass deposition monitors.[22] In 1982 T. Nomura and M. Okuhara found that the QCM could be oscillated in the liquid environment.[23] Mass sensing of the quartz crystal has already been explained in chapter two and its application has been given in chapter four of this thesis and in the literature widely.[24, 25] The use of thickness shear mode (TSM) quartz crystals for the determination of liquid properties[26-29] (such as conductivity,[30] density[31] - viscosity[9, 32] and contact angles[33]) has been studied as well. Additionally viscoelastic properties (exhibiting both viscous and elastic characteristics) of materials on the quartz crystal resonator have been researched.[34-37] This chapter specifically focuses on the change in the frequency and bandwidth of quartz crystal in contact with the DESs to provide a further characterisation of the viscosity of the DESs.

Figure 5.3 displays a thin AT-cut quartz disc with two electrodes, one on each surface. One surface of the quartz contacts with liquid and the other is exposed to the air. An AT-cut quartz crystal was used in this study because of its negligible intrinsic temperature dependence.[38]
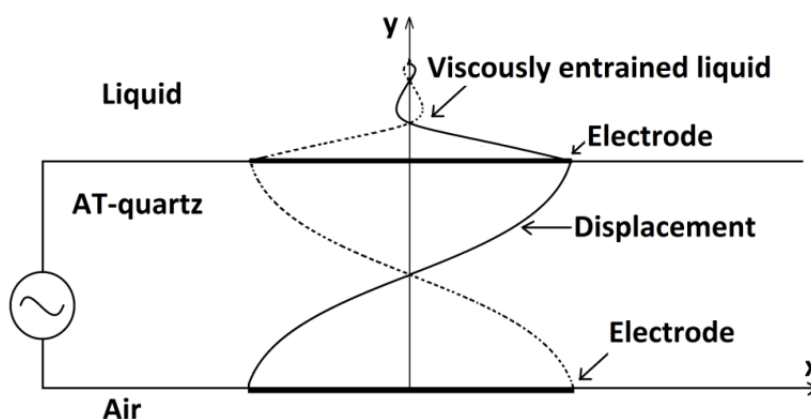
Figure 5.3: A quartz crystal oscillating in an alternating electric field.

When the QCM is operated at a high frequency (typically 10 MHz) in a liquid environment, its surface oscillation entrains liquid and the resonance is damped. Hence, the frequency decreases and the bandwidth increases (shown in Figure 5.6). Impedance-frequency data depending on resonant frequency and bandwidth of the crystal can be used to characterise some physical properties of the liquid (density, viscosity) contacting to the crystal. The loss of energy with frequency corresponding to the damping of the shear mode of oscillation, is observed in the bandwidth-frequency graph. The dissipation of energy is defined as D shown in Equ 5.4 and equal to the reciprocal of the q-factor

$$D = \frac{B}{f_s}$$
Equ 5.4

where f_s is the overtone frequency ($f_s = nf_0$, where f_0 is the fundamental frequency) and B is the bandwidth of the response of the QCM measured with network analyser. The decrease in square of the frequency and the increase in square of the bandwidth is proportional to the viscosity and density of the liquids measured with the QCM for Newtonian liquids[39, 40] described by Equ 5.5 and Equ 5.6, respectively.

$$\frac{\Delta f}{f_0} = -\frac{1}{Z_q}\left(\frac{f_s \eta \rho}{\pi}\right)^{\frac{1}{2}}$$
Equ 5.5

and

$$\frac{\Delta B}{f_0} = \frac{2}{Z_q}\left(\frac{f_s \eta \rho}{\pi}\right)^{\frac{1}{2}}$$
Equ 5.6

Where, Z_q is the specific acoustic impedance of the quartz $\left[Z_q = (\mu_q \rho_q)^{\frac{1}{2}} = 8.84 \times 10^6 \ kg \ m^{-2} \ s^{-1}\right]$, ρ is density of liquid and η is the viscosity of liquid contacted to the quartz crystal resonator. When changes in resonant frequency and bandwidth are correlated with each other, the combination of Equ 5.5 and Equ 5.6:

$$\frac{\Delta f}{\Delta B} = -0.5 \qquad\qquad \text{Equ 5.7}$$

Equ 5.7 can be used to determine whether the liquid response is Newtonian or non-Newtonian. As there is no known liquid which is perfectly Newtonian, when Δf/ ΔB is -0.5 ± 0.05, it is approximately Newtonian.[41-43] The frequency and bandwidth data obtained from QCM has already been used to assess whether ILs are Newtonian liquids or not and it was used to measure the viscosities of ILs.[8, 9, 44, 45] The originality of the work presented in this chapter is to use the TSM resonator for viscosity measurements under wide range of temperature.

The Kanazawa-Gordon equation,[32, 46] which can be used to measure viscosity of Newtonian liquids, is presented in Equ 5.8 which is arranged from Equ 5.5 and multiplied with 100 to calculate the viscosity of the samples in the unit of cP as viscosity in this chapter will be reported as centipoise (cP) (1 mPa·s = 1 cP) by RV.

$$\eta_L = \left(\frac{(\Delta f)^2}{f_0^3 \rho_L}\right) \pi \rho_q \mu_q 100 \qquad\qquad \text{Equ 5.8}$$

The viscosities, calculated from Equ 5.8, are compared with viscosities measured from a conventional method (RV) and the activation energy of flow for both sets of data obtained from different methods (QCM and RV) is analysed in this study.

5.1.2. Aims and Objectives

This chapter had two main aims which were 1) to determine whether the QCM technique could be used to calculate the viscosity of the DESs at wide range of temperature (from 25 °C to 90 °C) to observe the applicability of this technique for viscosity characterisation of ILs; 2) to identify the transport behaviour of DESs used as electrolyte of PANI based supercapacitor applications in chapter six.

To compare viscosity results, calculated from QCM, with viscosity, measured by means of RV, a cell must be designed to obtain viscosity of DESs in tandem by both techniques. Cell design for a wide range of temperature was also important for the

comparison of the QCM and RV results. The rationale behind this was to match QCM results as close to RV results as possible. The last aim was to identify if there is any difference between the activation energy for viscous flow obtained from these techniques.

5.2. Results

5.2.1. Experimental (Cell) Development

This section will focus on the cell development for viscosity measurements in a wide range of temperature by the QCM experiments. Viscosities of fluids are most commonly measured by U-shaped glass viscometer and RV.[47] The viscosities of DESs have been measured by RV.[18, 48-50] As one of the main aims of this work was to establish a method to measure the viscosity of ionic liquid electrolytes over a wide range of temperature, DESs were selected as a model electrolyte to show that the QCM can be used as a viscometer. To compare the QCM and RV results, an experimental set-up was designed as shown in Figure 5.4.
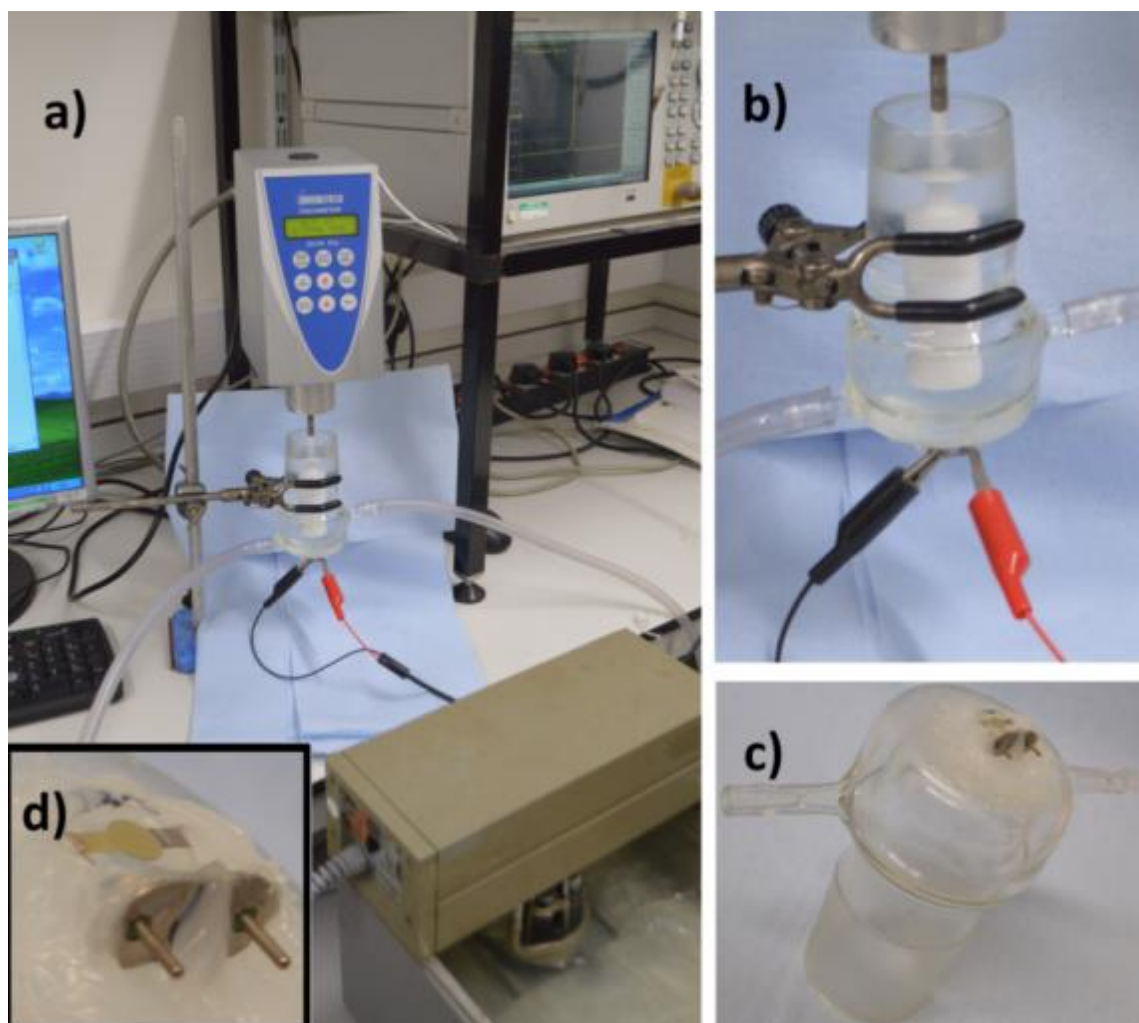
Figure 5.4: Experimental set-up with water bath to measure viscosity of DESs by the QCM and RV in-situ; a) general set-up connected to RV and the QCM; b) the glass cell used, RV probe is inside and; c) AT-cut polished quartz crystal attached the bottom of the cell; d) closer image of the crystal.

Initially a jacketed cell with a capacity of 200 mL, shown in Figure 5.4, was designed for viscosity measurement. As the response of a smooth TSM resonator in liquid, entraining a layer of contacting liquid, could depend on the liquid density and viscosity[26] and unpolished quartz causes frequency changes other than from physical properties of the liquids[42]; a polished quartz crystal was glued at the bottom of the cell which had an opening of 5 mm radius. Silicon based adhesive (not sensitive to temperature changes and solvents) was used to attach the crystal to the glass cell to ensure the seal was watertight, additionally ensuring that glue did not touch the active area of the crystal. The cell jacket was connected with its inlet and outlet to a water

bath (as seen in panel a of Figure 5.4) to control the temperature of the fluid every 5 °C from 25 °C to 80 °C. When a DES was heated in the cell using water bath (typically 10 minutes to reach equilibrium at given temperature), a reading of RV and QCM data were taken. Viscosity of DESs were obtained *in-situ* from RV and frequency difference of QCM data to avoid any small changes in viscosity values because choline chloride, formed DESs, is hydrophilic and thus DESs could uptake water from the atmosphere or could be contaminated in open system and these factors (small water contents or contamination) could cause a change in the viscosity of the liquids. Therefore all measurements in this study are taken using QCM in tandem with RV.

To obtain the same viscosity data (at least as close as possible) from both techniques; firstly it must have been ensured that the viscosity results were measured accurately by classical RV. Therefore, it was decided to calibrate RV with a number of commercially available calibration fluids purchased from Brookfield which have different range of viscosity from 10 to 5000 cP. After calibration of RV, a new cell, with more than 600 mL capacity suggested by the manual of Brookfield equipment, was designed shown in Figure 5.5 to obtain reliable RV results and compare these results with QCM results. Additionally, external factors such as the vibration of the laboratory bench, which could affect the accuracy of the frequency of the quartz crystal, was eliminated by relocating all equipment (RV, QCM, and computers) and set-up in an isolated area specifically designed for the experiments.
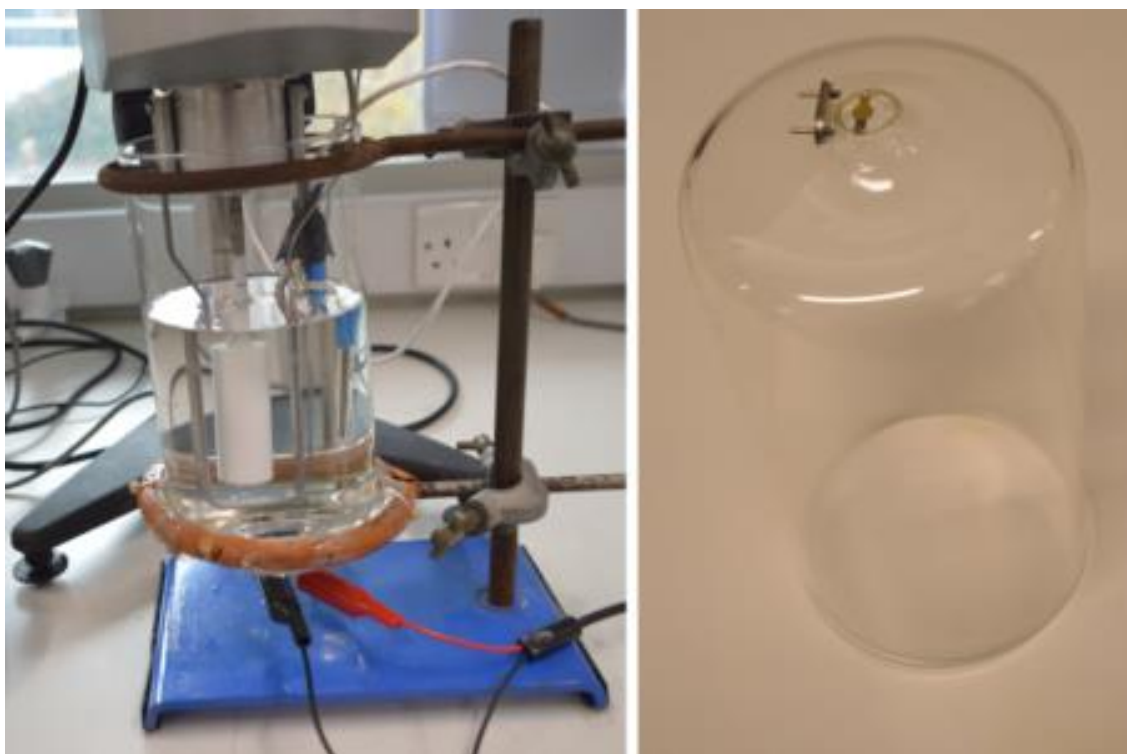
Figure 5.5: left side) experimental set-up for in-situ measurement of viscosity by QCM and RV; right side) the glass cell used for measurement with a polished quartz crystal.

Heating the cell by a water bath for each temperature was a time consuming process. Therefore, the selected DES was heated up (typically to 100 °C) and then poured into the new glass cell (see Figure 5.5) to cool down to 25 °C. During the cooling down of the liquid, the spectra of network analyser were recorded and the temperatures were measured with the thermocouples in both techniques: RV and QCM. The spectra of QCM data recorded during the cooling down process of the liquid are shown in Figure 5.6.
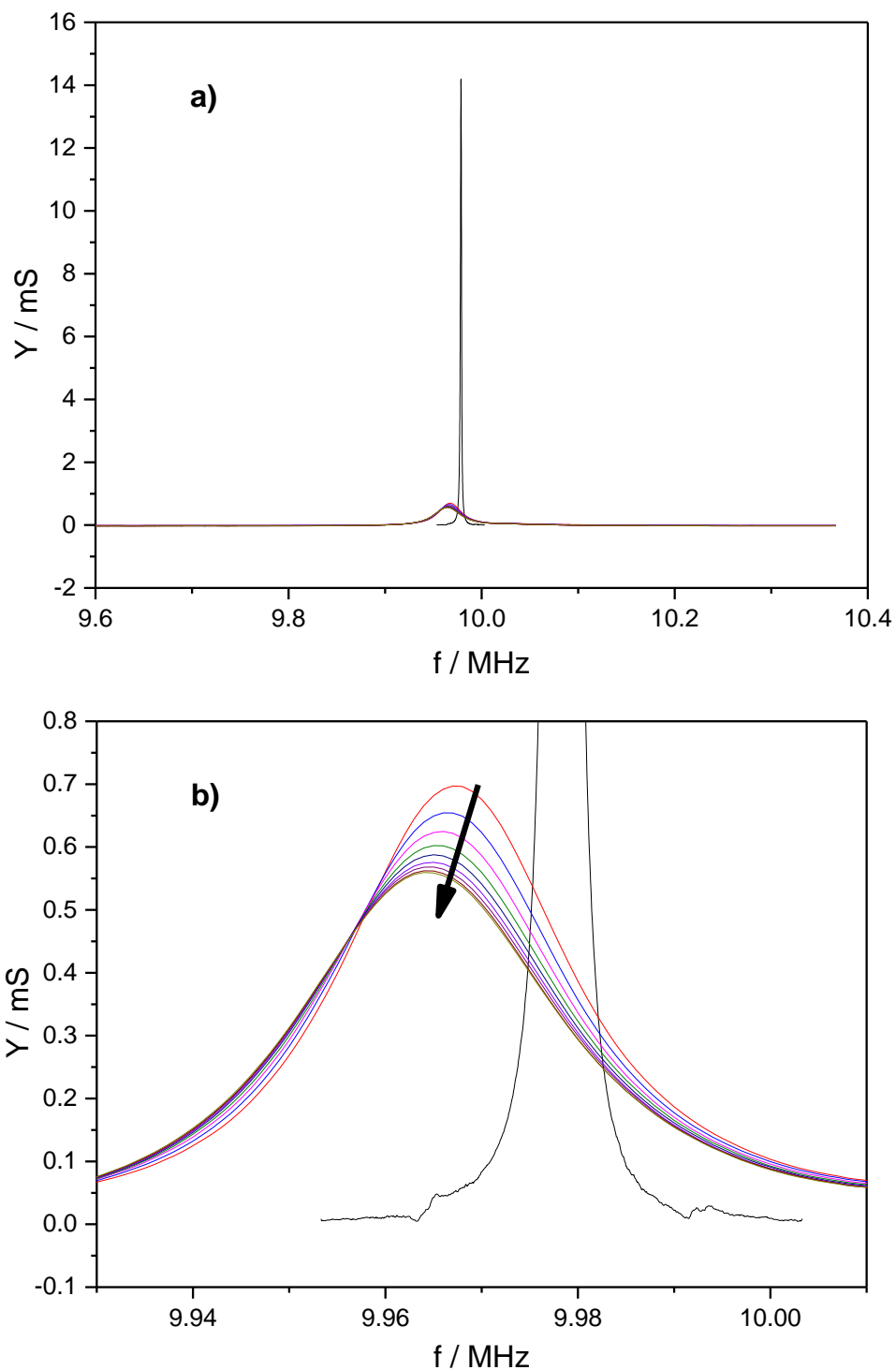
Figure 5.6: a) spectra of Y vs. f obtained from QCM analysis, the long, narrow peak represents the response of unloaded (bare Au exposed to air) and; b) small peaks (around 0.6 mS) represent the responses of Ethaline loaded quartz crystal, the arrow indicates the data taken every 10 minutes. Ethaline was heated up (typically to 100 °C) and then poured into the glass cell.

A typical data set comprise 1000 acoustic spectra recorded by the QCM during viscosity measurement and a thermocouple was connected to the multimeter of network analyser to calculate the temperature for each spectrum of the resonator. Two thermocouples were connected to the guard leg placed close together (see Figure 5.5). One of them was a built-up thermocouple connected to RV which did not require any intervention. Another thermocouple was connected to the voltmeter of network analyser to measure the voltage for each spectrum during cooling down of the solution. To achieve this, a value in volts from thermocouple was recorded with its corresponding temperature, RV showed. The typical graph of this is shown in Figure 5.7.
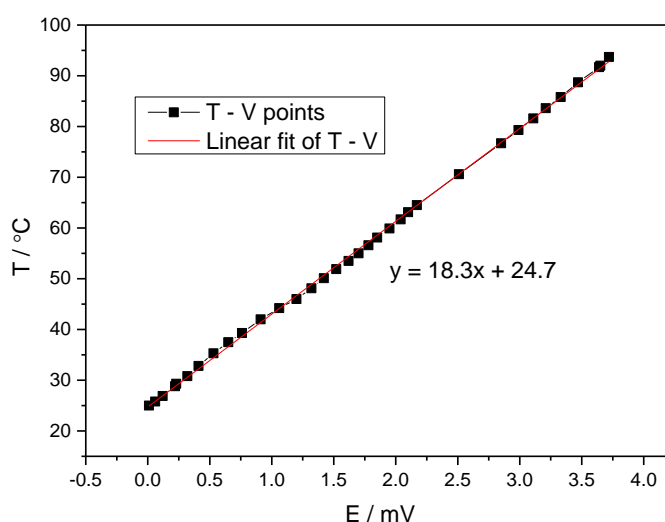
Figure 5.7: A typical calibration curve produced by a thermocouple (Omega J type) connected to the voltmeter of the QCM giving voltage output as a function of the temperature of RV. This value was used for the results given in Figure 5.8.

The calibration curve was linear over the complete temperature given in Figure 5.7. The equation of the graph was used to calculate the temperature from potential shown by multimeter and recorded with each corresponding QCM spectrum.

The viscosity results of RV had been ensured by the calibration of the Brookfield equipment with known-viscosity solution and designing a new cell with larger volume capacity. The temperature was continuously controlled to compare viscosity of QCM

with RV during wide range of temperature. Following the change in the experimental conditions, the *in-situ* experiment was repeated. Ethaline was heated and poured into the cell with the set-up shown in Figure 5.5. Viscosity data of Ethaline measured with RV and QCM data for viscosity calculation were collected. To calculate viscosity with Equ 5.8, frequency of bare crystal (unloaded) (f_0), frequency differences (Δf) (the difference of unloaded and loaded in Ethaline) and density of the liquid are required as other constants are known. Frequencies (f_0 and Δf) are taken from the raw spectra data (typical one is shown in Figure 5.6) and the density used in that formula is tabulated in Table 5. 1.

Table 5. 1: Measured density values of DESs at room temperature.

Liquid	Density (g cm^{-3})
Ethaline	1.11
Glyceline	1.17
Reline	1.21

After using Kanazawa-Gordon equation (Equ 5.8 in page 139) for raw QCM data and correlated with temperature, Figure 5.8 was obtained.
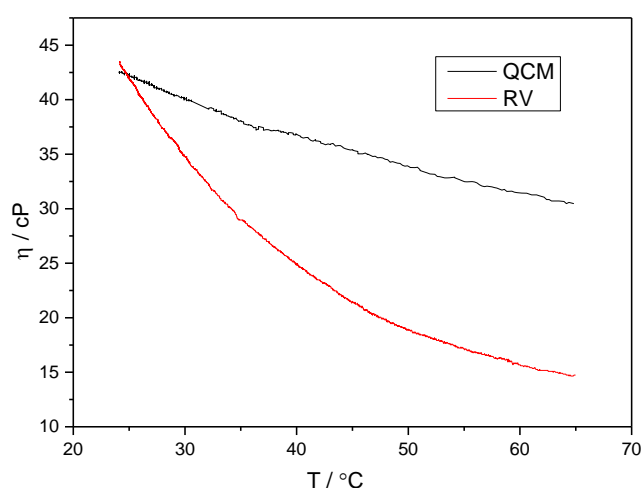
Figure 5.8: Viscosity of Ethaline given by RV (red line) and calculated from QCM frequency change (black line).

Figure 5.8 shows that the viscosity temperature graphs of RV and the QCM for Ethaline are quite different. While viscosity calculated from QCM data is close to the viscosity measured with RV (~2%) at low temperatures (around 25 °C), viscosities obtained from the QCM are much higher (>100%) than viscosities obtained from RV at high temperatures. It was believed that there was no question about the temperature measurement as the data of both techniques (RV and QCM) ended at the same point. There was no question about RV measurement as well because RV was calibrated with commercial liquids. Ethaline viscosity with temperature decrease gave a near straight line plot (see black line of Figure 5.8) because the change in frequency recorded by network analyser during measurement was small. The same shape were obtained for Glyceline and Reline as well. The unexpected shapes of viscosity obtained by the QCM were attributed to uneven cooling of the DESs within the glass cell. The quartz crystal was attached to an opening at the bottom of the glass cell and hence the rate of cooling of DESs in the vicinity of the quartz crystal was different than bulk of the liquid measured with RV. The viscosity measured by RV was generally lower than viscosity calculated from QCM data (see Figure 5.8) because the fluid closest to quartz crystal cooled faster than bulk fluid as quartz crystal was exposed to the atmosphere. In addition, the temperature differences between two surfaces of the crystal (air and Ethaline) were large. To counteract these problems, one surface of the quartz crystal was immersed into the bulk fluid. Therefore a new cell (a crystal probe) was designed (given in panel c of Figure 5.9) attaching to the guardleg of the RV in order to locate the crystal in similar area of the spindle of RV. The crystal probe could measure the fluid in the same area at the same temperature with RV in order to eliminate uneven cooling of the DESs.
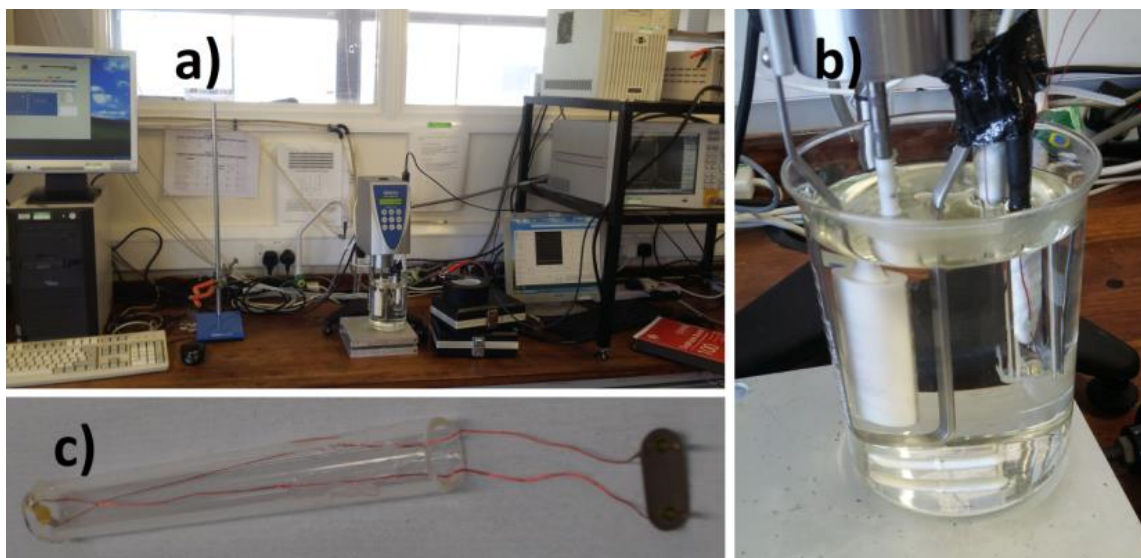
Figure 5.9: a) experimental set-up of viscosity measurement in-situ by QCM and RV; b) closer view of the cell connected to network analyser and probe of RV with their thermocouples sketched in panel b of Figure 5.11 (page 150); c)the crystal probe produced to immerse into the fluids.

The quartz crystal removed from its holder, was glued onto a glass tube to produce the crystal probe. Conductive wires (shown in panel c of Figure 5.9) were connected to the gold contacts on the crystal with silver conductive paint and it was glued. One side of the crystal was immersed into the fluid. The cotton wool was immersed into the other side of the crystal probe up to 1 cm height from the crystal surface (see panel b of Figure 5.9) to minimize the temperature differences between two surfaces of the crystal.

After the crystal probe was produced, it was attached to guardleg with the spindle of RV and thermocouples, all together were immersed into hot DESs with a temperature of around 100 °C and viscosity data were collected. Viscosity data of Ethaline from the QCM and RV with new set-up (photographed in panel a of Figure 5.9) are presented in Figure 5.10.
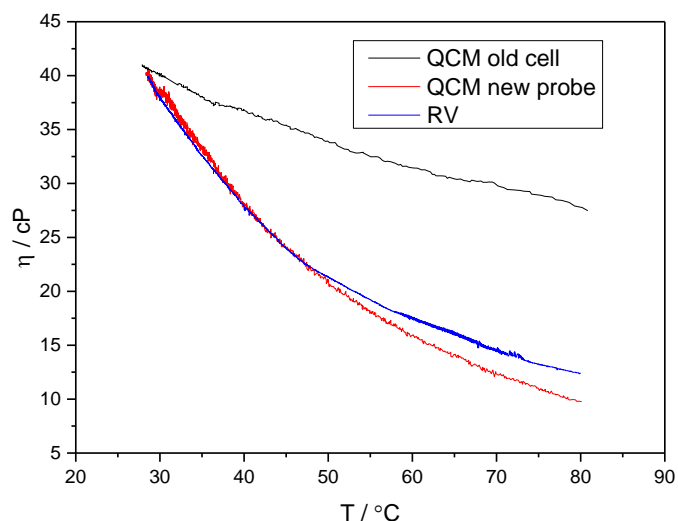
Figure 5.10: The viscosity of Ethaline measured with RV (blue line) and calculated from QCM data (red line) in which the crystal probe was attached to the guardleg of the RV. Black line, where crystal positioned at the bottom of the cell, is given for comparison.

After the quartz crystal was repositioned, the linear plot of viscosity-temperature line (black line of Figure 5.10) changes to the expected shape close to one taken from RV (red line of Figure 5.10). A new set-up was designed to control the slow decrease in temperature (shown in Figure 5.11) in order to obtain the same viscosity results from both techniques for all range of temperature. There was cotton wool wall for extra insulating layer around the beaker including liquid to manage this.
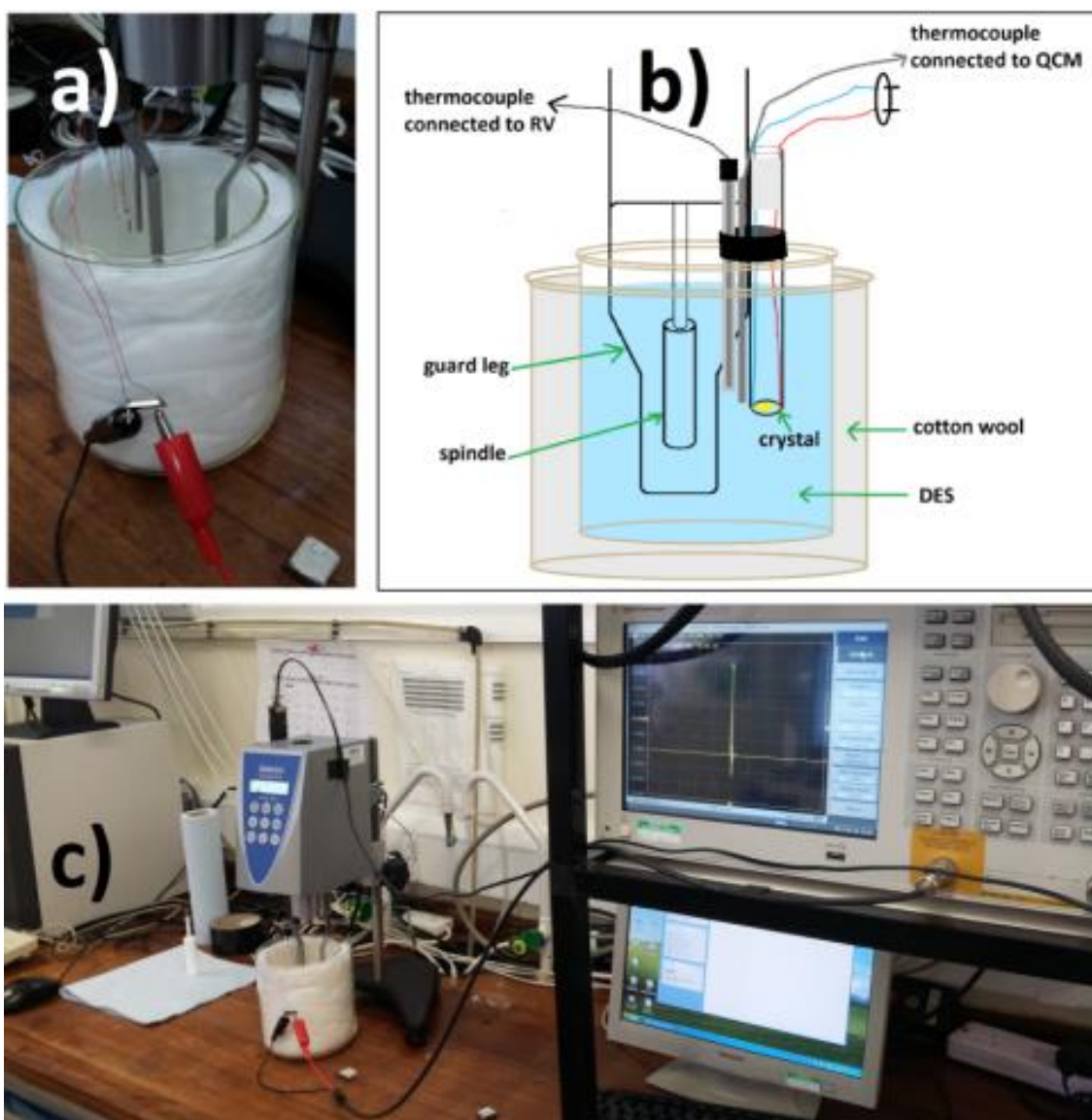
Figure 5.11: a) experimental set-up the same as Figure 5.9 but extra beaker to keep temperature constant for longer time; b) schematic drawing of the crystal probe and the set-up produced for use in this investigation; c) general set-up and the equipment.

The newly designed set-up, shown in Figure 5.11, gave similar results as shown in Figure 5.10. Therefore, measurements could be done without cotton wool insulation and second beaker. It was found by some researchers[8, 51] that the frequency change measurement provided by the third harmonics were more accurate than other harmonics. However, Saramago *et al.*[52] indicated that first harmonic of the fundamental frequency has best accuracy of the viscosity measurement. Therefore, the spectra for fundamental frequency (10 MHz, N = 1) was compared with higher

overtones: third (30 MHz, N = 3), fifth (50 MHz) and seventh (70 MHz) harmonic. The resonant frequencies were applied for unloaded quartz crystal and loaded one exposed to the DESs in order to calculate the viscosity to examine different harmonics and (if possible) to have a viscosity – temperature line closer to RV results. However, none of the results of harmonics frequency calculated by QCM data were as close as the fundamental frequency to RV. Therefore, the frequency shift of the first harmonic was found to provide the closest viscometer to RV results. The differences of works conducted by other researchers in literature could be due to the different network analyser used. While the viscosity of Ethaline obtained from RV and the QCM were similar for the first harmonic of fundamental frequency, viscosity of Ethaline calculated by the QCM applied with higher harmonics (N = 3, 5 and 7) were quite different (more than 100%, not shown in this chapter). Therefore, only the results of fundamental harmonic are presented in this thesis. In addition, location of the QCM equipment did not affect the viscosity results. However, smoothing and averaging function of devices were important to calculate viscosity by QCM close to RV. Therefore, the averaging and smoothing functions on the network analyser were turned on to minimize noise of spectrum to obtain smooth admittance *vs.* frequency spectra (Y – f graph) (typical spectra for applying average and smooth function are shown in Figure 5.13). The orders of cell calibration were changed to obtain the best result. When the cell was exposed to air, it was calibrated and the same cell was recalibrated in the liquids (as done for electrochemical experiments), the results of viscosity calculated from QCM data were very different than viscosities obtained RV. The crystal, calibrated by exposing to the air (bare crystal) and not calibrated again in liquids, gave the best results.

All changeable variations for the QCM measurements (crystal harmonics, temperature control of liquid, location of analyser, the position of crystal in liquid) were tested to find out the optimum conditions (cell and experimental design) and the viscosities obtained from the QCM and RV do not match for all range of temperature hence it was decided to implement the set-up, applied for viscosity measurements, shown in Figure 5.10. The viscosity differences between techniques will be explained and compared with the limited range of temperatures for example 25 – 40 °C.

5.2.2. Viscosity Measurement

5.2.2.1. Ethaline

Ethaline viscosity data, acquired using the QCM and RV are shown as a function of temperature in Figure 5.12.
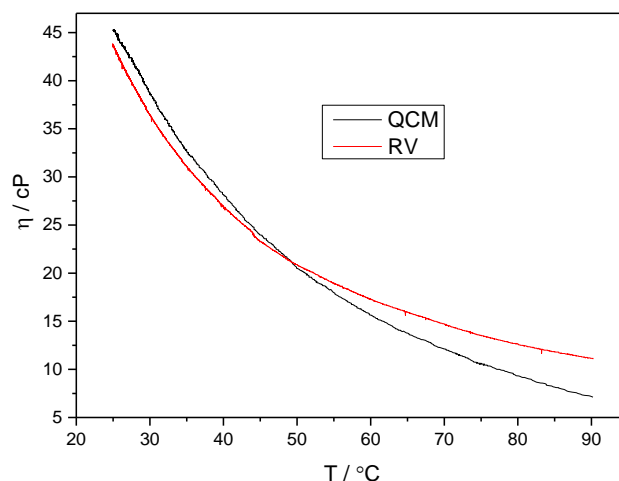
Figure 5.12: Viscosity of Ethaline measured from RV (red line) and calculated from frequency change of the QCM (black line).

While viscosities obtained from both techniques followed the same trend, the values were not exactly the same. Viscosities obtained from RV and the calculation of QCM data look similar at low temperature and the represented viscosities for the temperature of 25 °C obtain from QCM and RV are tabulated in Table 5.2. The ratio of viscosities, obtained from RV and the QCM, was 0.97 at 25 °C. However, the ratio increased significantly after 60 °C up to 1.58 at 90 °C as given in Table 5.2.

Table 5.2: Viscosity value of Ethaline at 25 °C and 90 °C obtained from RV and the QCM.

T / °C	η_{RV} / cP	η_{QCM} / cP	η_{RV}/η_{QCM}
25	43.7	45.2	0.97
90	11.2	7.1	1.58

At the beginning of this chapter it was said that the QCM as a viscometer can be used just for Newtonian fluids which could be indicated by the slope of $\Delta f/\Delta B$ (Equ 5.7). The value of $\Delta f/\Delta B$ slope, obtained from QCM results, should be -0.5 for Newtonian fluids. Before calculation $\Delta f/\Delta B$ slope from its graph, raw data of bare Au crystal and the crystal probe in Ethaline are shown in Figure 5.13.
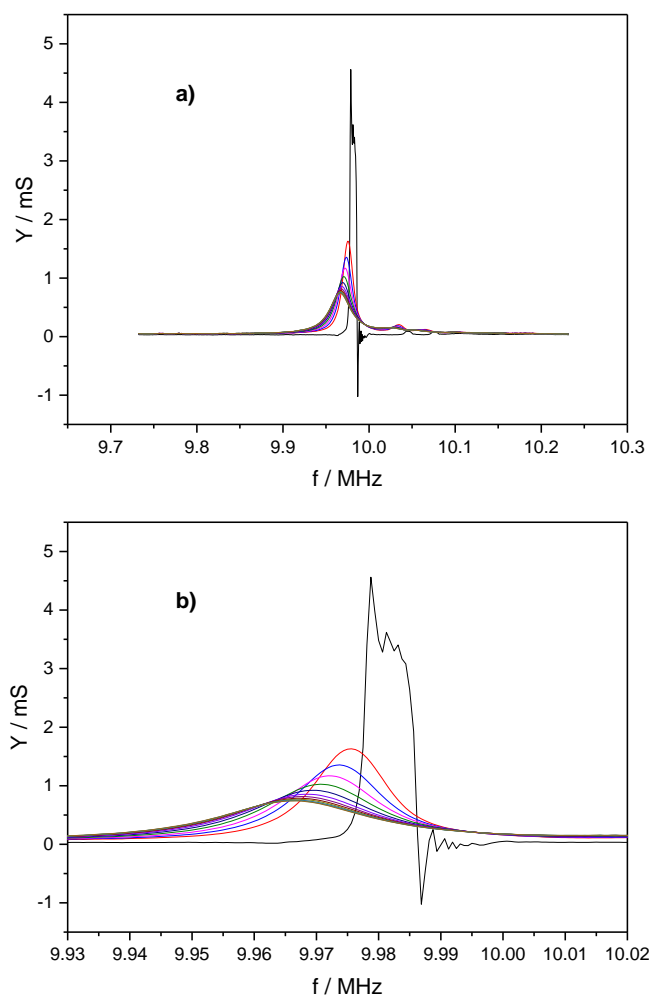
Figure 5.13: a) The raw spectra data of Y vs. f obtained from QCM analysis, black line around 4 mS is for unloaded crystal (bare Au exposed to air); b) closer view of the graph for Ethaline loaded quartz crystal. The red line represent the data of 90 °C. The data are taken every 20 minute until 25 °C.

Δf and ΔB data of the crystal probe in Ethaline for wide range of temperature, calculated from raw data of Figure 5.13, are shown in Figure 5.14.
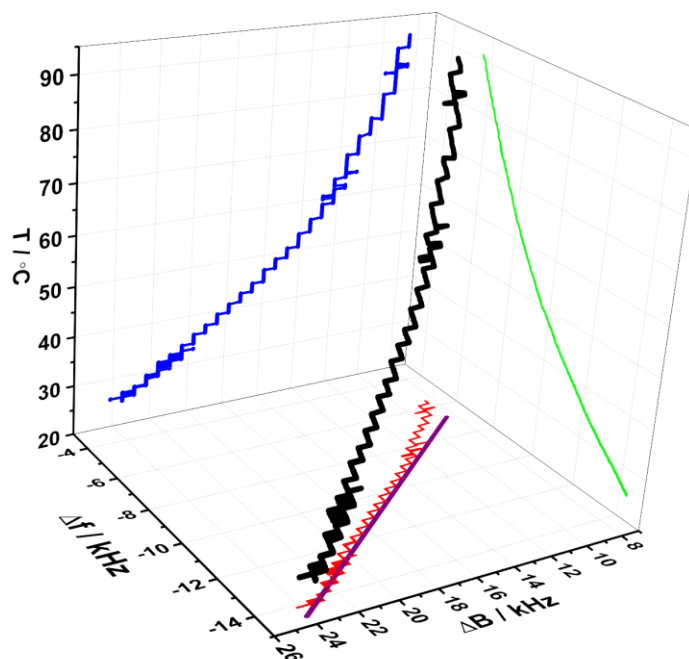
Figure 5.14: Δf and ΔB data of the crystal probe in Ethaline (25 ≤ T / °C ≤ 90 °C).

As expected, the increase in the frequency and decrease in the bandwidth of spectrum occurred with increasing temperature because Ethaline is less viscous at higher temperature, causing less loss of energy and less damping of shear mode oscillation of the liquid on the quartz surface. Frequency-bandwidth change of the liquid was studied previously.[26-29] Figure 5.14 has been given to observe and calculate the slope of Δf/ΔB. The plot of Figure 5.14 looks like the stairs because of the feature of the data acquisition system.

The slope of Δf/ΔB for Ethaline is -0.55 for all temperature given (from 25 °C to 90 °C). Ethaline could be considered a Newtonian liquid as Δf/ΔB slope is close to -0.5 for this range of temperature. However the graph of Δf/ΔB was not linear as shown in red line of Figure 5.14. While the slope of Δf/ΔB is -0.53 for Ethaline at low temperatures from 25 °C to 55°C, the slope is -0.66 for higher temperatures between 55 °C and 90°C. The slopes for some other range of temperature are given in Table 5.3.

Table 5.3: Δf/ΔB slopes of the crystal probe immersed into Ethaline for different range of temperatures.

T / °C	the slope of Δf/ΔB for Ethaline
25 – 40	-0.54
60 – 90	-0.65

As Figure 5.12 shows that the best agreement between RV and the QCM for Ethaline viscosity was at low temperature between 25 °C – 40 °C, this corresponds to where the slope of Δf/ΔB equal -0.54 (Table 5.3) which is the prediction for a Newtonian like behaviour. However, the slope of Δf/ΔB deviates significantly from -0.5 to -0.65 with increasing temperature of Ethaline indicating the deviation of Newtonian behaviour of Ethaline with increasing temperature. Therefore, it can be concluded that Ethaline has Newtonian behaviour at low temperatures but it deviates from Newtonian behaviour at higher temperatures. This can explain why viscosity of Ethaline calculated from the QCM was the same as viscosity measured with RV around room temperature but quite different at higher temperatures as presented in Figure 5.12. Therefore, mismatching result of the QCM and RV was not due to the experimental measurement or set-up; it was related to the liquid itself. The viscosity of Ethaline was measured several times by the QCM and each time it has non-Newtonian behaviour at high temperatures presumably because of changing the strength of hydrogen bonding in molecular structure at higher temperatures.

McHale *et al.*[8] found that the square root of viscosity-density of pure ILs higher than 18 $kgm^{-1}s^{-1/2}$ are not Newtonian but lower than that limit they were identified as Newtonian fluids. However, this has been not observed for DESs as Ethaline is Newtonian at low temperature and non-Newtonian at high temperatures. McHale *et al.*[8] used quartz crystal impedance analysis by using frequency shift and bandwidth change to deduce whether a water-miscible ionic liquid was a Newtonian fluid after addition of different water volumes. The viscosity of ILs, obtained by the QCM for wide range of temperature, was given in the literature[52] but the Newtonian (or non-Newtonian) behaviour of ILs was not mentioned in this work. However; the work

presented here is the first study that combines these two studies,[8, 52] in which the QCM has been used to observe the change of Newtonian behaviour of a liquid for a wide range of temperature.

5.2.2.2.   Glyceline

Viscosity data for Glyceline, obtained from RV and QCM responses (as explained in section 5.1), are given in Figure 5.15 as a function of temperature.
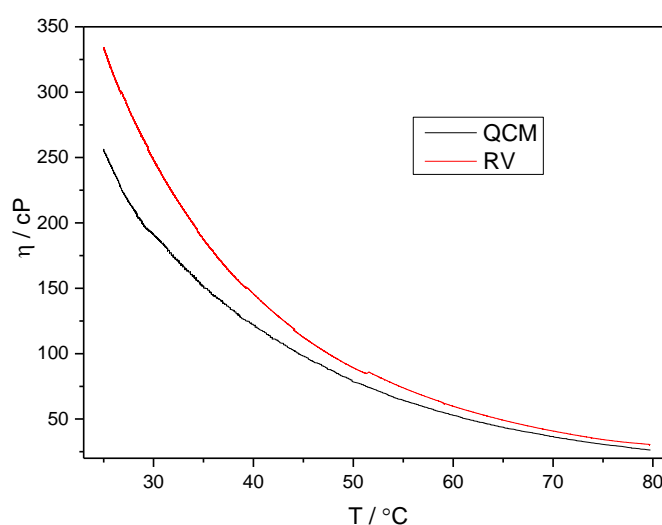
Figure 5.15: Viscosity of Glyceline obtained from RV (red line) and calculated from the frequency change of the QCM run concurrently (black line).

The viscosities calculated from QCM data were higher than viscosities obtained from RV. The viscosities, at high temperatures, appear to correlate reasonably well for both sets of data. As Glyceline was cooled, the viscosities from different methods began to diverge and this divergence of data sets increase significantly with decreasing temperature. There is a difference of 3.9 cP between viscosity obtained from RV and QCM at high temperatures (80 °C) with RV viscosity recorded as 30.2 cP and QCM viscosity calculated at 26.3 cP. However, the ratio of viscosity obtained from different techniques is given in Table 5.4 for both 25 °C and 80 °C to have meaningful comparison.

Table 5.4: Glyceline viscosities recorded from RV and calculated from QCM data at 25 °C and 80 °C.

T / °C	η_{RV} / cP	η_{QCM} / cP	η_{RV}/η_{QCM}
25	334.1	256.0	1.31
80	30.2	26.3	1.15

There was a relatively good agreement on the viscosity of Glyceline at high temperatures as the ratio of viscosities obtained from RV and the QCM is 1.15. However, the ratio of viscosities obtained from RV and QCM data appears to increase significantly at low temperatures (the ratio becomes 1.31 as shown in Table 5.4).

Figure 5.16 examines to what extent Glyceline is close to the Newtonian response during viscosity measurement run by the QCM.
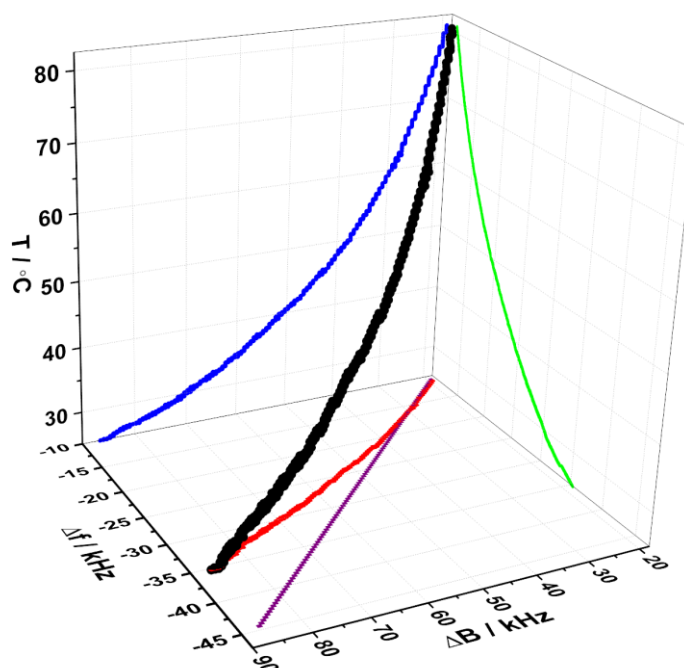
Figure 5.16: Δf and ΔB data of the crystal probe in Glyceline (25 ≤ T / °C ≤ 80 °C).

The spectra of Y-f is not presented here for Glyceline as it was similar to Y-f graph of Ethaline given in Figure 5.13. The only differences between the spectra of Ethaline and Glyceline are the magnitude of Δf (and ΔB) which can be observed from Figure 5.14 and Figure 5.16. Δf decreased approximately 14 kHz for Ethaline and 35 kHz for Glyceline which was arisen from higher mechanical impedance of Glyceline. The slope of Δf/ΔB for Glyceline for wide range of temperature was not linear as well (see red line of Figure 5.16). While the slope of Δf/ΔB in Figure 5.16 was -0.32 for temperature range between 25 °C and 55 °C, it was -0.46 for higher temperatures (from 55 °C to 80 °C). The magnitude of Δf/ΔB slopes for different range of temperature is given in Table 5.5.

Table 5.5: The slope of Δf/ΔB for the quartz crystal exposed to Glyceline for different temperatures.

T / °C	the slope of Δf/ΔB for Glyceline
25 – 40	-0.31
60 – 80	-0.47

As the slope of Δf/ΔB was getting close to -0.5 at high temperature, non-Newtonian behaviour of Glyceline at low temperatures approached to Newtonian behaviour upon increasing temperature of Glyceline. Therefore viscosities of Glyceline calculated by the QCM were close to the RV measurement at high temperatures but not low temperatures. The discrepancy between the two techniques was not attributed to experimental limitations of the QCM and/or RV (size and speed of spindle). Indeed this difference, as it was concluded for Ethaline in section 5.2.2.1, was due to the behaviour of the material (Glyceline).

5.2.2.3. Reline

The range of Ethaline viscosity is between 13 and 44 cP across the temperature range 80 °C to 25 °C (shown in section 5.2.2.1). For the same temperature range, the viscosity of Glyceline ranges from 30 cP to 334 cP (in section 5.2.2.2). Ethaline and

Glyceline viscosities were obtained by the QCM. Reline viscosity varies more than Ethaline and Glyceline between 50 cP – 1000 cP[53] depending on temperature. Reline was therefore selected to measure its viscosity as well to see a wide range of viscosities measured by the QCM. The higher viscosity of Reline can be explained by Hole theory which has been studied widely.[48, 54, 55] The difference in hole sizes arises from the degree of hydrogen bonding between the molecules of DESs. Large degree of hydrogen bonding decreases the void size in DESs, leaded to an increase in viscosity.[56-58] Figure 5.17 show the viscosities of Reline for wide range of temperatures between 25 and 90 °C obtained by RV and concurrently by the QCM.
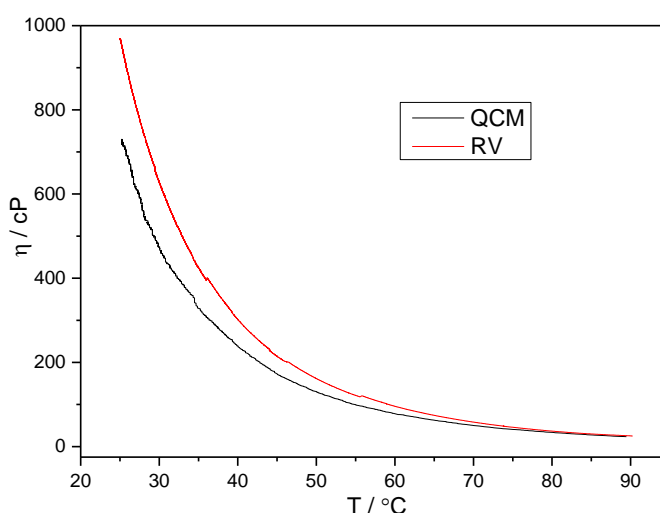
Figure 5.17: Viscosity of Reline obtained from RV (red line) and calculated from the frequency data of QCM (black line).

Agreement between RV and the QCM for Reline depending on temperature was similar to Glyceline: viscosities are different at low temperatures but very close to each other at high temperatures. While at high temperature (90 °C) viscosity differences of Reline between data set of RV and QCM was just 1.6 cP, dissimilarity between viscosity from the QCM and RV increased with cooling up to 242.1 cP at 25 °C. The viscosities value obtained from the both techniques at two temperatures (25 °C and 90 °C) and the ratio of them are given in Table 5.6.

Table 5.6: Viscosity value of Reline at 25 °C and 90 °C obtained from RV and frequency changes of the QCM.

T / °C	η_{RV} / cP	η_{QCM} / cP	η_{RV}/η_{QCM}
25	969.4	727.3	1.33
90	25.1	23.5	1.07

To test whether the difference between viscosity values was related to the Newtonian (or non-Newtonian) behaviour of Reline depending on temperature, the slope Δf/ΔB was again utilised. Figure 5.18 is shown to observe whether Reline is Newtonian fluid at high temperature and deviated from Newtonian behaviour at low temperatures.
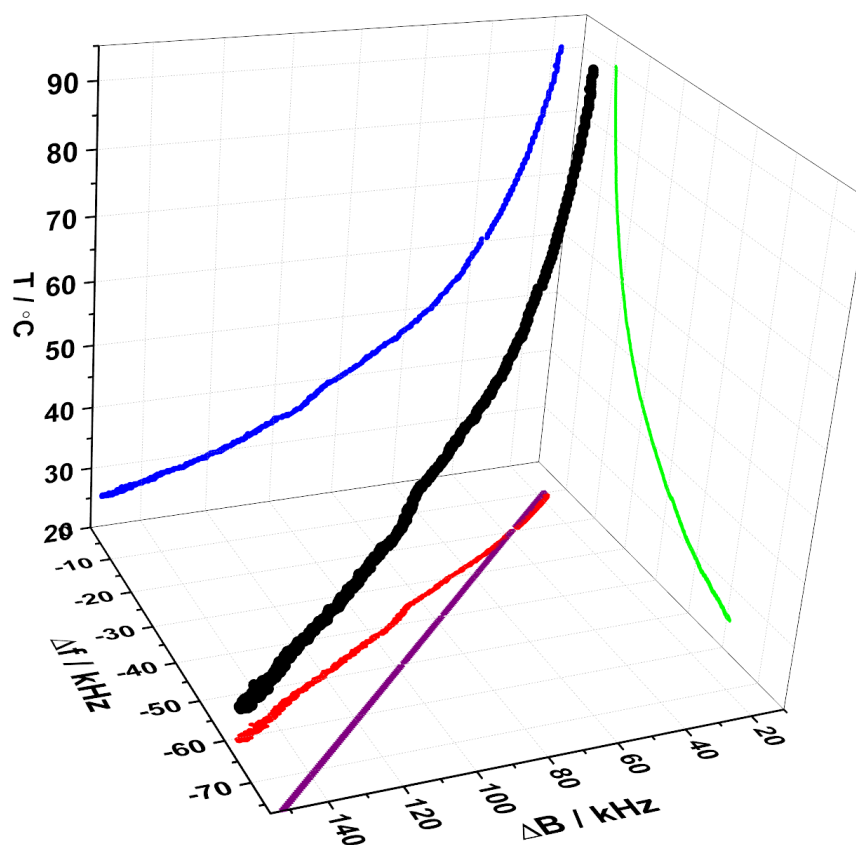
Figure 5.18: Δf and ΔB data of the crystal probe in Reline (25 ≤ T / °C ≤ 80 °C).

As the viscosity of Reline is greater than viscosities of Glyceline and Ethaline, the values of Δf and ΔB for Reline (more identical at low temperatures) are higher than Glyceline and Ethaline. Ethaline, Glyceline and Reline has ΔB value of 24, 87 and 155 kHz, respectively.

The slope of $\Delta f/\Delta B$, shown in Figure 5.18, is not linear. The slope of $\Delta f/\Delta B$ is equal to -0.36 for temperature between 25 °C and 55 °C representing the non-Newtonian characteristic of Reline at this range of temperature and therefore the mismatching of viscosity, calculated by QCM data, with the viscosity of RV is explicable. At high temperature range (55 °C – 90 °C), $\Delta f/\Delta B$ slope is -0.43 and the slopes for some other temperature ranges are given in Table 5.7.

Table 5.7: $\Delta f/\Delta B$ slopes of the crystal probe immersed into Reline for different range of temperatures.

T / °C	the slope of $\Delta f/\Delta B$ for Reline
25 – 40	-0.36
60 – 90	-0.46

Reline therefore seems to behave in a non-Newtonian manner at low temperatures but becomes to behave as Newtonian fluid at higher temperatures; the value of $\Delta f/\Delta B$ slope approaches to -0.5 with increasing temperature. Therefore QCM data could be used to calculate the correct viscosity as it was just 1.6 cP (η_{RV}/η_{QCM} = 1.07) different than RV measurement.

5.2.3. Activation Energy for Viscosity Flow

As seen in the previous section, viscosity become smaller with increasing temperature because of the increasing of kinetic motion promoting the breaking of intermolecular bonds between the close layers. The *Arrhenius – like* equation (Equ 5.9) is the simple model to analyse viscosity-temperature dependence of fluids.

$$\eta = Ae^{\left(\frac{E_a}{RT}\right)} \qquad\qquad \text{Equ 5.9}$$

in which E_a is the activation energy for viscous flow, A is the pre-exponential factor. The only difference between Equ 5.9 and the Arrhenius equation, describing the rate constant of a chemical reaction depending on temperature is a negative sign, Equ 5.9 does not have. Therefore, viscosity of fluid is smaller with increasing temperature. When Equ 5.9 is written in the logarithmic form:

$$\ln\eta = \ln A + \left(\frac{E_a}{R}\right)\frac{1}{T} \qquad\qquad \text{Equ 5.10}$$

The slope of ln(η) *vs.* 1/T line is multiplied with universal gas constant (R) to calculate the activation energy of viscous flow for the fluids obeying Equ 5.10. The activation energy for viscous flow is the value of the energy required for flowing a fluid for a given temperature range. The value of the activation energy of viscosity calculated for Ethaline, Glyceline and Reline from the QCM and RV data are given in the following sections.

5.2.3.1.   Ethaline

The graph of ln(η) *vs.* 1/T for Ethaline obtained from Figure 5.12 is given in Figure 5.19.
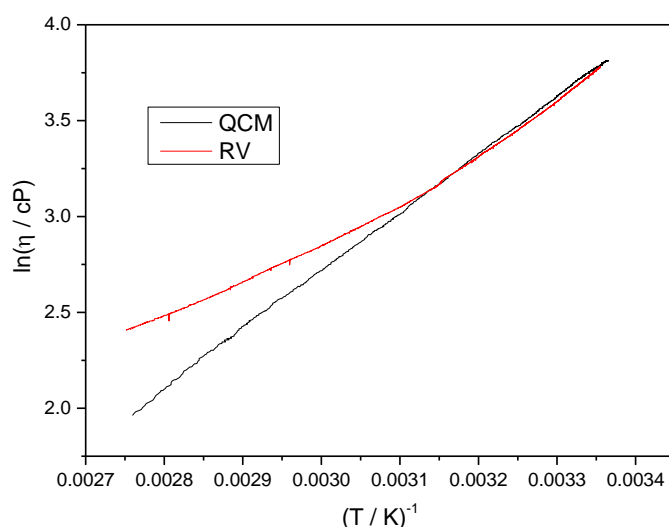
Figure 5.19: Plot of log viscosity vs. reciprocal of temperature for Ethaline. The viscosities vs. temperature, calculated from QCM data and obtained by RV, are given in Figure 5.12.

The graph of the QCM derived viscosity data for Ethaline displayed in Figure 5.19 is overlapped with RV derived viscosity data at low temperature diverge at high temperature.

The activation energy of Ethaline viscosity for QCM and RV was calculated from the gradient of Figure 5.19 for high and low temperature range given in Table 5.8. The ratio between two sets of data was compared with the $\Delta f/\Delta B$ which were the indication of Newtonian behaviour given in Table 5.8 as well.

Table 5.8: The values of the activation energy for viscous flow of Ethaline given in Figure 5.19.

T / °C	RV E_a / kJ mol^{-1}	QCM E_a / kJ mol^{-1}	E_{aRV}/E_{aQCM}	Slope of $\Delta f/\Delta B$
25 – 40	25.4	25.0	1.02	-0.54
60 – 90	15.1	25.9	0.58	-0.65

The activation energies for viscosity calculated from QCM and RV data are close to each other when the slope of Δf/ΔB is close to -0.5 at low temperature ranges (25 °C – 40 °C) in which Ethaline has Newtonian behaviour indicated by Δf/ΔB. It is observed in Figure 5.19 that the graph for the QCM data is linear but the graph for RV data has two different slopes. As the activation energy of Ethaline viscosity calculated from QCM data are close to each other for low and high temperatures 25.0 and 25.9 kJ mol^{-1}, respectively; rather than RV data which are 25.4 kJ mol^{-1} and 15.1 kJ mol^{-1}, given in Table 5.8, one could deduce the QCM is more reliable method because the results given by the QCM obey the Arrhenius equation in a wider temperature range. However, as indicated in section 5.2.2 the viscosities obtained by QCM data are correct only at the temperatures the liquid have Newtonian response.

It is known that viscosity values for the majority of RTILs do not obey the Arrhenius equation.[59-61] The RTILs, which do not obey The Arrhenius equation, were fitted with the Vogel–Tammann–Fulcher (VTF) equation.[62-65] Adherence to the Arrhenius or VTF equation depends on the size (high or low molar mass) of ions in the ILs, ion shape (symmetrical or not) and the functional groups (for example C-O, C=O) ions present.[66] Saramago et al.[52] used the QCM as a viscometer and applied both Arrhenius and VTF model to RTILs but without considering the possibility of non-Newtonian behaviour. Toniolo et al.[67] also used quartz crystal coated with some RTILs to analyse flavors by QCM measurements, assuming the Newtonian behaviour of RTILs.

Ethaline does not obey the Arrhenius equation as the slope of ln(η) vs.1/T for Ethaline is not constant (red line of Figure 5.19) and the activation energy of viscous flow, calculated for different range of temperatures, is different given in Table 5.8. The activation energy for viscous flow calculated from RV data at low temperature is very close to the activation energy calculated from QCM data in which the liquid has Newtonian behaviour. Therefore, calculation of the activation energy from the QCM results may not be authentic without considering Newtonian behaviour of liquid.

5.2.3.2. Glyceline

ln(η) *vs.*1/T data, extracted from Figure 5.15, are plotted in Figure 5.20 for calculation of the activation energy of Glyceline flow with different temperature ranges.
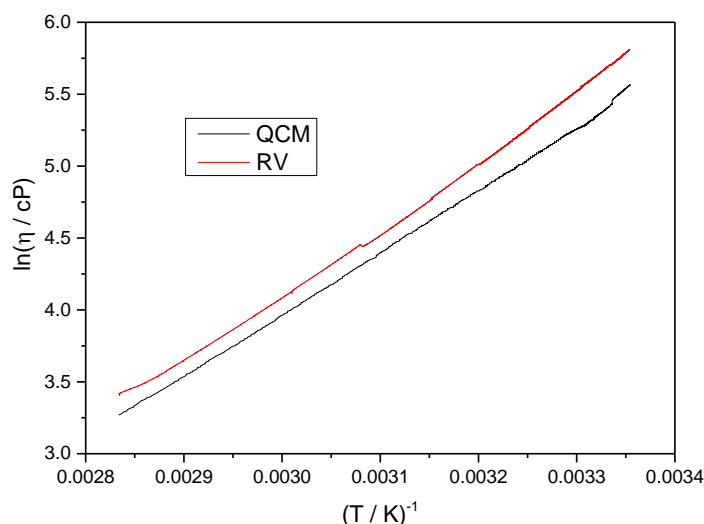
Figure 5.20: Plot of log viscosity vs. reciprocal of temperature for Glyceline. Data from Figure 5.15.

Table 5.9: The values of the activation energy for Glyceline flow. Data calculated from Figure 5.20.

T / °C	RV E_a / kJ mol^{-1}	QCM E_a / kJ mol^{-1}	E_{aRV}/E_{aQCM}	$\Delta f/\Delta B$
25 – 40	43.5	38.0	1.15	-0.31
60 – 80	35.5	34.7	1.02	-0.47

The activation energy of Glyceline viscosity calculated from RV for temperature between 25 °C and 40 °C was 43.5 kJ mol^{-1}. However, from QCM data it was 38.0 kJ mol^{-1} and ratio of them (1.15) was higher than the ratio of the activation energy obtained at temperature between 60 °C and 80 °C which was 1.02. As the behaviour of

165

Glyceline was Newtonian at high temperatures ($\Delta f/\Delta B$ = -0.47 between 60 – 80 °C), the difference (also ratio) between the activation energies obtained from QCM and RV is lower at this temperature range which are 34.7 and 35.5 kJ mol^{-1}, respectively. The activation energy obtained from RV ranged from 35.5 kJ mol^{-1} to 43.5 kJ mol^{-1} when temperature range changed from 60 °C – 80 °C to 25 °C – 40 °C (given in Table 5.9) but ΔE_a was 3.3 kJ mol^{-1} for QCM data. Therefore the slope of QCM data is linear for wider temperatures but indeed it is not reliable as Glyceline was deviated from Newtonian behaviour with the decrease in the temperature. Pandey *et al.*[68] found that temperature dependence of viscosity of Glyceline (measured by RV) from 283.15 to 363.15 K to be better described by VTF model rather than Arrhenius Model.

5.2.3.3. Reline

The data of Figure 5.17 is used to draw Figure 5.21 for calculation of the activation energy of Reline as a function of temperature.
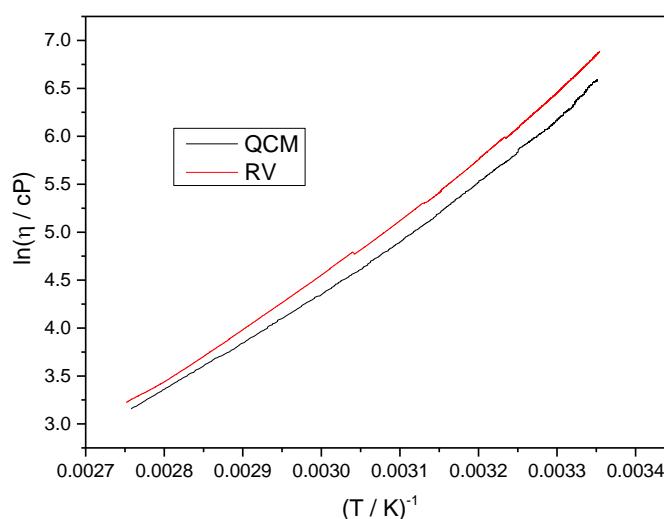
Figure 5.21: Plot of log viscosity vs. reciprocal of temperature for Reline. Data from Figure 5.17.

The slopes of ln(η) *vs.* 1/T are not constant for both QCM and RV data and the activation energies for 25 °C – 40 °C and 60 °C – 90 °C are shown in Table 5.10.

Table 5.10: The values of the activation energy for Reline flow. Data calculated from plot given in Figure 5.21.

T / °C	RV E_a / kJ mol^{-1}	QCM E_a / kJ mol^{-1}	E_{aRV}/E_{aQCM}	Slope of $\Delta f/\Delta B$
25 – 40	61.0	60.1	1.02	-0.36
60 – 90	45.4	41.1	1.11	-0.46

For Reline (shown in Table 5.10) the temperature dependant trend of the change in the activation energy were close for both techniques: while RV shows that E_a was 61.0 kJ mol^{-1} for temperature between 25 °C and 40 °C and 45.4 kJ mol^{-1} for 60 °C – 90 °C, QCM shows E_a was 60.1 kJ mol^{-1} for 25 °C – 40 °C and 41.1 kJ mol^{-1} for 60 °C – 90 °C. Abbott *et al*. found that viscosity-temperature profiles for Ethaline, Glyceline and Reline follow the Arrhenius behaviour.[50, 69] The Arrhenius equation could be applied to the RTILs for limited temperature range[70] which we also consider the activation energy of DESs flow for limited range of temperature (different ranges) in this work as our main aim is to compare QCM with RV. However, the dynamics of Reline viscosity depending on wide range of temperature was described more properly by VFT model studied by Pandey *et al*.[53]

The ratio of E_a obtained from RV and the QCM results are slightly higher (1.11) at high range of temperatures (60 °C – 90 °C) at which Reline behave like Newtonian fluids ($\Delta f/\Delta B$ = -0.46), given in Table 5.10. The ratios of between the activation energies are low at lower temperature range (25 °C – 40 °C) but Reline does not have Newtonian behaviour. Even if the ratio between the activation energy was higher at high temperature, QCM result obtained for high temperature Reline should be considered for the activation energy of Reline because the behaviour of Reline was Newtonian at high temperatures ($\Delta f/\Delta B$ = -0.46). Indeed the ratio at the temperature range which Reline is Newtonian is not very high (1.11). In addition, RV and QCM for higher temperature give similar activation energy of Reline flow 45.4 kJ mol^{-1} and 41.1 kJ mol^{-1}, respectively.

5.2.4.   Comparison of Rotational Viscometer and QCM

When the viscosity results obtained from the QCM and RV were compared with each other, they were not compared to literature results as the viscosity measurements were conducted for complementary study and the viscosities of DESs could be affected by moisture contents. For example the viscosity of Glyceline measured by Pandey *et al.*[68] was higher than viscosity measurement of Glyceline measured by Abbott *et al.*[50] Some studies[71, 72] showed that the presence of small amount of water decreases the viscosity of Reline. When Xie *et al*[71] compared the viscosity results of Reline (403 mPa·s at 313.2 K) with the viscosity measurement at the same temperature conducted by other researchers: Abbott *et al.*[19], Ciocirlan *et al.*[73] and Pandey *et al.*[53]; these literature results were 48%, 16% and 41%, respectively less than measurement given by Xie *et al.* It can be concluded that there are some discrepancies which were caused by the trace amount of water contents,[74] impurities and the set-up of experiments and thus the viscosity results shown in this study are not compared with the results in literature, they are just compared with the *in-situ* measurements of RV with the QCM.

The QCM operates shear mode oscillation on the surface. When it is operated in a liquid environment, the liquid is entrained by surface oscillation. The penetration depth (δ) from the interface is typically less than 1 μm[30] for Newtonian liquids [$\delta = (\eta/\pi f_s \rho)^{1/2}$] Therefore; only a few mL liquid is enough to measure the viscosity. However, RV requires large amount of sample (hundreds of mL liquids) for measuring viscosity as a small amount of liquid measurement with RV could not guarantee correct measurement. The small amount of sample used by the QCM causes lower production cost and increase the rate of liquid characterisation giving optimum information for use.

RV requires experimental set-up such as altering spindle type, size and speed depending on viscosity range of fluids. However, the QCM does not require variable experimental factors and does not have macroscopic moving parts: it could be used for all fluids without changing experimental settings. The speed of the spindles of RV is supposed to be changed during measurement the viscosity of the liquids, having wide range of viscosity with changing temperature whereas the QCM could be continuously

used without any changing. For example, when viscosity of Reline was measured between 90 °C and 25 °C, rotation per minutes was changed three times depending on the range of viscosity but the QCM was not stopped. Therefore, the QCM method could give faster data than RV. If a program were uploaded to the computer, the QCM could be operated easier by non-expert users after a suitable program, which can allow in situ monitoring of physical properties of fluids such as deviation from Newtonian fluids and viscosity of Newtonian fluids, is written.

The QCM can easily give information about the Newtonian behaviour or the deviation from Newtonian behaviour for a wide range of temperature. However, the speed of spindle (shear rate) should be altered at each temperature to deduce the behaviour of the fluids by RV which takes long duration.

RV should be calibrated by known liquids but the QCM does not need to be calibrated by any liquids. The calibration process in the QCM is required just for the crystal used during measurement.

The quartz crystal, using for the calculation viscosity, could be designed to measure other physical properties of the electrolyte. For example two quartz crystals were glued to a T-tube and their surfaces were used to measure the conductivity of a liquid by conductivity meter as shown in Figure 5.22.
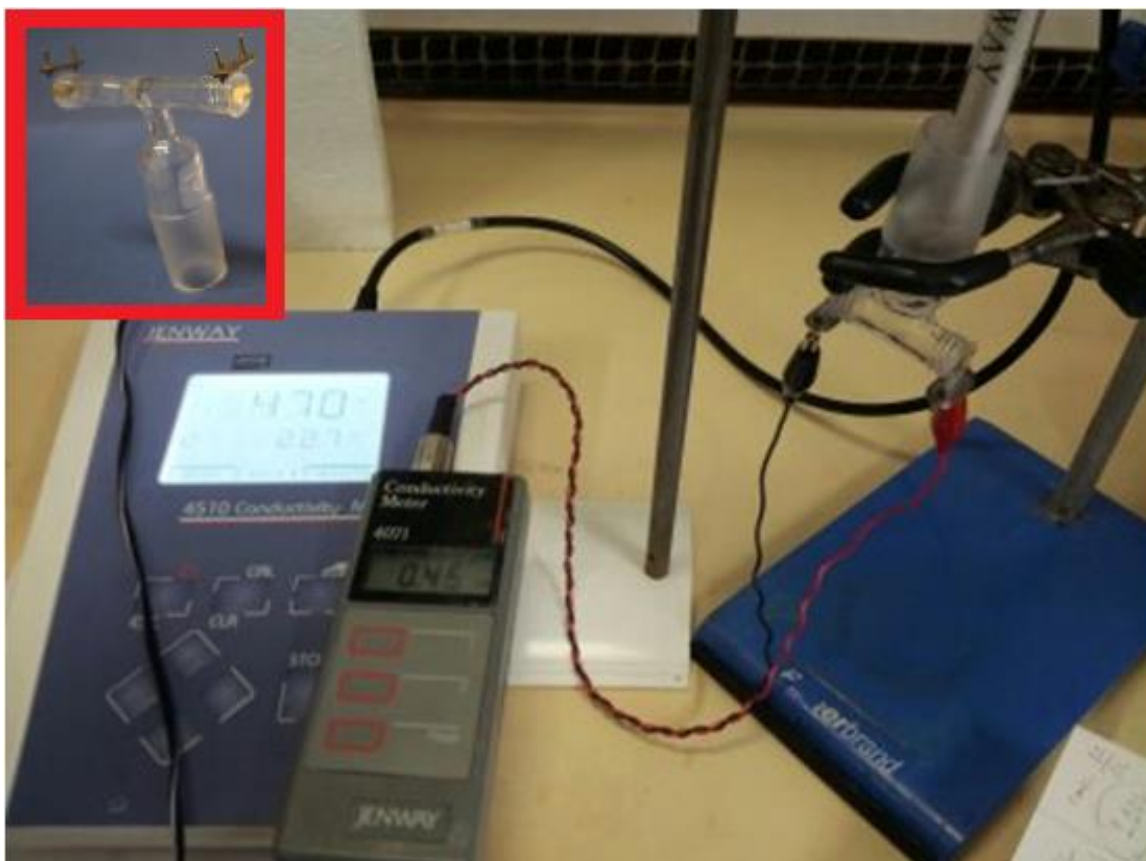
Figure 5.22: A quartz crystal cell designed for measuring viscosity and conductivity of DESs electrolyte. Inset: earlier designed cell.

The cell, shown in Figure 5.22, was used for wide range of conductivity measured with conductivity meter and compared with classical conductivity meter probe: there was maximum 3% difference in conductivity between two methods. Indeed, the QCM itself was used to measure conductivity by surface of a QCM which was in contact with a liquid and the parallel resonant frequency was influenced by liquid conductivity.[30, 75-77] A new cell could be designed for measuring multiple physical purposes by means of the QCM.

5.3. Conclusions

The viscosity of DESs across the temperature range of 25 °C to 80 °C were determined by using two techniques: QCM and RV. The general result is that these two techniques give the same answer over certain temperature ranges and they give significantly

different answers at other temperature ranges. The question is whether the origin of those differences an instrumental problem or is it the fact that two techniques measure different things representing the physical chemistry of the liquids.

Quartz crystal impedance analysis was for the first time used to determine whether ILs are a Newtonian fluid or not over wide range of temperature and/or how viscosity of ILs could change its manner form/to the Newtonian or non-Newtonian with changing temperature. Since QCM data can be used to calculate the viscosity of the Newtonian liquids, the value of $\Delta f/\Delta B$ should be calculated. When the slope of $\Delta f/\Delta B$ is -0.5, the liquid behaves in the Newtonian manner. The deviation of $\Delta f/\Delta B$ from -0.5 is the indicator of a non-Newtonian liquid.

The viscosity of a DES calculated from QCM data was similar to viscosity measured by RV at the temperature range of the DES, in which the slope of $\Delta f/\Delta B$ was close to -0.5. Values of viscosity demonstrated good agreement with standard measurement techniques (RV) at the temperature ranges where the DESs are Newtonian. The summary of results is given in Table 5.11.

	Ethaline				Glyceline				Reline			
T / °C	25 °C		90 °C		25 °C		80 °C		25 °C		90 °C	
Techniques	RV	QCM	RV	QCM	RV	QCM	RV	QCM	RV	QCM	RV	QCM
η/cP	43.7	45.2	11.2	7.10	334	256	30.2	26.3	969	727	25.1	23.5
$\Delta f/\Delta B$ Slope	-0.54		-0.65		-0.31		-0.47		-0.36		-0.46	

Table 5.11: Summary of viscosity results given in this chapter. $\Delta f/\Delta B$ is for low temperatures between 25 °C – 40 °C and for high temperatures between 60 °C – 90 °C, but high temperature of Glyceline is between 60 °C – 80 °C. When the slope of $\Delta f/\Delta B$ approaches to -0.5, viscosities obtained from QCM close to the viscosities measured by RV.

Actually the first aim of this work was to measure the viscosity of DESs (ILs) over a wide range of temperature by means of the QCM. However, the results showed that the viscosity of ILs could not be measured with the QCM because of temperature dependant Newtonian behaviour of DESs. Experimental set-up was considered as problematic for ages but indeed the "problem" was the liquid itself. Ethaline, having the Newtonian behaviour at low temperatures (25 °C – 40 °C), becomes non-Newtonian liquid with increasing temperature and therefore viscosity of Ethaline calculated from the QCM were similar to viscosity measured with RV at low temperatures but very different than RV at higher temperatures. However, Reline and Glyceline showed non-Newtonian behaviour at low temperatures and behaved in the Newtonian manner at high temperatures (60 °C – 80 °C) and viscosity data of QCM were close to viscosity data of RV at high temperatures.

The activation energy of viscous flow of DESs, calculated from QCM data, were identical to the activation energy of viscosity obtained from RV data at the temperature range the QCM identified as Newtonian. Viscosity of DESs does not obey Arrhenius-like behaviour for wide range of temperature (from 25 °C to 90 °C). However, it can obey Arrhenius-like equation for part ranges of temperatures at low or high temperatures.

The QCM is a diagnostic technique which can be used to decide whether or not the liquid is Newtonian. After the range of temperature in which the liquids are Newtonian, is determined, the activation energy for viscous flow can easily be calculated for this range of temperature.

The viscosity agreement between RV and QCM, in which the behaviour of liquid is Newtonian at the range of temperature, can open a new door to test the range of temperature at which ILs could have Newtonian response and measure viscosity of ILs at these temperatures.

5.4. References

1 T. L. Greaves and C. J. Drummond, *Chem. Soc. Rev.,* 2013, **42**, 1096-1120.

2 P. Huang, J. Latham, D. R. MacFarlane, P. C. Howlett and M. Forsyth, *Electrochim. Acta,* 2013, **110**, 501-510.

3 Z. Lei, C. Dai and B. Chen, *Chem. Rev.,* 2013, **114**, 1289-1326.

4 C. Maton, N. De Vos and C. V. Stevens, *Chem. Soc. Rev.,* 2013, **42**, 5963-5977.

5 A. E. Somers, P. C. Howlett, D. R. MacFarlane and M. Forsyth, *Lubricants,* 2013, **1**, 3-21.

6 J. Yuan, D. Mecerreyes and M. Antonietti, *Progress in Polymer Science,* 2013, **38**, 1009-1036.

7 M. Freemantle, *An introduction to ionic liquids*, RSC Publishing, Cambridge, 2010.

8 G. McHale, C. Hardacre, R. Ge, N. Doy, R. W. Allen, J. M. MacInnes, M. R. Bown and M. I. Newton, *Anal. Chem.,* 2008, **80**, 5806-5811.

9 N. Doy, G. McHale, M. I. Newton, C. Hardacre, R. Ge, J. MacInnes, D. Kuvshinov and R. Allen, *Biomicrofluidics,* 2010, **4**, 014107.

10 Z. Parlak, C. Biet and S. Zauscher, *Measurement Science and Technology,* 2013, **24**, 085301.

11 M. Moreno, M. Montanino, M. Carewska, G. Appetecchi, S. Jeremias and S. Passerini, *Electrochim. Acta,* 2013, **99**, 108-116.

12 H. Zhao and G. A. Baker, *Journal of Chemical Technology and Biotechnology,* 2013, **88**, 3-12.

13 A. M. O. Azevedo, D. M. G. Ribeiro, P. C. A. G. Pinto, M. Lúcio, S. Reis and M. L. M. F. S. Saraiva, *Int. J. Pharm.,* 2013, **443**, 273-278 .

14 N. Ferlin, M. Courty, S. Gatard, M. Spulak, B. Quilty, I. Beadham, M. Ghavre, A. Haiß, K. Kümmerer and N. Gathergood, *Tetrahedron,* 2013, **69**, 6150-6161.

15 E. B. Fox, A. E. Visser, N. J. Bridges and J. W. Amoroso, *Energy Fuels,* 2013, **27**, 3385-3393.

16 L. Demarconnay, E. Calvo, L. Timperman, M. Anouti, D. Lemordant, E. Raymundo-Piñero, A. Arenillas, J. Menéndez and F. Béguin, *Electrochim. Acta,* 2013, **108**, 361-368.

17 M. Zalas, M. Walkowiak, B. Gierczyk, M. Osińska-Broniarz, P. Półrolniczak and G. Schroeder, *Electrochim. Acta,* 2013, **108**, 736-740.

18 A. P. Abbott, E. I. Ahmed, R. C. Harris and K. S. Ryder, *Green Chem.,* 2014, **16**, 4156-4161.

19 A. P. Abbott, G. Capper, D. L. Davies, R. K. Rasheed and V. Tambyrajah, *Chemical Communications,* 2003, **1**, 70-71.

20 E. L. Smith, A. P. Abbott and K. S. Ryder, *Chem. Rev.,* 2014, **114**, 11060-11082.

21 Brookfield Engineering Laboratories, **21.12.2014** (DOI:http://www.viscometers.org/PDF/Downloads/More%20Solutions.pdf).

22 G. Sauerbrey, *Zeitschrift für Physik,* 1959, **155**, 206-222.

23 T. Nomura and M. Okuhara, *Anal. Chim. Acta,* 1982, **142**, 281-284.

24 A. R. Hillman, *Journal of Solid State Electrochemistry,* 2011, **15**, 1647-1660.

25 C. Lee, Y. Tsai and C. Chen, *Electrochim. Acta,* 2013, **104**, 185-190.

26 S. J. Martin, G. C. Frye and K. O. Wessendorf, *Sensors and Actuators A: Physical,* 1994, **44**, 209-218

27 J. Auge, P. Hauptmann, J. Hartmann, S. Rösler and R. Lucklum, *Sensors Actuators B: Chem.,* 1995, **24**, 43-48.

28 R. Thalhammer, S. Braun, B. Devcic-Kuhar, M. Groschl, F. Trampler, E. Benes, H. Nowotny and P. Kostal, *Ultrasonics, Ferroelectrics and Frequency Control, IEEE Transactions on,* 1998, **45**, 1331-1340.

29 H. Nowotny and E. Benes, *J. Acoust. Soc. Am.,* 1987, **82**, 513-521.

30 M. Rodahl, F. Höök and B. Kasemo, *Anal. Chem.,* 1996, **68**, 2219-2227.

31 F. Herrmann, D. Hahn and S. Büttgenbach, *Sensors and Actuators A: Physical,* 1999, **78**, 99-107.

32 K. K. Kanazawa and J. G. Gordon, *Anal. Chem.,* 1985, **57**, 1770-1771.

33 Z. Lin and M. D. Ward, *Anal. Chem.,* 1996, **68**, 1285-1291.

34 A. R. Hillman, I. Efimov and K. S. Ryder, *J. Am. Chem. Soc.,* 2005, **127**, 16611-16620.

35 V. Gruia, A. Ispas, M. Wilke, I. Efimov and A. Bund, *Electrochim. Acta,* 2014, **118**, 88-91.

36 R. Lucklum and P. Hauptmann, *Sensors Actuators B: Chem.,* 2000, **70**, 30-36.

37 A. R. Hillman, M. A. Mohamoud and I. Efimov, *Anal. Chem.,* 2011, **83**, 5696-5707.

38 F. Eichelbaum, R. Borngräber, J. Schröder, R. Lucklum and P. Hauptmann, *Rev. Sci. Instrum.,* 1999, **70**, 2537-2545.

39 H. L. Bandey, S. J. Martin, R. W. Cernosek and A. R. Hillman, *Anal. Chem.,* 1999, **71**, 2205-2214.

40 R. W. Cernosek, S. J. Martin, A. R. Hillman and H. L. Bandey, *Ultrasonics, Ferroelectrics and Frequency Control, IEEE Transactions on,* 1998, **45**, 1399-1407.

41 J. Kuntner, G. Stangl and B. Jakoby, 2003, **2**, 956-960.

42 N. Cho, J. N. D'Amour, J. Stalgren, W. Knoll, K. Kanazawa and C. W. Frank, *J. Colloid Interface Sci.,* 2007, **315**, 248-254.

43 A. Saluja and D. S. Kalonia, *Aaps Pharmscitech,* 2004, **5**, 68-81.

44 N. Doy, G. McHale, M. I. Newton, C. Hardacre, R. Ge, R. Allen and J. MacInnes, *Frequency Control Symposium, Joint with the 22nd European Frequency and Time forum. IEEE International. IEEE,* 2009, 1043-1045.

45 D. Wei and A. Ivaska, *Anal. Chim. Acta,* 2008, **607**, 126-135

46 K. Keiji Kanazawa and J. G. Gordon II, *Anal. Chim. Acta,* 1985, **175**, 99-105.

47 S. Goel, P. Venkateswaran, R. Prajesh and A. Agarwal, *Fuel,* 2015, **139**, 213-219.

48 A. P. Abbott, R. C. Harris and K. S. Ryder, *The Journal of Physical Chemistry B,* 2007, **111**, 4910-4913.

49 Y. Ju, C. Lien, K. Chang, C. Hu and D. S. Wong, *J. Chin. Chem. Soc.,* 2012, **59**, 1280-1287.

50 A. P. Abbott, R. C. Harris, K. S. Ryder, C. D'Agostino, L. F. Gladden and M. D. Mantle, *Green Chem.,* 2011, **13**, 82-90.

51 D. Johannsmann, *J. Appl. Phys.,* 2001, **89**, 6356-6364.

52 J. Restolho, A. P. Serro, J. L. Mata and B. Saramago, *Journal of Chemical & Engineering Data,* 2009, **54**, 950-955.

53 A. Yadav and S. Pandey, *Journal of Chemical & Engineering Data,* 2014, **59**, 2221-2229.

54 R. Fürth, *Math.Proc.Cambridge,* 1941 **37**, 252-275.

55 J. Bockris and G. Hooper, *Discuss. Faraday Soc.,* 1961, **32**, 218-236.

56 A. P. Abbott, J. C. Barron, K. S. Ryder and D. Wilson, *Chemistry-A European Journal,* 2007, **13**, 6495-6501.

57 A. P. Fröba, H. Kremer and A. Leipertz, *The Journal of Physical Chemistry B,* 2008, **112**, 12420-12430.

58 S. Magazù, F. Migliardo, N. P. Malomuzh and I. V. Blazhnov, *The Journal of Physical Chemistry B,* 2007, **111**, 9563-9570.

59 W. Xu, E. I. Cooper and C. A. Angell, *The Journal of Physical Chemistry B,* 2003, **107**, 6170-6178.

60 A. Noda, K. Hayamizu and M. Watanabe, *The Journal of Physical Chemistry B,* 2001, **105**, 4603-4610.

61 J. S. Wilkes, *Journal of Molecular Catalysis A: Chemical,* 2004, **214**, 11-17

62 H. Vogel, *Phys.Z,* 1921, **22**, 645-646.

63 G. S. Fulcher, *J Am Ceram Soc,* 1925, **8**, 339-355.

64 G. Tammann and W. Hesse, *Z.Anorg.Allg.Chem,* 1926, **156**, 245-257.

65 M. Gericke, K. Schlufter, T. Liebert, T. Heinze and T. Budtova, *Biomacromolecules,* 2009, **10**, 1188-1194.

66 O. Okoturo and T. VanderNoot, *J Electroanal Chem,* 2004, **568**, 167-181.

67 R. Toniolo, A. Pizzariello, N. Dossi, S. Lorenzon, O. Abollino and G. Bontempelli, *Anal. Chem.,* 2013, **85**, 7241-7247.

68 A. Yadav, S. Trivedi, R. Rai and S. Pandey, *Fluid Phase Equilib.,* 2014, **367**, 135-142

69 A. P. Abbott, G. Capper and S. Gray, *ChemPhysChem,* 2006, **7**, 803-806.

70 J. G. Huddleston, A. E. Visser, W. M. Reichert, H. D. Willauer, G. A. Broker and R. D. Rogers, *Green Chem.,* 2001, **3**, 156-164.

71 Y. Xie, H. Dong, S. Zhang, X. Lu and X. Ji, *Journal of Chemical & Engineering Data,* 2014, **11**, 3344-3352.

72 D. Shah and F. S. Mjalli, *Physical Chemistry Chemical Physics,* 2014, **16**, 23900-23907.

73 O. Ciocirlan, O. Iulian and O. Croitoru, *Rev Chim (Bucharest),* 2010, **8**, 721-723.

74 K. R. Seddon, A. Stark and M. Torres, *Pure and Applied Chemistry,* 2000, **72**, 2275-2287.

75 M. Yang and M. Thompson, *Anal. Chem.,* 1993, **65**, 1158-1168.

76 Z. A. Shana and F. Josse, *Anal. Chem.,* 1994, **66**, 1955-1964.

77 G. C. Dunham, N. H. Benson, D. Petelenz and J. Janata, *Anal. Chem.,* 1995, **67**, 267-272.

Chapter 6: Optimization of Polyaniline Ion Exchange Dynamics in Deep Eutectic Solvents for Supercapacitor Applications

6.1. Introduction

6.1.1. Overview

The development of polymers from chemically modified natural materials (rubber, nitrocellulose) to completely synthetic molecules (polyethylene, polypropylene) continues with conducting polymers. Charles Goodyear was the inventor and developer of the process of vulcanisation (mixing sulphur with heated natural rubber) in 1839. To make rubber harder, more durable and less soluble he tailored natural rubber with additives for manufacturing processes and he tried to make everything in daily life with natural rubber (elastic hydrocarbon polymer). In the 20th century, the discovery of plastic has displaced many traditional materials including leather, paper, metal, glass, ceramic, wood and stone. Therefore, polymers could have a wide application area with usage in automobiles, aerospace and household goods. However, there was a field where plastic could not replace the role of metals which was the electronic technology which relies on electrical conductivity. In 1977, the result of high conductivity in oxidized iodine-doped polyacetylene (conducting polymer)[1] promised to make Charles Goodyear's dream come true for modern days. It was time to use plastic in electronic technology.

Conducting polymers, as the main topic of this thesis, are of great interest in polymer science due to their interesting structure and chemical nature[2-5] as discussed in chapter one. Oxidation of conducting polymers can be easily controlled by applying voltage and their redox processes, involving the intercalation of anions or cations during charging/discharging, can be used to switch properties of conducting polymers such as optical, electrical, electrochemical, magnetic or mechanical properties.

The properties of conducting (π-conjugated) polymers have been studied for numerous novel technological devices such as organic light-emitting diodes,[6] organic photodetectors,[7] organic solar cells,[8, 9] organic thin film transistors[10] sensor devices,[11] electrochromic devices,[12] water treatment[13] (see chapter seven of this thesis), corrosion inhibitors,[14] actuators[15] and electromagnetic interference shielding.[16] Conducting polymers can also be a good candidate to be used in energy

storage/conversion devices.[17, 18] In this chapter polyaniline (PANI) films, which were grown potentiodynamically and were studied in chapter four, will be transferred to a novel medium for the investigation of energy storage purposes.

Energy is an important issue at present due to the probable energy crisis and environmental issues. Researchers avoid using fossil fuels and their attention has turned to renewable and clean energy. Additionally, energy storage has received significant attention for portable devices and hybrid electrical vehicles recently. While fuel cell devices and batteries have typical low specific power, conventional capacitors have high specific power. Supercapacitors can provide higher energy density than conventional dielectric capacitors, close to batteries and higher power density than batteries as high as conventional capacitors.[19, 20] Therefore supercapacitors can be a bridge between batteries and conventional capacitors as explained by Ragone plots.[21]

There are two types of supercapacitors: electric double-layer capacitors (EDLC) and pseudocapacitors. While pseudocapacitors involve a faradaic process, EDLC store charge at the electrode/electrolyte interface. Carbon based materials (activated carbon, carbon fibres, carbon aerogels) are used for EDLC. Metal oxides/hydroxides and conducting polymers are a family of materials used in pseudocapacitors. While some metal oxides, with high specific capacitances (ruthenium oxide),[22] have high cost; other metal oxides made of inexpensive materials have low specific capacitance.[23] Conducting polymers have been studied recently for pseudocapacitor applications because of having high charge density, low cost[24] and ease of fabrication compared with metal/metal oxides. Therefore, conducting polymers can alternatively be used instead of metal/metal oxides in supercapacitor application.

The problem of the degradation of conducting polymers during cycling was attempted to be solved by preparing composite materials based on conducting polymers and additives, some of which are poly(3,4-ethylenedioxythiophene)/carbon nanotubes (CNTs),[25] PPy/CNTs,[26] PANI-CNT,[27] PANI-graphene oxide.[28] In addition, PPy-Graphite oxide,[29] PPy-Graphene,[30] PEDOT/Graphene,[31] PPy/Graphene/CNT ternary composite systems[32] have been extensively applied to improve the performance of supercapacitors and exhibiting a large surface area of devices. PANI derivative (poly *o*-

toluidine) was used to enhance the electrochemical capacitance.[33] A comparative study of a composite of graphene-PANI derivatives (methoxyaniline, methylaniline with graphene) was prepared for supercapacitor application.[34] All combinations of these experiments were designed to improve the capacitance performance (with large surface areas of devices), providing higher cycling stability.

Nowadays the research related to supercapacitors is not only focused on increasing the performance but also changing the physical properties of conducting polymer based supercapacitors (multifunctional properties). Flexible PANI-graphene composite paper[35] and a nylon Lycra fabric coated with PPy[36] were produced for supercapacitor applications. In addition, the integration of supercapacitor and electrochromic properties is also combined in a flexible device using PANI.[37]

PANI, amongst other conducting polymers, has received significant attention in supercapacitor applications due to its environmental stability and higher theoretical capacitance performance in comparison with other conducting polymers.[38] The polymerisation methods of PANI and its derivatives were given in chapter four.

Most of the studies on supercapacitors focus on the deposition and cycling of the electrode process explained in previous paragraphs. As commonly known, all devices based on electrochemistry consist of two main parts: electrodes (anode, cathode) and electrolyte (material between electrodes). The study of the electrolyte for supercapacitor applications has not received as much attention to date as the electrodes. As the concept of environmental sustainability is required, ionic liquids are expected to be a good electrolyte candidate for future energy storage devices.[39] Ionic liquid electrolyte is widely studied for electric double layer capacitors.[40, 41] However, in the literature there are limited studies about ionic liquid electrolytes in conducting polymer based supercapacitors.[42, 43] Therefore, more scientific research related to ionic liquid electrolyte in pseudocapacitors, should be performed.

In this chapter, the combination of a novel electrolyte (DESs) (chapter five) with PANI modified electrodes (chapter four) will be presented. This work will shed some lights on supercapacitor based conducting polymers and DESs. The focus points of most of

the studies conducted to date are related to increasing the performance, stability and processability of supercapacitors. They have not given a significant attention to understanding the ion exchange dynamics during faradaic reaction of pseudocapacitance which is the main goal of this chapter.

6.1.2.   Aims and Objectives

In this work, the first objective was the determination whether PANI film has a redox reaction in DESs. After observing the redox reaction of PANI film in DESs, the next step was the exploration of repetitive cycling with the effect of surface coverage. The second objective was the identification of rate limiting processes for the PANI films having different surface coverages and grown under different conditions.

The third objective of this work, indeed the main aim of the work, was to understand the ion dynamics during charging/discharging of PANI films in DES media. In this case, the objective of this work included the determination of how the individual contributions of cations and anions (ion fractions), in maintaining the electroneutrality throughout redox switching, depends upon timescale (by changing potential scan rate), physical properties of the film (thickness, growth conditions). The fourth objective was the determination of electrolyte composition by changing components of DESs and the temperature of the electrolyte.

The fifth objective, more related to supercapacitor engineering, was the examination of capacitance performance and stability of PANI films in DES medium in terms of applying voltage and under open-circuit conditions. Since cold weather could be a problem for application using ionic liquid causing solidification of electrolyte in the case of energy storage devices, the last objective was electrochemical characterisation of PANI films in the form of the crystallisation of DESs to ascertain whether extended redox cycling leads to deterioration of PANI capacitance performances.

To achieve some of these objectives, in which the EQCM measurements were conducted, the response of acoustic resonator should be gravimetrically controlled.

Therefore, a pre-requisite measurement is to establish to the measurement mass using the Sauerbrey Equation.[44]

6.2. Results

6.2.1. Film Preparation

PANI can be deposited by electrochemical polymerisation from monomer solution in an aqueous acidic medium onto a conducting substrate. The typical experimental data obtained from the EQCM for electrochemical deposition of PANI films from 0.1 M aniline and 1 M H_2SO_4 were given in section 4.2.3. Therefore, EQCM data for the growth of PANI films are not shown in this chapter. However, the growth conditions of the films used in this chapter are given in Table 6.1.

Table 6.1: Experimental conditions for the deposition of PANI films used in this chapter.

Film name	Potential Window V	Scan rate v / mV s^{-1}	Number of scans	Coverage Γ / nmol cm^{-2}
Film A	-0.2 to 0.95	100	15	72
Film B	-0.2 to 0.95	100	12	35
Film C	-0.2 to 0.95	100	10	13
Film D	-0.2 to 0.95	50	7	46
Film E	-0.2 to 0.95	50	6	31
Film F	-0.2 to 0.95	10	3	386
Film G	-0.2 to 0.95	10	2	41
Film H	-0.2 to 0.9	10	5	354
Film I	-0.2 to 0.9	5	2	54

The polymerisation was driven by applying voltage from -0.2 V to 0.9 V (or 0.95 V) *vs.* Ag/AgCl (sat. KCl), for various cycles (2 - 15 cycles) at various scan rates (5 mV s^{-1} - 100 mV s^{-1}) as shown in Table 6.1 and in the experimental procedures of polymer growth in chapter three. The effect of scan rate, potential window and the number of scans during PANI growth and calculation of surface coverage of PANI were given in section

4.2.3.1. After the films were deposited onto 10 MHz AT-cut Au polished quartz crystal, the growth of the films was stopped at the reduced end of the potential cycle (E = -0.2 V) and the film was then rinsed with deionised water. Subsequently, the freshly prepared films were transferred into DES electrolyte to explore PANI p-doping dynamics at various scan rates applying voltage from 0 V (or 0.2 V) to 0.6 V (*vs.* Ag wire as all PANI film potentials cycling in DESs given in this chapter with respect to Ag wire). Prior to transferring PANI from aqueous acidic (deposition) solution to DESs, the films were washed with deionised water and rinsed several times (typically six-seven) with the hot DESs under investigation to try to remove aqueous solution from the voids of PANI films.

6.2.2. PANI Redox Cycling in Ethaline (Choline Chloride + Ethylene Glycol)

The films, transferred into DES electrolyte, were analysed by ion-exchange during redox switching by means of EQCM. In this section, PANI films will be cycled in Ethaline at various scan rates, potential windows and temperatures. Following that, in section 6.2.3, PANI cycling in different DESs (Reline, Propaline, Glyceline and Wateline), will be analysed.

Prior to measuring mass changing during electrochemical experiments, admittance spectra were used to establish whether the film was acoustically thin (rigid) to enable use of the Sauerbrey equation for gravimetric analysis. Here, acoustic admittance for film F, which had the highest surface coverage among films used in this chapter, is shown as an example in Figure 6.1.
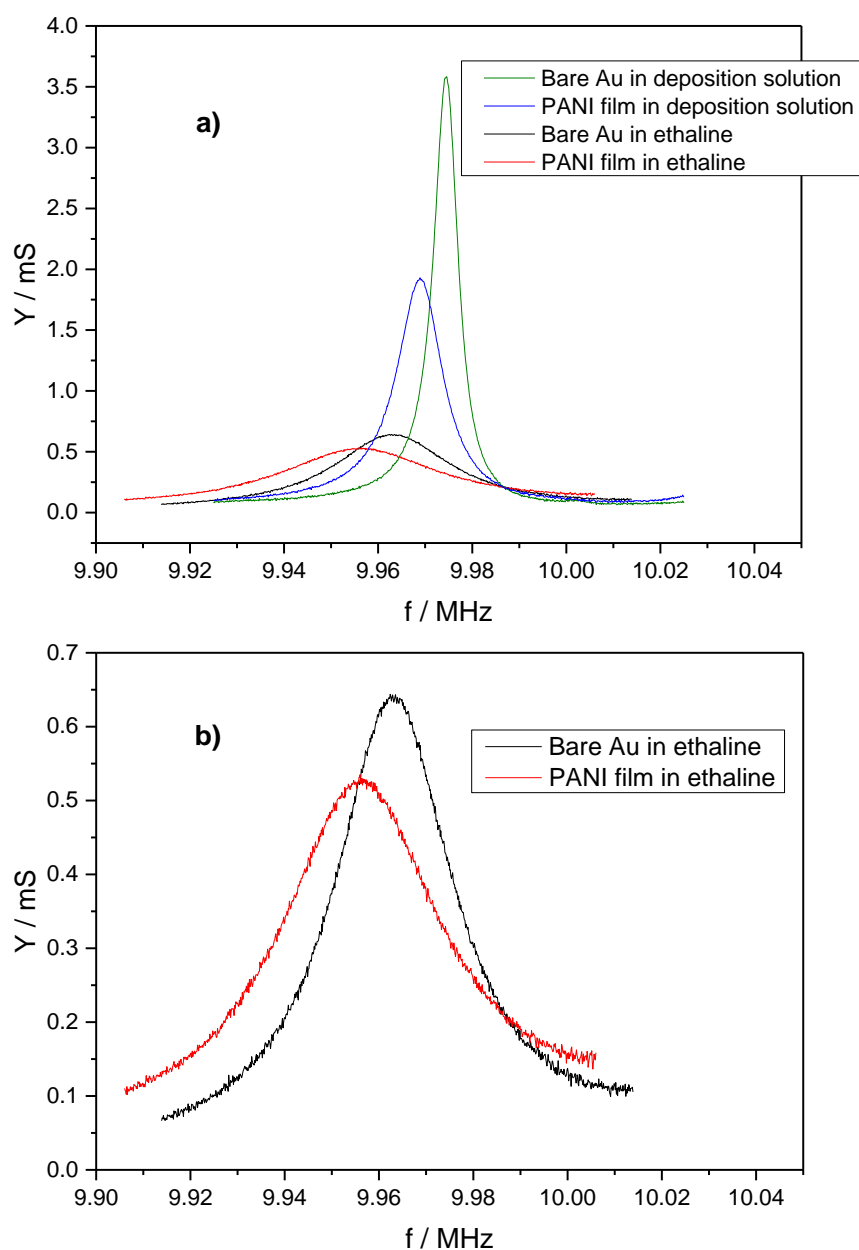
Figure 6.1: Acoustic admittance spectra for: a) bare crystal in deposition electrolyte (0.1 M aniline + 1 M H_2SO_4 aqueous solution) before growth (green line); PANI loaded crystal in deposition electrolyte after growth (blue line); bare crystal in Ethaline (black line); PANI loaded crystal in Ethaline (red line); b) crystal just in Ethaline before and after growth. The results are for film F (Γ = 386 nmol cm^{-2}) the thickest film used in this chapter.

Panel a of Figure 6.1 shows the admittance spectra for the quartz resonator of film F before and after growth in the deposition solution and in Ethaline. There is a shift to lower resonant frequency and lower admittance. The admittance of the unloaded quartz resonator in aqueous electrolyte was 3.58 mS and after deposition it had

dropped to 1.93 mS. The admittance peak decreased 46% in deposition solution and the damping associated with growth in the system is substantial. Normally, 20% decrease in admittance was allowed to use the Sauerbrey equation as presented in chapter four. Therefore, the film growth shown in panel a of Figure 6.1 has the characteristic of an acoustically thick (simplistically "non-rigid") film, for which the EQCM response is viscoelastically interpretable (discussed in chapter two). The characterisation of viscoelastic properties of PANI was studied in aqueous solution previously.[45-47] Here, admittance spectra in Ethaline should be considered when PANI film, throughout redox switching, is studied in Ethaline. Panel b of Figure 6.1 shows that the admittance of the unloaded quartz resonator in Ethaline was 643 μS and after deposition, when transferred to Ethaline, it was 535 μS. It is observed that there is a small decrease in admittance (17%) verifying that the film is acoustically thin in Ethaline. The dissipation of acoustic energy in PANI film in Ethaline is sufficiently low due to higher viscosity of Ethaline as given in chapter five. The frequency shift during redox switching of PANI in Ethaline can be converted to the mass change using the Sauerbrey equation given in chapter two. Panel b of Figure 6.1 shows the result for PANI film, having the highest coverage (Γ = 386 nmol cm^{-2}), is rigid. Therefore, all other PANI films, having less coverage than film F, studied in this chapter, given in Table 6.1, are also rigid, hence not essential to present their admittance spectra in this thesis.

6.2.2.1.   Effect of Numbers of Scan

As indicated in previous sections, the stoichiometry between choline chloride (Ch$^+$Cl$^-$) and ethylene glycol (EG), formed Ethaline, is 1:2. As a chloride anion is coordinated by the hydrogen bond donor (HBD),[48] the ionic species in Ethaline can be shown as EG$_2$Cl$^-$ and Ch$^+$. Indeed there are some other EG ligands in Ethaline but the equilibrium is between Ch$^+$ and EG$_2$Cl$^-$. In this thesis movement ions are consider as Ch$^+$ and EG$_2$Cl$^-$. Figure 6.2 shows current and mass responses of PANI film (film E) cycled in Ethaline at room conditions.

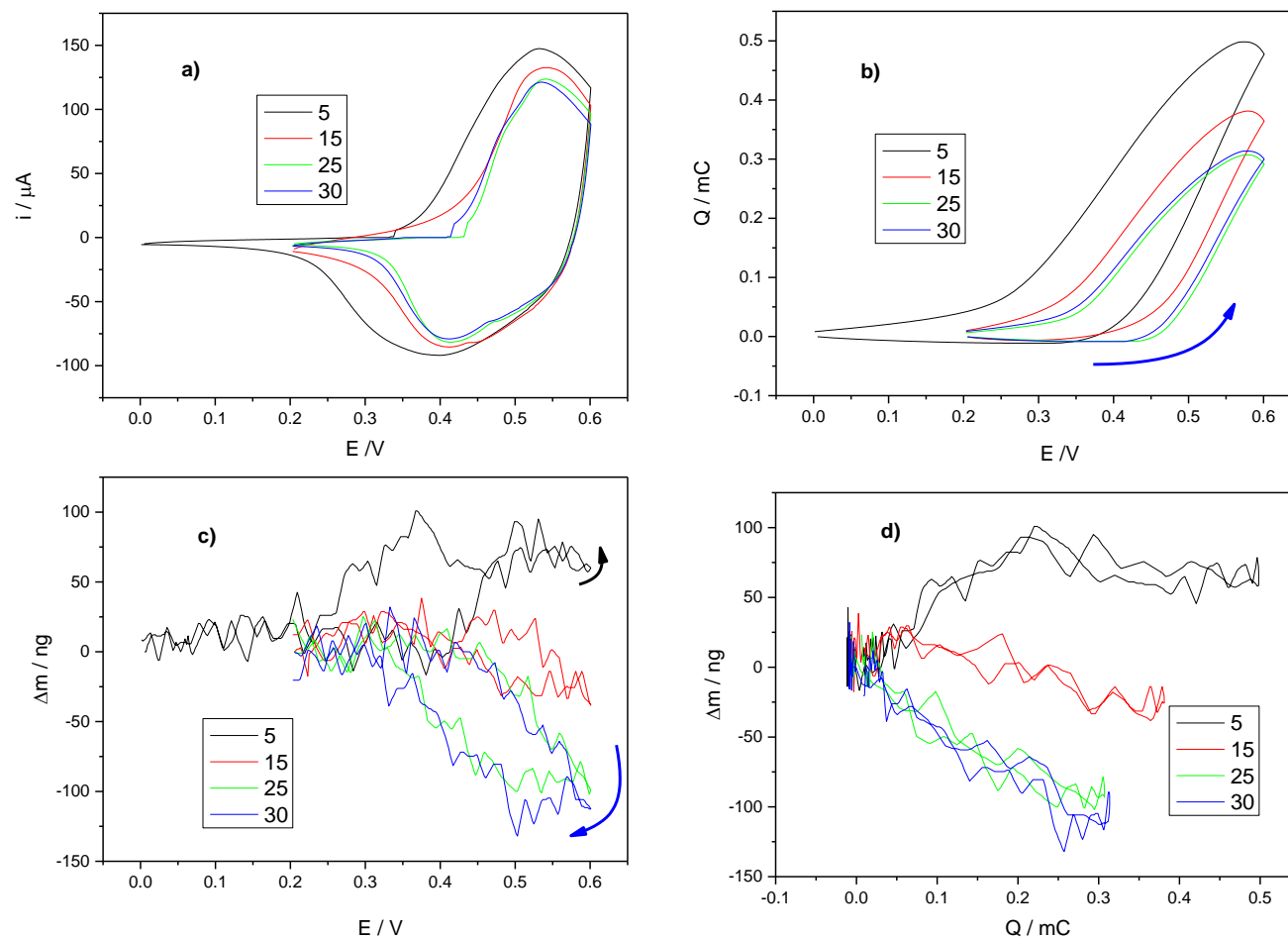*Figure 6.2: EQCM data for redox switching of film E (Γ = 31 nmol cm^{-2}) exposed to Ethaline. v = 50 mV s^{-1}. a) current; b) charge and; c) mass change responses; d) Δm vs. Q responses. The numbers indicate the scan numbers. Film mass changes calculated using Sauerbrey Equation given in chapter two. The arrows indicate the direction of the changes.*

Panel c of Figure 6.2 shows that the mass of PANI film increases upon the film oxidation at 5th scan suggesting that anions are incorporated into the film for the maintenance of electroneutrality. It is deduced that anion transfer dominates the redox switching process. The results of a typical EQCM experiment for a PANI film exposed to aqueous acidic medium (as given in section 4.2.4.6.1) showed that proton expulsion from the film (low molar mass) in the early stage of film oxidation and anion incorporation into the film (larger molar mass) in the latter stages. Therefore, the overall redox switching process of PANI in an aqueous acidic medium is dominated by anion transfer which is a well-known behaviour.[49-51] Overall mass changing of PANI in Ethaline in early cycles is similar to PANI cycling in aqueous acidic electrolyte which is anion dominated. However, mass direction of PANI, during redox switching in Ethaline, is changed to just cation dominated reaction with increasing number of scans observed after 15 scans illustrated in panel c of Figure 6.2. Evolution of mass change response is observed with increasing the number of scans. The evolution of ion transfer characteristics arises from the difference between the counter ion and polymer interaction. Cyclic voltammetry data of cycling PANI itself, given in panel a of Figure 6.2 cannot be a perfect indicator of PANI film equilibration with Ethaline as the *i-E* curves are identical. The molar mass (M_m) of the species exchanged during the redox cycling of PANI can be compared to monitor the evolution of the PANI films. M_m is defined as $F\Delta m/Q$, where F is the Faraday constant and Δm-Q is the slope of the mass change *vs.* charge plot presented in panel c of Figure 6.2.

The mass-charge graph for the 5th scan of the oxidation of PANI in Ethaline is different to other scans because PANI had not evolved yet. The end-to-end Δm-Q slopes are +11, -6.3, -30.2 and -31.2 g mol^{-1} for 5th, 15th, 25th and 30th scans, respectively (see Table 6.2). As Δm-Q of 25th and 30th film could not be evolved with just with few scans, the negative signs of M_m show that one of them (either charge or mass change) is opposite direction to another for redox cycling. The dominant ion in mass transport process was changed from Ch^+ ($M_m = +11$ g mol^{-1}) to EG_2Cl^- ($M_m = -32.1$ g mol^{-1}) which is known as the *memory effect* because the films were deposited from aqueous acidic medium and transferred to DESs medium.

The *memory effect*, after transfer of a PANI modified electrode from 1 M H_2SO_4 to Ethaline electrolyte, was studied for PANI films having different thickness explained in the next section. Quantitative analysis of the exchanging ions, in PANI exposed to Ethaline during electrochemical analysis, is also given in section 6.2.2.3 for evolved films. In this section, the effect of number of scans is presented. Figure 6.3 shows the long-term cycling performance of PANI film D exposed to Ethaline electrolyte applying voltage from 0 V to 0.6 V at a scan rate of 100 mV s^{-1} for over 30 000 cycles.

Table 6.2: Experimental end-to-end molar masses (M_m) for redox switching of PANI film E (Γ = 31 nmol cm^{-2}) in Ethaline. M_m values calculated from mass change and charge passed during potential sweep given in Figure 6.2. When the charge and mass changing are at the same direction, charge neutrality is dominated by anion transfer, shown with positive sign. Opposite of it is cation transfer and shown with negative sign.

Scan numbers	Molar mass / g mol^{-1}
5	11
15	-6
25	-30
30	-31

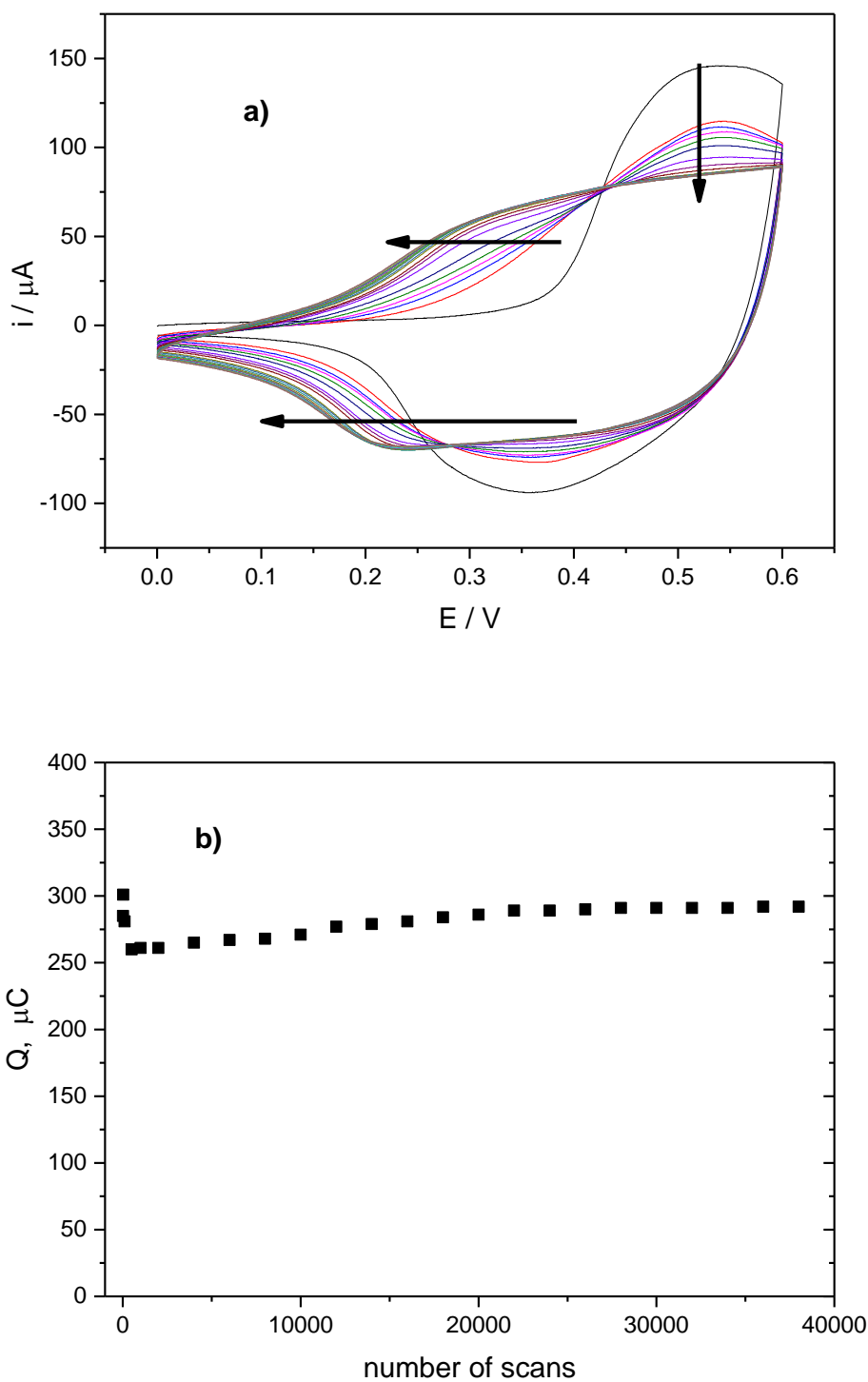*Figure 6.3: Cyclic voltammetry data of PANI film D (Γ = 46 nmol cm^{-2}) in Ethaline during long-term scanning, measured at 100 mV s^{-1}. Black curve shows 1st scan and the arrows indicate every 2000 scans up to 38 000th scan. b) Q vs. number of scans responses, charge is calculated from the integration of current response in panel a.*

The cyclic-life data of PANI showed large capacitance drop after 10 000 cycles with approximately 25% retention of its initial value,[6] thus researchers are interested to increase cyclic stability of conducting polymers[27, 52, 53] particularly with conducting polymer-nanocomposite structure,[54, 55] as explained in the introduction part of this chapter. For instance, the study of carbonaceous shell-coated PANI film reached capacitance retention of 85% after 10 000 cycles.[6] As panel b of Figure 6.3 indicates the PANI film itself (without any pre-treatment modification) in Ethaline has negligible loss of capacitance after 30 000 cycles indicating the excellent cyclic stability of PANI. This stability can be proven by cyclic voltammetry responses for film D, given in panel a of Figure 6.3, exposed to Ethaline for each 2000 scans up to 38 000 scan indicating the film is evolved and curve of cyclic voltammetry of PANI resemble to a constant curve gradually. The strategy here is not to apply a voltage to cause overoxidation. All experiments in this chapter are the responses of PANI films undergoing p-doping/undoping in Ethaline electrolyte not exceeding 0.6 V *vs.* Ag wire pseudo-reference electrode. Applying higher voltage (typically higher than 0.7 V) could cause deterioration of PANI[56] and reduce cycle stability dramatically as Mazeikine *et al.* indicated that the fully oxidised (pernigraniline) form of PANI causes fast degradation.[57]

Poor cycling stability of conducting polymers, in aqueous solution for long term cycling performance, is attributed to large volumetric swelling and shrinking during doping and de-doping reaction.[37, 38, 58] PANI films, cycled in Ethaline, could shrink/swell throughout redox switching shown in panel c of Figure 6.2 (also in next sections). Its electrochemical stability is shown to be much higher than the ones presented in the literature which suggest that the problem of instability of PANI films, after thousands of cycles, is not arisen from swelling and shrinking during redox cycling.

The specific capacitance, an important parameter to store an electrical charge in supercapacitors for 1st and $38\ 000^{th}$ cycles, are calculated to be 292 F g^{-1} to 253 F g^{-1}, respectively obtained at a scan rate of 100 mV s^{-1} (the calculation given in section 6.2.2.4 from Equ 6. 2). Despite the capacitance retentions of PANI in Ethaline were achieved to 97% after 30 000 cycles; our focus is not to increase the stability or

performance of conducting polymers in DESs, it is to analyse the dynamic of ion transfer processes of DESs qualitatively and quantitatively throughout redox switching of PANI films.

6.2.2.2. Effect of Surface Coverage

Figure 6.4 shows EQCM responses of 50th scan of PANI films, having different coverage, in Ethaline.

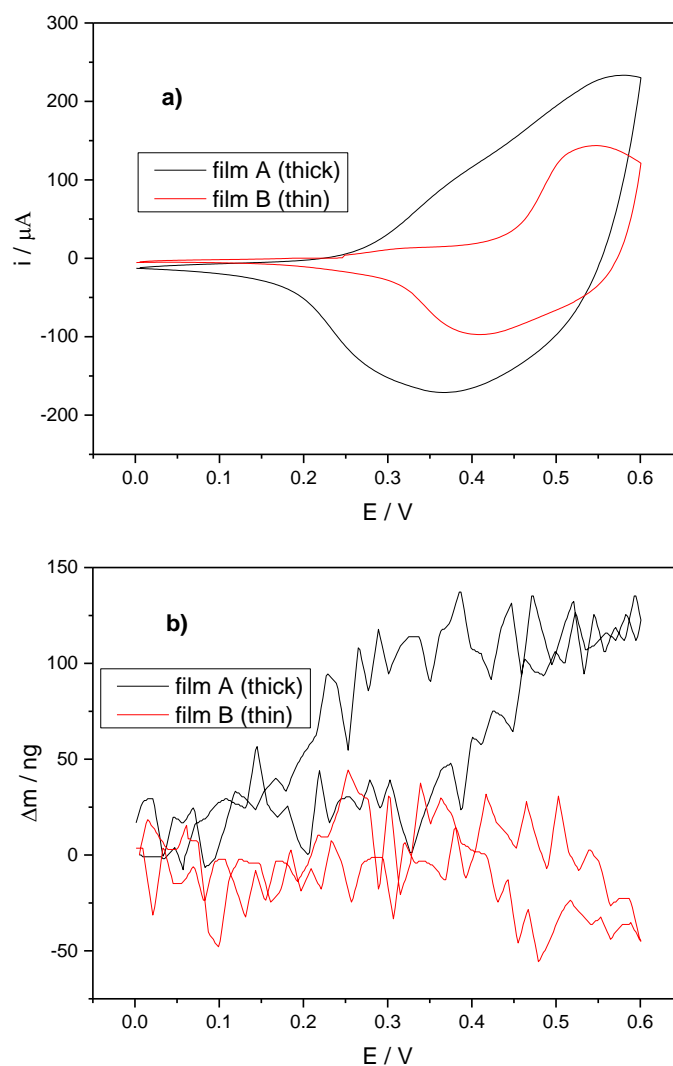*Figure 6.4: EQCM data for redox switching of PANI film A (Γ = 72 nmol cm^{-2}) (black line) and film B (Γ = 35 nmol cm^{-2}) (red line) PANI films exposed to Ethaline (v = 50 mV s^{-1}). Data are for the 50th voltammetric cycles; a) i vs. E; b) Δm vs. E.*

Panel a of Figure 6.4 shows current responses of PANI films undergoing redox switching upon exposure to Ethaline. Current peak of film having more surface coverage, shown with black line, is at more positive potential (at 0.58 V) than the film, having less coverage (at 0.54 V) due to the thickness of the film. For a much thicker film, shown in panel a of Figure 6.5, no oxidation peak was observed as it could not complete its oxidation until switching point. This is typical behaviour of conducting polymers that thicker films require more time to be fully oxidised, while thinner films can complete its p-doping transiently.[59]

Panel b of Figure 6.4 shows the mass changes of PANI films with different thickness corresponding to the voltammograms of panel a of Figure 6.4 for 50th voltammetric cycle. While mass direction of film B (Γ = 35 nmol cm^{-2}) was returned to cation domination, film A (Γ = 72 nmol cm^{-2}), deposited from the same conditions of film B for just more 3 scans, was still anion dominated reaction. PANI films were changed from anion domination reaction to cation domination reaction but the equilibration between PANI and Ethaline was slower for thicker films. The changing of ion domination (from anion to cation) is shown in Figure 6.5 for a much thicker film (Γ = 386 nmol cm^{-2}) (film F) than film A and film B.
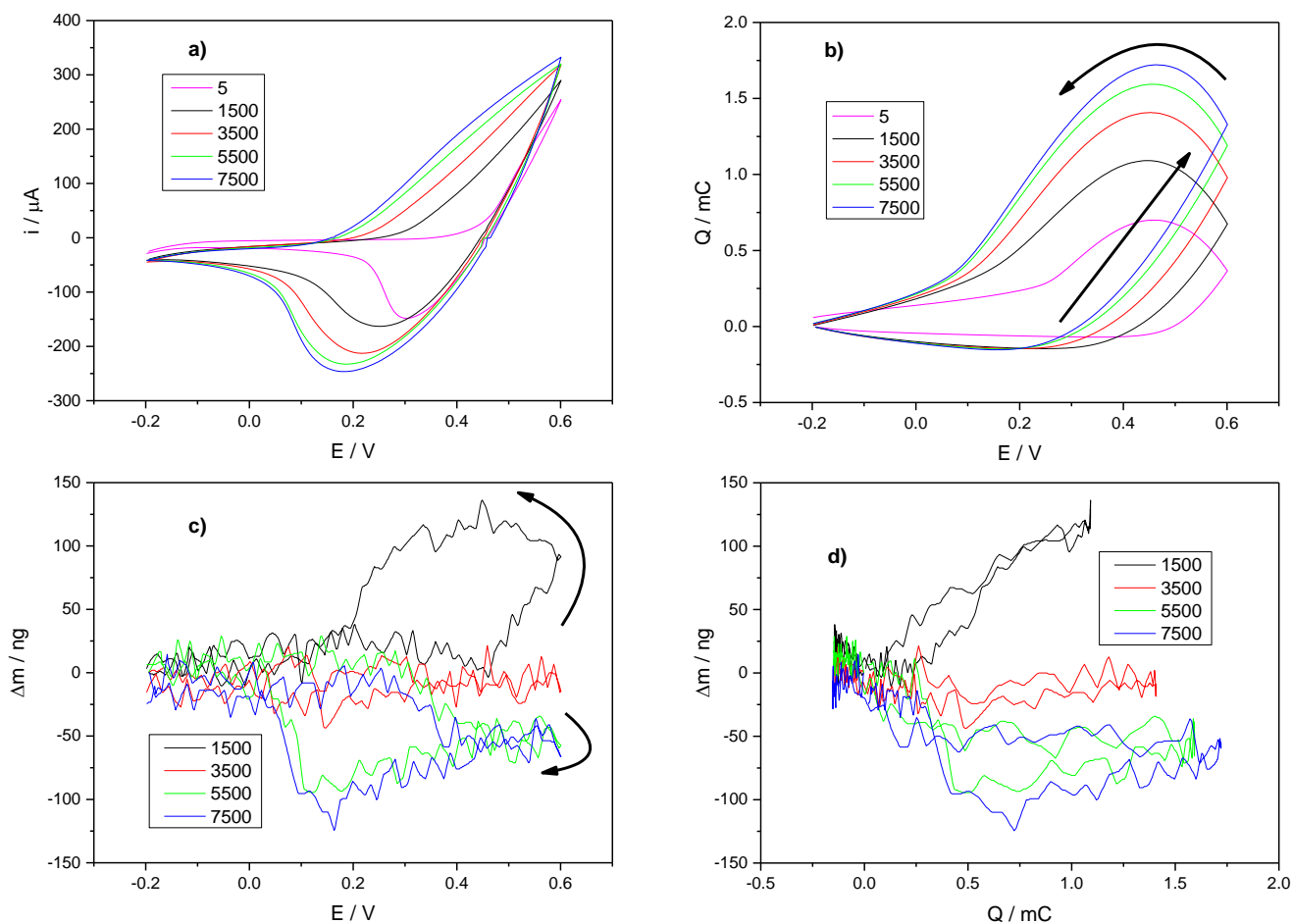
Figure 6.5: EQCM data for redox switching of a PANI film (Γ = 386 nmol cm^{-2}) (film F) exposed to Ethaline, v = 50 mVs^{-1}. a) i vs. E; b) Q vs. E c) Δm vs. E; d) Δm vs. Q where charge is calculated from the integration of current shown in panel a. Film mass changes calculated using Sauerbrey Equation in chapter 2. The arrows indicate the direction of changes.

Figure 6.5 shows the responses obtained during p-doping of PANI in Ethaline by cycling the voltage from -0.2 V to 0.6 V at a scan rate of 50 mV s^{-1} commencing with 5th scan and ending with 7500th scan and selected scans (1500th, 3500th and 5500th) are shown for clarity of presentation.

Panel c of Figure 6.5 shows a series of mass change vs. potential curves for selected potential scans. End-to-end Δm-Q slopes, calculated from panel d of Figure 6.5, are given in Table 6.3. The molar mass for ion exchange during the reaction can be a good indicator to show conducting polymer equilibrium with DESs. While the molar mass of the 1500th scan was 12.2 g mol^{-1} which is anion dominated, it approached a point that there was no mass changing during redox switching (3500th cycle in panel d of Figure 6.5): the mass of anion ingress and cation egress were the same for oxidation or there was no ingress/egress of the ions (explained in section 6.2.2.4). Indeed molar mass of EG$_2$Cl$^-$ (159.6 g mol^{-1}) and Ch$^+$ (104.2 g mol^{-1}) (consider as -104.2 because opposite direction to EG$_2$Cl$^-$) are not the same value; hence, the fraction of these ions is different when mass changing of them in opposite direction equal. Fraction calculation is given in section 6.2.2.4. Charge of the 7500th scan, given in panel b of Figure 6.5, is slightly higher than 5500th scan but molar mass of them are identical with approximately 4 g mol^{-1}. Therefore, as Δm–E curve evolves continuously with cycling, the evolution of this thick PANI film (Γ = 386 nmol cm^{-2}) (film F) persists for much longer time scales than thin films shown in Figure 6.3 and Figure 6.4. Indeed the gap between molar mass of Ch$^+$ and EG$_2$Cl$^-$ is very big (159.6 g mol^{-1} + 104.2 g mol^{-1} = 263.8 g mol^{-1}) therefore the fraction of ion exchange from the 1500th scan to 7500th scan (from 12 g mol^{-1} to -4 g mol^{-1}) are not excessive. However, there is still *memory effect* taking long duration when film F (Γ = 386 nmol cm^{-2}) is transferred from aqueous to Ethaline electrolyte. The fraction of cation and anion for PANI films are calculated in section 6.2.2.4.

Panel c of Figure 6.5 shows that the long-term cycling stability of film F was examined by cyclic voltammogram at a scan rate of 50 mV s^{-1}. The specific capacitance of the film F system (calculation from charge is given in section 6.2.2.4) gradually increased to

more than 100% over 7000 cycles which reveals this film has excellent long-term cyclic performance of the film.

Table 6.3: Experimental end-to-end molar masses (M_m) for redox switching of PANI (Γ = 386 nmol cm^{-2}) (film F) in Ethaline. M_m values calculated from mass change and charge passed during potential sweep given in Figure 6.5. When the charge and mass changing are at the same direction, charge neutrality is dominated by anion transfer, shown with positive sign. Opposite of it is cation transfer and shown with negative sign.

Scan numbers	Molar mass / g mol^{-1}
1500	12.2
3500	-0.5
5500	-3.9
7500	-4.0

Panel c of Figure 6.5 illustrates the mass decreasing at 7500th scan continued even after switching at 0.6 V until 0.25 V. The Q-E graph, shown in panel b of Figure 6.5, indicates the charge increase after potential switching (returning from 0.6 V) confirming the PANI film was not fully oxidised at 0.6 V (suggesting slow kinetic redox reaction). Therefore oxidation was not stopped until around 0.45 V. Panel a and b of Figure 6.5 shows that oxidation of PANI starts around 0.25 V. However, on the time scale of the experiment (until 0.6 V) PANI cannot be fully oxidised because of surface coverage of the film (Γ = 386 nmol cm^{-2}). A significant potential (time or overpotential) must be applied for fully charged thick PANI film to have sufficient time to obtain fully oxidised PANI film. Charge and mass switching of thinner films (Γ = 31 nmol cm^{-2}), given in panel b and c of Figure 6.2 respectively, show that oxidation of PANI almost was completed at around 0.6 V for the scan rate of 100 mV s^{-1}.

All PANI films, prepared from aqueous solution and transferred to Ethaline, evolve continuously with repetitive potential cycling. A PANI film, presented in Figure 6.5, was selected for emphasising a particular feature that equilibration between a thick PANI film and its bathing DESs was very slow. However, the equilibrium could be reached

rapidly (with just three scans) by cycling PEDOT in DESs.[60, 61] Figure 6.6 shows the number of scans required for the steady state of PANI films, with different coverage. The number of scans, for changing the direction of ion transfer of PANI redox reaction in Ethaline, are from anion domination (early scans) up to approximately zero mass change.
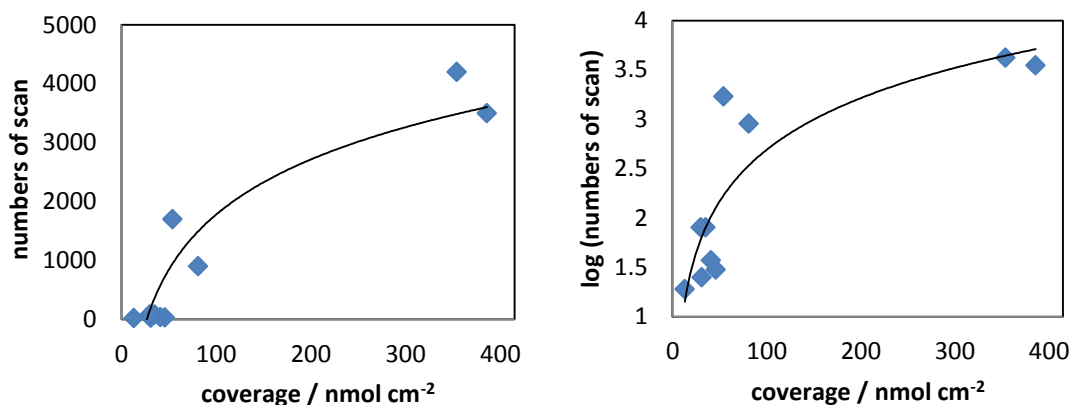

Figure 6.6: Evolution of PANI film from anion dominated to cation dominated transfer in Ethaline. Data shows from anion dominated to almost no mass changing scans. a) number of scans vs. the coverage of PANI film; b) logarithmic form of numbers of scan vs. the coverage.

The changes of directions of mass graphs, from anion domination to an approximate number of scans that cation domination started, presented in Figure 6.6 were conducted at a scan rate of 50 mV s^{-1}. The films, whose direction changing could not be recognised, were not taken into account. This confirms thicker films take longer duration to reach the steady state. In panel b of Figure 6.6, a logarithmic graph is given to provide clear presentation of films having less than 50 nmol cm^{-2} surface coverage. All films used for Figure 6.6 graphs were rigid. Therefore, the mass change was calculated using the Sauerbrey equation. The QCM cannot measure mass changes of a non-rigid film (more than 400 nmol cm^{-2}) because of the deviation from the Sauerbrey equation. If a non-rigid film (thicker than 386 nmol cm^{-2}) were formed, it would take more scans (possibly more than tens of thousands) to reach the steady state.

Panel a of Figure 6.7 and Figure 6.8 show cyclic voltammetric responses after evolution of PANI films with 35 nmol cm^{-2} (film B) and 13 nmol cm^{-2} (film C) coverage, respectively, to see the effect of surface coverage at different scan rates. Their growth conditions were exactly the same but the numbers of deposition cycle were different. While film B was grown with 12 deposition cycles, film C was grown with 10 deposition cycles. Panel b of Figure 6.7 and Figure 6.8 show the logarithmic form of current peaks *vs.* logarithmic form of scan rate data taken from cyclic voltammetric responses of film B and film C, given in panel a of Figure 6.7 and Figure 6.8, respectively.
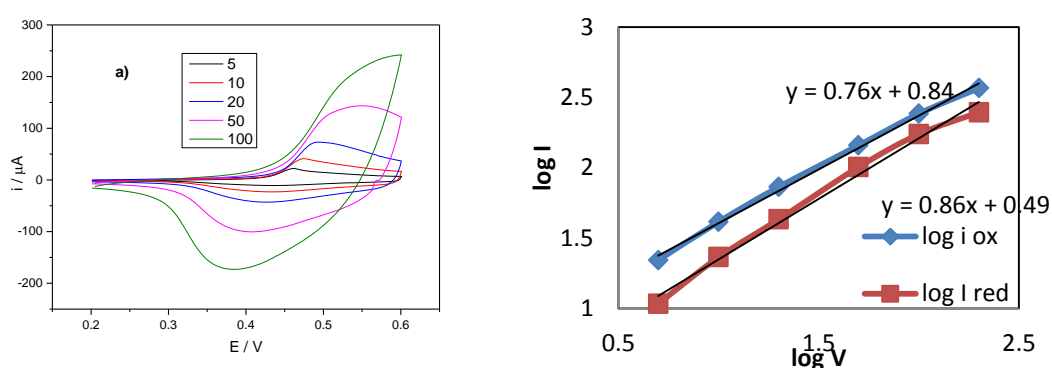

Figure 6.7: a) Cyclic voltammetric responses of redox switching of PANI film B (Γ = 35 nmol cm^{-2}) exposed to Ethaline at various scan rates, growth conditions of the film were given in Table 1, numbers indicate potential scan rate (in mV s^{-1}); b) log (i$_p$) vs. log(v) of PANI given in panel a, blue data for oxidation; red data for reduction half cycles. The line of best fit of the data is represented with black solid line.

Figure 6.8: a) Cyclic voltammetric responses of redox switching of PANI film C (Γ = 13 nmol cm^{-2}) exposed to Ethaline with at various scan rate (in mV s^{-1}), growth conditions of the film were given in table 1, numbers indicate potential scan rate; b) log (ip) vs. log(v) of PANI given in panel, blue data for oxidation; red data for reduction half cycles. The line of best fit of the data is represented with black solid line.

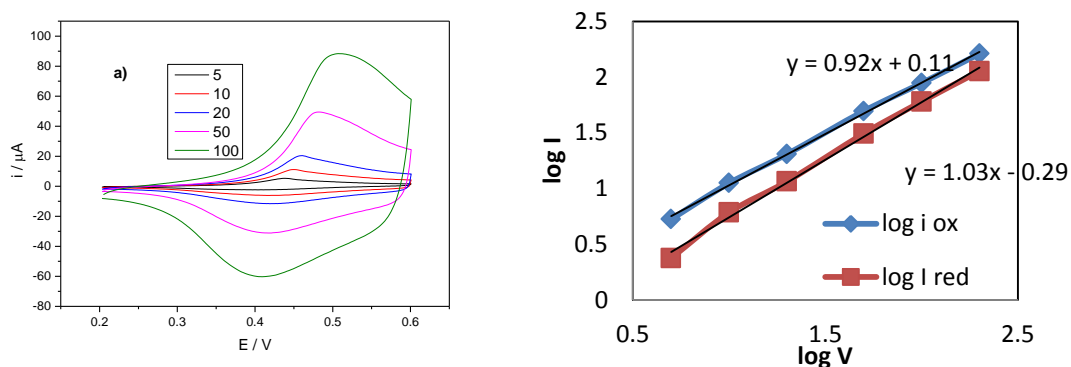The reason why film B and film C were selected to present here is because i) their growth conditions are identical and ii) they have the same characteristics as they are both thin enough films to observe the oxidation and reduction peaks for a wide range of scan rates: from 5 mV s^{-1} to 100 mV s^{-1}. Therefore, it is plausible to measure the slope of log(i_p) *vs.* log(v) to distinguish the control of the redox cycling; diffusional control, diffusionless control or some extent between these two.

While the slope of log(i_p) *vs.* log(v) of relatively thinner film during oxidation, given in panel b of Figure 6.8, is 0.92 (close to 1), the slope of thicker film oxidation (given in panel a of Figure 6.7) is 0.76. Therefore, PANI kinetics processes were different. PANI film (film C) having less coverage was surface controlled which was related to just film redox reaction not diffusion control. However, it is observed that diffusion control mechanism could play an important role as well with surface control reaction of PANI film (film B) having more coverage.

6.2.2.3.   Effect of Growth conditions

Panel a of Figure 6. 9 shows the electrochemical responses of a PANI film I (Γ = 54 nmol cm^{-2}) in Ethaline at various scan rate. Film B and film C, presented in Figure 6.7 and Figure 6.8 respectively, were grown with the same potential window and scan rate but

different number of scans. The growth conditions of film I (Γ = 54 nmol cm^{-2}) are different to those of film B summarized in Table 6.1: different potential window, scan rate and numbers of scans. All other variables (RE, electrolyte) for the growth of films I, B and C were kept constant. The data for film I, shown in this section, were collected after 2000 times cycling of the film in Ethaline to reach the steady state.

Panel b of Figure 6. 9 shows the data of log (i_p) *vs.* log(v) corresponding to PANI film I given in panel a of Figure 6. 9. The slope of the graph (close to 1) indicates the redox switching of PANI (film I) in Ethaline was controlled by surface reaction.

From the comparison of log (i_p) *vs.* log(v) slopes of film B (Γ = 35 nmol cm^{-2}) and film C (Γ = 13 nmol cm^{-2}), it can be concluded that films having relatively low surface coverage, undergo complete redox reaction while films having high surface coverage do not. Indeed the surface coverage of film I (Γ = 54 nmol cm^{-2}) was higher than film B (Γ = 35 nmol cm^{-2}) and film C (Γ = 13 nmol cm^{-2}). While the surface coverage of film I is 4 times higher than film C, film I has more likely surface controlled reaction rather than film C. Small differences during growth can make big differences in switching responses of PANI in Ethaline. This is because of structural or morphological variations (as explained in chapter four as a function of the amount of water during growth of PANI). As a result, the reaction kinetics not only depend on surface coverage but also on growth conditions of the film.

Scatter of data in Figure 6.6 arises from the effect of growth conditions. The effect of the growth conditions will be shown in the next section, with p-doping PANI dynamics in Ethaline as well.
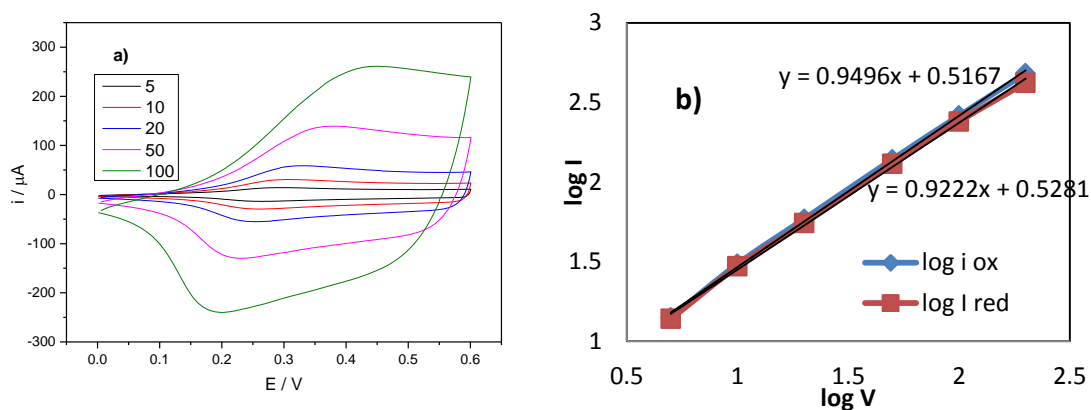
Figure 6. 9: *a) Cyclic voltammetric responses of redox switching of PANI film I (Γ = 54 nmol cm^{-2}) exposed to Ethaline at various scan rates, growth conditions of the film were given in Table 1, numbers indicate potential scan rate (in mV s^{-1}); b) log (i$_p$) vs. log(v) of PANI given in panel a, blue data for oxidation; red data for reduction half cycles. The line of best fit of the data is represented with black solid line.*

6.2.2.4.   Effect of Scan Rates

Panel a of Figure 6.10 shows the cyclic voltammetric responses of PANI film (film G) (Γ = 41 nmol cm^{-2}) in Ethaline cycling at scan rates ranging from 1 mV s^{-1} to 100 mV s^{-1}. When film G was cycled in Ethaline, during some voltammetric cycles (in this case 60 cycles), the response of the film evolved; thereafter it was reproducible. All results used in this section, are after the evolution of the film. For example, the results of film H (Γ = 354 nmol cm^{-2}) experiments were the responses of the EQCM conducted after 5000 voltammetric cycles.
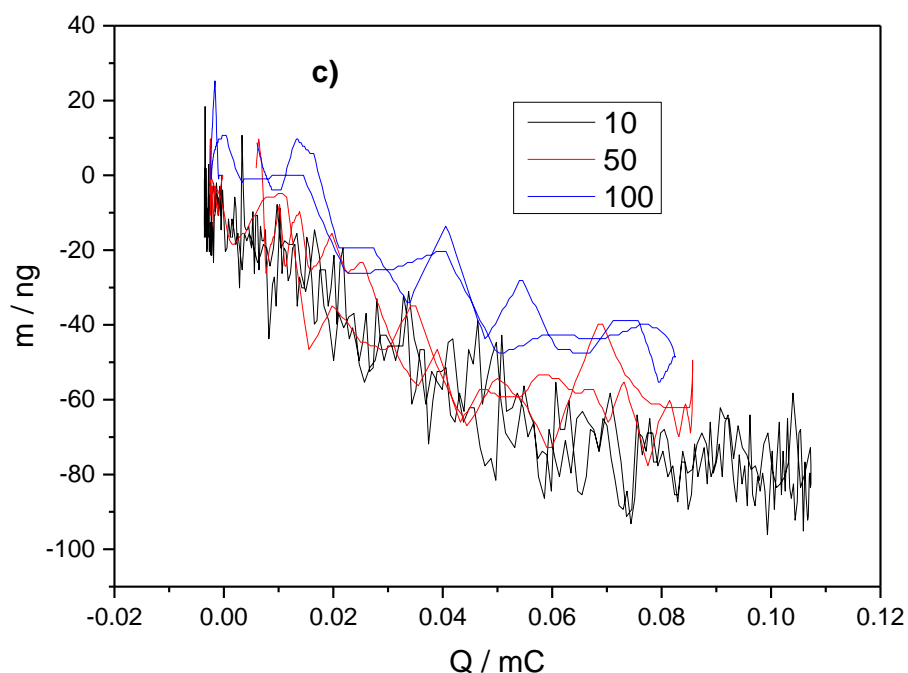
202
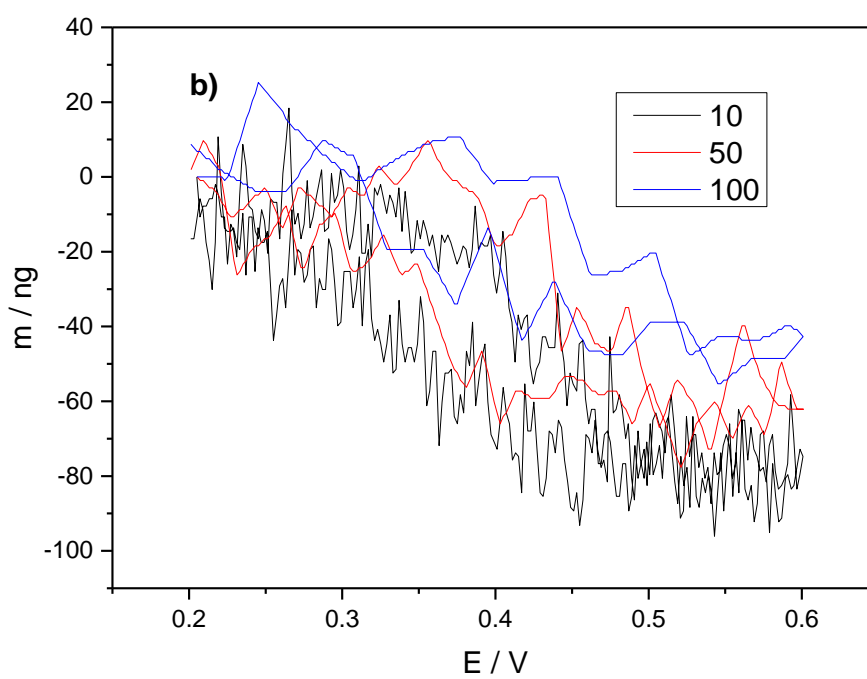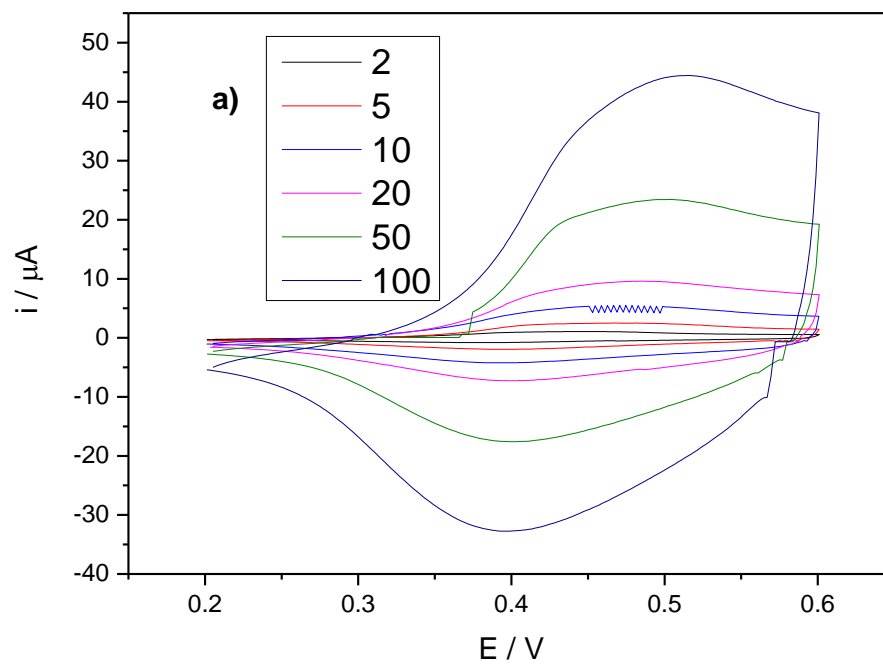
Figure 6.10: EQCM data for redox switching of a PANI film G (Γ =41 nmol cm^{-2}) exposed to Ethaline at various scan rates .a) i vs. E; b) Δm vs. E; c) Δm vs. Q where charge is calculated from the integration of current shown in panel a. Film mass changes calculated using Sauerbrey Equation shown in chapter two. Numbers indicate scan rates.

The EQCM gravimetric response of film G, at a scan rate of 10 mV s^{-1}, 50 mV s^{-1} and 100 mV s^{-1} (shown in panel b of Figure 6.10) corresponding to cyclic voltammetry data given in panel a of Figure 6.10, shows that expulsion (incorporation) of cation is the dominant mechanism by which electroneutrality was maintained during oxidation (reduction). Panel c of Figure 6.10 (Δm-Q), calculated from panel a and b of Figure 6.10 (charge and mass change responses, respectively) shows reasonable linearity and similarity for different scan rates.

Before the presentation of the effect of scan rate, it would be better to compare the mechanism of PANI oxidation in an aqueous acidic medium with Ethaline medium. Mass changing of PANI, switched in an aqueous acidic medium, consists of two steps: 1. proton egress in the early stages of film oxidation and 2. anion ingress in the later stages of film oxidation. Anion (as its molar mass is larger than proton molar mass) dominates the overall gravimetric responses of the redox process of PANI during p-doping/dedopoing as shown in literature[49, 50, 62, 63] and section 4.2.4.6.1. Anion

participation is predominant for PANI cycled in non-aqueous electrolyte as well (cycled in monomer-free solutions of LiClO$_4$, NaClO$_4$ and (C$_4$H$_9$)$_4$NClO$_4$ in propylene carbonate or acetonitrile solutions).[64] Some conducting polymers, for example polypyrrole grown in the presence of macromolecules (polystyrenesulfonate), can be used as cation exchangers.[65] However, PANI films, grown in the presence of high molar mass anions (dodecylsulphate) are anion dominated as well.[66] To our knowledge, PANI has not previously been shown to have cation domination reaction in any electrolyte.

The generally accepted scheme[62, 67-72] for PANI redox chemistry in aqueous acidic electrolyte is that the leucoemeraldine form of PANI is found as partially protonated containing an equal amount of anions. In the early stage of oxidation of PANI, deprotonation occurs and the protons exit from the film. Further oxidation of PANI can form a double charged species having quinoid and benzoid structures (second electron transfer: bipolaron). Incorporation of anion (in later oxidation stage) makes a stable emeraldine form. However, there should not be protonation/deprotonation in Ethaline because there is no proton source. Therefore, the oxidation stages of PANI, involving the transition of leucoemeraldine to emeraldine form, consist of just EG$_2$Cl$^-$ ingress and Ch$^+$ egress, represented in Figure 6.11.
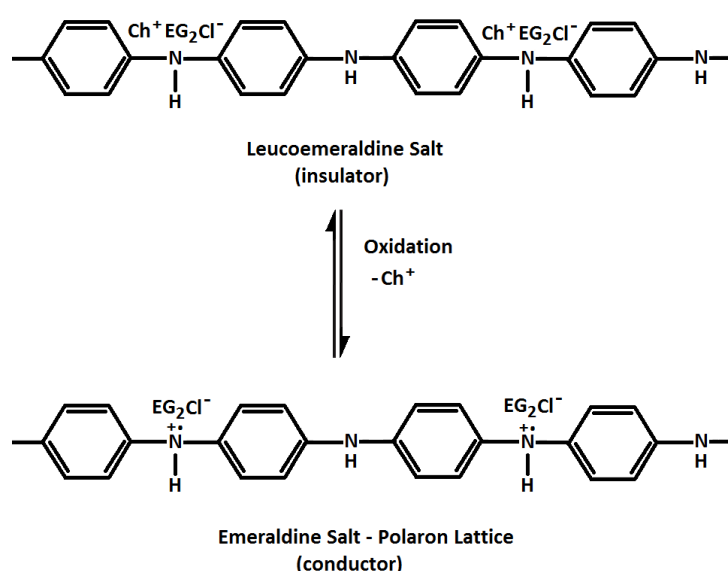

Figure 6.11: Schematic representation of PANI oxidation in Ethaline electrolyte.

The apparent molar mass (M_m) of the species exchanged during the redox switching of PANI data in panel c of Figure 6.10 and analogues at other scan rates are summarised in Table 6.4. Data given in Table 6.4 were calculated from the experiments of Figure 6.9 for film G at various scan rates and calculated for other films which are not shown in this chapter. Growth conditions of all films were given in Table 6.1 (page 184). Table 6.4 shows the value of M_m for film G in Ethaline is approximately -70 g mol^{-1} for all scan rates. The sign confirms that the dominant transferring ion, for balancing electron removal, is Ch$^+$ (M_{mCh+} = -104.2 g mol^{-1} for Ch$^+$). Some anions ($M_{mEG2Cl-}$ = 159.6 g mol^{-1} for EG$_2$Cl$^-$) allow transfer into the film (in the opposite direction to Ch$^+$), to reach the point of M_m. There is no solvent neutral molecules to transfer unlike the aqueous case.

Table 6.4: Molar mass changes (end-to-end) for the oxidation half cycle of PANI films, Δm F/Q, as a function of potential scan rate during redox switching in Ethaline. Films detail are given in Figure 6.1.

v / mV s^{-1}	Film B /g mol^{-1} (Γ = 35 nmol cm^{-2})	Film C /g mol^{-1} (Γ = 13 nmol cm^{-2})	Film H /g mol^{-1} (Γ = 354 nmol cm^{-2})	Film G /g mol^{-1} (Γ = 41 nmol cm^{-2})	Film E /g mol^{-1} (Γ = 31 nmol cm^{-2})
5	-27	-34	-3.9	-63	-35
10	-20	-30	-3.3	-69	-32
20	-16	-26	-1.9	-65	-34
50	-19	-32	-2.0	-69	-36
100	-22	-28	-0.1	-72	-38
200	-21	-30	-0.1	-70	-39

M_m of ion exchange data, given in Table 6.4, is drawn as a graph presented in Figure 6.12 for clarification of comparison with each other (panel b of Figure 6.12) and with molar masses of Ch$^+$ and EG$_2$Cl$^-$ (panel a of Figure 6.12). When the films are compared in terms of M_m values, M_m values may depend on film deposition conditions and coverage. Therefore, to analyse the differences of ion dynamics in a more appropriate way, the films grown with the same conditions (film B and film C) should be compared with each other or the films having extremely different surface coverage (film H and film G) can be compared with each other to eliminate the effect of growth conditions.

Films B and C are compared in terms of M_m because their growth conditions are the same but number of scans are different, as summarized in Table 6.1. M_m data is -32 g mol^{-1} for film C and -19 g mol^{-1} for film B (both for v = 50 mV s^{-1}) given in Table 6.4. Panel a of Figure 6.12 also demonstrates that M_m data of film C are more negative than those of film B for all scan rates ranging from 5 mV s^{-1} to 200 mV s^{-1}. Film C, which is thinner than film B, is more cation dominated than film B. M_m during the reduction of PANI is identical to M_m during the oxidation of PANI. For example, while the oxidation Δm-Q slope was -69 g mol^{-1} for film G (v = 50 mV s^{-1}), its reduction slope was 73 g mol^{-1}. Therefore, in this section M_m data for just the oxidation half cycles of PANI films are discussed.

Δm-Q slopes of Film B, film C and film E are the same as film G which is linear and independent of scan rate shown in panel c of Figure 6.10. There were some films whose Δm-Q slope were dependent of scan rate, these could be i) as a sum of slope of two different sites: cation expulsion in early stage of oxidation and anion incorporation in the latter stage of oxidation part of PANI presented in Figure 6.15 (page 216); ii) variable depending on scan rates given in Figure 6.16. The data shown in Table 6.4 had linear Δm-Q graph apart from film H shown in Figure 6.16.

M_m of film H was calculated from the end-to-end data of Δm-Q graph illustrated in panel c of Figure 6.16. It can be deduced from Table 6.4 that M_m of film H is around -3 g mol^{-1} which is the lowest negative value among the data. This confirms that thicker films are less cation dominated than the thinner ones. However, panel b of Figure 6.12 shows that there are no big differences in M_m of ions because of the huge gap between the molar mass of Ch^+ and EG_2Cl^-. If just one of ions in Ethaline (Ch^+ or EG_2Cl^-) is dominant, M_m of ion exchange would be -104.2 and +159.6 g mol^{-1} respectively (shown in panel b of Figure 6.12). Therefore, it is better to calculate the fraction of Ch^+ and EG_2Cl^- for each film redox cycling.
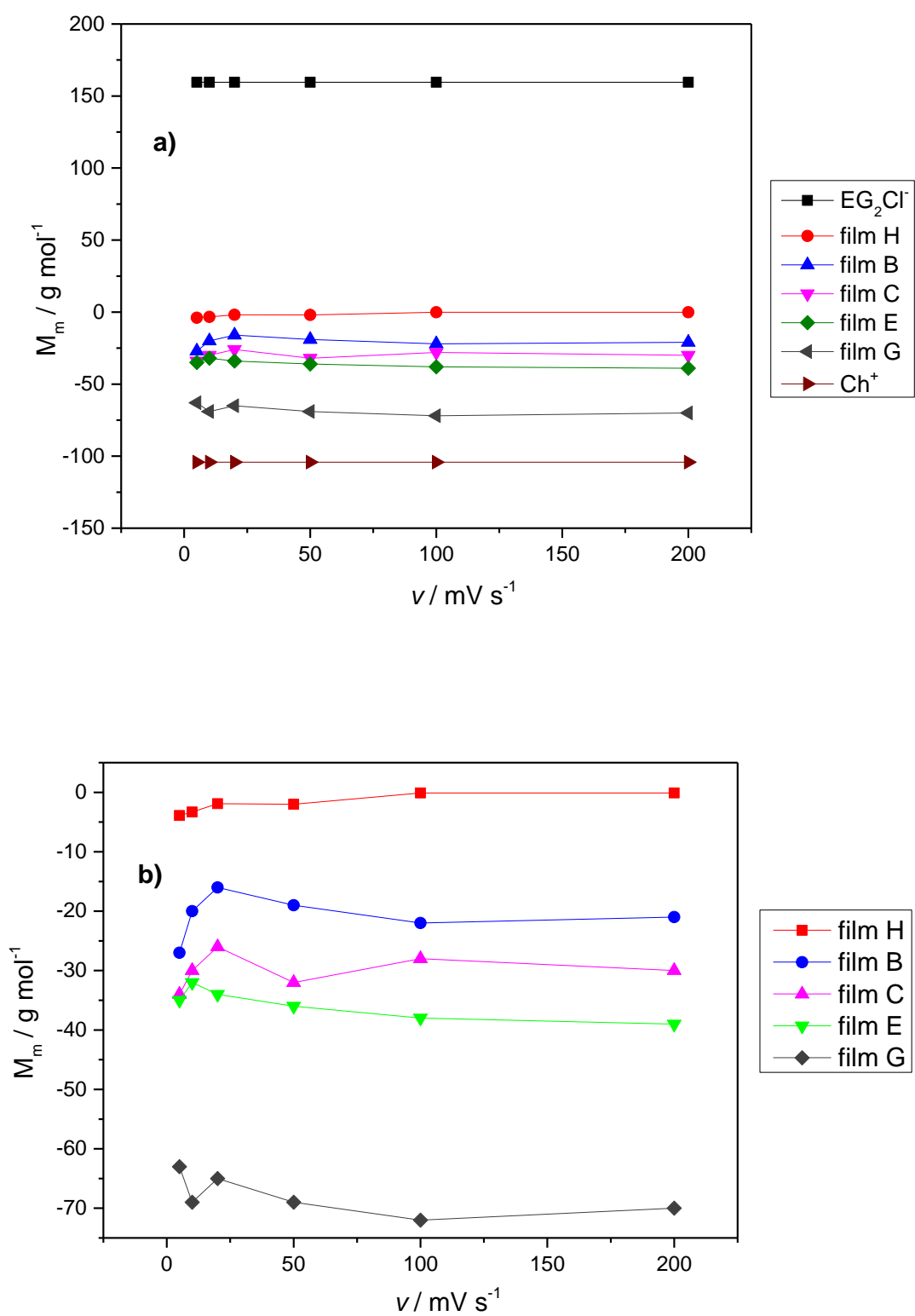
Figure 6.12: M_m changes for the oxidation half cycle of PANI films exposed to Ethaline as a function of scan rate a) comparison of films with Ch^+ and EG_2Cl^-. b) comparison of films without Ch^+ and EG_2Cl^-. Data taken from Table 6.4.

M_m for the oxidation of film G, cycling in Ethaline at a scan rate of 50 mV s^{-1}, is -69 g mol^{-1}, shown in Table 6.4. There are components of Ch$^+$ entry (104.2 g mol^{-1}, satisfying a fraction x of charge electroneutrality) and EG$_2$Cl$^-$ exit (159.6 g mol^{-1}, satisfying a fraction 1-x of charge electroneutrality). The calculation is shown in Eq 6. 1.

$$x\ M_{Ch+} + (1-x)\ (M_{EG2Cl-}) = M_m$$

$$x = [(M_{EG2Cl-}) - M_m] / [(M_{EG2Cl-}) - M_{Ch+}] \qquad \text{Eq 6. 1}$$

$$x = (159.6 - M_m) / 263.8$$

x = 0.87 is calculated from the Eq 6. 1 for -69 g mol^{-1} (film G, v = 50 mV s^{-1} given in Table 6.4) and presented in Table 6.5. This means; when overall 0.87 mole Ch$^+$ is expelled from the film, overall 0.13 mole EG$_2$Cl$^-$ is incorporated into the film during the oxidation of film G (Γ = 41 nmol cm^{-2}), corresponding to per mole of electronic charge transferred of PANI in Ethaline at a scan rate of 50 mV s^{-1}. The fraction of Ch$^+$ for film H (Γ = 354 nmol cm^{-2}), which is much thicker than film G (Γ = 41 nmol cm^{-2}), is less than film G, at 0.60. It suggests; when a thin PANI film (film G) is oxidised, more cation (Ch$^+$), per mole of redox electrons, leaves the film than film H. In thick film (consider film H), there are more salt (Ch$^+$ and EG$_2$Cl$^-$) inside the voids of PANI branches than thin film because total porosity of film H is higher than film G as their coverages are so different (354 nmol cm^{-2} and 41 nmol cm^{-2}, respectively) (see schematic explanation of thin and thick film in Figure 6.13).

PANI film   **Thicker PANI film**

Electrode surface   Electrode surface
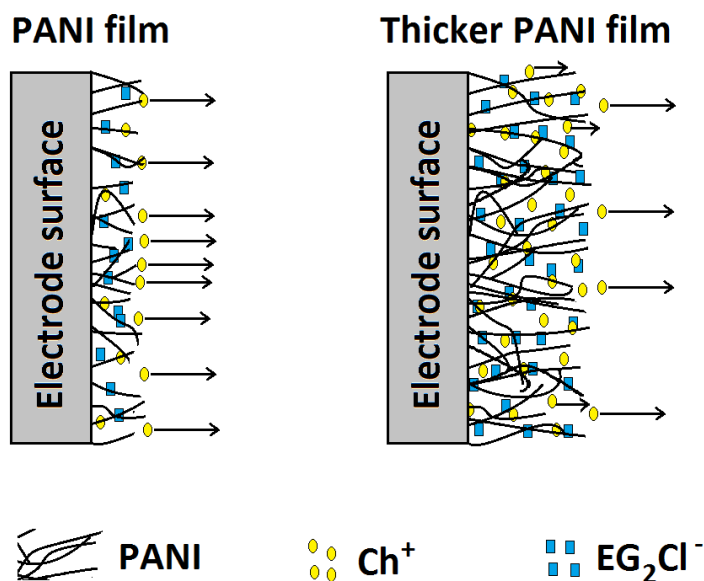
✎ **PANI**   ⦚ **Ch$^+$**   ⬚ **EG$_2$Cl$^-$**

Figure 6.13: Schematic representation of Ch$^+$ transfer during the oxidation of a thin (film G) and thick (film H) PANI film. The behaviour of Ch$^+$ is shown. However, EG$_2$Cl$^-$ transfer, in the opposite direction, is not indicated. Some of ionic salts are immobile in the films.

When just the fraction of cation egress of thick (film H) is compared with the fraction of cation egress of thin film (film G), it could be concluded that the thick PANI film retained more cation into the voids of its branches. In this step, two scenarios are possible to explain the ion dynamics during oxidation of the film H: 1) as explained previously when cation exit from the film, some anions incorporate into the film and more anion incorporates into film H per redox site of PANI than film G to maintain electroneutrality; 2) EG$_2$Cl$^-$ molecules of ionic salt, inside porosity of PANI structure (leucoemeraldine salt form of PANI), were oriented toward into the PANI chains during oxidation of PANI and Ch$^+$ molecules could be excluded to outer stage of (PANI)$_2$$^+EG_2Cl^-$ chains. PANI undergoes a redox reaction to store charge as observed from the cyclic voltammetry of film H (see panel a of Figure 6.16). However, Ch$^+$, inside porous surface on PANI, could diffuse to out of PANI chains (but still inside the voids of film). While the amount of Ch$^+$, diffused out from the film) was higher in thin film (film G) during oxidation of PANI film and hence Ch$^+$ can leave the film easily. In thick films, Ch$^+$ cannot depart quickly (film H) so it lost less Ch$^+$ because some of them are still inside thick PANI film (film H). Therefore, in thin films M_m is more negative than M_m of thick films as shown in Figure 6.12 where M_m of film H reaction is much less negative than

film G. Mass change of film H during oxidation, depending on scan rate, will be analysed in the end of this section.

Table 6.5: Fractions of Ch^+ egress and EG_2Cl^- ingress during oxidation of PANI films cycled in Ethaline at a scan rate of 50 mV s^{-1}. Data calculated from Table 6.4. See the text for details about calculations.

Film names	Fraction of Ch^+ ejection	Fraction of EG_2Cl^- injection
Film B	0.68	0.32
Film C	0.73	0.27
Film H	0.60	0.40
Film G	0.87	0.13
Film E	0.74	0.26

While the surface coverage of film E is 2.4 times higher than the surface coverage of film C, their transferred ion fractions are identical as presented in Table 6.5. This can be explained by the effect of growth conditions as explained in section 6.2.2.3. It would be better to compare two films having the same growth conditions as indicated earlier. Deposition conditions of film B and film C were the same, apart from scan numbers which were for controlling film thickness, (see Table 6.1). Therefore, film B and film C could be compared. When the fractions of transferred ions for these two films are compared, it can be seen that the fraction of Ch^+ in thin film (film C) (0.73) is higher than thick film's Ch^+ fraction (0.68) (film B). While, the fractions of Ch^+ were slightly different, still this difference could be explained with the presence of more amount of ionic liquid in thicker film as described with the comparison on film H and film G.

The variation in the charging of film B and film C as a function of scan rate, from 5 mV s^{-1} to 200 mV s^{-1}, is presented in panel a of Figure 6.14. While the oxidation charge of film C is around the same level for all the scan rates given, the oxidation charge of film B decreases significantly with increasing scan rate. This means film C (thin film) can be fully charged at short time while film B (thick film) takes longer time to be fully charged. Timescale of charging of the system is an important parameter in energy

storage devices to save the time. For better comparisons, the specific capacitance value of the films are given in panel b of Figure 6.14 for film B and film C corresponding to data given in panel a of Figure 6.14.

The specific capacitance (C_s / F g^{-1}) is calculated by integrating the area under the cyclic voltammogram curves for PANI oxidation using the following equation:

$$C_s = \frac{Q}{m\,\Delta V}$$
Equ 6. 2,

where Q (C) is charge calculated for oxidation of the film, m (g) is the mass of the active material calculated from cyclic voltammogram curve of oxidation of PANI deposition presented in section 4.2.3 and ΔV (V) is the applied potential window.

The specific capacitance for film B, film C and film I is summarised in Table 6.6. The calculation results of film I here are given for the comparison of the effect of growth conditions as given in section 6.2.2.3.
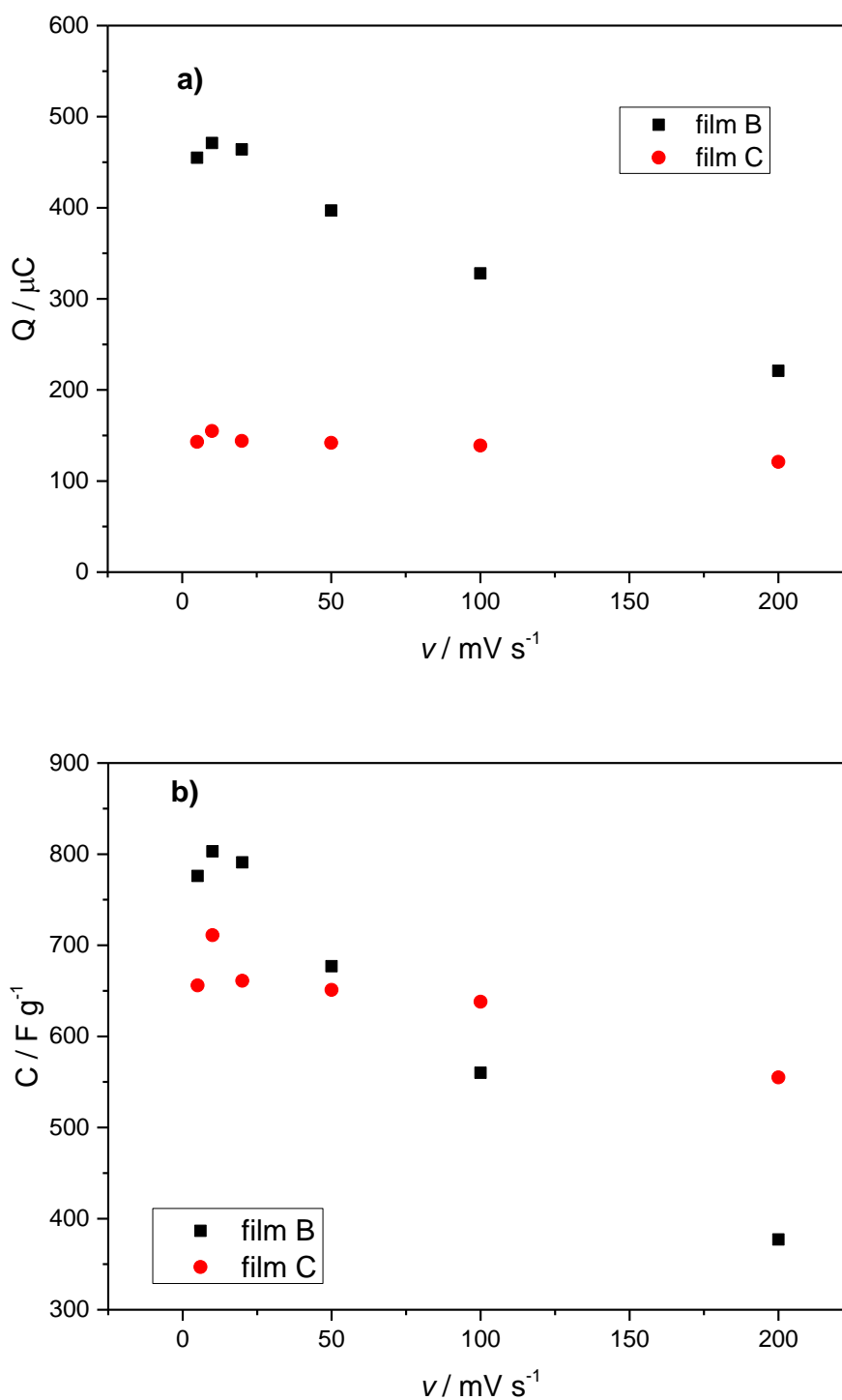
Figure 6.14: a) Oxidation charge of different surface coverage PANI films as a function of scan rate (from 5 to 200 mV s^{-1}) in Ethaline. Films grown similarly (given in section 6.2.1) red symbols: film C (Γ = 13 nmol cm^{-2};) blue symbols: film B (Γ = 35 nmol cm^{-2}). Potential window was started from 0.2 V to potential reversal at 0.6 V (ΔE = 0.4 V) (given in Figure 6.7 and Figure 6.8, respectively. b) specific capacitance of the data, corresponding to panel a of this graph data, as a function scan rate. The mass is related to polymer weight.

Table 6.6: Specific capacitances of PANI film B, film C and film I. Calculation given in the text for the films shown in Figure 6.14.

| v / mV s^{-1}	Film B / F g^{-1}	Film C / F g^{-1}	Film I / F g^{-1}
5	776	656	715
10	803	711	760
20	791	661	722
50	677	651	693
100	560	638	634
200	377	555	529

The specific capacitance of film C decreased just 16% (from 656 F g^{-1} to 555 F g^{-1}) with changing scan rate from 5 to 200 mV s^{-1}, as shown in Table 6.6, indicating high power density of the materials. The specific capacitance decreasing of film C (16%) is lower than metal oxides where capacitance decreasing is 61% between 10 mV s^{-1} and 200 mV s^{-1} (from 621 F g^{-1} to 377 F g^{-1}).[73] However, the specific capacitance of film B decreased 51% (from 776 F g^{-1} to 377 F g^{-1}) at the same scan rates, indicating there is incomplete charge recovery at faster scan rates. log(v)-log(i_{ox}) slopes could give qualitative information about the specific capacitance data change with scan rates. A slope, close to 1, causes less decreasing in specific capacitance with increasing scan rate. log(v) - log(i_{pox}) slopes of film B and C were 0.76 and 0.92 respectively as shown in Figure 6.7 and Figure 6.8. These are consistent with specific capacitance decreasing with scan rate. The specific capacitance of film I decreased 26% (from 715 F g^{-1} to 529 F g^{-1}). If one electron transfer is assumed for PANI oxidation (corresponding to two aniline ring: 182 g mol^{-1}) and using the Equ 6.2. for a 0.4 V potential window, the maximum theoretical capacitance of PANI is obtained as 1325 F g^{-1}).

The log(v) - log(i_{pox}) slope of film I was 0.95. Although the surface coverage of film I (Γ = 54 nmol cm^{-2}) is higher than the surface coverage of film B, film I could be charged

faster for the same charge ratio. This also confirms the effect of growth conditions. Therefore, optimum growth conditions of film should be identified prior to designing of the PANI based supercapacitors in DESs electrolyte. These high capacitance values presented in Table 6.6 can be attributed to high surface area of PANI film structure shown in section 4.2.4.8.

Film I has been previously shown, in the beginning of this section, that Δm-E and Δm-Q slopes of film B, film C, film G and film E for different scan rate were linear (mass changing dynamic is almost independent of scan rate) and as film G was shown as a represented data in Figure 6.10. Now we will see two different films (film H and film I) having different mass changing behaviour (mass changing dynamic is strongly dependent on scan rate). Figure 6.15 shows EQCM data for redox switching of film I in Ethaline. Panel a of Figure 6.15 shows cyclic voltammetric responses of film I represented in section 6.2.2.3 at scan rates up to 200 mV s^{-1}.
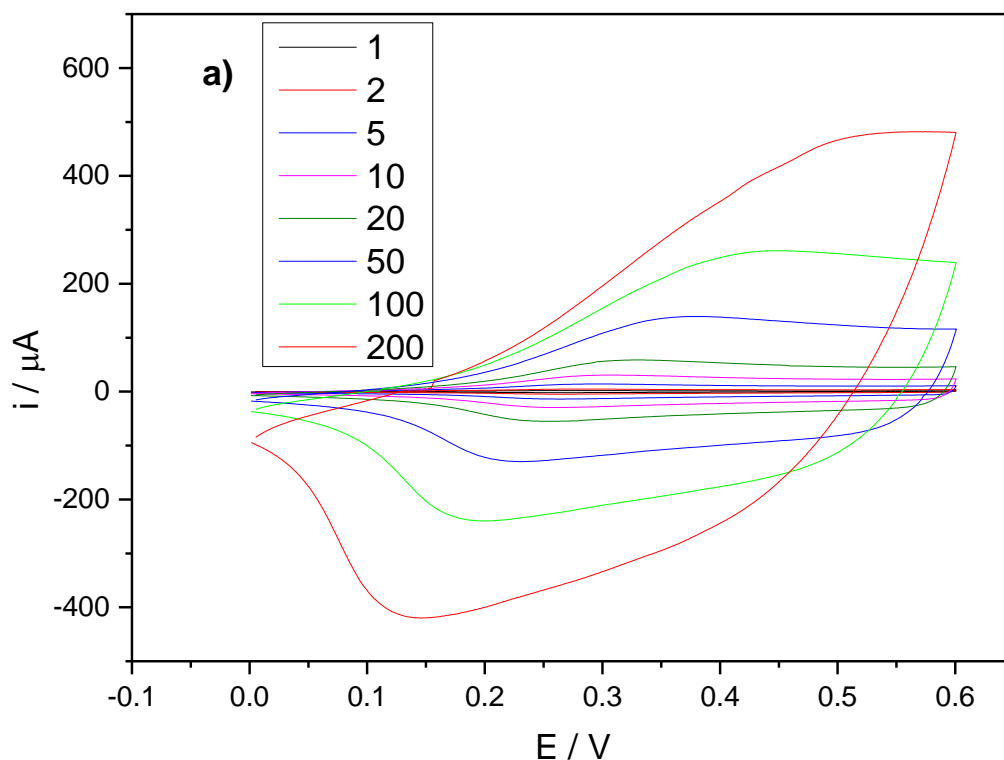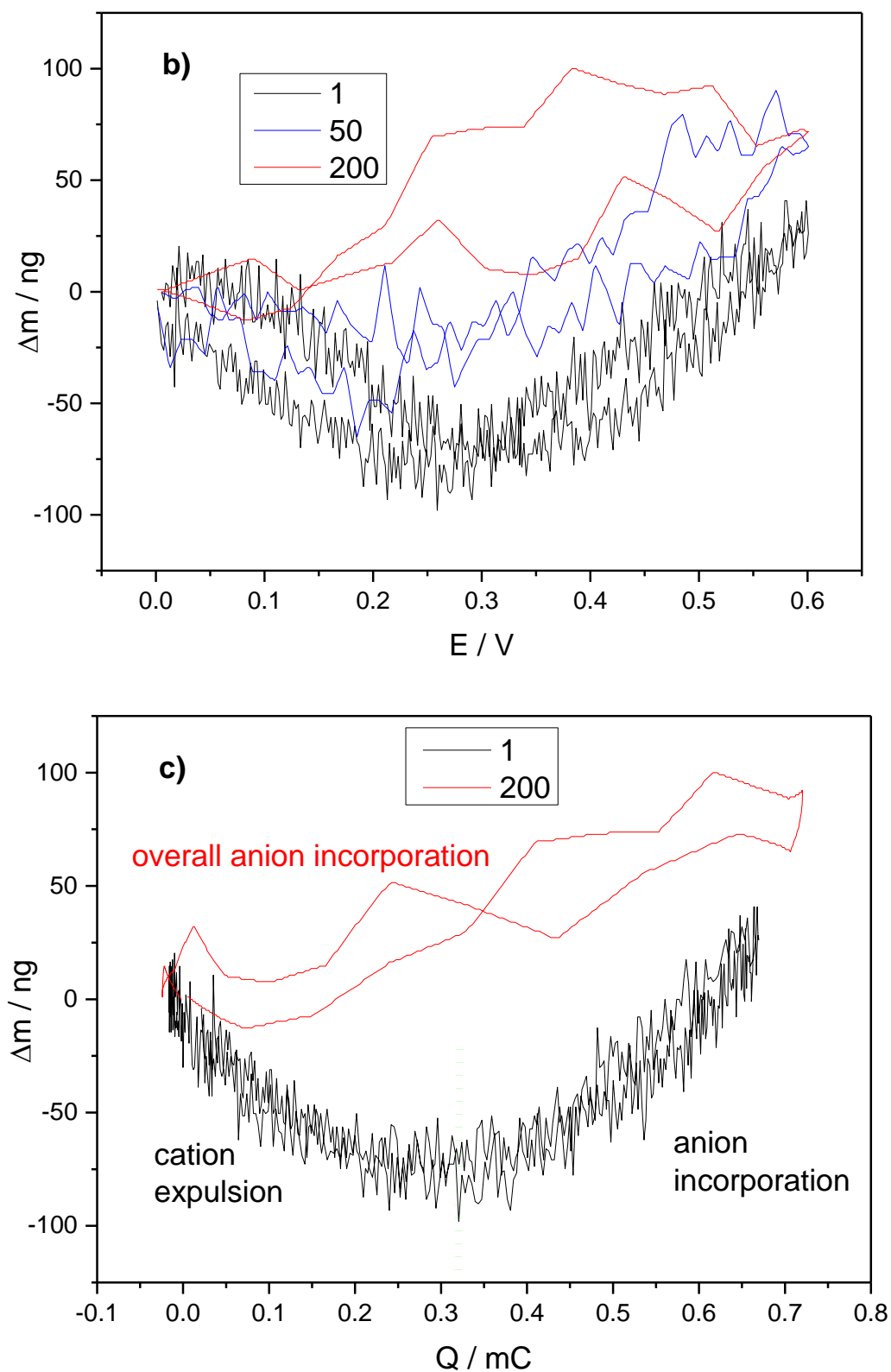
Figure 6.15: EQCM data for redox switching of a PANI film (Γ = 54 nmol cm^{-2}) (film I) exposed to Ethaline at various scan rates .a) i vs. E (scan rate, v, from 1 mV s^{-1} to 200 mV s^{-1}); b) Δm vs. E; c) Δm vs. Q where charge is calculated from the integration of current shown in panel a. The numbers indicate the potential scan rates.

Surprising mass change results during switching of this film in PANI were obtained and some of them at different scan rates were selected and presented in panel b of Figure 6.15. Mass changing was just anion dominated at a scan rate of 200 mV s^{-1}. However, at a scan rate of 1 mV s^{-1}, there were two stages: a mass decrease until 0.3 V of PANI oxidation followed by mass increase from 0.3 V to 0.6 V during oxidation of film I and *vice versa* for reduction as shown in panel b of Figure 6.15. As indicated in section 6.2.2.3, film I was cycled in Ethaline 2000 times between 0 V and 0.6 V for equilibrium. The exchanged molar mass values of cation expulsion and anion incorporation are calculated for all scan rates and given in Table 6.7.

Table 6.7: Molar mass exchanged during the oxidation of film I cycled in Ethaline. Data taken from Figure 6.15.

Scan rate: $v / mV\,s^{-1}$	Cation expulsion regime $M_m / g\,mol^{-1}$	Anion incorporation regime $M_m / g\,mol^{-1}$
1	-32	36
2	-28	23
5	-35	17
10	-29	15
20	-27	16
50	-22	18
100	-19	15
200	n/a	13

The general trend of cation domination in the early stages of oxidation decreased slightly with increasing scan rate. The fraction of Ch$^+$ was 0.73 at v = 1 mV s^{-1}, increasing to 0.68 at v= 100 mV s^{-1}. There was no significant cation domination for a scan rate of 200 mV s^{-1}, hence the fraction of Ch$^+$ for 200 mV s^{-1} was 0.61. The general trend of anion domination in the latter stage of oxidation decreased as well with

increasing scan rate. The fraction of EG_2Cl^- was 0.53 for a scan rate of 1 mV s^{-1} but it became 0.45 when the scan rate was 100 mV s^{-1}. This V-shaped behaviour of mass changing was observed with some other films (*e.g.* with PANI film (Γ = 162 nmol cm^{-2}) grown potentiodynamically cycled 5 times from -0.2 V to 0.9 V at a scan rate of 10 mV s^{-1}). The reason why film I was selected here was to give the representative result of V-shaped behaviour of mass change as film I was given previously in section 6.2.2.3. These V-shaped behaviours were not observed for the PANI films. The V-shaped behaviour (cation expulsion-anion incorporation during oxidation) was showed before by Hillman *et al.* with PPy in Ethaline[74] and PEDOT (Γ = 204 nmol cm^{-2}) in Propaline.[60] It is known that conducting polymer films are not homogenous.[75] While the bottom of the films could have more compact structure, the top of the films could have a more open structure. The height ratio of compact and porous area could be different depending on the growth conditions.[75-78] Although, cyclic voltammetric responses of film I do not show different peaks as shown in panel a of Figure 6.15 (all have one oxidation and one reduction peak), mass changing directions and ratio were dependent on timescale (scan rate) given in panel b and c of Figure 6.15. Therefore, Δm-Q results suggest that ion movements dynamic in Ethaline are different (dependent on scan rate) and not the same as film G, film B, film C and film E because of the variation in height (amount) of the compact and open zone stimulated with changing potential scan rate. Film H (Γ = 354 nmol cm^{-2}) is shown in Figure 6.16 for mass change of thicker films (another unexpected mass changing behaviour depending on timescale). The data presented in this chapter are representative data to emphasise particular features of mass change of the films.
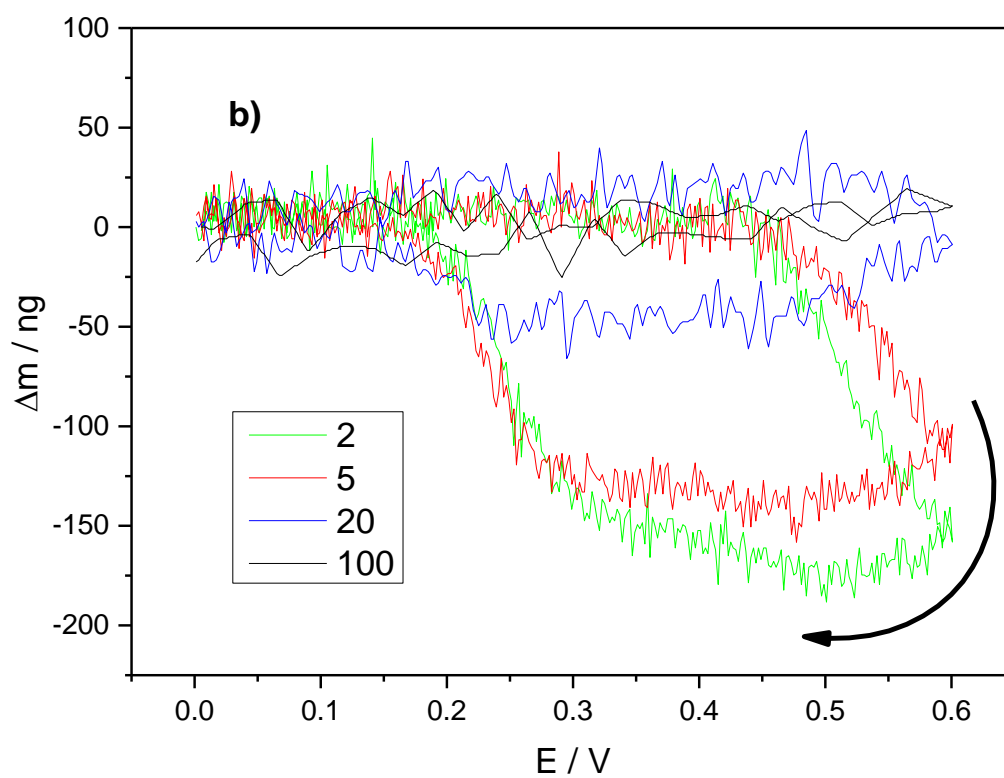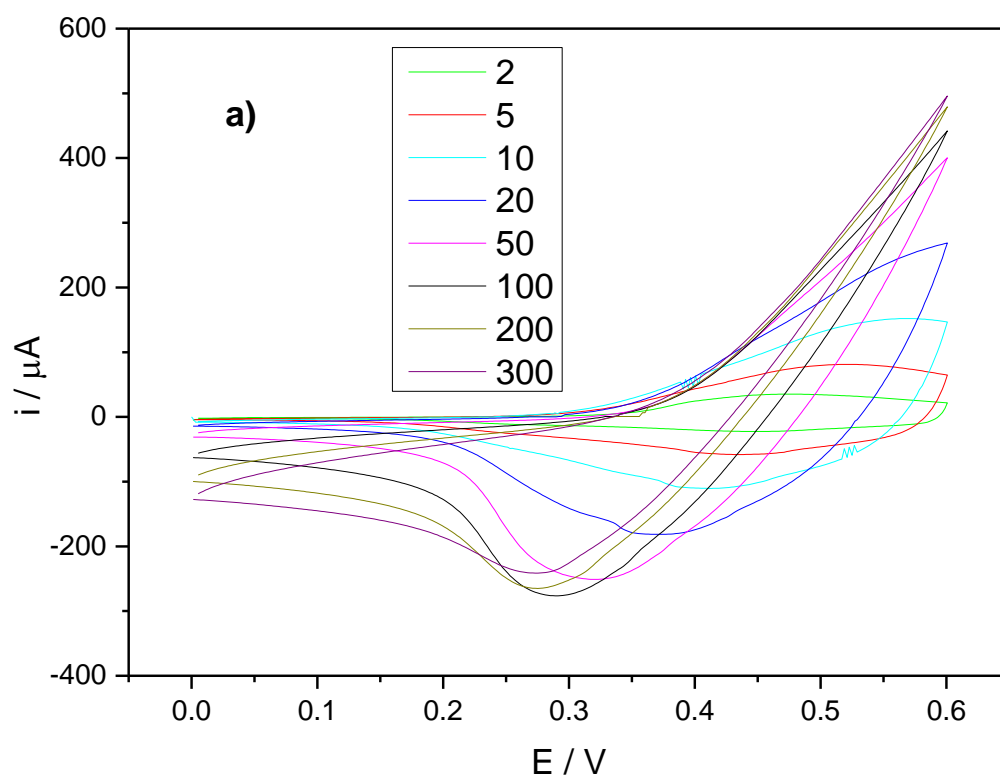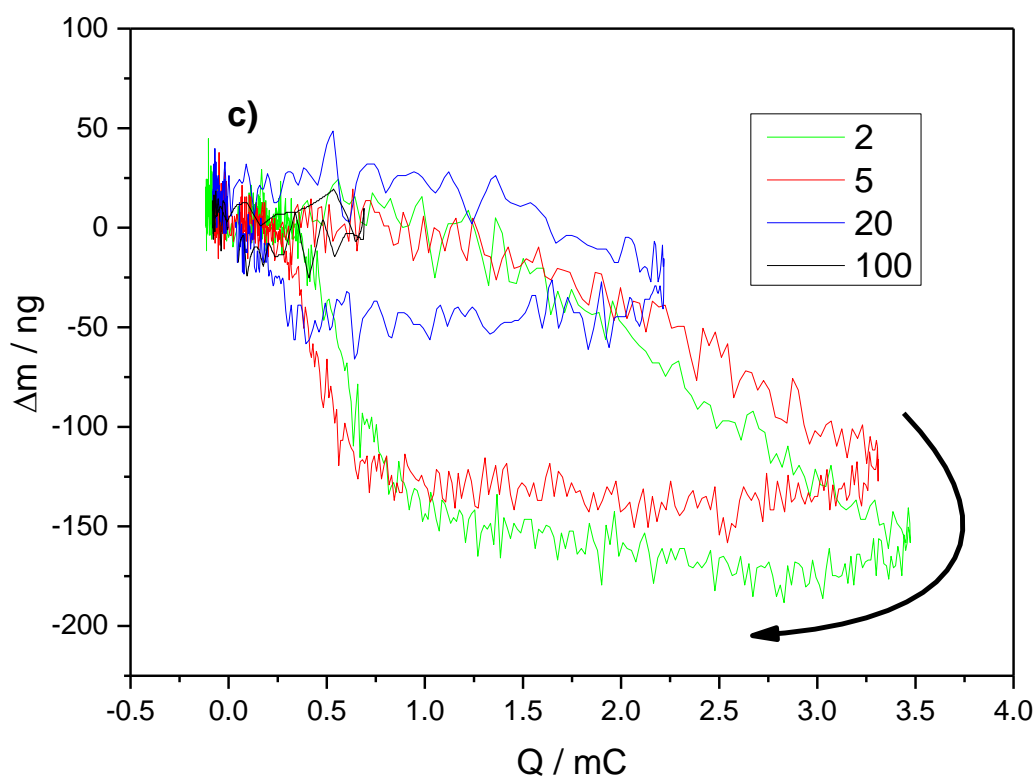
Figure 6.16: EQCM data for redox switching of a PANI film (Γ = 354 nmol cm^{-2}) (film H) exposed to Ethaline at various scan rates .a) i vs. E (v is from 2 mV s^{-1} to 300 mV s^{-1}); b) Δm vs. E; c) Δm vs. Q where charge is calculated from the integration of current shown in panel a. Film mass changes calculated using the Sauerbrey Equation. Numbers indicate the potential scan rates. The arrows indicate direction of changes.

Cyclic voltammetric responses of the film H in Ethaline shown in panel a of Figure 6.16, cycled from 0 V to 0.6 V, do not show oxidation peaks for higher scan rates (v > 20 mV s^{-1}) due to high surface coverage as discussed in section 6.2.2.2. Ion dynamics of Ethaline during redox cycling of PANI is the main topic in this stage. Panels b and c of Figure 6.16 show Δm-E and Δm-Q graphs, corresponding to the data in panel a of Figure 6.16. Panel b of Figure 6.16 illustrates that total mass change of PANI film is almost zero at a scan rate of 100 mV s^{-1}. However, at lower scan rates (see 5 mV s^{-1} in panel c of Figure 6.16), the mass change of film H during oxidation is around zero until 0.45 V. After this potential the mass of the film decreases (*ca.* 100 ng).

When the thicknesses of the films were compared at the beginning of this section, the diffusion of Ch^+ ions to out of the film is less and hence the fraction of Ch^+ was lower for thicker films. Here, the effect of timescale for a thick film shows that Ch^+ could be egressed from the film at longer timescale (lower scan rate). M_m values of film H, given in Table 6.4, show that lower scan rates are more cation dominant: while the M_m value for 5 mV s^{-1} is -3.9 g mol^{-1}, it is 0.1 g mol^{-1} for 100 mV s^{-1} and 200 mV s^{-1}, respectively. The differences in these scan rates are not high because at lower scan rate charge of oxidation is relatively higher than the charge in high scan rate (see x-axis of panel c of Figure 6.16). Therefore, total mass comparison could indicate that Ethaline ions can be retained into thick films at low timescale but if there is sufficient time (at higher timescale) Ch^+ ions could push out from PANI film.

6.2.2.5.　　　Effect of Waiting Time

All PANI films, prepared from aqueous solution, evolve continuously with cycling in Ethaline (see section 6.2.2.1). An equilibration between thick PANI films and their bathing DESs was very slow taking thousands of cycles (see section 6.2.2.2). This "Memory effect" with equilibrium, taking a long time from aqueous to Ethaline electrolyte, was a mystery. Does it occur with electrochemical cycling or it could happen just because of the contacting of PANI with Ethaline? To answer this question, a fresh film (film D) was deposited and left for long duration in Ethaline under open circuit conditions in which there was no external source of electrons. Prior to presenting data acquired under open-circuit conditions, the mass change of a film D, which was cycled in Ethaline straight after it was transferred to Ethaline, is shown in Figure 6.17. Before starting cycling of PANI in Ethaline, all films were rinsed with hot Ethaline several times to remove aqueous electrolyte in PANI film. Hot Ethaline is less viscous (given in chapter five) than 20 ± 2 °C Ethaline, hence each rinsing took less time.

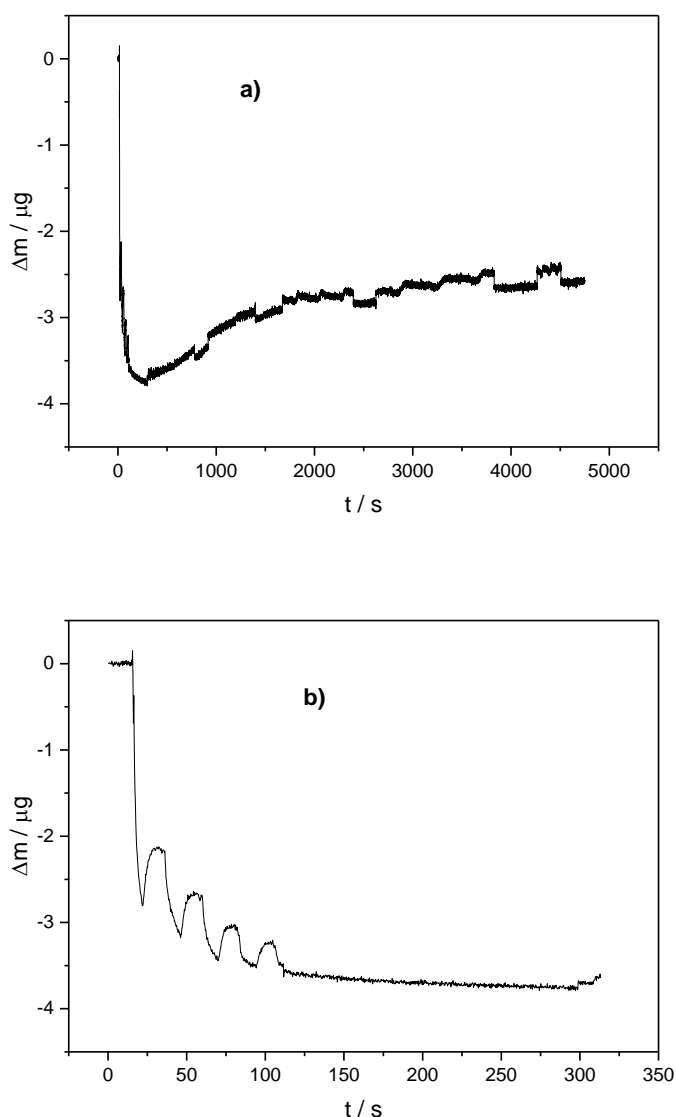*Figure 6.17: Δm vs. t plots of film D after exposure to Ethaline at 20 °C ± 2 °C a) conducted electrochemical experiments cycled from 0 V to 0.6 V just after film preparation; b) initial of the redox experiments (up to 300 seconds).*

Mass decreases initially after electrochemical cycling of PANI in Ethaline were initiated shown in panel b of Figure 6.17. The fluctuation of mass until around 110th second, (see panel b of Figure 6.17) was due to the fast mass change of the film after electrochemical experiment was started. There was 3.7 µg of decrease in the mass of the film. The reason behind the decrease in the mass could be both egress of aqueous electrolyte (from deposition solution) and egress of Ethaline (from rinsing solution) to

reach the equilibrium. The film, presented in Figure 6.17, was not in equilibrium as explained in section 6.2.2.1. There was an increase in mass between 300-1700 seconds shown in panel a of Figure 6.17 which was due to Ethaline entrance and accommodation in the film. This was probably a result of the waiting effect which was not related to just the applying voltage. The total lost in the mass of the film was about 2.6 µg.

Film D was prepared freshly again and this time, it was left for 88 000 seconds under open circuit conditions to observe the mass change (see panel a of Figure 6.18).
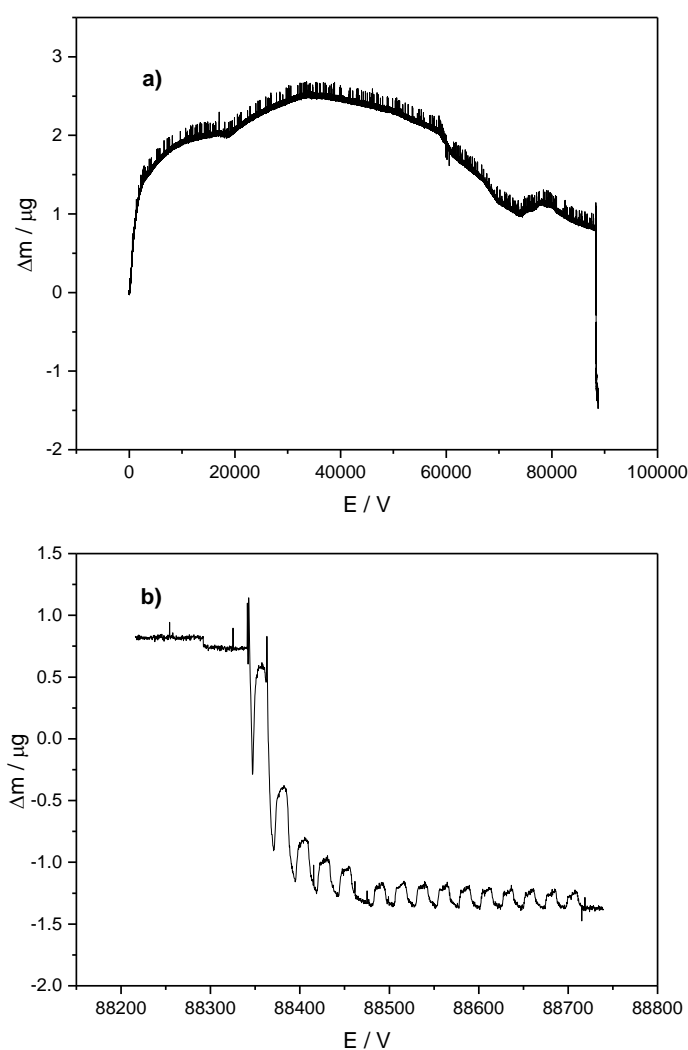

Figure 6.18: Δm vs. t plots of PANI film D exposure to Ethaline a) under open circuit conditions; b) starting electrochemical experiment after 88 300 seconds.

223

Figure 6.17 shows that the mass of the film decreased immediately after starting electrochemical experiment. However, here in Figure 6.18, without electrochemical control, the mass of the film first increased by about 2 µg in 10 000 seconds possibly due to overall Ethaline entrance into the film. The fluctuation of the film mass (after 10 000 seconds) could be arisen from the exchange of water with Ethaline and/or the viscosity change of the electrolyte during the measurement (see Figure 6.19). Temperature differences of the room during the measurement causes frequency (mass) shift as shown in chapter five and section 6.2.2.6. The measurement of film D, shown in Figure 6.18, took over 24 hours and changes in viscosity of electrolyte during the measurement could affect the frequency (mass) of the film. When the electrochemical experiment was started after 88 300 seconds shown in panel b of Figure 6.18, the mass of the film decreased by about 2 µg in 200 seconds. The reason for this decrease could be Ethaline and aqueous solution exclusion. This experiment showed that PANI film is not evolved with waiting under open circuit, so polymer relaxation needs electrochemical reaction. This shows the stability of the film without redox switching.

6.2.2.6.   Effect of Electrolyte Temperature

All Ethaline electrolyte experiments, shown until now, are conducted at 20 ± 2 °C. Ion transfer dynamics were checked for higher temperatures of electrolyte to understand the effect of temperature (viscosity) of electrolyte. Figure 6.19 shows the redox cycling of PANI film B2 (Γ = 29 nmol cm^{-2}) in Ethaline. The growth conditions of the film termed as film B2 were the same as film B given in Table 6.1. However, surface coverage of it was slightly less than film B presumably because of small shifting of the voltage of Ag/AgCl reference electrode during electrodeposition of PANI used at different days. Therefore, the starting point of the polymerisation of aniline (*ca.* 5 mV – 10 mV) could be shifted. This causes different surface coverage even with the same conditions (potential window, scan rate, number of scans). All films, grown with the same as the conditions given in Table 6.1 but had different surface coverage, were labelled with digits after film name (*e.g.* film B2). During switching of film B2, the temperature of the cell was increased from 20 ± 2 °C to 50 °C using a homemade

designed cell to see mass change during increase in temperature. The homemade designed cell for high temperature experiment was shown in chapter three.

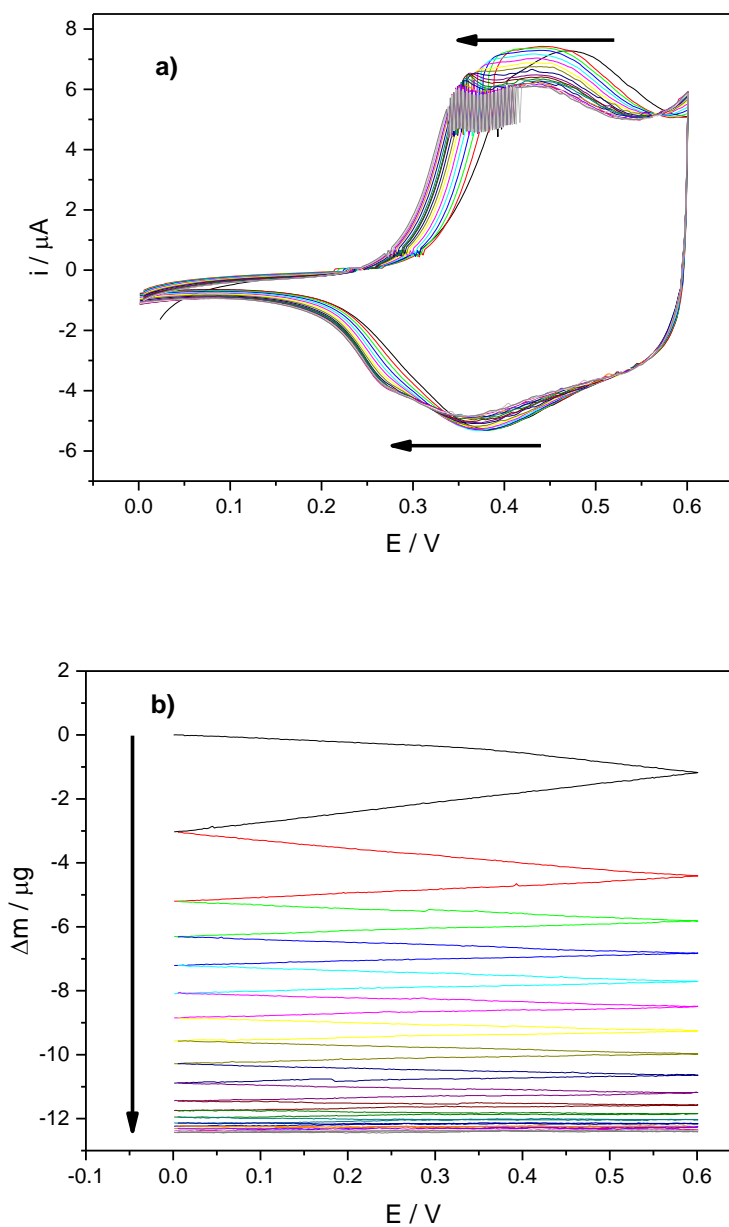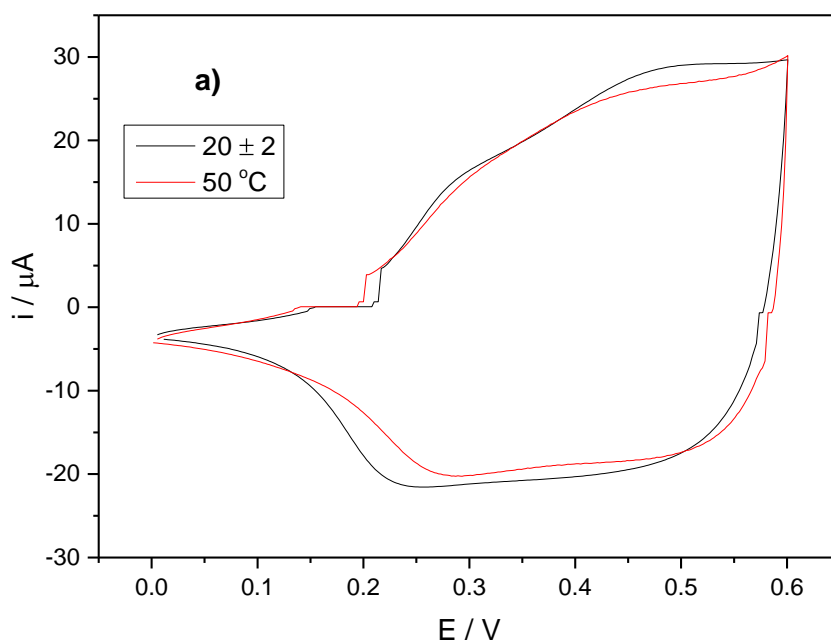*Figure 6.19: EQCM data for redox switching of film B2 deposited at 20 ± 2 °C exposed to Ethaline (v = 10 mV s^{-1}, 20 scans). During the cycling, the water bath temperature was increased from 20 ± 2 °C to 50 °C. a) i vs. E; b) Δm vs. E. The arrows indicate the direction of current peak shifting and mass decreasing from 1st to 20th cycle.*

Panel a of Figure 6.19 illustrates that the cyclic voltammogram of PANI responses did not change significantly during the increase in temperature of electrolyte. Panel b of Figure 6.19 shows that the viscously coupled mass decreased (> 12 μg). Indeed this decrease could not be real mass loss of PANI film but was the viscosity change of Ethaline electrolyte. Viscosity of DESs decreases with increasing temperature as explained in chapter five. The decrease in viscosity (with increasing temperature) causes an increase in the frequency and the admittance of the quartz as the mechanical resistance (impedance) on the quartz decreases. Increase in frequency is proportionally related to decrease in mass (the Sauerbrey equation). Therefore, mass decrease of film B2, presented in panel b of Figure 6.19, was not related to electrochemical reaction it was because of the viscosity change during increase in temperature of Ethaline. As viscosity effect is sufficiently large, mass and viscosity effect could be separated. It would be better to compare for each temperature after Ethaline is cycled several times in high temperature. Figure 6.20 shows EQCM responses of PANI film B2 cycling in Ethaline electrolyte (after 8000 scans) from 0 V to 0.6 V at a scan rate of 50 mV s^{-1} at different temperatures (20 ± 2 °C and 50 °C).
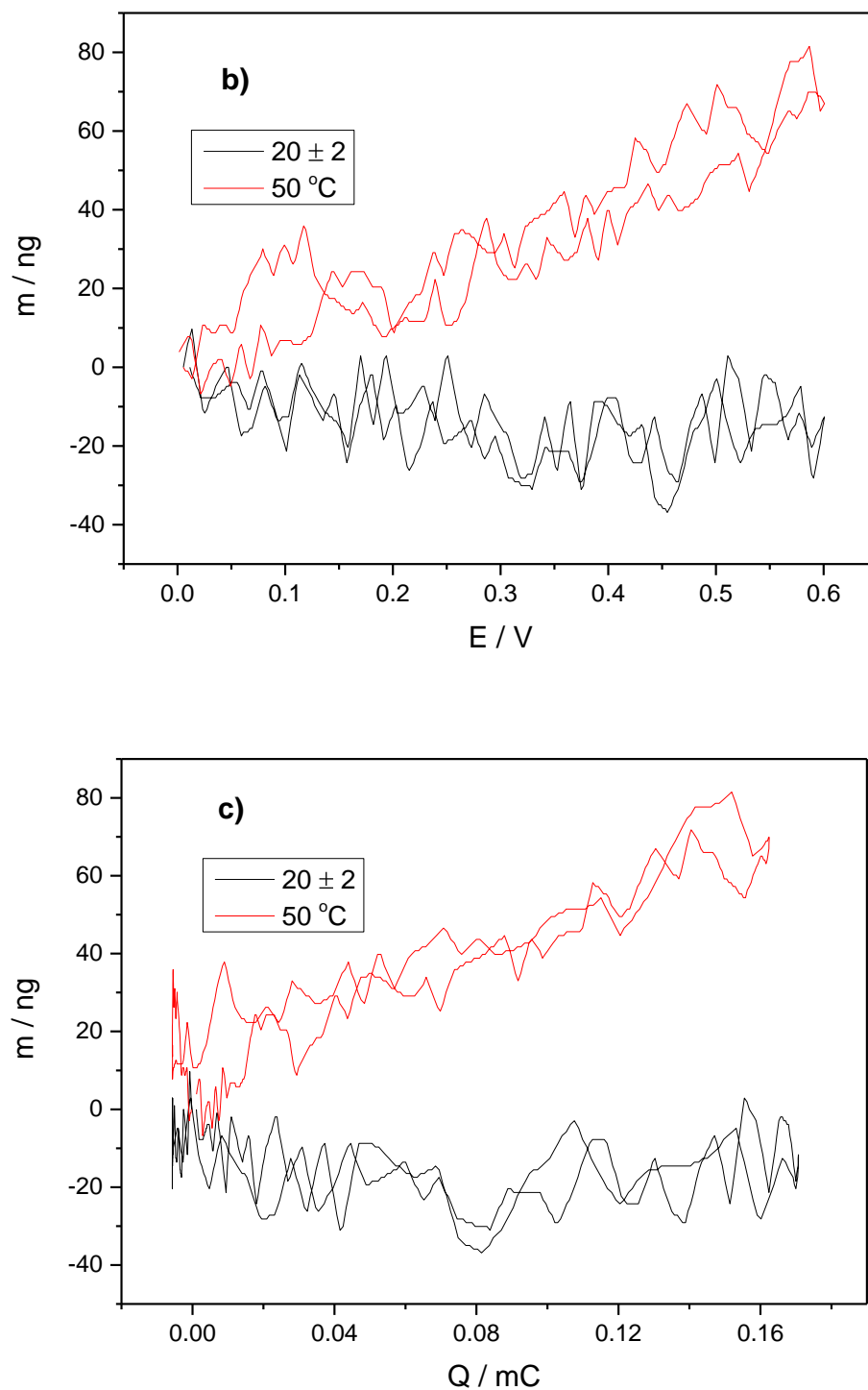
Figure 6.20: EQCM data for redox switching of film B2 (Γ = 29 nmol cm^{-2}) exposed to Ethaline (v = 50 mV s^{-1}). a) i vs. E; b) Δm vs. E. black line is the results of the film B2 conducted at 20 ± 2°C , red line is the results of the same film conducted at 50 °C.

Cyclic voltammetric responses of PANI, cycling in Ethaline at 20 ± 2 °C and 50 °C, were identical as presented in panel a of Figure 6.20. However, charges (area under cyclic voltammogram curve) of PANI film cycling in Ethaline at different temperature were not the same at all the time for all the films produced, sometimes decreasing and sometimes increasing depending on the film used.

Mass change data, corresponding the cyclic voltammogram given in panel a of Figure 6.20, were very different during redox cycling at different temperatures as presented in panel b of Figure 6.20. While the mass slightly decreased during oxidation of film B2 at 20 ± 2 °C (as seen in previous sections as well), the mass of the same film increased at 50 °C which was typical of an anion dominated reaction. The movement of ions in conducting polymers, throughout redox switching, could be affected by the temperature of solution. Polypyrrole cycled with different dopants (p-toluene sulfonate, dodecylsulfate and dodecylbenzenesulfonate counterions) at different solution temperatures (2 °C and 60 °C) was investigated and temperature of electrolyte significantly affects the ion-exchange properties,[79] but more studies for other conducting polymers are required to understand the effect of electrolyte temperature. Here, it has been shown that temperature of Ethaline also affects the PANI ion-exchange dynamics. M_m of exchanged ions were 41 g mol^{-1} and -12 g mol^{-1} for 50 °C and 20 ± 2 °C experiments, respectively calculated from panel c of Figure 6.20. Therefore, the fraction of Ch$^+$ for 50 °C was 0.45 and less than for 20 ± 2 °C experiment which was 0.65. Throughout redox switching of film B2, ingress of EG$_2$Cl$^-$ is faster than egress of Ch$^+$ at high temperature. For all experiments, conducted both at 20 ± 2 °C and 50 °C, fraction of Ch$^+$ egress decreased to some extent with increasing temperature but just some representative data sets were shown in this section since there are some other parameters, such as scan rate, growth conditions and surface coverage which also affect fractions of ions as described above. The mass changing behaviour of some PANI films, cycled at high temperatures, were found to be dependent on scan rate as well.

6.2.2.7. Effect of Potential Window

When cyclic voltammetry is used for the measurement of E-i-t, three parameters are varied: the number of scans, scan rate and potential window depending on working electrode (modified PANI film) and electrolyte (Ethaline). The effect of the numbers of scans and scan rate were presented in section 6.2.2.1 and 6.2.2.4 respectively. Figure 6.21 shows the EQCM responses of film H cycling in Ethaline between different potential windows at a scan rate of 50 mV s^{-1}.

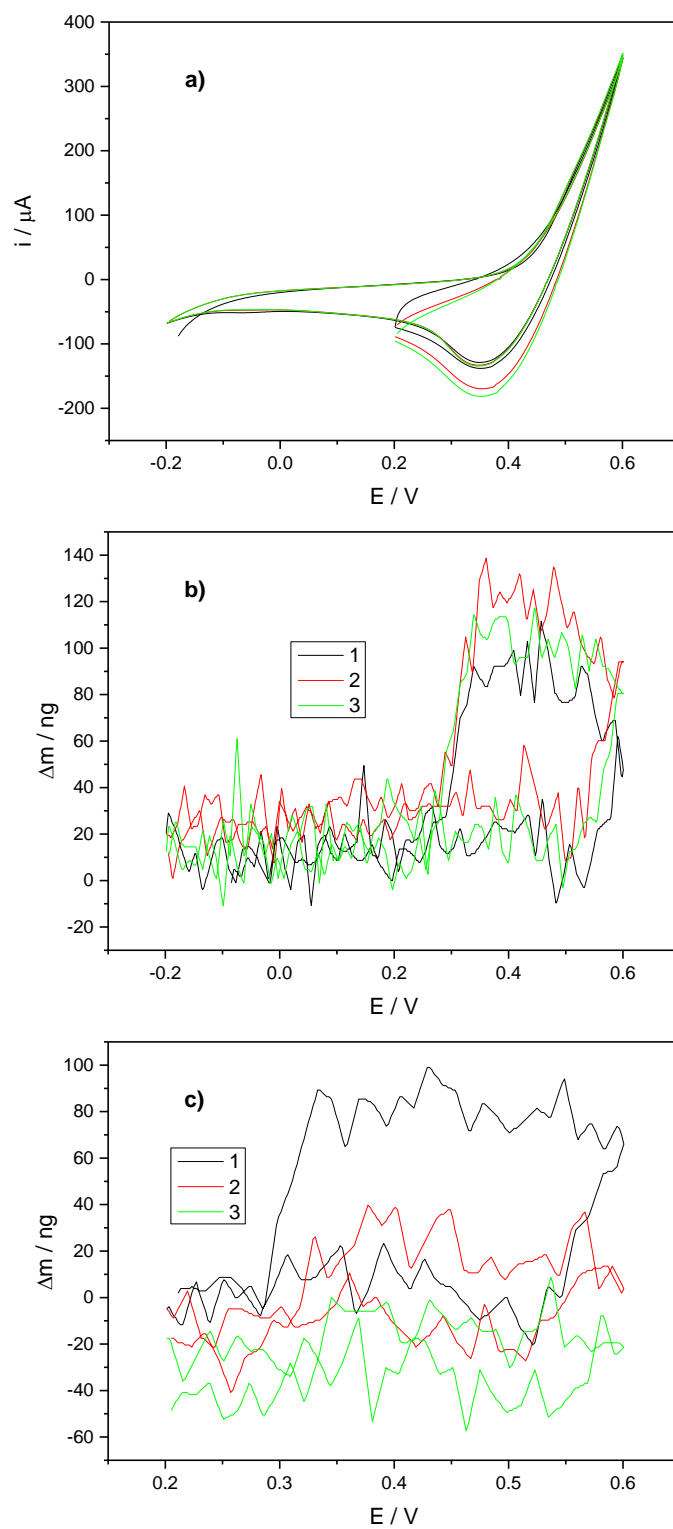*Figure 6.21: EQCM data for redox switching of film H (Γ = 354 nmol cm^{-2}) exposed to Ethaline (v = 50 mV s^{-1}), with different potential windows. a) i-E of PANI cycled from -0.2 V to 0.6 V and from 0.2 V to 0.6 V; b) Δm-E for the experiment conducted between -0.2 V and 0.6 V potential window; c) Δm-E for the experiment conducted between 0.2 V and 0.6 V potential window.*

Panel a of Figure 6.21 shows cyclic voltammogram responses of PANI film (2000 scans), cycled between different potential windows, have the same oxidation current and reduction peaks. Panel b Figure 6.21 illustrates the mass changing of the film, during redox switching between -0.2 V and 0.6 V, are identical for all scans but the first three scans are shown here to represent the data. The mass for three scans increased until about 100 ng. Panel c of Figure 6.21 shows first cycling of PANI, in Ethaline from 0.2 V to 0.6 V, had the same mass changing behaviour with panel b of Figure 6.21 results up to around 100 ng. However, the mass change during the 2nd and 3rd scans of PANI, presented in panel c of Figure 6.21, were different (scattering around +20 ng and -40 ng), did not increase as much as it increased during the first scan. When a wide potential window was applied, ion exchange could be at equilibrium (with the relaxation of the polymers) and the mass change of PANI could be the same for all number of scans presented in panel b of Figure 6.21. However, the PANI film could not be fully returned to its initial stage at narrow potential window as there was not enough time for the configurational change of PANI film. Thus, mass change behaviours of PANI could differ from the first scan, given in panel c of Figure 6.21. Mass change, as expected, occurs at the potential range where the redox reaction is driven and hence the effect of potential window is not often great. It could be important just when polymer relaxation takes long time.

6.2.3.   PANI Redox Cycling in Other DESs

6.2.3.1.   Changing Medium of Film

It must be ascertained that the PANI films, whose ion transfers were studied in Ethaline, return their initial form so that ion transfer dynamics in different DESs can be studied. The current responses of PANI film E2 (Γ = 29 nmol cm^{-2}) in aqueous monomer-free electrolyte (1 M H_2SO_4), before and after cycling in Ethaline, are shown Figure 6.22.
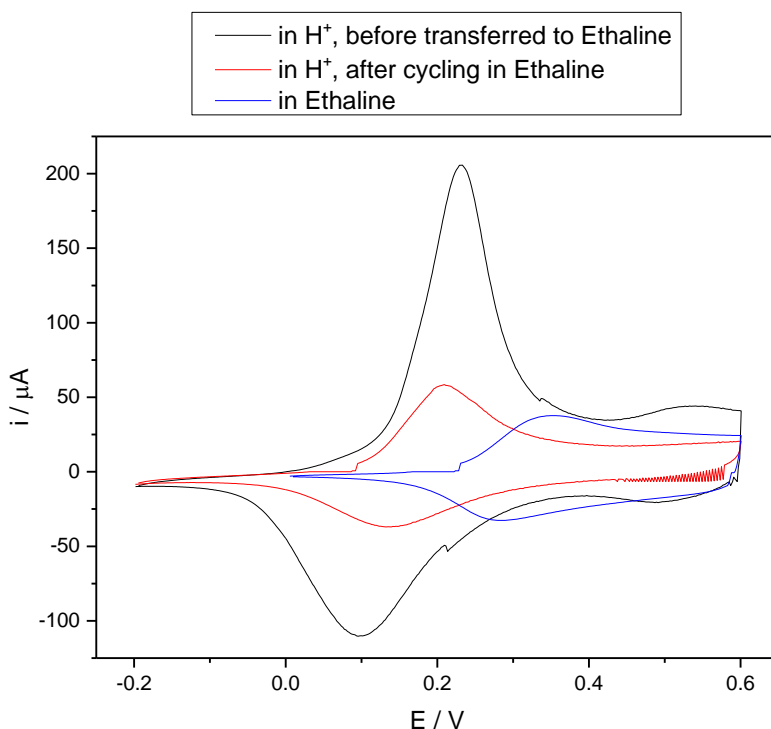
Figure 6.22: Cyclic voltammetric responses of film E2 (Γ = 29 nmol cm^{-2}) (v = 50 mV s^{-1}).
Black line: freshly prepared PANI film in 1 M H$_2$SO$_4$ cycled from -0.2 V to 0.6 V (vs. Ag/AgCl
RE) before transferring to ethaline; blue line: PANI film in Ethaline cycled from 0 V to 0.6 V
(vs. Ag wire pseudo RE); red line: PANI film in 1 M H$_2$SO$_4$ cycled from -0.2 V to 0.6 V (vs.
Ag/AgCl RE) after cycling in Ethaline.

A freshly prepared film E2 was cycled in monomer-free solution and its cyclic voltammogram is presented as a black line in Figure 6.22. This film was transferred into Ethaline to cycle more than 100 times (blue line of Figure 6.22). It is known that diffusion coefficient values decrease with increasing viscosity of electrolyte[80, 81]. After the charge and mass responses of film E2 reach a steady-state form, it retransferred to monomer-free solution (red line of Figure 6.22) to compare with freshly prepared film in 1 M H$_2$SO$_4$ before cycling in Ethaline. As shown in Figure 6.22, while the oxidation current peak of the film before cycling in Ethaline was 206 µA, after cycling with Ethaline it was 59 µA in 1 M H$_2$SO$_4$ when a scan rate of 50 mV s^{-1} applied indicating a decrease in current response of PANI. This difference was arisen from the presence of Ethaline ions retained in PANI. Because of this PANI, retransferred to 1 M H$_2$SO$_4$, was cation dominated not similar to PANI in aqueous acidic solution (anion dominated

shown in section 4.2.4.6.1) was similar to Ethaline in PANI (significant *memory effect*). Although the film, after cycling in Ethaline, was washed several times before retransferring into 1 M H_2SO_4, Ethaline in PANI voids could not be removed completely and the film could not be regenerated to use for new experiment. Therefore; the PANI film, transferred to one of the DESs, cannot be used for another DES and a fresh PANI film should be prepared for the analysis of each DES.

6.2.3.2. Effect of Electrolyte Composition

PANI films were studied in Ethaline, selected as a model electrolyte, to show the effect of experimental parameters (the effect of scan rate, the temperature of electrolyte, the thickness of the film, the growth conditions of film) during redox cycling in previous sections. Here, the EQCM analysis of freshly prepared PANI films transferred to different DESs with different ion sizes will be observed.

The growth conditions of PANI films, used in different DESs presented in this section, are the same as film B shown in Table 6.1. Since the surface coverage of these films could be slightly different, their coverage will be shown in the parentheses.

6.2.3.2.1. Glyceline (Choline Chloride + Glycerol)

The EQCM experiment data, acquired from redox switching of PANI film B3 (Γ = 32 nmol cm^{-2}) exposed to Glyceline, are shown in Figure 6.23.

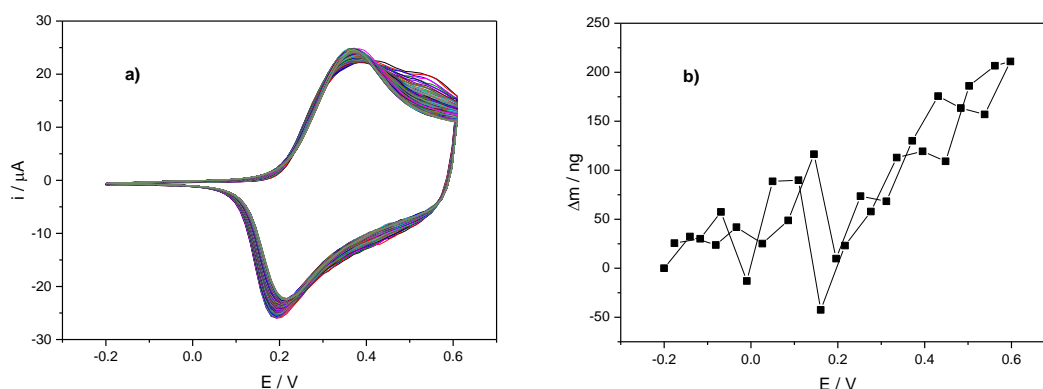*Figure 6.23: EQCM data for redox switching of a PANI film B3 (Γ = 32 nmol cm^{-2}) exposed to Glyceline (v= 10 mV s^{-1}) at 50 °C. a) i vs. E from 1st to 300th scans; b) Δm vs. E data of 100th scan.*

The experiment of PANI cycling in Glyceline was conducted at high temperature (50 °C). Electrochemical stability of PANI exposed to Glyceline is high. Over 300 cycles there is no significant change in the shape of cyclic voltammetric curve shown in panel a of Figure 6.23. An anion dominated reaction ($M_m = 18$ g mol^{-1}) is seen for PANI cycled in Glyceline, given in panel b of Figure 6.23, similar to Ethaline at 50 °C. M_m of ion exchange is presented in Table 6.8 (page 237) for comparison with other electrolyte.

6.2.3.2.2. Propaline (Choline Chloride + Propylene Glycol)

Propaline is found as liquid at room conditions shown in Figure 3.2. However, Propaline starts to be crystallised at 20 ± 2 °C when touching PANI film (typically in an hour) presented in Figure 3.2. The theory of the solidification of ionic liquids was discussed elsewhere.[82] Here, the electrochemical performance of PANI in Propaline was studied at 50 °C to have the same conditions as Glyceline electrolyte given in section 6.2.3.2.1. The EQCM data, for redox switching of PANI film B4 ($\Gamma = 35$ nmol cm^{-2}) exposed to Propaline at a scan rate of 10 mV s^{-1}, is given in Figure 6.24.
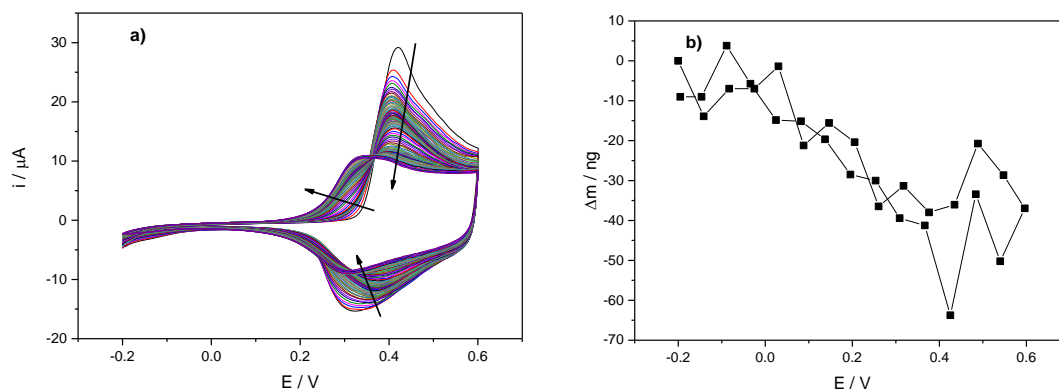

Figure 6.24: EQCM data for redox switching of a PANI film B4 ($\Gamma = 35$ nmol cm^{-2}) exposed to Propaline (v = 10 mV s^{-1}) at 50 °C. a) i vs. E from 1st to 100th scans; b) Δm vs. E data of 100th scan. The arrows indicate the direction of current with scans

Mass change of the 100th cycle of PANI in Propaline is presented here to compare with Ethaline (given in section 6.2.2 in detail) and Glyceline electrolytes (in section 6.2.3.2.1). Panel a of Figure 6.24 shows that the electroactivity of PANI in Propaline

decreased significantly up to a point (around 50th scan). After this point it was stable. The steady-state mass changing of PANI cycled in Propaline was picked up to compare with other electrolytes (shown in panel b of Figure 6.24). Mass decreasing of the film is the indication of a cation dominated reaction as indicated previously. Panel b of Figure 6.24 shows that PANI cycled in Propaline was a cation dominated reaction. However, PANI cycled in Ethaline and Glyceline at 50 °C was anion dominated reaction. Their M_m values are given in Table 6.8. Their ion fraction throughout redox switching could be calculated using Eq 6. 1. The rationale behind changing electrolyte (given in this section) is to show that the compositions of DESs also strongly affect the dynamics of PANI reaction in DESs. Therefore, detailed analysis is not conducted for different electrolyte since there are other effects as aforementioned in section 6.2.2.

6.2.3.2.3. Reline (Choline Chloride + Urea)

Figure 6.25 shows cyclic voltammogram responses of PANI film B5 (Γ = 37 nmol cm^{-2}) exposed to Reline electrolyte by cycling between -0.2 V and 0.6 V with 50 scans 20 ± 2 °C.
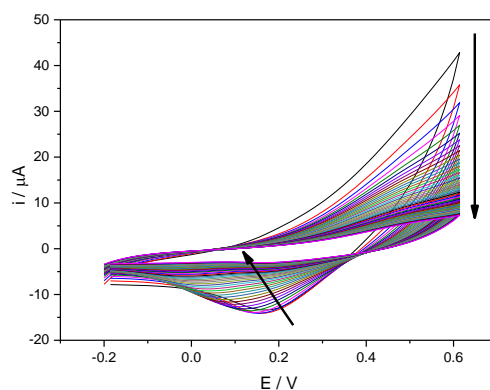
Figure 6.25: Cyclic voltammogram responses of PANI film B5 (Γ = 37 nmol cm^{-2}) cycled in Reline (v = 50 mV s^{-1}). The arrows indicate the direction of current with scans.

An oxidation peak was not observed for the oxidation of film B5 (Γ = 37 nmol cm^{-2}), cycled in Reline shown in Figure 6.25, at a scan rate of 10 mV s^{-1}. However, there was an oxidation peak for the PANI film in Ethaline (panel a of Figure 6.4), Glyceline (panel

a of Figure 6.23) and Propaline (panel a of Figure 6.24). As it was previously mentioned that diffusion coefficients value decreases with increasing viscosity of electrolyte.[80, 81] Reline viscosity is *ca.* 20 times higher than Ethaline (given in chapter five); hence diffusion of ions in Reline is slower than ions in Ethaline.

Figure 6.25 clearly shows that the current peaks for reduction of PANI decreased significantly with increasing number of scans. Electrochemical activity of PANI in Reline completely disappeared after 15 scans as presented in Figure 6.25. Several different films were prepared to investigate whether it is because of *the effect of growth conditions* or something else. However, current for all different films (therefore charge) decreased quickly. While the electrochemical stability of PANI films in Ethaline is high (tens of thousands of cycles) shown in Figure 6.4, PANI films in Reline deteriorated very quickly. At the beginning of the cycling the colour of the film in Reline was yellow-green, similar to PANI in Ethaline. The film colour was black at the end of the first oxidation cycle of PANI cycled in Reline. When oxidised PANI (emeraldine or pernigraniline) film is immersed in solution (pH > 4), the films turn to black and it cannot switch colour.[83, 84] PANI, oxidised in Reline, also did not return to its previous colour (yellow-green). However, any colour change was not observed by naked eye during redox switching of PANI film in Ethaline, Glyceline, Propaline and Wateline: they were greenish yellow. The only difference between Reline and other DESs (Ethaline, Glyceline, Propaline) is their HBDs. While Reline has amino group (urea) in its composition, Ethaline (or Glyceline, Propaline) has a hydroxyl group as shown in chapter three. Probably Reline, which has amino group, could stick strongly into the structure of PANI chains during oxidation and could not have ion exchange throughout switching. This can be deduced from the film colour change to black which is the indication of the formation of irreversible emeraldine salt form of PANI.

6.2.3.2.4.   Wateline (Choline Chloride +Water)

Figure 6.26 illustrates the cyclic voltammetric data for redox switching (400 times) of PANI film B6 (Γ = 36 nmol cm^{-2}) exposed to Wateline at a scan rate of 10 mV s^{-1} at 50 °C.
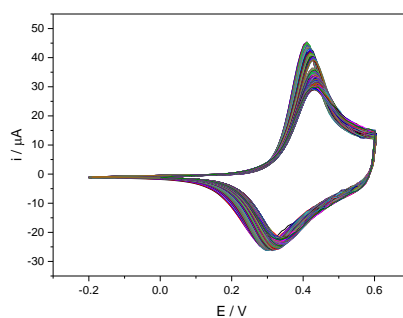
Figure 6.26: Cyclic voltammogram of film B6 (Γ = 36 nmol cm^{-2}) cycled in wateline (v = 10 mV s^{-1}) at 50 °C. The highest current peak is the first cycle.

Normally, Wateline is not crystallised at 20 ± 2 °C. However, a PANI film, in contact with Wateline, could facilitate nucleation of solidification of Wateline. Due to this reason, there is not much study in literature when compared with Ethaline, Reline and Glyceline.[85-87] Wateline, converted to its crystallised form at 20 ± 2 °C in PANI; was heated up to 50 °C for redox reaction. Figure 6.26 shows that the electrochemical stability of PANI films in Wateline is high. M_m of ion exchange for PANI film in Wateline is -2 g mol^{-1} presented in Table 6.8. Ion size order of HBD is Glyceline > Propaline > Ethaline > Wateline. However, M_m cannot have the same (or opposite) trend of this order. Therefore M_m of ion exchange in PANI is independent of ion sizes of electrolytes.

Table 6.8: M_m of ion exchange for the 100th scan of oxidation of PANI films in different electrolyte. Films are given in the text. v = 10 mV s^{-1}.

DESs	Glyceline	Propaline	Reline	Wateline
M_m / g mol^{-1}	18	-7	n/a	-2

Since Propaline and Wateline are crystallised in 20 ± 2 °C, one could suppose that these electrolytes could not be used in real life energy storage application. To investigate to how extend they could be used at 20 ± 2 °C, PANI was cycled in Wateline at 20 ± 2 °C at a scan rate of 10 mV s^{-1}, shown in panel a of Figure 6.27.
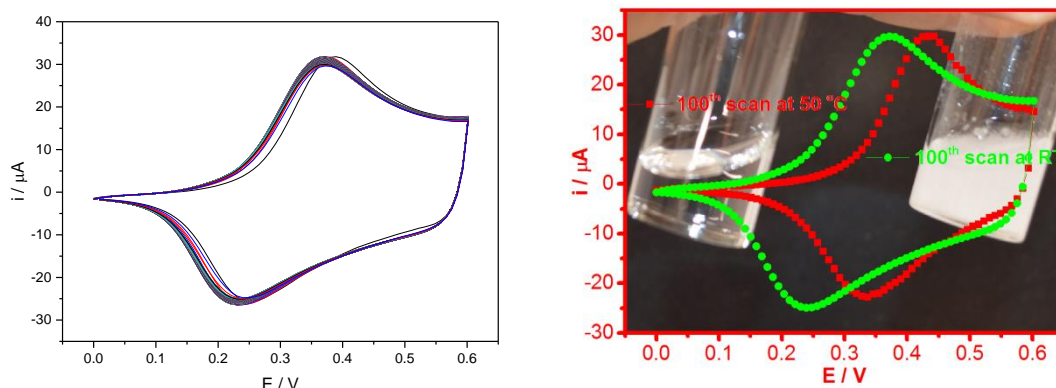
Figure 6.27: Cyclic voltammetric response of redox switching of PANI film B6 (Γ = 36 nmol cm^{-2}) exposed to Wateline (v = 10 mV s^{-1}) a) at 20 ± 2 °C, crystallized Wateline; b) comparison of temperature of electrolyte, red line is 50 °C, green line is the analysis conducted at 20 ± 2 °C.

PANI in crystallised Wateline has an excellent stability (no change up to 300 scans) shown in panel a of Figure 6.27. It means that even if DESs electrolyte were crystallised in supercapacitors, it would not cause electrochemical problems. Panel b of Figure 6.27 shows the difference of cyclic voltammetric responses when the temperatures of electrolytes were changed. The area of cyclic voltammetry curve (charge) of PANI cycled in crystallised Wateline was significantly larger than PANI cycled in high temperature Wateline (50 °C). Therefore, the capacitance of PANI film at 20 ± 2 °C (crystallisation of) Wateline is surprisingly higher than the capacitance of the same film in 50 °C Wateline. Specific capacitance of PANI film increased significantly with decreasing the temperature of Propaline as well.

6.3. Conclusions

Medium of PANI does not have to be acidic to have a redox reaction. When the PANI film is oxidised in Ethaline (with no protonation/deprotonation in Ethaline), the form of PANI is converted from leucoemeraldine salt to emeraldine salt and *vice versa* during reduction of PANI.

When PANI films, prepared from aqueous solution, are transferred to DESs; equilibration of the film in Ethaline takes a long time. This time range is broad ranging from tens to thousands of scans. All PANI films are evolved in Ethaline. While the mass direction of thin PANI films (typically less than 50 nmol cm^{-2}), during redox switching, changes from anion transfer domination to cation transfer domination; the evolution of ion transfer characteristics of thick PANI (typically more than 50 nmol cm^{-2}) films is slower.

PANI films of lower surface coverage were more likely to be a surface controlled process than PANI films of higher surface coverage. However, the mechanism of ion-exchange does not just depend on surface coverage but also depends on the growth conditions of the films. Small differences during growth of PANI films (scan rate, potential window) could cause big differences (because of structural or morphological variations) in switching responses of PANI in Ethaline. This could be used to control the behaviour of supercapacitors: some films of higher coverage could be just surface controlled reaction in DESs rather than some films of lower coverage due to effect of growth conditions.

There are salts (ions of DESs) inside the film and the oxidation progress of PANI in Ethaline consists of Ch$^+$ egress. Molar mass of ion exchange during redox switching of PANI in Ethaline is more negative for thinner films. Thicker films could retain more salts inside the void of polymer branches. On short timescales (high scan rate), Ch$^+$ could not diffuse out from the thick films and hence there is no overall mass changing of PANI film throughout redox switching at high scan rates ($v > 100$ mV s^{-1}). On longer timescales: after EG$_2$Cl$^-$ ions produces salt with PANI chain, Ch$^+$ ions could diffuse out from the film. In this case, it could be concluded that there is sufficient time to extract Ch$^+$ out of the PANI film and mass changing of PANI film is high during redox switching of PANI in Ethaline at slow scan rates ($v < 20$ mV s^{-1}).

A specific capacitance value of 803 F g^{-1} was obtained from PANI cycling in Ethaline which is only 61% of the theoretical value. The decreasing of specific capacitance of PANI is small with increasing scan rate indicating high power density of the materials. Excellent stability (more than 30 000 cycles) of PANI films in DESs was demonstrated.

While the mass change of the film in Ethaline is independent of scan rate for some films (with a linear Δm-Q slope), it is also possible that mass direction is dependent on scan rate (generally for thick films) depending on the growth conditions of the film. The range of the fraction of Ch^+ egress, during redox switching of different PANI films in different DESs, is between 0.45 and 0.87 ($\Delta mF/Q$ values from 44 g mol^{-1} to -69 g mol^{-1}) for all variable parameters (scan rate, temperature) applied.

PANI film does not evolve with waiting time under open-circuit conditions, polymer equilibrium in Ethaline needs electrochemical reaction (redox cycling). PANI film in Ethaline is stable without redox reaction (waiting time).

Although cyclic voltammograms of PANI in Ethaline at different temperatures are identical, ion dynamics are different with changing the temperature of the electrolyte. The fraction of Ch^+ egress decreases with increasing the temperature of Ethaline. Therefore, EG_2Cl^- ion movement in PANI, during redox switching in Ethaline, is faster at higher temperature.

The potential window of the experiments can restrict ion-exchange dynamics. The polymer can relax and reach equilibrium at wider potential window. However, ion movement could not reach equilibrium with film relaxation for some films at narrow potential window because of insufficient timescale.

Once PANI, deposited from aqueous solution, was evolved with Ethaline; its electrochemical performance in monomer-free electrolyte is lower than fresh PANI (without transferring to DESs) in acidic medium.

PANI film has excellent electrochemical stability in Glyceline and Wateline. However, its electrochemical stability decrease in Propaline up to a point and after that it has constant electrochemical performance. PANI film cycling in Reline loses its electrochemical activity due to the amino group of the HBD (urea) in Reline. While no colour change was observed by naked eye throughout redox switching of PANI cycled in Ethaline, Glyceline, Wateline and Propaline; PANI did not return to its previous colour (greenish-yellow) after the first oxidation half cycle in Ethaline (black).

While Glyceline ion dynamics in PANI film are similar to Ethaline in the PANI film at 50 °C (anion dominated), PANI film in Propaline (the same conditions with PANI in Glyceline) is cation dominated reaction. This shows the type of HBD forming electrolyte strongly affects the dynamic of PANI reaction in DESs. The fractions of ions in different electrolytes are independent of ion size of DESs component.

The electrochemical activity (specific capacitance) of PANI films is higher at 20 ± 2 °C Wateline (crystallization form) than high temperature Wateline (liquid) for the same film. Propaline shows the same behaviour (higher performance in crystallize Propaline) as well.

High specific capacitance, high power density, excellent stability, usability at 20 ± 2 °C (crystallization of DESs) and no evolution without electrochemical reaction make DESs a promising electrolyte candidate for conducting polymer based pseudocapacitor applications.

6.4. References

1 H. Shirakawa, E. J. Louis, A. G. MacDiarmid, C. K. Chiang and A. J. Heeger, *J.Chem.Soc., Chem.Commun.,* 1977, **16**, 578-580.

2 T. Park, C. Park, B. Kim, H. Shin and E. Kim, *Energy & Environmental Science,* 2013, **6**, 788-792.

3 K. Gurunathan, A. V. Murugan, R. Marimuthu, U. Mulik and D. Amalnerkar, *Mater. Chem. Phys.,* 1999, **61**, 173-191.

4 Y. Xia, K. Sun and J. Ouyang, *Adv Mater,* 2012, **24**, 2436-2440.

5 O. Bubnova, Z. U. Khan, H. Wang, S. Braun, D. R. Evans, M. Fabretto, P. Hojati-Talemi, D. Dagnelund, J. Arlin and Y. H. Geerts, *Nature materials,* 2014, **13**, 190-194.

6 T. Liu, L. Finn, M. Yu, H. Wang, T. Zhai, X. Lu, Y. Tong and Y. Li, *Nano letters,* 2014, **14**, 2522-2527.

7 B. Friedel, P. E. Keivanidis, T. J. Brenner, A. Abrusci, C. R. McNeill, R. H. Friend and N. C. Greenham, *Macromolecules,* 2009, **42**, 6741-6747.

8 N. S. Sariciftci, L. Smilowitz, A. J. Heeger and F. Wudl, *Science,* 1992, **258**, 1474-1476.

9 J. A. Chang, J. H. Rhee, S. H. Im, Y. H. Lee, H. Kim, S. I. Seok, M. K. Nazeeruddin and M. Gratzel, *Nano letters,* 2010, **10**, 2609-2612.

10 H. Klauk, *Chem. Soc. Rev.,* 2010, **39**, 2643-2666.

11 S. Nambiar and J. T. Yeow, *Biosensors and Bioelectronics,* 2011, **26**, 1825-1832.

12 K. Chang, H. P. Wang, T. Wu and I. Sun, *Electrochim. Acta,* 2014, **119**, 225-235.

13 Y. Huang, J. Li, X. Chen and X. Wang, *RSC Advances,* **107,** 2014, 62160-62178.

14 C. Peng, K. Chang, C. Weng, M. Lai, C. Hsu, S. Hsu, Y. Hsu, W. Hung, Y. Wei and J. Yeh, *Electrochim. Acta,* 2013, **95**, 192-199.

15 R. Kiefer, R. Temmer, N. Aydemir, J. Travas-Sejdic, A. Aabloo and T. Tamm, *Electrochim. Acta,* 2014, **122**, 322-328.

16 F. Wu, Z. Xu, Y. Wang and M. Wang, *RSC Advances,* 2014, **4**, 38797-38803.

17 A. Guerfi, J. Trottier, I. Boyano, I. De Meatza, J. Blazquez, S. Brewer, K. Ryder, A. Vijh and K. Zaghib, *J. Power Sources,* 2014, **248**, 1099-1104.

18 M. Ferrandon, X. Wang, A. J. Kropf, D. J. Myers, G. Wu, C. M. Johnston and P. Zelenay, *Electrochim. Acta,* 2013, **110**, 282-291.

19 K. Chen, Y. Yang, K. Li, Z. Ma, Y. Zhou and D. Xue, *ACS Sustainable Chemistry & Engineering,* 2013, **2**, 440-444.

20 L. Feng, Y. Zhu, H. Ding and C. Ni, *J. Power Sources,* 2014, **267**, 430-444.

21 T. Christen and M. W. Carlen, *J. Power Sources,* 2000, **91**, 210-216.

22 A. Burke, *J. Power Sources,* 2000, **91**, 37-50.

23 C. Lokhande, D. Dubal and O. Joo, *Current Applied Physics,* 2011, **11**, 255-270.

24 G. Wang, L. Zhang and J. Zhang, *Chem. Soc. Rev.,* 2012, **41**, 797-828.

25 X. Bai, X. Hu, S. Zhou, J. Yan, C. Sun, P. Chen and L. Li, *Electrochim. Acta,* 2013, **87**, 394-400.

26 Y. Hu, Y. Zhao, Y. Li, H. Li, H. Shao and L. Qu, *Electrochim. Acta,* 2012, **66**, 279-286.

27 H. Lin, L. Li, J. Ren, Z. Cai, L. Qiu, Z. Yang and H. Peng, *Scientific reports,* 2013, **3**.

28 Q. Zhang, Y. Li, Y. Feng and W. Feng, *Electrochim. Acta,* 2013, **90**, 95-100.

29 A. Singh and A. Chandra, *J. Appl. Electrochem.,* 2013, **43**, 773-782.

30 Y. Liu, H. Wang, J. Zhou, L. Bian, E. Zhu, J. Hai, J. Tang and W. Tang, *Electrochim. Acta,* 2013, **112**, 44-52.

31 D. Sun, L. Jin, Y. Chen, J. Zhang and J. Zhu, *ChemPlusChem,* 2013, **78**, 227-234.

32 X. Lu, F. Zhang, H. Dou, C. Yuan, S. Yang, L. Hao, L. Shen, L. Zhang and X. Zhang, *Electrochim. Acta,* 2012, **69**, 160-166.

33 C. Sivakumar, J. Nian and H. Teng, *J. Power Sources,* 2005, **144**, 295-301.

34 P. A. Basnayaka, M. K. Ram, E. K. Stefanakos and A. Kumar, *Electrochim. Acta,* 2013, **92**, 376-382.

35 H. Cong, X. Ren, P. Wang and S. Yu, *Energy & Environmental Science,* 2013, **6**, 1185-1191.

36 B. Yue, C. Wang, X. Ding and G. G. Wallace, *Electrochim. Acta,* 2012, **68**, 18-24.

37 K. Wang, H. Wu, Y. Meng and Z. Wei, *Small,* 2014, **10**, 14-31.

38 G. A. Snook, P. Kao and A. S. Best, *J. Power Sources,* 2011, **196**, 1-12.

39 M. Armand and J. Tarascon, *Nature,* 2008, **451**, 652-657.

40 A. Brandt, J. Pires, M. Anouti and A. Balducci, *Electrochim. Acta,* 2013, **108**, 226-231.

41 W. Zaidi, L. Timperman and M. Anouti, *RSC Advances,* 2014, **4**, 45647-45652.

42 A. M. Österholm, D. E. Shen, A. L. Dyer and J. R. Reynolds, *ACS applied materials & interfaces,* 2013, **5**, 13432-13440.

43 G. Bidan, P. Gentile, P. Weathers, F. Thissandier, V. Ruiz, P. Gomez-Romero, T. J. Schubert and H. Sahin, *RSC Advances,* 2014, **50**, 26462-26467.

44 G. Sauerbrey, *Zeitschrift für Physik,* 1959, **155**, 206-222.

45 M. A. Mohamoud and A. R. Hillman, *Electrochim. Acta,* 2007, **53**, 1206-1216.

46 A. R. Hillman, Q. Dong, M. A. Mohamoud and I. Efimov, *Electrochim. Acta,* 2010, **55**, 8142-8153.

47 M. A. Mohamoud and A. R. Hillman, *Journal of Solid State Electrochemistry,* 2007, **11**, 1043-1050.

48 A. R. Hillman, K. S. Ryder, C. J. Zaleski, C. Fullarton and E. L. Smith, *Zeitschrift für Physikalische Chemie International journal of research in physical chemistry and chemical physics,* 2012, **226**, 1049-1068.

49 M. Miras, C. Barbero, R. Kötz and O. Haas, *J Electroanal Chem,* 1994, **369**, 193-197.

50 A. R. Hillman and M. A. Mohamoud, *Electrochim. Acta,* 2006, **51**, 6018-6024.

51 Y. Liu, Z. Su, Y. Zhang, L. Chen, T. Gu, S. Huang, Y. Liu, L. Sun, Q. Xie and S. Yao, *J Electroanal Chem,* 2013, **709**, 19-25.

52 G. Ma, H. Peng, J. Mu, H. Huang, X. Zhou and Z. Lei, *J. Power Sources,* 2013, **229**, 72-78.

53 R. Ramya, R. Sivasubramanian and M. V. Sangaranarayanan, *Electrochim. Acta,* 2013, **101**, 109-129.

54 N. A. Kumar and J. Baek, *Chemical Communications,* 2014, **50**, 6298-6308.

55 H. Zhou, G. Han, Y. Chang, D. Fu and Y. Xiao, *J. Power Sources,* 2014, **267**, 1-8.

56 T. Kobayashi, H. Yoneyama and H. Tamura, *Journal of electroanalytical chemistry and interfacial electrochemistry,* 1984, **161**, 419-423.

57 R. Mazeikiene and A. Malinauskas, *European polymer journal,* 2002, **38**, 1947-1952.

58 C. Zhou, Y. Zhang, Y. Li and J. Liu, *Nano letters,* 2013, **13**, 2078-2085.

59 M. Vilas-Boas, I. C. Santos, M. J. Henderson, C. Freire, A. R. Hillman and E. Vieil, *Langmuir,* 2003, **19**, 7460-7468.

60 A. R. Hillman, K. S. Ryder, C. J. Zaleski, C. Fullarton and E. L. Smith, *Zeitschrift für Physikalische Chemie International journal of research in physical chemistry and chemical physics,* 2012, **226**, 1049-1068.

61 A. R. Hillman, K. S. Ryder, V. C. Ferreira, C. J. Zaleski and E. Vieil, *Electrochim. Acta,* 2013, **110**, 418-427.

62 G. Inzelt, *Electrochim. Acta,* 2000, **45**, 3865-3876.

63 C. Gabrielli, M. Keddam, N. Nadi and H. Perrot, *J Electroanal Chem,* 2000, **485**, 101-113.

64 H. Varela and R. M. Torresi, *J. Electrochem. Soc.,* 2000, **147**, 665-670.

65 C. Weidlich, K. Mangold and K. Jüttner, *Electrochim. Acta,* 2001, **47**, 741-745.

66 S. de Albuquerque Maranhao and R. Torresi, *Electrochim. Acta,* 1999, **44**, 1879-1885.

67 D. Orata and D. A. Buttry, *J. Am. Chem. Soc.,* 1987, **109**, 3574-3581.

68 C. Barbero, M. Miras, O. Haas and R. Kötz, *J. Electrochem. Soc.,* 1991, **138**, 669-672.

69 A. G. MacDiarmid and A. J. Epstein, *Faraday Discuss. Chem. Soc.,* 1989, **88**, 317-332.

70 C. M. Cruz and E. A. Ticianelli, *J Electroanal Chem,* 1997, **428**, 185-192.

71 Z. Ping, H. Neugebauer, J. Theiner and A. Neckel, *Journal of the Chemical Society, Faraday Transactions,* 1997, **93**, 121-129.

72 E. Genies, A. Boyle, M. Lapkowski and C. Tsintavis, *Synth. Met.,* 1990, **36**, 139-182.

73 K. Rajendra Prasad and N. Miura, *Electrochemistry Communications,* 2004, **6**, 1004-1008.

74 M. A. Skopek, M. A. Mohamoud, K. S. Ryder and A. R. Hillman, *Chem. Comm.,* 2009, **8**, 935-937.

75 M. Skompska, A. Jackson and A. R. Hillman, *Physical Chemistry Chemical Physics,* 2000, **2**, 4748-4757.

76 H. Randriamahazaka, C. Plesse, D. Teyssie and C. Chevrot, *Electrochemistry communications,* 2003, **5**, 613-617.

77 A. R. Hillman, I. Efimov and M. Skompska, *Faraday Discuss.,* 2002, **121**, 423-439.

78 M. Skompska, *Electrochim. Acta,* 1998, **44**, 357-362.

79 R. Ansari Khalkhali, W. Price and G. G. Wallace, *React Funct Polym,* 2003, **56**, 141-146.

80 P. Hapiot and C. Lagrost, *Chem. Rev.,* 2008, **108**, 2238-2264.

81 L. Barrosse-Antle, A. Bond, R. Compton, A. Mahony, E. Rogers and D. Silvester, *Chem.Asian J,* 2010, **5**, 202-230.

82 A. Mudring, *Aust. J. Chem.,* 2010, **63**, 544-564.

83 R. Prakash, *J Appl Polym Sci,* 2002, **83**, 378-385.

84 A. Watanabe, K. Mori, Y. Iwasaki, Y. Nakamura and S. Niizuma, *Macromolecules,* 1987, **20**, 1793-1796.

85 D. Carriazo, M. C. Serrano, M. C. Gutiérrez, M. L. Ferrer and F. del Monte, *Chem. Soc. Rev.,* 2012, **41**, 4996-5014.

86 Q. Zhang, K. D. O. Vigier, S. Royer and F. Jérôme, *Chem. Soc. Rev.,* 2012, **41**, 7108-7146.

87 E. L. Smith, A. P. Abbott and K. S. Ryder, *Chem. Rev.,* 2014, **114**, 11060-11082.

Chapter 7: Application of Aniline-based (Co)polymers for Extraction of Fluoride Ion from Water

7.1. Introduction

7.1.1. Overview

Numerous applications of conducting polymers (CP) have been studied in recent years, as described in detail in chapter one. Among these applications, "electrically switched ion exchange" (ESIX) process has not been studied as much as other potential applications including sensors, energy technologies, electroluminescent and electrochromic devices, corrosion protection and electrocatalysis.[1]

ESIX is the exchange of ions between a deposited film on a conducting substrate and electrolyte accompanying the redox switching. In ESIX, an electroactive film can be oxidised (reduced) to lose (gain) electron(s) by modulating the potential of the film and ion uptake/ejection occurs to maintain electroneutrality. The idea is that *charging/discharging in ESIX process, accompanied by the exchange of ions,* can be used for effective water purification.

Several studies using CP based ESIX have been carried out. Saleh *et al.*[2, 3] and Weidlich *et al.*[4-6] tailored polypyrrole as a cation and anion exchanger for water softening. Lin *et al.* used polypyrrole ion exchanger with graphene[7] and carbon nanotubes[8] for removing perchlorate. A P(ANI-OAP) copolymer was also used to remove perchlorate ions from industrial wastewaters.[9] Defluoridation of water was investigated by using PANI[10] and P(ANI-OAP)[11] modified electrode. The work on removing fluoride from water will be extended further in this study.

Fluoridation of water has beneficial effects on dental health therefore; drinking water is fluoridated in some countries.[12] On the other hand high fluoride levels cause some health problems. The recommended limit of fluoride in water by the World Health Organization (WHO, 2004)[13] is 1.5 mg/L; above this, remediation is required. Drinking water containing fluoride at a level greater than 1.5 mg/L, causes skeletal fluorosis,[14] which is a disease of the bone, and results in pain and the damage of bones-joints, in South America and some part of East Asia.[15]

Common methods used to eliminate fluoride from drinking water and wastewater are precipitation (calcium or aluminium salts),[16] membrane techniques (reverse osmosis, nanofiltration, electrodialysis, Donnan dialysis, electrocoagulation),[17] ion exchange[18] and adsorption.[19] These methods have high operational and maintenance costs, toxic by-products and slow and/or complex processes.[20] In this chapter, the study of conducting (co)polymer based ESIX for defluoridation of water will be presented.

7.1.2. Aims and Objectives

The general objectives of the work in this chapter are to understand the dynamic, mechanism, performance and regeneration ability of the (co)polymer films for the defluoridation of water. This has entailed to:

1. Investigate whether PANI, POT, POAP, P(ANI-OT) and P(ANI-OAP) films could remove fluoride from water/wastewater in ESIX process.
2. Study cyclic voltammetry mode of the EQCM of PANI film in fluoride solution at different scan rates and explore the reaction kinetics.
3. Identify the concentration range of fluoride that PANI could extract from aqueous solutions.
4. Examine whether the (co)polymers can be regenerated. If not, investigate the conditions in which extraction is reproducible.
5. Investigate the reusability of PANI and its derivatives for water treatment application based ESIX.
6. Examine the change in the structure of the film after fluoride treatment and regeneration.
7. Compare the performance of the films for ESIX with other defluoridation techniques and other CPs studied for defluoridation.

7.2. Results

All films were grown and characterised in H_2SO_4. The preparation of the films was explained in chapter 4 and the figure references for all films characterisation and growth graphs are given in Table 7.1.

Table 7.1: The figures of growth conditions and characterisation of the (co)polymer films used in this chapter.

| Polymer/copolymer	Growth shown in	Characterisation in H_2SO_4 shown in
PANI	Figure 4.3.	Figure 4.18 panel a
POT	Figure 4.7.	Figure 4.18 panel b
POAP	Figure 4.9	Figure 4.18 panel c
P(ANI-OT) (75:25)	Figure 4.13	Figure 4.20 panel a
P(ANI-OT) (95:5)	Figure 4.14	Figure 4.20 panel b
P(ANI-OAP) (80:20)	Figure 4.15	Figure 4.21 panel a
P(ANI-OAP) (98:2)	Figure 4.17	Figure 4.21 panel b

All film growths (given in Table 7.1) were stopped at the reduced end (E = -0.2 V) and rinsed with deionised water for the investigation of voltammetric behaviour in 0.1 M NaF electrolyte by cycling the voltage from -0.2 V to 0.6 V (*vs.* Ag/AgCl, in saturated solution of potassium chloride) at a scan rate of 50 mV s^{-1} unless otherwise indicated. All experiments were conducted at room temperature (20 ± 2 ^{o}C).

7.2.1. Fluoride Extraction Using (co)Polymer Films

7.2.1.1. Polyaniline

7.2.1.1.1. Cyclic Voltammetry

The electrochemical behaviour of PANI films was investigated using cyclic voltammetry and the EQCM in electrolytes containing 0.1 M fluoride as shown in Figure 7.1.
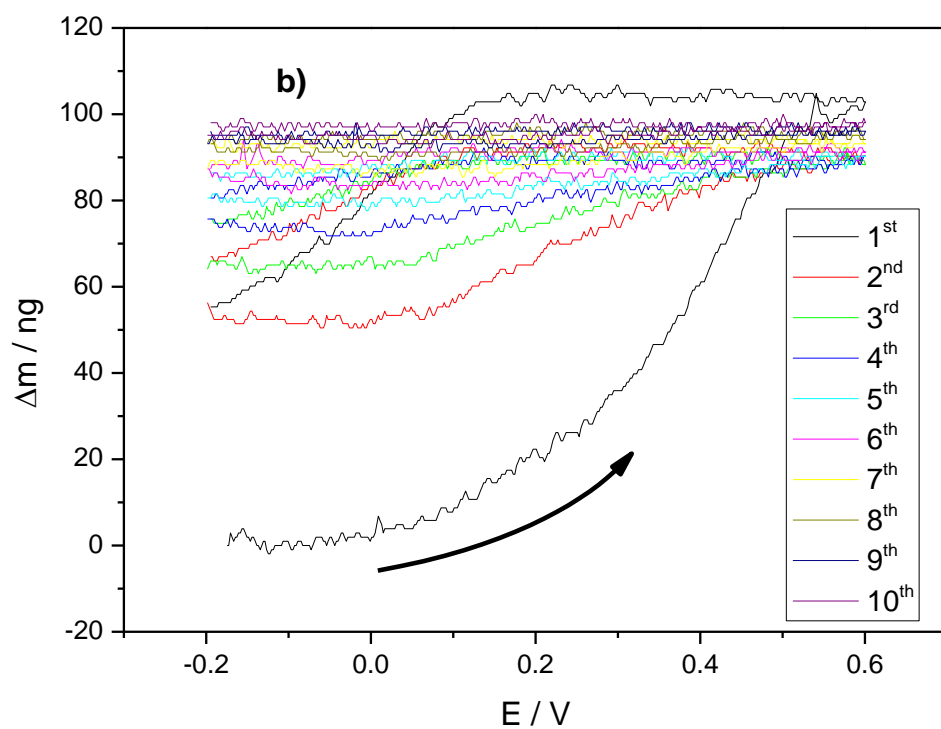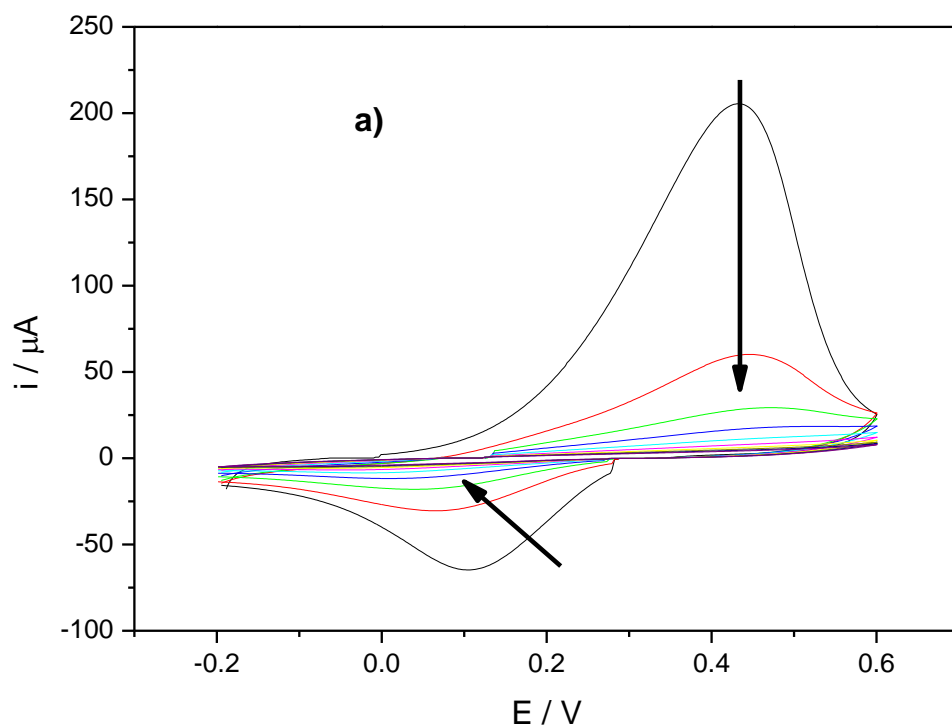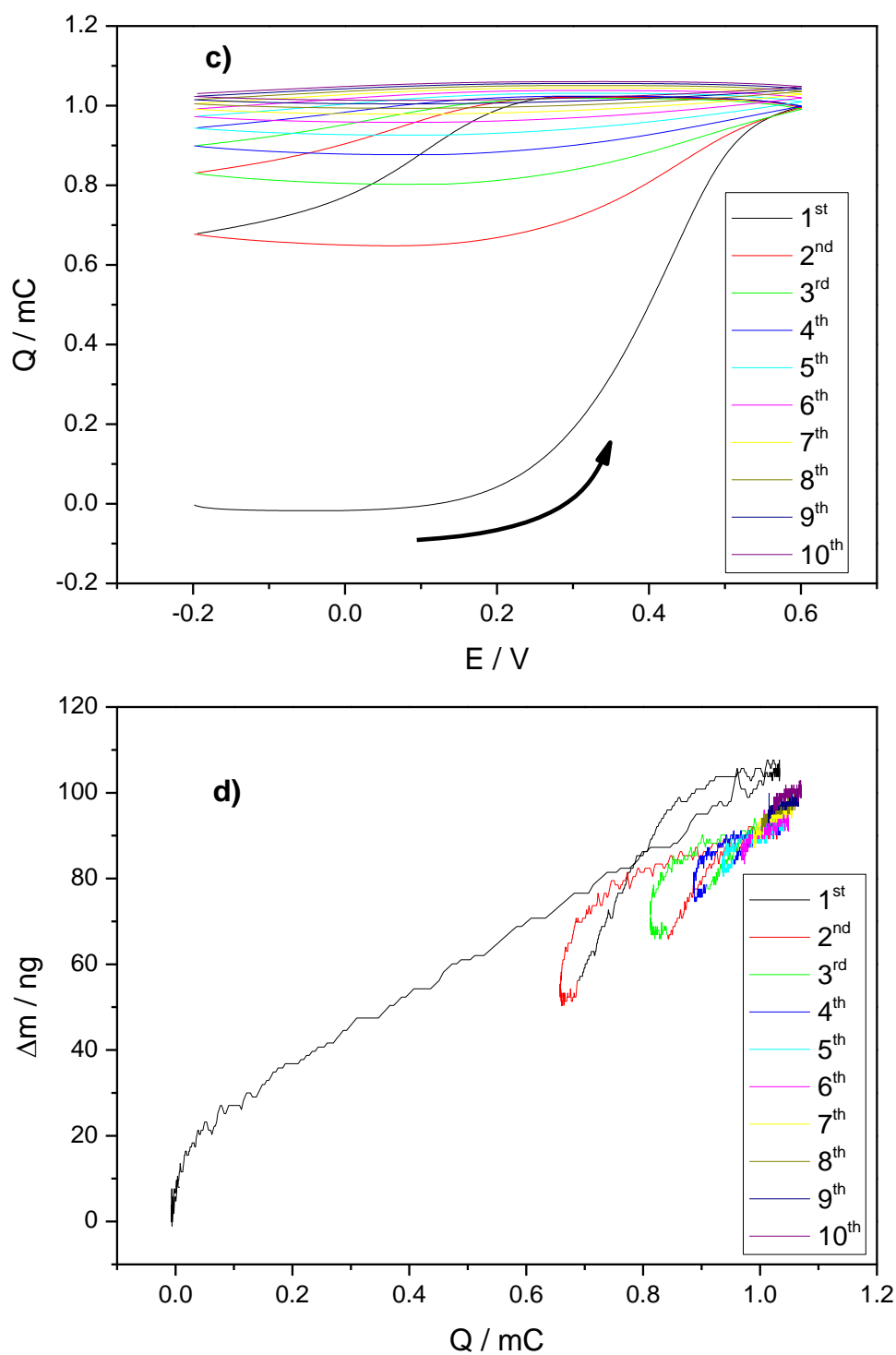
Figure 7.1: EQCM current, charge and mass responses of PANI ($\Gamma = 27.5$ nmol cm^{-2}) in 0.1 M NaF scanned at a scan rate of 50 mVs^{-1}; a)i-E response, arrows indicate direction of current change; b) Δm-E, film mass changes calculated using Sauerbrey Equation, arrow indicates mass increase of first cycle curves; c)Q-E response, the arrow indicates current change of first cycle, d) mass change as a function of charge (from panel b and c), numbers indicate potential scans of response.

A sharp oxidation peak around 0.45 V was observed in panel a of Figure 7.1 corresponding to increasing mass, as shown in panel b of Figure 7.1. PANI oxidation is accompanied by anion uptake to maintain electroneutrality. Hence, the film captures F^- ions in F^- containing solution. It can be attributed to the transformation of Leucoemeraldine Base (LB) to Emeraldine Salt (ES) (mentioned in chapter 1). Normally, PANI undergoes a redox reaction in aqueous acidic medium (typically pH<4).[21] However, the solution here is basic as HF is a weak acid, the pH of a solution of 0.1 M NaF was calculated as 8.6 and it is seen in Figure 7.1, PANI can take anions from a basic solution. However, the charge for reduction of PANI, was much smaller than for oxidation, shown in panel c of Figure 7.1, indicating that all current was not reversed. During oxidation where an electrochemical reaction was observed, PANI film was p-doped (at 0.6 V) and a salt including F^- (ES) was formed and, as seen from panel b of Figure 7.1, the reduction of PANI film cannot force the release of all the F^- anions from the film because medium must be acidic (pH < 4) for electrochemical reversible conversion of ES to LB form of PANI. The colour of PANI film was changed to black after oxidation (p-doped of the film)[22] and kept black after reduction, because ES form of PANI was dominant even at negative potential (at -0.2 V) due to the pH of the electrolyte.

The effect of multiple voltammetric cycles on PANI film in F^- solution, illustrated in Figure 7.1, shows that more F^- was retained in PANI film with each cycle. However, each time F^- entrance ratio decreased. Panel b of Figure 7.1 illustrates that the mass changing for the second cycle (at 0.6 V) was not the same amount as the first cycle but the total charge increased up to the same maximum level. These mass differences were probably from the film relaxation but after 2nd cycle total mass increased up to the same level. Panel d of Figure 7.1 illustrates that after 6 cycles mass and charge were stable. The film was fully saturated with fluoride and there was not a significant electroactive reaction after the 6th cycle.

EQCM data from multiple voltammetric cycles on PANI film in F^- solution ($v = 5$ mV s^{-1}) are given in Figure 7.2. The only difference from the experiment in Figure 7.1 was the scan rate applied to compare time scale.
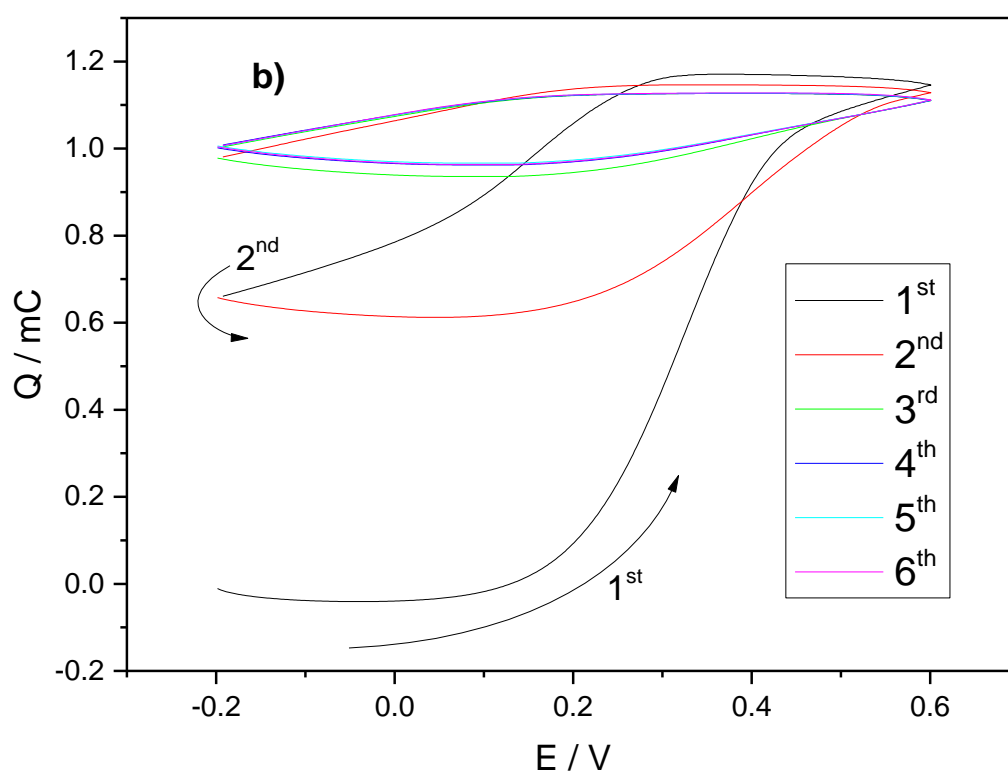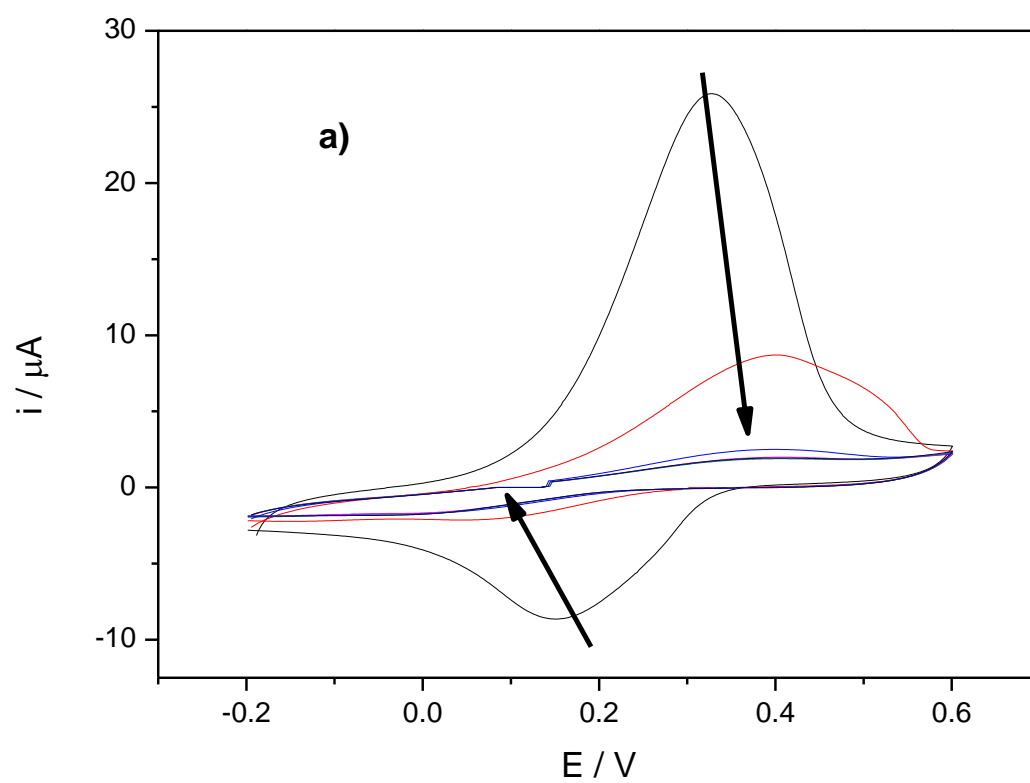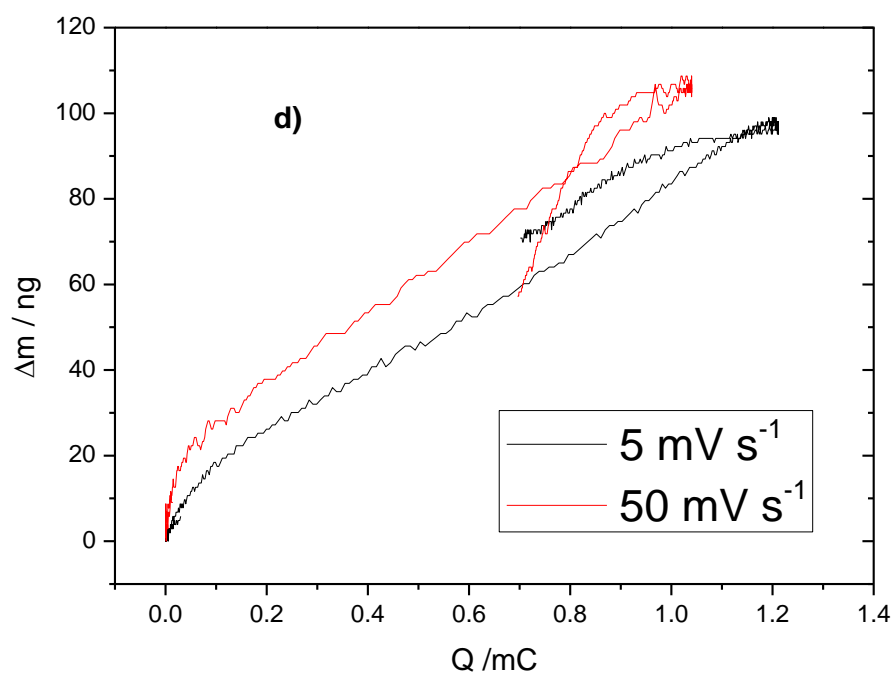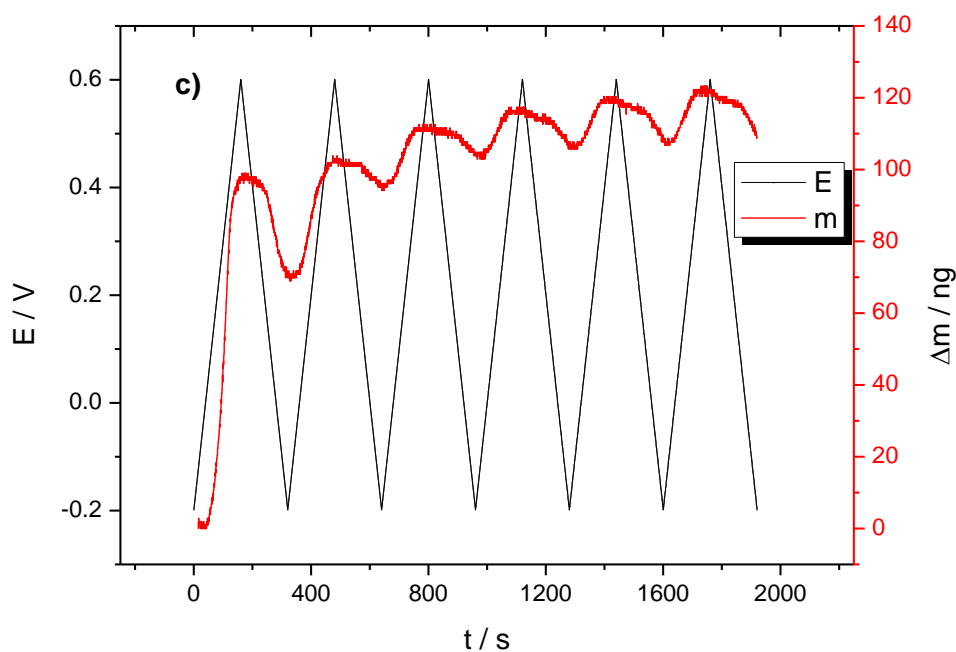
Figure 7.2: EQCM responses of a PANI (Γ = 27.5 nmol cm^{-2}) in 0.1 M NaF; a) i-E response scanned at 5 mV s^{-1}, arrows indicate direction of current change; b) Q-E response scanned at 5 mV s^{-1}, the arrow indicates current increase of first cycle, numbers indicate potential scans of response; c) mass and voltage change as a function of time, scanned at 5 mV s^{-1}, mass changes calculated using Sauerbrey Equation; d) Δm-Q for scan rates of 5 mV s^{-1} and 50 mV s^{-1}.

The trend of current and mass changing at 5 mV s^{-1} shown in Figure 7.2 was identical to 50 mV s^{-1} as given in Figure 7.1. The oxidised form of PANI, was positively charged, extracted F$^-$ from the solution (at E = 0.6 V), can be illustrated as PANI$^+$F$^-$ for easier explanation. Some of PANI$^+$F$^-$ produced during the forward scan did not have a reversible electron transfer. When the time scale of the experiment was longer, PANI$^+$F$^-$ response could be influenced more significantly by uptaking F$^-$ ions; therefore its reduction peak at the reverse forward was diminished earlier than 50 mV s^{-1}. This can be seen by comparing the reduction peaks of the 2nd scans for 5 mV s^{-1} and 50 mV s^{-1}. Panel a and b of Figure 7.2 indicate that after 3 cycles, the film was almost fully saturated with F$^-$. This saturation was observed after 6 scans for 50 mV s^{-1}.

Panel d in Figure 7.2 shows charge-mass graph for 5 mV s^{-1} and 50 mV s^{-1} and Table 7.2 illustrates end-to-end molar mass calculated from Q-m graph (slope was multiplied with Faraday constant).

Table 7.2: End-to-end values of the molar mass (value of ΔmF/Q) for PANI in 0.1 NaF for different scan rates.

v / mV s^{-1}	100	50	20	10	5
Ox (g mol^{-1})	10.2	9.9	8.9	8.1	7.8
Red (g mol^{-1})	12.8	12.3	6.8	4.7	4.2

Molar mass differences can be explained by the mechanisms including 2 steps: first one is F$^-$ entrance (with relaxation of the film) and second one is F$^-$ accommodation into the film body. During oxidation, which is related to F$^-$ entrance, there is not enough time for full relaxation at short time scales (at higher scan rates). However, the relaxation of PANI is easier at long time scales (at lower scan rates), hence mass changing and molar mass of higher scan rate was higher. During reduction, which is related to accommodation of F$^-$ into the film irreversibly, F$^-$ that entered into the PANI

structure could stay there. If there is more time (at lower scan rates), it can constantly produce PANI$^+$F$^-$ salt because there is appropriate time and relatively more F$^-$ accommodates in the body of PANI, making it more compact while film can be swollen/shrunk easier at low scan rates than at high scan rates. Therefore, mass of reduction (and so molar mass) is less for lower scan rate during reduction, as seen in Table 7.2.

Figure 7.3 shows the cyclic voltammograms of PANI film at various scan rates in 1 M NaF solution cycled between -0.2 V and 0.6 V.
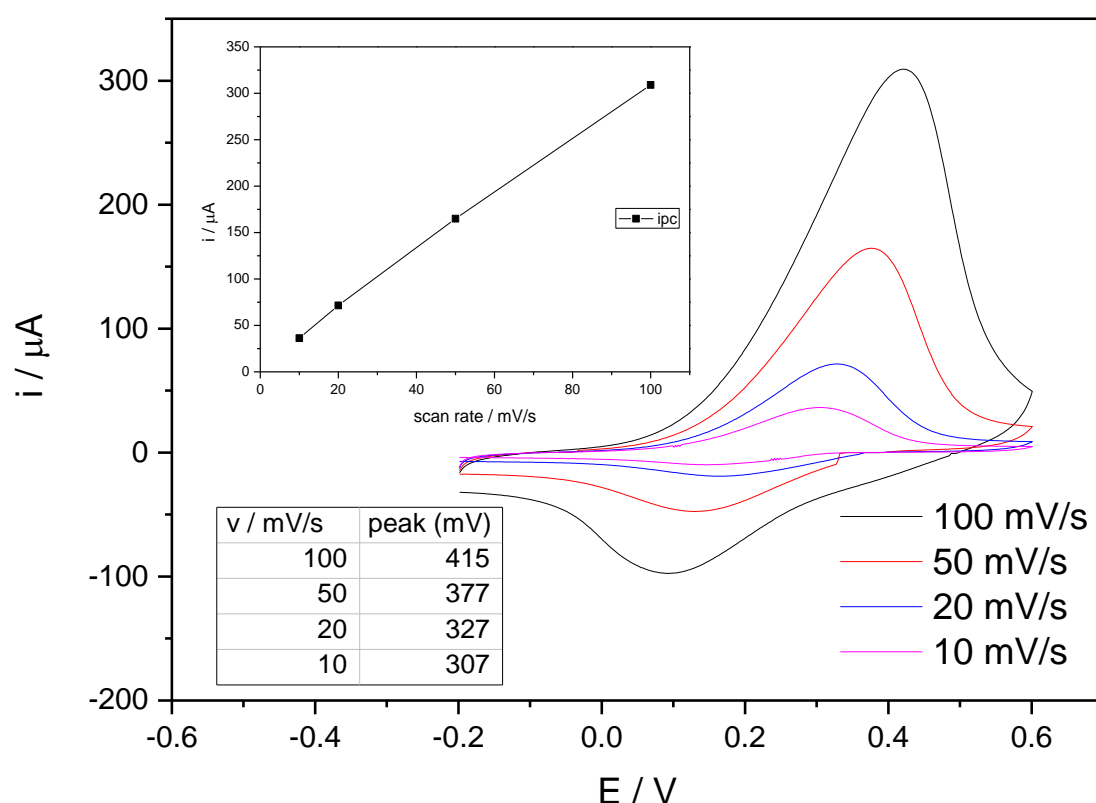

Figure 7.3: PANI film (Γ = 27.5 nmol cm^{-2}) in 0.1 M NaF, first scans at different scan rates, inset: dependence of anodic peak current on scan rate. Inset table is for peak points of oxidation peaks of PANI film for data of the graph.

The linear relationship of the anodic peak current to the scan rate, shown in the inset of Figure 7.3, describes a surface-controlled electrode process. The table in Figure 7.3, which has been produced using the peak points of oxidation at different voltage,

confirms that the electrochemical reaction of PANI in the F⁻ containing solution was not diffusional-controlled mechanism [the slope of $\log(i_p)/\log(v)$ was 0.93].

7.2.1.1.2. Chronoamperometry

The cyclic voltammetry is studied for understanding the mechanism of electrochemical reactions; however potential step is easier to operate films in real life applications. Potential step experiment, which is shown in Figure 7.4, was used to see F⁻ molarity range PANI could extract from aqueous solutions. Figure 7.4 shows the response of the QCM during potential step experiment, in which -0.2 V was applied for 10 seconds and then 0.6 V was applied for 30 seconds to PANI film in different F⁻ concentration.
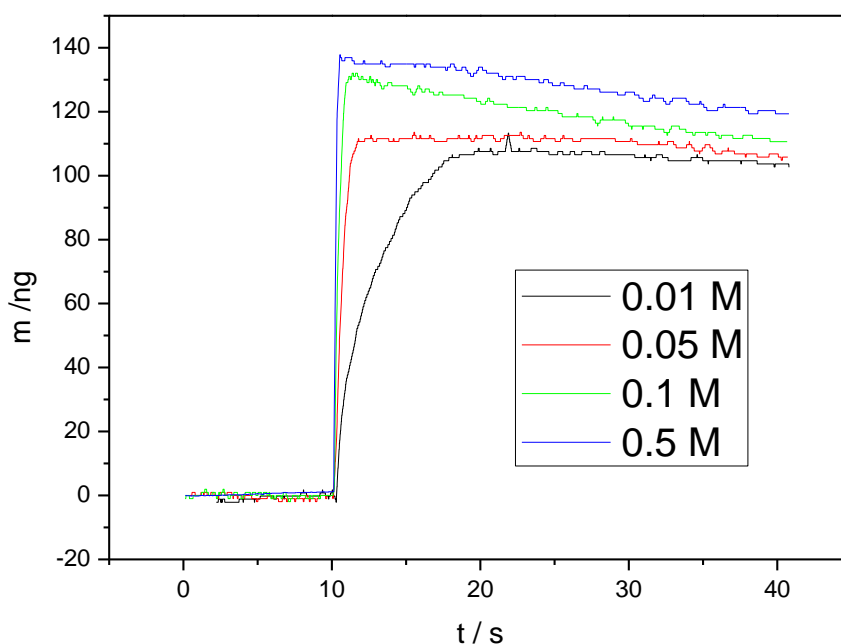

Figure 7.4: Mass responses of chronoamperometric mode of the EQCM for PANI film (Γ = 27.5 nmol cm^{-2}) in the solution of different NaF concentration, 10 seconds for -0.2 V and 30 seconds for 0.6 V (vs. Ag/AgCl) applied.

Chronoamperometry study demonstrates that the process of extracting F⁻ (mass increasing of PANI film) could end within 17 seconds for diluted F⁻ solution (0.01 M NaF) and a few seconds for concentrated F⁻ solution, as PANI itself was the limiting

reagent. For concentrated solution (0.5 M) the mass of F^- entered into PANI increased straight after 0.6 V potential was applied but after film relaxation and F^- accommodation, PANI$^+$F$^-$ was still stable. The amount of F^- absorption approached to about the same level for all of different concentration solutions. The range of fluoride concentration which PANI can extract was very wide ranging, from 0.01 M (19 ppm) to 0.5 M (850 ppm), thus it could be used not only for waste stream of the factories including high F^- concentration cleaning but also drinking water defluoridation. Even after PANI electrode was removed from three electrode set-up (open circuit), the colour of PANI was black overnight, indicating that PANI can keep F^- in its body and could not lose it easily, which can be stated as an advantage for this application.

7.2.1.2. Poly(o-toluidine)

POT electrode, the growth of which was shown in Figure 4.7, was investigated by using the cyclic voltammetry mode of the EQCM in 0.1 M fluoride solution and presented in Figure 7.5.
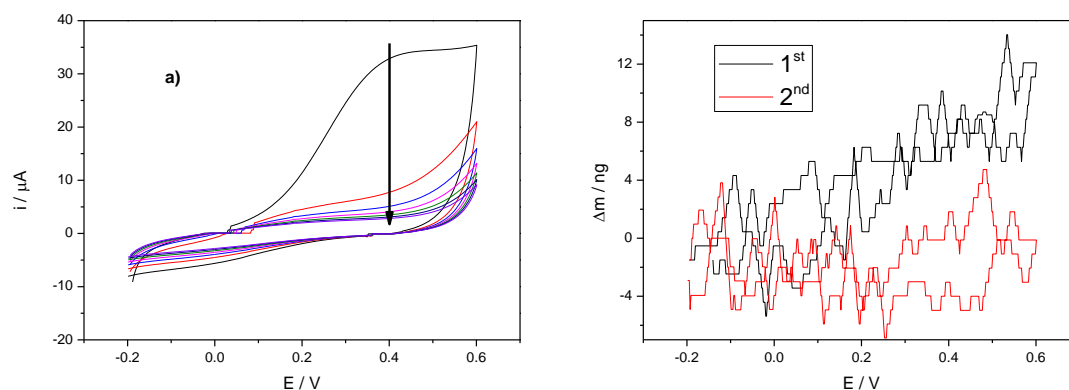

Figure 7.5: The EQCM responses of POT film (Γ = 10.2 nmol cm^{-2}) in 0.1 M NaF scanned at 50 mV s^{-1}; a) i-E curves, the arrow indicates the direction of current decrease ; b) Δm-E, film mass changes calculated using Sauerbrey Equation, numbers indicate potential scans of response.

There was an oxidation peak for first cycle (see panel a of Figure 7.5) but not reduction peak which had similar behaviour with PANI shown in panel a of Figure 7.1. Fluoride ions were taken up by POT during oxidation, as illustrated in panel b of Figure 7.5.

Electrochemical properties and mass transfer in acidic medium of POT were similar to PANI as compared in panel a and b of figure 4.18. Fluoride uptaking in POT was also similar to fluoride uptaking in PANI.

7.2.1.3. Poly(*o*-aminophenol)

POAP electrode, whose growth was shown in Figure 4.9, was investigated by the EQCM data in 0.1 M NaF solution.
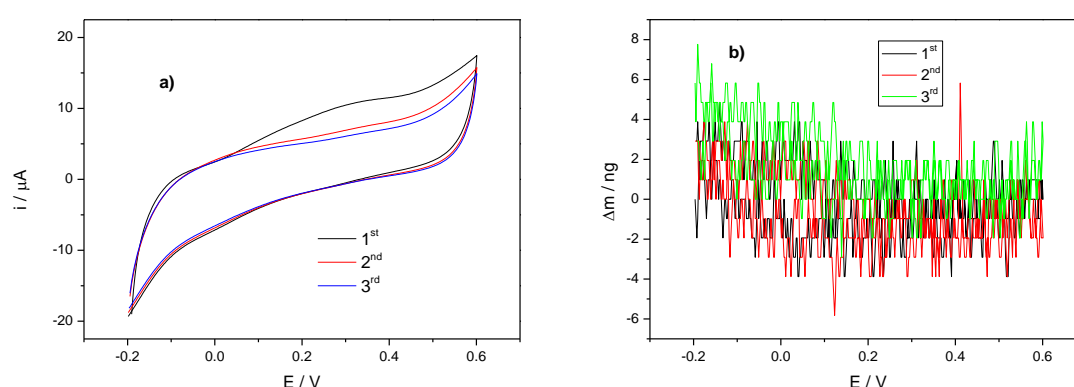

Figure 7.6: EQCM responses of POAP film (Γ = 15.3 nmol cm^{-2}) in 0.1 M NaF scanned at 50 mV s^{-1}, numbers indicate potential scans of response; a) i-E curves; b) Δm-E, film mass changes calculated using Sauerbrey Equation.

When the POAP film was directly transferred into 0.1 M NaF solution and the experiment was initiated after 10 minutes (to give some time to have an equilibrium between the film and electrolyte), there was no oxidation peaks shown in panel a of Figure 7.6 that suggests POAP did not take F$^-$ presented in panel b Figure 7.6.

While PANI and POT were anion dominated, POAP was cation dominated in aqueous acidic electrolyte, shown in Figure 4. 18. Here, in 0.1 M NaF solution, the mechanism of POAP was also different than PANI and POT in terms of not taking F$^-$ ions.

7.2.1.4. Poly(aniline-*co-o*-toluidine)

The cycling of designed polymers and copolymers was studied in aqueous acidic medium in chapter four. In this chapter the focus will be the investigation of the p-doping and dedoping of the copolymers in NaF solution.

The prepared P(ANI-OT) (75:25) and P(ANI-OT) (95:5) copolymers, whose growth curves were given in Figure 4.13 and 4.14, were cycled in 0.1 M NaF solution, shown in Figure 7.7 and Figure 7.8, respectively.
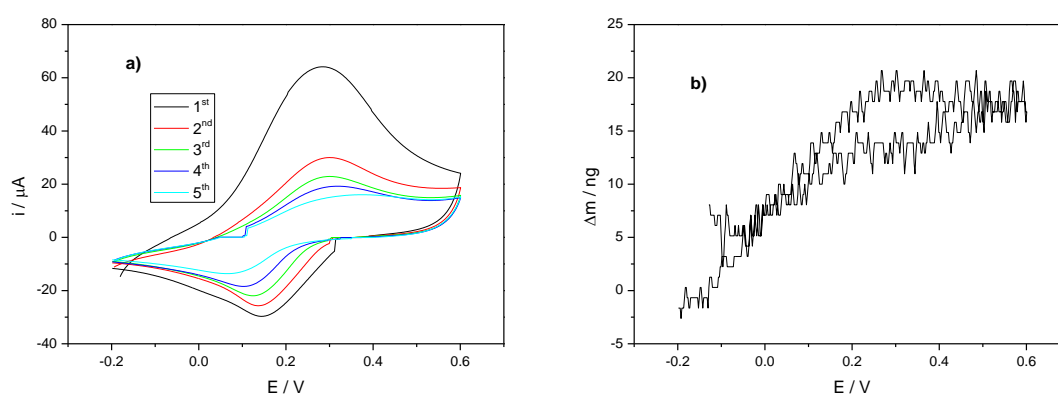
Figure 7.7: EQCM responses of P(ANI-OT) (75:25) film (Γ = 21.9 nmol cm^{-2}) in 0.1 M NaF scanned at 50 mV s^{-1} a) i-E curves, numbers indicate potential scans of response; b) Δm - E, film mass changes calculated using Sauerbrey Equation.

P(ANI-OT) (75:25), which was characterised and shown in Figure 4.20, also had similar behaviour to PANI (as mass increase during oxidation) and the uptaking of F$^-$ was also similar to PANI, which is ion uptake during oxidation.

Figure 7.8: The EQCM responses P(ANI-OT) (95:5) film (Γ = 35.8 nmol cm^{-2}) in 0.1 M NaF scanned at 50 mV s^{-1}, numbers indicate potential scans of response; a) i-E curves; b) Δm-E, film mass changes calculated using Sauerbrey Equation.

P(ANI-OT) (95:5), which was PANI dominated shown in section 4.2.4.6.2, could take F^{-} similar to PANI itself, given in Figure 7.1.

7.2.1.5. Poly(aniline-*co-o*-aminophenol)

The prepared P(ANI-OAP) (80:20) and P(ANI-OAP) (98:2) copolymers, whose curves of growth were shown in Figure 4.15 and 4.17, were cycled in 0.1 M F^{-} solution, given in Figure 7.9 and Figure 7.10, respectively.
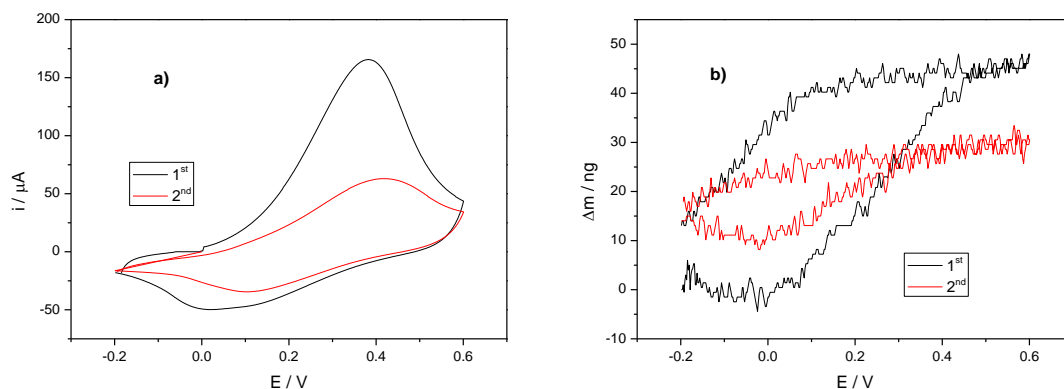

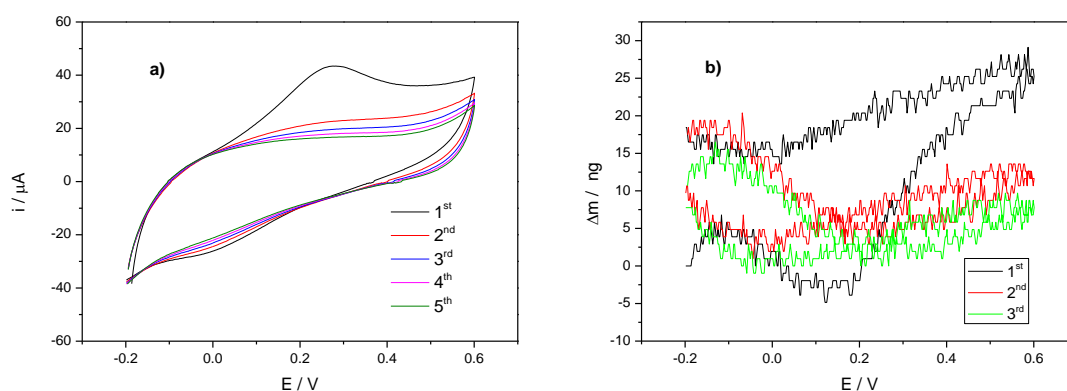*Figure 7.9: EQCM responses P(ANI-POAP) (80:20) film (Γ = 46.6 nmol cm^{-2}) in 0.1 M NaF scanned at 50 mV s^{-1}, numbers indicate potential scans of response; a) i-E curves; b) Δm-E, film mass changes calculated using Sauerbrey Equation.*

P(ANI-OAP) (80:20) had a small oxidation peak, much smaller than in aqueous acidic medium shown in Figure 4.21, which was irreversible showing similar behaviour as PANI given in section 7.2.1.1. P(ANI-OAP) (80:20), as given in section 4.2.4.6.2, had different mass transfer dynamics than both PANI and POAP homopolymers and different optical behaviour when compared with PANI and POAP in section 4.2.4.7. Figure 7.9 illustrates that P(ANI-OAP) (80:20) could not extract fluoride from water.

P(ANI-OAP) (80:20) was anion dominated, which means that an anion can enter into the film from aqueous acidic medium during oxidation. However, P(ANI-OAP) (80:20) did not take up fluoride, therefore showing similar behaviour to POAP.
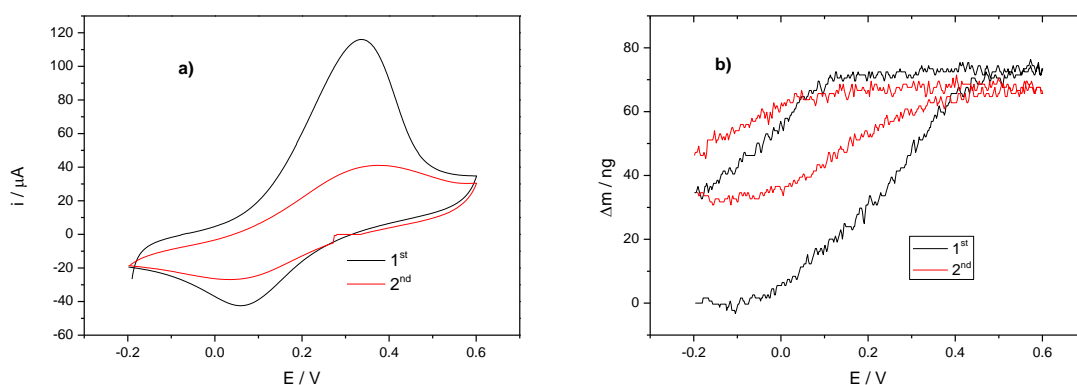
Figure 7.10: EQCM responses P(ANI-POAP) (98:2) film (Γ = 35.5 nmol cm^{-2}) in 0.1 M NaF scanned at 50 mV s^{-1}, numbers indicate potential scans of response; a) i-E curves; b) Δm-E, film mass changes calculated using Sauerbrey Equation.

P(ANI-OAP) (98:2), which was approached to PANI given as electrochemical and optical results indicated in chapter four, could extract F$^-$ from the water with the same way as PANI shown in Figure 7.1.

Among all polymers studied in chapter 4, POAP and POAP dominated copolymer could not be utilized to extract fluoride ion from water. All other films could be used as "electrically switched ion exchange" to extract fluoride from water as fluoride ions move into the polymer film's body, this technique can be referred to as a "*absorption technique*".

7.2.2. Film Regeneration

The aim was to design a conducting polymer that can uptake F^- during oxidation and release F^- during reduction to provide reusability. This process was performed in two steps: first step is fluoride ion uptake; the second one is fluoride ejection. Cyclic voltammetry experiments showed that during oxidation, fluoride ions could be absorbed into the PANI, POT, P(ANI-OT), P(ANI-OT) (75:25), P(ANI-OT) (95:5) and P(ANI-OAP) (98:2) films. There was not any problem about inserting fluoride into the (co)polymers mentioned. This was confirmed by potential step experiment that fluoride could be removed using PANI with applying 0.6 V for a while typically for 10 seconds. In this step, PANI film becomes emeraldine salt form and is not regenerated in the same electrolyte containing fluoride ions, which was a basic solution, as our polymers are only electroactive in aqueous acidic medium.

The (co)polymers, which absorbed fluoride ions during oxidation, could not release all fluoride ions during reduction. Therefore, one can deduce from cyclic voltammetry (section 7.2.1) that this technique is not reproducible because films have already been poisoned by fluoride when it was p-doped and fluoride cannot be eluted from the film during reduction (when -0.2 V applied). Normally "poisoning" has a negative meaning. However, with regard to water treatment applications, using ESIX based polymers, modified film poisoned by ions is required to remove unwanted ions.

7.2.2.1. Chronoamperometry

PANI is known to be electroactive in aqueous acidic medium, pH<4. Hence, upon transferring PANI poisoned by F^- (oxidised form of PANI) to aqueous acidic electrolyte and applying -0.2 V can force F^- exit from the film to form the reduced state of PANI (leucoemeraldine base).

PANI film, absorbed fluoride, shown in Figure 7.4, was transferred to 0.1 M H_2SO_4 represented in Figure 7.11.
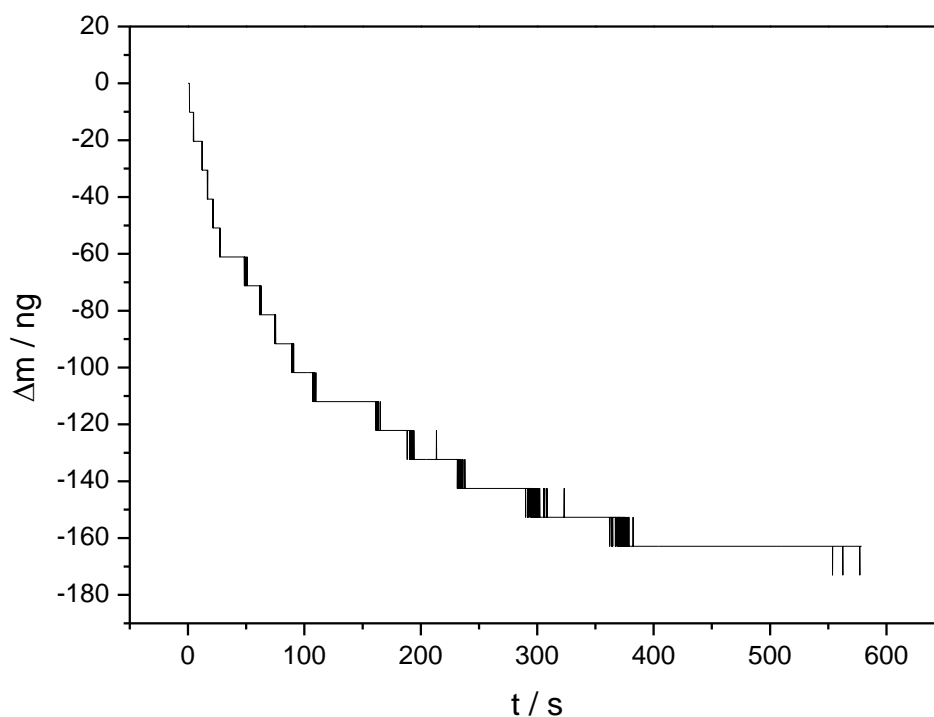
Figure 7.11: Mass response of PANI film which had absorbed fluoride, in 1 M H₂SO₄, without applying voltage (open circuit).

It was clearly observed that fluoride could be released from PANI, which had been saturated by fluoride, even by applying no voltage when it was in an acidic electrolyte, as shown in Figure 7.11. During the process, the mass of the film decreased gradually indicating the amount of fluoride exiting from the film. Although fluoride uptake for PANI was about 110 ng shown in Figure 7.4, fluoride elution was about 160 ng from the same film. These differences could arise from the relaxation of PANI film. PANI film could have different structure in different electrolyte, hence the water insertion/ejection can be different and this can cause mass differences.

Normally, modified films used in electrochromic devices, batteries or artificial muscles are in the same electrolyte for oxidation and reduction. If PANI is used for these applications, pH of the electrolytes have to be less than 4 for electroactive polymers. However, in the case of water treatment, the electrolyte could be changed individually in oxidation and reduction steps of PANI. Conducting polymer films could be used for

fluoride uptake from water during oxidation. After that the PANI film containing fluoride can be transferred to an acidic solution (as shown in Figure 7.11) for elution of fluoride.

Figure 7.12 presents the schematic illustration of fluoride ion uptake of PANI from water and PANI regeneration in acidic medium.
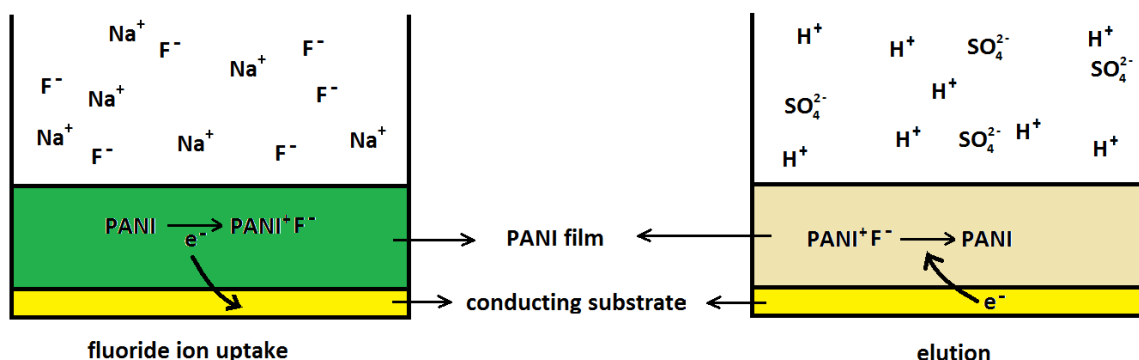

Figure 7.12: Schematic illustration of the fluoride ion uptake using film and regeneration of the film in acidic medium.

When 0.6 V is applied to the PANI electrode, shown in left side of Figure 7.12 as shown at the beginning of this section as well, the electrochemical oxidation of PANI is accompanied by uptake of F⁻ ions to maintain electroneutrality of the film. When the PANI electrode is in aqueous acidic medium, as we have observed in this section, PANI can be discharged in aqueous acidic electrolyte and fluoride ions can be released from the film, shown in the right side of Figure 7.12. Cyclic voltammetry studies can also be carried out to see how reproducible these films are in the applications of water purification.

7.2.2.2. Cyclic Voltammetry

Section 7.2.1 demonstrated that fluoride could be absorbed into the films and changed the film from LB to a stable salt (EB) in its own electrolyte (basic fluoride solution). The current – voltage response of these films indicated that the films were not reusable in the fluoride solution. As it was mentioned in previous section (7.2.2.1), the electrolyte could be changed to regenerate the films in aqueous acidic medium.

Therefore, it would be better to compare the electrochemical behaviour of the films, which were poisoned by fluoride, in aqueous acidic medium to investigate the film regeneration.

7.2.2.2.1. Polyaniline

Figure 7.13 shows the current voltage curve of $PANI^+F^-$ film in 1 M H_2SO_4 solution cycling from -0.2 V to 0.6 V at a scan rate of 50 mV s^{-1}. $PANI^+F^-$ film, which had already been poisoned by fluoride, was transferred into 1 M H_2SO_4 electrolyte and the cyclic voltammogram is shown in Figure 7.13 as 1st regenerated film. After the PANI film was at LB state (regenerated to reduced form), it was used again to extract fluoride for the 2nd time, either using cyclic voltammogram or chronoamperometry. PANI film, which absorbed fluoride, was transferred into the same aqueous acidic medium to see its behaviour shown as 2nd regeneration in Figure 7.13. Uptaking of fluoride into the PANI film from a basic solution and then releasing it into the aqueous acidic solution process were continued to compare the electroactive differences for more cycles to see its reproducibility. PANI film was regenerated to use either in extracting fluoride from different ratio of solution for potential step experiment or the effect of scan rate for cyclic voltammetry studies. Actually all PANI film have been studied in this chapter is the same for all experiments because it was regenerated.
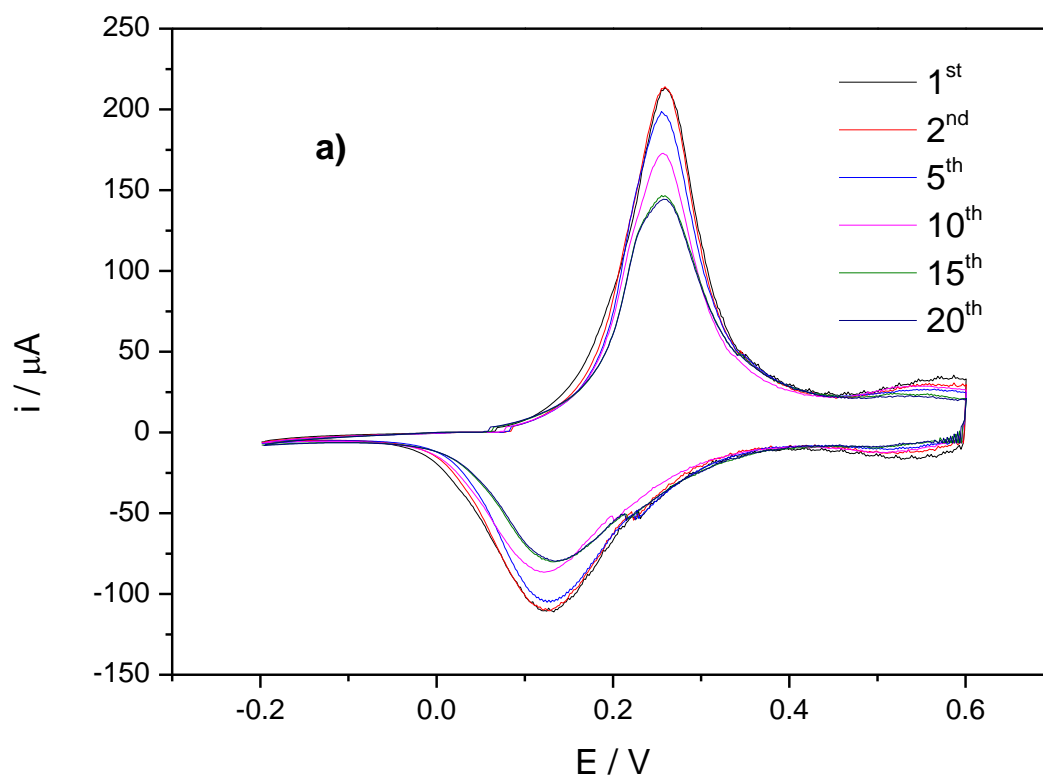
Figure 7.13: Regeneration of PANI film (Γ = 27.5 nmol cm^{-2}) in 1 M H$_2$SO$_4$, at a scan rate of 50 mV s^{-1}, numbers indicate the 1st, 2nd, 5th, 10th, 15th and 20th regenerations.

The performance of a PANI film to fluoride uptake (area under cyclic voltammetry curve of Figure 7.13) was not significantly different from 1st to 20th regeneration. The cyclic voltammetry of 15th and 20th regenerations of PANI were exactly the same as each other, suggesting how high reproducibility performance they have.

The extracting (section 7.2.1.1.) and regeneration (Figure 7.13) steps of PANI film for fluoride intake and elution are shown in Figure 7.14.
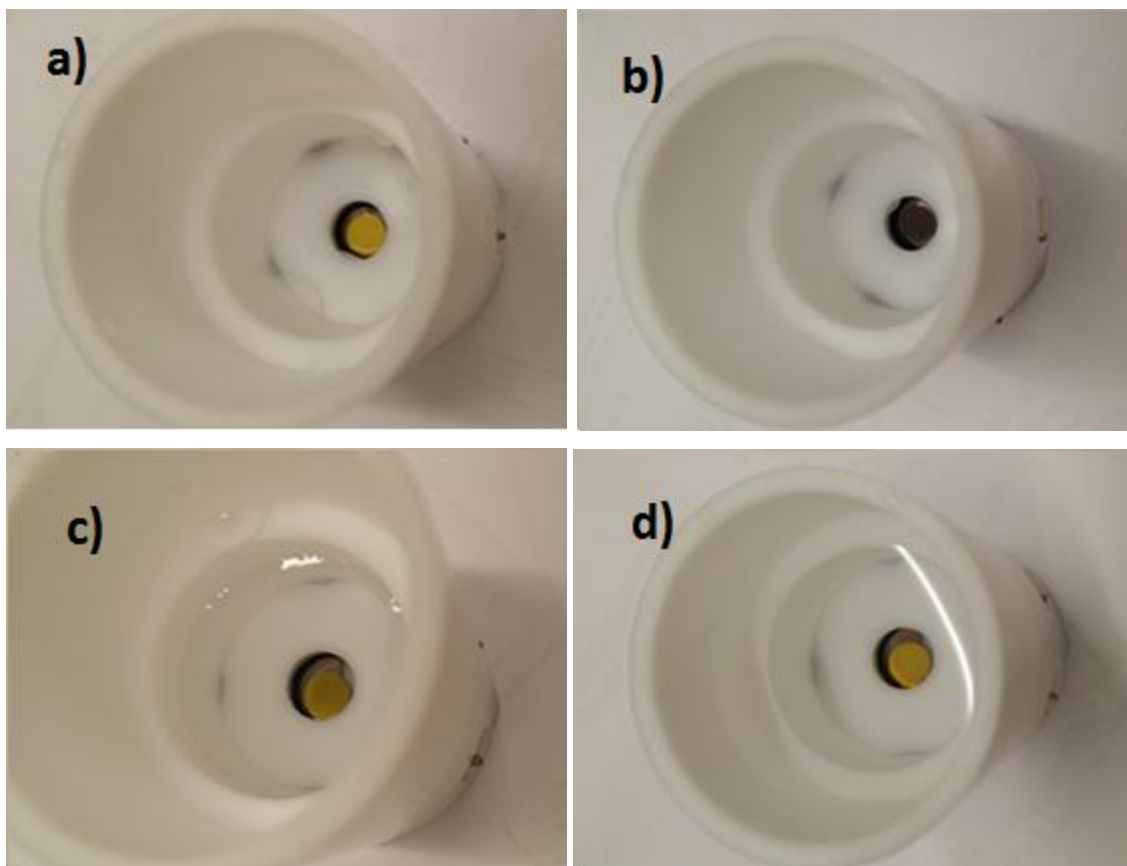
Figure 7.14: Images of PANI films, a) film before fluoride treatment; b) film after electrochemical fluoride removal; c) after 1 M H_2SO_4 is put into the cell for regeneration; d) after cycling in 1 M H_2SO_4.

Panel a of Figure 7.14 illustrates the colour of PANI film before fluoride uptake, yellow Au surface of WE was hardly seen as the PANI film was relatively thin. Panel b of Figure 7.14 shows the image of $PANI^+F^-$, which the PANI extracted fluoride from 0.1 M NaF solution. The colour of $PANI^+F^-$ film was turned into black while extracting fluoride and was changed to emeraldine salt. Straight after H_2SO_4 solution was contacted to black PANI including fluoride, the film become yellowish (not as shiny yellow as shown in panel a Figure 7.14. When -0.2 V was applied in three electrode system in 1 M H_2SO_4 solution, the colour of the film was changed and turned into the same colour as prior to fluoride treatment (see panel a and d of Figure 7.14). Electrochemical reduction of the film in aqueous acidic medium was accompanied by elution of fluoride. The photos, here, show the regeneration of the PANI film, which was conducted for the QCM experiments (therefore thin films). However, when we had thicker film (Γ = 203 nmol cm^{-2}), which could not be used for EQCM measurement, colour of films after the

269

fluoride uptake and regeneration was different. Figure 7.15 shows the images of thick PANI films after and before the process.
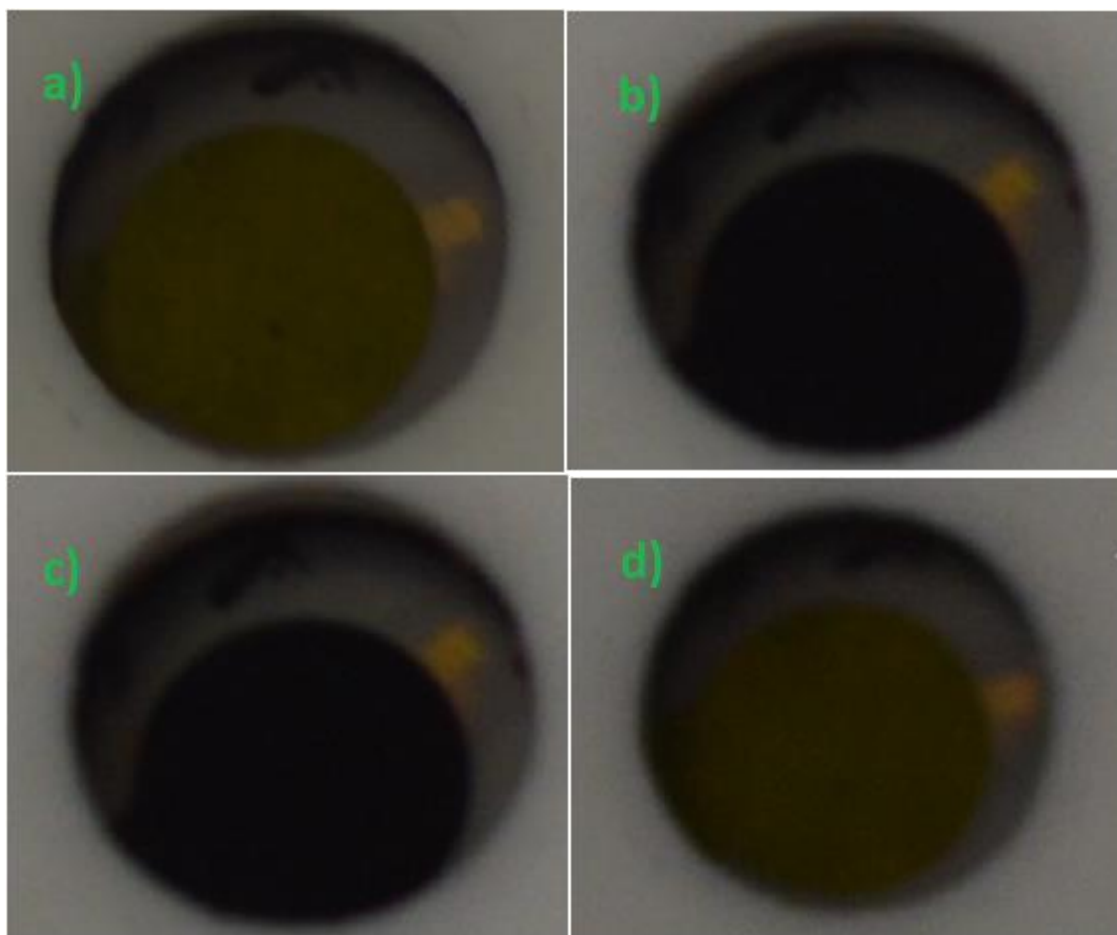

Figure 7.15: Images of thick PANI films (Γ = 203 nmol cm^{-2}), a) film before fluoride treatment; b) film after electrochemical fluoride removal; c) after 1 M H$_2$SO$_4$ is added into the cell for regeneration; d) after cycling in 1 M H$_2$SO$_4$.

PANI shown in panel a of Figure 7.15 was greener than PANI in panel a of Figure 7.14 as indicated in chapter 4 that the film having more surface coverage of PANI film is greener. In panel a of Figure 7.15, the PANI film was pale green before fluoride treatment. Panel b of Figure 7.15 presents that the PANI film (black) was extracted fluoride from 0.1 M NaF solution upon applying 0.6 V and changed into PANI$^+$F$^-$. When 0.1 M sulphuric acid was added into black PANI including fluoride, the colour of film did not become green (thin PANI film had been quickly turned to yellowish in panel c of Figure 7.14). The thick film in aqueous acidic solution was still black after 10

minutes, as shown in panel c of Figure 7.15, because, not all ES form of PANI was converted into LB form. However, applying -0.2 V to film in 1 M H_2SO_4 electrolyte changed the colour of PANI film to its pre-treatment colour (pale green) given in panel d of Figure 7.15. These findings suggest that the regeneration of PANI can easily be conducted when -0.2 V (*vs.* Ag/AgCl) is applied in a three electrode system.

7.2.2.2.2. Poly(o-toluidine)

Both thin and thick PANI films can be used to extract fluoride from water and regenerated. Now, the results of the regeneration of the films of the PANI derivatives, POT and POAP films. Figure 7.16 illustrates the CV of POT, which was used for fluoride uptake in Figure 7.5, in 1 M H_2SO_4 solution cycling from -0.2 V to 0.6 V at a scan rate of 50 mV s^{-1}.
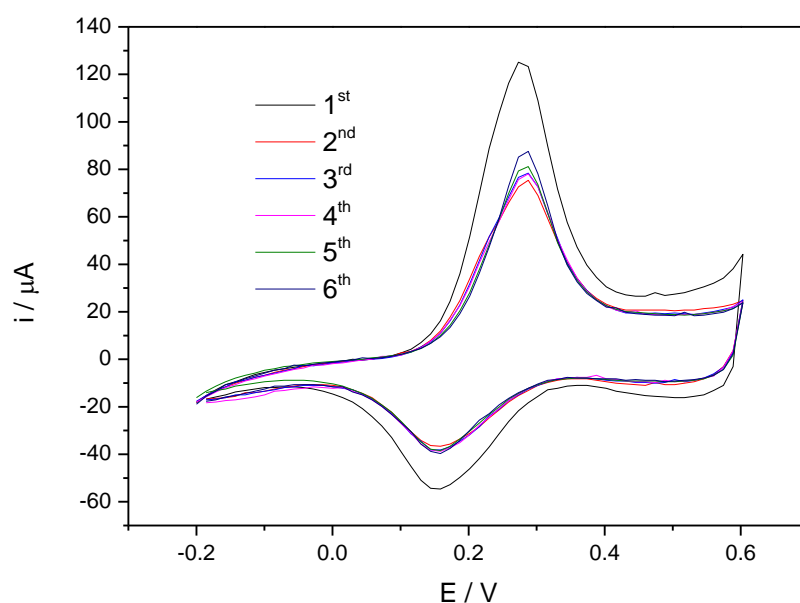

Figure 7.16: Regeneration of POT in 1 M H_2SO_4, at a scan rate of 50 mV s^{-1}, numbers indicate the regenerations.

The regeneration trend of POT was similar to PANI, discussed in section 7.2.2.2.1. There was a relatively big difference between 1st and 2nd regeneration scan as seen in

Figure 7.16, but after 2nd regeneration, CV curves are identical, meaning that the capacity of fluoride uptake became stable.

Figure 7.17: Images of POT films, a) film before fluoride treatment; b) film after electrochemical fluoride removal; c) after 1 M H_2SO_4 is put into the cell for regeneration; d) after cycling in 1 M H_2SO_4.

Colours of POT shown in Figure 7.17 at fluoride absorption and regeneration were the same as PANI presented in Figure 7.14, black and yellow respectively.

7.2.2.2.3. Poly(o-aminophenol)

POAP film was deposited as explained in chapter 4 (see Figure 4.9.) and its redox characterisation in 1 M H_2SO_4 electrolyte was presented in Figure 4.18, which was surprisingly cation dominated. In section 7.2.1.3. we observed that POAP film could not take fluoride. POAP as shown in Figure 7.18, had two oxidation peaks and one reduction peak in aqueous acidic medium. When POAP film, which was cycled in fluoride solution, was again transferred to 1 M H_2SO_4 solution, the cyclic

voltammogram of the film had just one oxidation peak. However, mass changing of POAP during redox reaction was similar to previous one (inset of Figure 7.18).

Figure 7.18: POAP film in 1 M H$_2$SO$_4$, after treatment with fluoride, at a scan rate of 50 mV s^{-1}, inset: m-E graph of POAP for each try.

When the colour of POAP films in fluoride and acidic electrolyte were compared (see Figure 7.19), no significant change was observed between pre and post fluoridic or acidic treatment, even the colour of the POAP film was similar after treatment (blackish film).
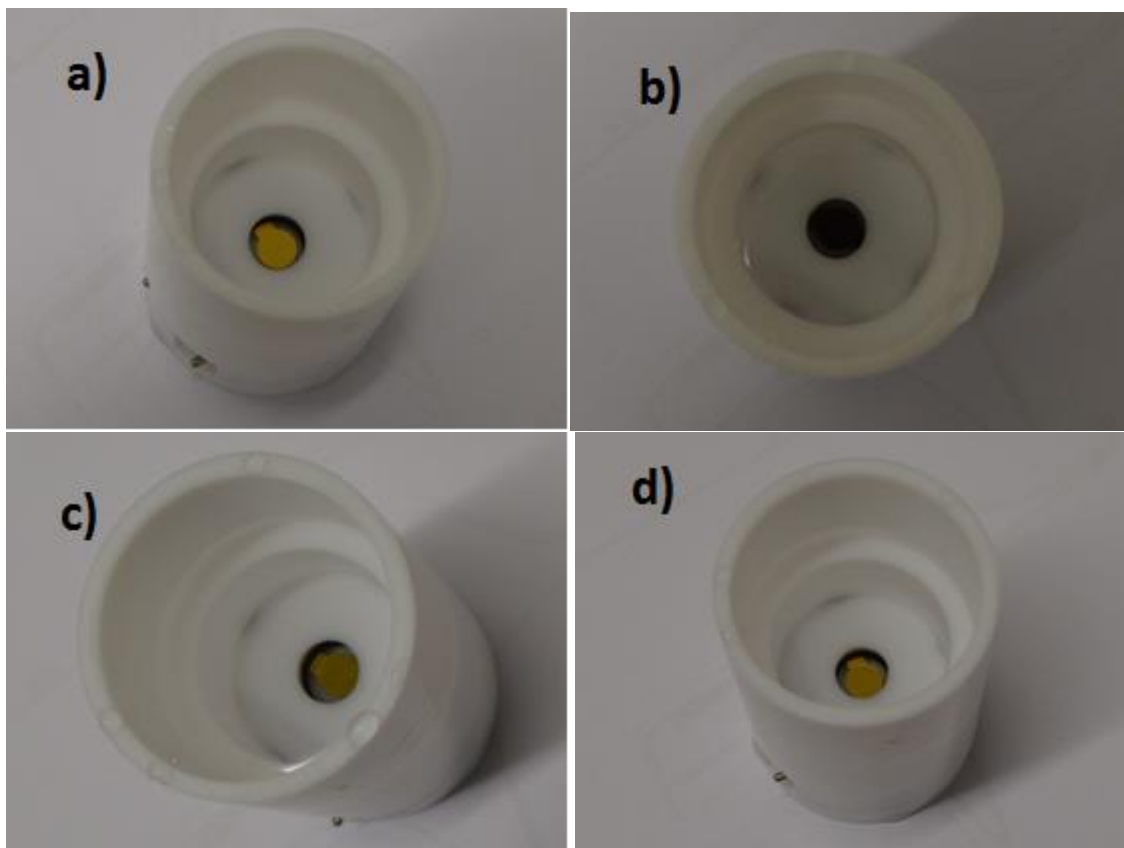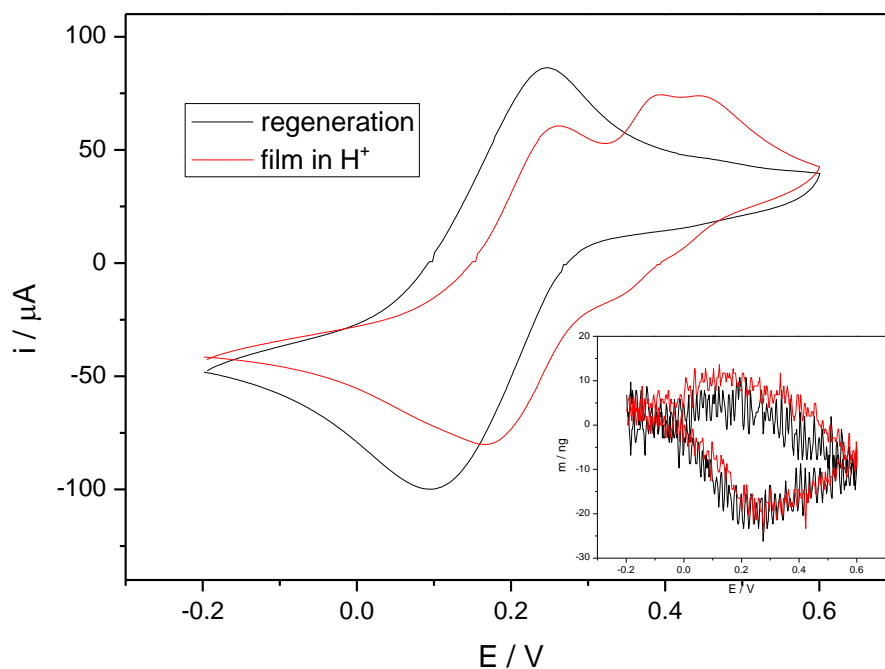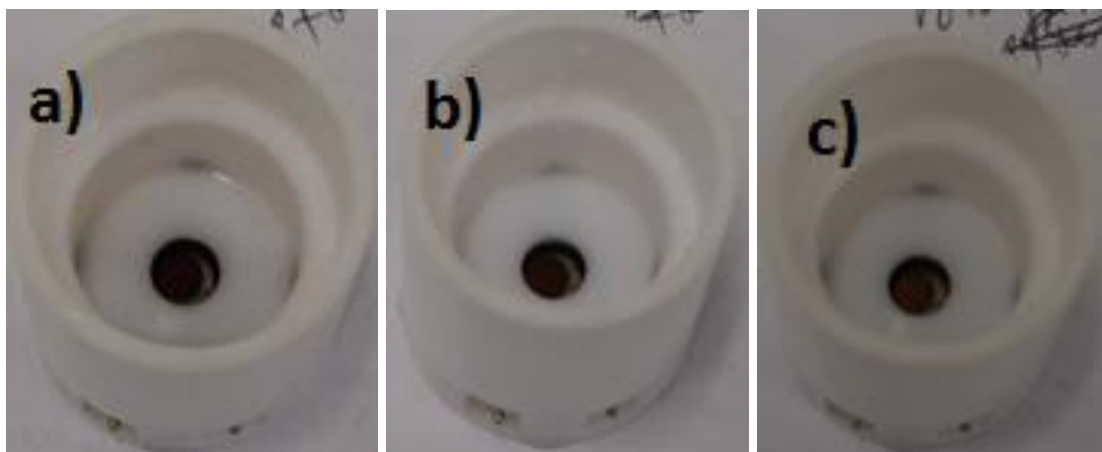
Figure 7.19: Images of POAP films, a) film before fluoride treatment; b) film after electrochemical fluoride removal; c) after cycling in 1 M H₂SO₄ for regeneration.

7.2.3.   Film Imaging

Images in section 7.2.2 showed that the colour of polymers, macroscopic scale seen by eyes, were changed as it was doped with fluoride from water treatment or dedoped in aqueous acidic medium. Cyclic voltammograms of the film confirmed the atomic scale change of the film during redox reaction. SEM was conducted to see micro/nano scale changing of the film. Figure 7.20 and Figure 7.21 illustrate (respectively 1000x and 2500x) SEM images of PANI just after the growth and after fluoride extraction.
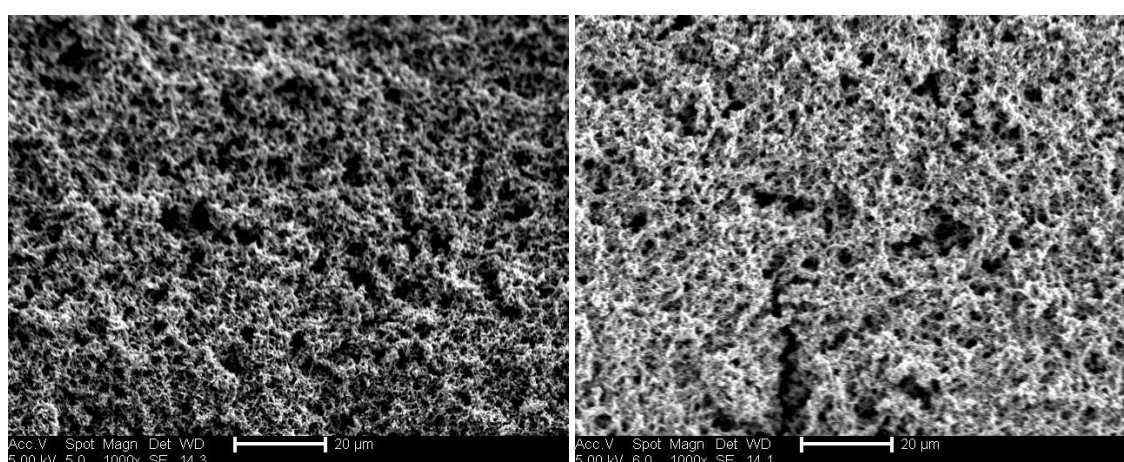
Figure 7.20: SEM images of PANI a) after growth b) after electrochemical fluoride removal (1000x).

When panel a and panel b of Figure 7.20 were compared (1000x), no obvious difference in the morphology, between grown PANI and PANI extracting fluoride, was found.
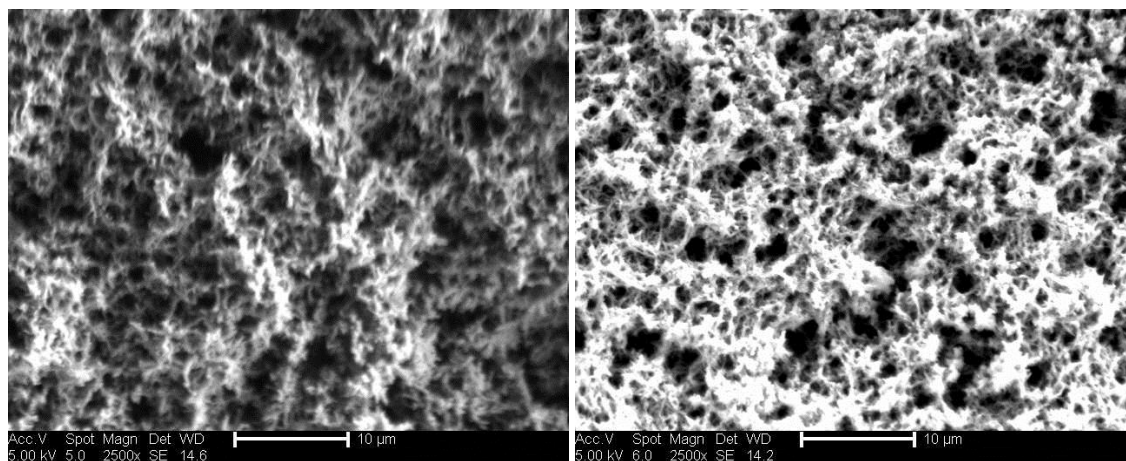
Figure 7.21: SEM images of PANI a) after growth b) after electrochemical fluoride removal (2500x).

To see a close-up of the PANI structure (2500x), Figure 7.21. presented that the porosity and homogeneity for the films pre and post fluoride treatment was similar.

SEM image in panel a of Figure 7.22, which was PANI including fluoride, was the same as panel b of Figure 7.22, which was the regeneration of PANI in aqueous acidic medium.
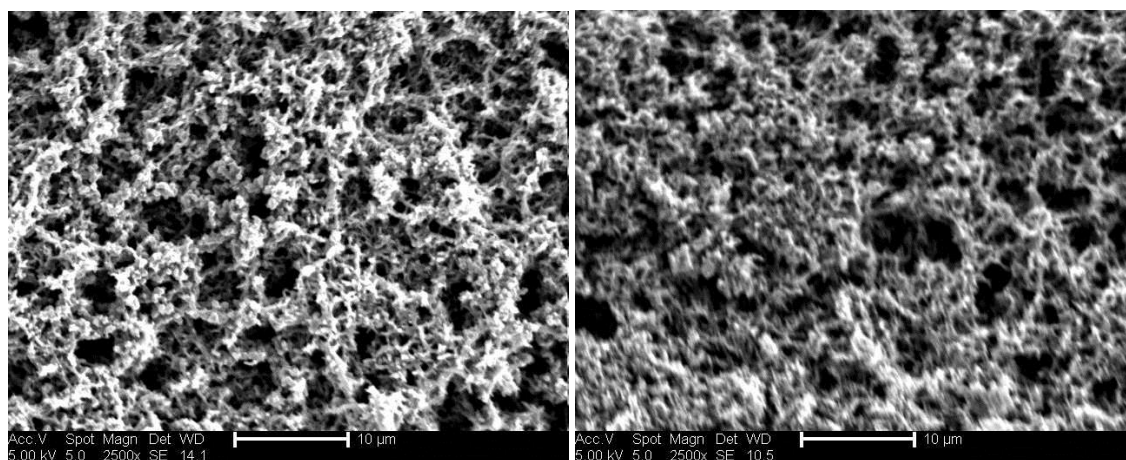
Figure 7.22: SEM images of PANI a) including fluoride b) after regeneration (2500x).

Figure 7.22 confirms that there was not structural difference in dry PANI film before and after regeneration as well. Although there was some change in atomic level, as seen in cyclic voltammogram and colour differences after fluoride treatment, SEM could not show any structural differences because atomic level (angstrom) seen by cyclic voltammetry is much smaller than microscopic level seen by SEM.

7.2.4.   Comparison with Other Studies

All the techniques used for defluoridation of water have some benefits and drawbacks.[23] In summary: precipitation process involving the addition of chemicals and formation of the precipitates is the most common method for defluoridation. In precipitation process,[16] chemicals (*e.g.* aluminium salts) cannot be used for high level of fluoride containing water (*e.g.* dissolved aluminium can affect health). Membrane based processes, including reverse osmosis, nanofiltration, and electrodialysis, are highly effective techniques, do not need chemicals and can work under a wide range of pH. However, their limitations are their relatively high cost and not being suitable for water having high salinity and total dissolved solids. Adsorption is an easy technique but the process is dependent on pH.[24] Ion-exchange methods,[18] used so far, are effective. In this technique, fluoride ions are forced to exchange with other ions (*e.g.* exchanging between fluoride and chloride) but it has relatively high cost.[20] After treatment with this method, water can have high exchanged ions concentration (*e.g.* high chloride concentration).[25] PANI, POT and PANI copolymers shown in previous sections were used in ESIX process and it shows different mechanism than ion-exchange methods. In ESIX, fluoride ions can be absorbed/released by just the voltage changing.

Conducting polymers were used previously by other researchers for defluoridation of water. Some of the advantages of CPs are being non-toxic[26, 27] and having relatively low cost. Kartikeyan *et al.* removed fluoride with PANI,[28] polypyrrole (PPy),[29] PANI-alumina and PPy-alumina,[30] PANI-chitosan and PPy-chitosan,[31] PANI-montmorillonite and PPy- montmorillonite.[32] Amongst these studies, the maximum amount of fluoride

ion per unit mass of the adsorbents, which were conducting polymers and their composites formed, was observed to be 8 mg g^{-1} at 30 ^{o}C and 10 mg g^{-1} at 50 ^{o}C. Bhaumik et al.[33] designed PPy/Fe$_3$O$_4$ nanocomposite for defluoridation and its capacity was observed to be 22.31 mg g^{-1}. PANI-tamarindus indica was used for defluoridation by Subramanian et al.[34] and the highest adsorption capacity was found to be 10.7 mg g^{-1}. In all these studies mentioned above, polymers (and their composites) were used as adsorbent (or ion exchange just between fluoride and chloride from the electrolyte from which the film was prepared). Their fluoride uptaking performance could be higher if they had used polymer based on ESIX. Cui et al. prepared PANI[10] and P(ANI-OAP)[11] ESIX film in which applying voltage could control the uptake and elute of fluoride. They discovered that fluoride extracted up by PANI was 20 mg g^{-1} at room temperature.[10] However, 1.5 V was applied to PANI film in order to remove fluoride, which could cause deterioration of PANI.[22] Therefore, it could only be regenerated a few times. In our work, we applied 0.6 V to avoid overoxidation/deterioration of polymer films at higher potential and to reproduce the films dozens of times.

The surface coverage of PANI film, we used, was calculated from oxidation of Figure 7.13 (613 μC) for 1st regeneration was 1.16 μg for dimeric aniline as p-doped of PANI has one electron per two aniline units. The mass of fluoride extracted from water by PANI (shown in Figure 7.4) was 103 ng for 0.01 M fluoride solution. Therefore, fluoride ion per gram of the adsorbents was calculated as 89 mg g^{-1} at room temperature. Theoretically, PANI capacity should be 104 mg g^{-1} [(0.5 mol F$^-$/1 mol ANI in polymer) = (950 mg F$^-$/91 g PANI) = (104 mg F$^-$/g PANI)] because during oxidation, each aniline monomer could bear a 0.5 charge.[35]

Cui et al. said[10] that PANI could be used just in aqueous acidic electrolyte for defluoridation. Therefore, they prepared P(ANI-OAP)[11] using wide range of pH. Other researchers[28-31, 33] also tried to find optimum pH for defluoridation. What we have shown in our results is that pH is not an important issue, thus PANI (and POT) can be used to extract fluoride from basic electrolyte, described in section 7.2.2.2. Therefore, there is no need to design a copolymer for defluoridation; PANI itself can be used for removing fluoride from water.

The researchers[10, 11, 28-34] were also interested in the initial concentrations of fluoride solution which result in different capacity of absorbent/adsorbent. However, PANI can be used in very wide range of fluoride concentration as shown in section 7.2.1.1.2. The critical point, PANI could have, for defluoridation is the selectivity which requires further studying.

7.3. Conclusions

PANI can effectively be used for the defluoridation of water. POT and its copolymer combinations with PANI can also extract fluoride from water but POAP and P(ANI-OAP) (80:20) copolymer cannot.

PANI oxidation at pH 8.6 is accompanied by fluoride uptake, but reversal of the potential does *not* result in fluoride elimination in the basic solution. When the time scale of the experiment was longer, $PANI^+F^-$ response could be influenced more significantly by interaction of PANI with F^-. The responses suggest a surface-controlled electrode process.

PANI can be used to extract fluoride from the solution containing a wide range of initial fluoride concentration. After extraction, PANI can hold fluoride without applying voltage (in open circuit).

Elution of fluoride is expected to occur when electrolyte is changed to acidic and the potential is altered to cathode, which forces the F^- to move out from the film and into the waste pool, for the reusability of film. PANI and POT have been shown to have high reproducibility of performance.

Thin PANI film is yellow in reduced form. Upon uptaking fluoride in oxidation form, it turns into black. The colour of thick film is changed from pale green to black in reduced and oxidized form, respectively. POT colour changing is similar to PANI during redox reaction. The porosity of the PANI is the same after growth, before fluoride removal and after regeneration.

In summary: the method using PANI (and others film indicated above) as ESIX for defluoridation of water and wastewater is effective, non-toxic, reproducible, economical and can be applied in wide range of initial fluoride concentration and wide range of pH of electrolyte.

7.4. References

1 J. Schultze and H. Karabulut, *Electrochim. Acta,* 2005, **50**, 1739-1745.

2 M. M. Saleh, C. Weidlich, K. Mangold and K. Jüttner, *J. Appl. Electrochem.,* 2006, **36**, 179-186.

3 M. M. Saleh, *Desalination,* 2009, **235**, 319-329.

4 C. Weidlich, K. Mangold and K. Jüttner, *Electrochim. Acta,* 2001, **47**, 741-745

5 C. Weidlich, K. Mangold and K. Jüttner, *Electrochim. Acta,* 2005, **50**, 5247-5254

6 C. Weidlich, K. Mangold and K. Jüttner, *Electrochim. Acta,* 2005, **50**, 1547-1552

7 S. Zhang, Y. Shao, J. Liu, I. A. Aksay and Y. Lin, *ACS applied materials & interfaces,* 2011, **3**, 3633-3637.

8 Y. Lin, X. Cui and J. Bontha, *Environ. Sci. Technol.,* 2006, **40**, 4004-4009.

9 Y. Zhang, S. Mu, B. Deng and J. Zheng, *J Electroanal Chem,* 2010, **641**, 1-6

10 H. Cui, Q. Li, Y. Qian, R. Tang, H. An and J. Zhai, *Water Res.,* 2011, **45**, 5736-5744

11 H. Cui, Y. Qian, H. An, C. Sun, J. Zhai and Q. Li, *Water Res.,* 2012, **46**, 3943-3950

12 B. Wang, B. Zheng, C. Zhai, G. Yu and X. Liu, *Environ. Int.,* 2004, **30**, 1067-1073.

13 World Health Organization, *Guidelines for drinking-water quality: First addendum to volume 1, Recommendations*, World Health Organization, 2006.

14 Y. Shivarajashankara and A. Shivashankara, *Journal of Clinical and Diagnostic Research [serial online],* 2012, 740-744.

15 G. Jacks, P. Bhattacharya, V. Chaudhary and K. Singh, *Appl. Geochem.,* 2005, **20**, 221-228.

16 Meenakshi and R. C. Maheshwari, *J. Hazard. Mater.,* 2006, **137**, 456-463

17 J. Schoeman and A. Steyn, *WRC Report TT,* 2000, **124.1**.

18 N. Chubar, V. Samanidou, V. Kouts, G. Gallios, V. Kanibolotsky, V. Strelko and I. Zhuravlev, *J. Colloid Interface Sci.,* 2005, **291**, 67-74.

19 Y. Wang and E. J. Reardon, *Appl. Geochem.,* 2001, **16**, 531-539.

20 S. Jagtap, M. K. Yenkie, N. Labhsetwar and S. Rayalu, *Chem. Rev.,* 2012, **112**, 2454-2466.

21 W. W. Focke, G. E. Wnek and Y. Wei, *J. Phys. Chem.,* 1987, **91**, 5813-5818.

22 T. Kobayashi, H. Yoneyama and H. Tamura, *Journal of electroanalytical chemistry and interfacial electrochemistry,* 1984, **161**, 419-423.

23 V. Tomar and D. Kumar, *Chem. Cent. J.,* 2013, **7**, 1-15.

24 M. Habuda-Stanić, M. E. Ravančić and A. Flanagan, *Materials,* 2014, **7**, 6317-6366.

25 R. Maheshwari, *J. Hazard. Mater.,* 2006, **137**, 456-463.

26 P. R. Bidez, S. Li, A. G. MacDiarmid, E. C. Venancio, Y. Wei and P. I. Lelkes, *Journal of Biomaterials Science, Polymer Edition,* 2006, **17**, 199-212.

27 S. Kamalesh, P. Tan, J. Wang, T. Lee, E. Kang and C. Wang, *J. Biomed. Mater. Res.,* 2000, **52**, 467-478.

28 M. Karthikeyan, K. Satheeshkumar and K. Elango, *J. Hazard. Mater.,* 2009, **163**, 1026-1032.

29 M. Karthikeyan, K. Satheeshkumar and K. Elango, *J. Hazard. Mater.,* 2009, **167**, 300-305.

30 M. Karthikeyan, K. Satheesh Kumar and K. Elango, *J. Fluorine Chem.,* 2009, **130**, 894-901.

31 M. Karthikeyan, K. Kumar and K. Elango, *Desalination,* 2011, **267**, 49-56.

32 M. Karthikeyan, K. Satheesh Kumar and K. Elango, *Environ. Technol.,* 2012, **33**, 733-739.

33 M. Bhaumik, T. Y. Leswifi, A. Maity, V. Srinivasu and M. S. Onyango, *J. Hazard. Mater.,* 2011, **186**, 150-159.

34 E. Subramanian and R. D. Ramalakshmi, *J. Sci. Ind. Res.,* 2010, **69**, 621-628.

35 W. Huang, B. D. Humphrey and A. G. MacDiarmid, *Journal of the Chemical Society, Faraday Transactions 1: Physical Chemistry in Condensed Phases,* 1986, **82**, 2385-2400.

Chapter 8: General Conclusions and Future Work

8.1. General Conclusions

Prior to the characterisation of PANI modified electrodes, its derivatives (POAP and POT) and copolymers [P(ANI-OT) and P(ANI-OAP)], their growth mechanism were studied. While POT and PANI growth result from an autocatalytic reaction, POAP growth does not. After some cycles, mass of the POAP film increased but the electroactive area of the film was constant. Mass-charge ratio of POAP during deposition was significantly higher than mass-charge ratio of POT and PANI films. Therefore, the use of POAP is not as effective as POT and PANI for energy storage devices. While early oxidation stage of PANI and POT is associated with proton exit and the latter stages were associated with anion entry, POAP is a cation dominated reaction during redox cycling in aqueous acidic medium. The ratio of the two monomers and the number of scans forming copolymer influence the electrocopolymerisation and the electrochemical behaviour of the copolymers produced. One of the monomers can be dominant in electrocopolymerisation depending on its ratio and the numbers of polymerisation scan. The resulting film can illustrate similar optical behaviour to the dominant one shown by FTIR.

The viscosity, the most significant physical property of electrolyte diffusion, was determined by QCM across wide range of temperature (25 °C to 80 °C). When the viscosity of DESs obtained from the QCM data were compared to the viscosity value obtained from rotational viscometer RV, it was found that two set of the results were different at some temperatures due to the temperature dependent behaviour of DESs. Quartz crystal impedance analysis was for the first time used to determine the change in fluid behaviour from/to Newtonian depending on the temperature.

Ethaline, which is Newtonian at low temperatures (25 °C – 40 °C), deviated from Newtonian behaviour with increasing temperature. However, Reline and Glyceline which are non-Newtonian at low temperatures, become Newtonian at high temperatures (60 °C – 80 °C). Values of viscosity obtained from the QCM have a good agreement with viscosity obtained from RV at the temperature ranges where the DESs are Newtonian. Therefore, the activation energy of viscous flow of DESs, calculated from the QCM data, were identical to the activation energy of the viscosity obtained

from RV data when the QCM data represent that a DES is Newtonian. The activation energies of viscous flow of DESs are around 40 kJ mol^{-1} (approximately 4 kJ mol^{-1} for water).[1] While the viscosities of DESs do not obey Arrhenius-like behaviour for the temperature range between 25 °C and 90 °C, they can obey Arrhenius-like equation at the limited range of temperature depending on the DESs.

One of the major issues electrochemists attempt to find the solutions are to design energy storage devices for sustainable environment.[2] As charge transfer and mass transports in energy storage devices can be improved by using nano materials having more surface area leading to an increase in the power.[3] One suggestion is to design three-dimensional multifunctional nanoscale electrodes.[4] However, polymer modified electrodes themselves are porous in nature and offer a large reactive surface area having an intrinsically 3D reaction zone. Therefore, a great species flux can enter into the bulk of the polymer modified films leading to an increase in the capacitance which makes them suitable candidate for energy storage devices.

After characterisation of modified electrodes and DESs electrolyte, ion dynamics of the PANI in DESs electrolyte were investigated for supercapacitor applications. PANI films, prepared from aqueous solution and transferred into DESs, takes long duration to reach equilibrium from anion transfer domination to cation transfer domination. The equilibrium time is ranging from tens to thousands of potential cycles depending on the surface population and growth conditions. The evolution of ion transfer characteristics of thick PANI films (>100 nmol cm^{-2}), changed from anion transfer domination to cation transfer domination (after thousands of scans), is slower than thin film (tens of scans for Γ > 40 nmol cm^{-2}) during redox switching.

Generally thinner modified films more likely have surface control mechanism which is desirable properties for energy storage devices. However, the results showed that the rate limiting process does not just depend on film coverage but also depends on the growth conditions of the films in which changes in the growth conditions such as scan rate, potential window during polymerisation could lead to different switching responses and performance of resulting films.

The ions of DESs in PANI film behave in a different manner depending on film thickness and growth conditions. Generally, thin PANI films have a more cation dominated reaction (more negative molar mass of ion exchange) during redox switching. Thick films have two significant characteristics depending on timescale. When the cation in Ethaline (Ch^+) could not diffuse out from the thick films at higher scan rate ($v > 100$ mV s^{-1}), the overall mass change of PANI film throughout redox reaction is almost zero. However, at longer timescale, as there is sufficient time for the movement of Ch^+ ions, the mass of the film decreases during the oxidation process at slow scan rates ($v < 20$ mV s^{-1}). Not only potential scan rate, growth conditions and surface population affect the ion dynamics of PANI but also temperature of electrolyte can change it. EG_2Cl^- ion transfer from/to film is faster with increasing the temperature electrolyte as the fraction of Ch^+ decreases during redox switching of PANI in Ethaline. Ch^+ fraction for all variables were between 0.45 and 0.87, corresponded the values of $\Delta mF/Q$ from 44 g mol^{-1} to -69 g mol^{-1}.

The type of HBD forming electrolyte also affects the dynamic of PANI reaction in DESs as mass directions are different and the fraction of ion exchange is independent of the size of the HBDs. PANI film has excellent electrochemical stability in Ethaline, Glyceline and Wateline but PANI film cycling in Reline loses rapidly its electrochemical activity. No colour change was observed on the PANI films cycled in Ethaline, Glyceline, Wateline and Propaline but the green-yellow colour of PANI changed to black after first oxidation in Reline.

Normally PANI is not electroactive when pH > 4 but it is electroactive in DESs which is attributed to the conversion of leucoemeraldine salt to emeraldine salt during p-doping and *vice versa* during un-doping. PANI and copolymers were used in another non-acidic (pH = 8.6) medium to extract fluoride ion from water. At the beginning of the study, copolymers were designed to use PANI based copolymers in neutral/basic solution. However sometimes later it was found that PANI itself could be used for defluoridation of water.

As more porous surface electrodes have higher electroactive area and are desirable for energy storage devices, porous membranes are also required for water treatment. The

oxidation process of PANI, accompanied by fluoride uptake at pH 8.6, makes PANI electroinactive and hence reduction of PANI$^+$F$^-$ does not result in fluoride elimination to the basic solution. The key word here is the "basic solution". If PANI$^+$F$^-$ is transferred to an aqueous acidic medium, elution of fluoride is possible. This simple method, which is uptaking fluoride from basic fluoridated solution and eliminating it in the acidic solution, can be effectively used for defluoridation of water.

POT and its combinations with PANI [P(ANI-OT) copolymers) can extract fluoride from water but POAP and P(ANI-OAP) (80:20) copolymer could not be used for defluoridation. PANI and POT have been shown to have high reproducibility performance (even after 20 regenerations).

PANI can be used for defluoridation of water having wide range of NaF concentration. The fluoride extracted can be hold by PANI under open circuit. The colour of PANI film in reduced form (yellow or green depending on thickness) turns into black upon uptaking fluoride in oxidised form. During reduction of PANI in acidic medium for elimination of fluoride, the colour of PANI film turns into colour of leucoemeraldine base (yellow-green) but the porosity of the PANI film is the same before and after fluoride removal.

The method using PANI as ESIX for defluoridation of water and wastewater is effective, non-toxic, reproducible, economical and ease of application in wide range of initial fluoride concentration and wide range pH of electrolyte.

8.2. Future Work

PANI nanostructures have been studied intensively since the last decade to enhance the performance of PANI film in wide range of application (reviewed recently).[5] As the work presented in this thesis showed energy capacitance behaviour and ion dynamics of bare PANI in DESs and found that growth condition (in some cases rather than surface population) can significantly affect rate limiting process. Some of the nanostructured PANI films and composites of PANI (or copolymer) can be synthesized and tested for energy storage performance. PANI films grown in aqueous acidic

solution transferred to DESs in the current research and the equilibrium between PANI film and DESs took long duration. PANI film can be grown in DESs medium and cycled in the same deposition solution (*i.e.* without medium change) to examine the stability and ion exchange dynamics during redox switching.

As the viscosity of DESs were measured between 25 °C and 80 °C by means of the QCM and found that they can deviate from Newtonian behaviour in certain temperatures, the range of temperature could be widened to observe how their behaviour change continuously depending on temperature. New cells could be designed for measurement of multiple physical behaviour of the electrolytes.

The most critical aspect for electrochemical sensors and membrane is selectivity. As expected, it is a major issue for conducting polymers as well. Recently, PEDOT deposited on glassy carbon electrode was coated with potassium selective membranes to use as ion-to-electron transducer.[6] The same strategy could be used for PANI films for defluoridation. A fluoride ion selective membrane can be deposited on the top of PANI for high selectivity.

8.3. References

1 R. Horne, R. Courant, D. Johnson and F. Margosian, *J. Phys. Chem.,* 1965, **69**, 3988-3991.

2 D. Larcher and J. Tarascon, *Nature Chemistry,* 2014, **7**, 19-29.

3 P. V. Braun and R. G. Nuzzo, *Nature Nanotechnology,* 2014, **9**, 962-963.

4 D. R. Rolison, J. W. Long, J. C. Lytle, A. E. Fischer, C. P. Rhodes, T. M. McEvoy, M. E. Bourg and A. M. Lubers, *Chem. Soc. Rev.,* 2009, **38**, 226-252.

5 G. Ćirić-Marjanović, *Synth. Met.,* 2013, **177**, 1-47.

6 U. Vanamo and J. Bobacka, *Electrochim. Acta,* 2014, **122**, 316-321.